

AN ABSTRACT OF THE DISSERTATION OF

Preeti Mani for the degree of Doctor of Philosophy in Mechanical Engineering
presented on October 29, 2012.

Title: Local Heat Transfer Rate and Bubble Dynamics during Jet Impingement
Boiling.

Abstract approved:

Vinod Narayanan

Characterization of local boiling trends, in addition to the typically reported area-averaged trends, is essential for the robust design and implementation of phase change technologies to sensitive heat transfer applications such as electronics cooling. Obtaining the values of heat fluxes corresponding to locally varying surface temperatures has been a challenge limiting most investigations to area-averaged results. This thesis illustrates the importance of a spatially local heat transfer analysis during boiling.

Pool and submerged jet impingement boiling scenarios on a silicon surface are considered at the macroscale (27.5 mm heater with multiple nucleation sites) and microscale (1000 μm heater for isolated bubble generation), by the use of two thin

film serpentine heater geometries. The macroscale heater highlights the effect of spatial variations in imposed heat flux on boiling heat transfer with a circumferentially uniform but radially non-uniform heat flux distribution. The microscale heater simulates a local hot-spot for spot cooling on an electronic device.

Spatial variation in boiling heat transfer and bubble dynamics with and without a jet flow are documented using thin film voltage sensors along with qualitative and quantitative high speed imaging and infra-red thermography. Unique to this study is the documentation of local boiling curves for different radial locations on the heat transfer surface and their comparison with the corresponding area-averaged representations. It is shown here that sectionally averaged representations of boiling curves over regions of like-imposed heat flux can substantially simplify the interpretation of data while retaining important information of the local variations in heat transfer.

The radial influence of the convective jet flow on the bubble dynamics and boiling heat transfer is assessed for a single circular submerged jet configuration. Varied parameters include jet exit Reynolds numbers, nozzle geometry, test fluid (deionized water and FC-72), fluid subcooling and the supplied heat flux. Distinct modifications of the surface temperature distribution imposed by the impinging jet flow are highlighted by comparing radial temperature profiles during pool and jet impingement boiling. It is demonstrated that in contrast with pool boiling, thermal overshoots

during jet impingement boiling for a highly wetting fluid like FC-72 are highest in regions farthest from the impingement point.

The effect of jet inertia on bubble departure characteristics are compared with pool boiling under subcooled conditions for FC-72. Qualitative high speed visualization indicates the presence of two modes of bubble generation during jet impingement boiling (a) bubble departure from the surface and (b) bubble separation from the source resulting in sliding bubbles over the surface. The effect of jet flow on bubble entrainment is depicted. Quantitative results indicate that in general departure diameters for pool and jet impingement boiling increase and plateau at a maximum value with increasing power input while no notable trends were observed in the corresponding departure frequencies. The largest departure diameters for jet impingement boiling at fixed fluid subcoolings of 10°C and 20°C were found to be smaller than that for the corresponding pool boiling test by a factor of 1.6 and 2.3, respectively.

©Copyright by Preeti Mani

October 29, 2012

All Rights Reserved

Local Heat Transfer Rate and Bubble Dynamics during Jet Impingement Boiling

by

Preeti Mani

A DISSERTATION

submitted to

Oregon State University

in partial fulfillment of
the requirements for the
degree of

Doctor of Philosophy

Presented October 29, 2012

Commencement June 2013

Doctor of Philosophy dissertation of Preeti Mani presented on October 29, 2012.

APPROVED:

Major Professor, representing Mechanical Engineering

Head of the School of Mechanical, Industrial and Manufacturing Engineering

Dean of the Graduate School

I understand that my dissertation will become part of the permanent collection of Oregon State University libraries. My signature below authorizes release of my dissertation to any reader upon request.

Preeti Mani, Author

ACKNOWLEDGEMENTS

The completion of this journey owes thanks to some very special people. First and foremost I thank my parents, my in-laws and husband Devdeep for their endless love and patience. I am especially grateful to my sister Priya and brother-in-law Adwait for being my pillars and inspiration always. Special thanks to my niece Annika and nephew Krish for their priceless smiles. I thank my advisor, Dr. Vinod Narayanan for this challenging research opportunity that has helped me professionally and my master's advisor Dr. Heiner Linke for his support and encouragement when it was most needed. I am grateful to my doctoral committee members, Dr. Pence, Dr. Apte, Dr. Liburdy and Dr. Spitz for their time and guidance. I am indebted to Ruander Cardenas for all his collaboration and valuable advice. Thanks to Rick Presley for the clean-room training and to Brian Pelatt and Ram for help with the E-beam deposition. Special mention goes to Eric Truong and Thomas L'Estrange for their assistance with machining and IR file format conversions. Thanks to Shashank Natesh and Naveenan Thiagarajan for assisting with the high speed image processing algorithms. I acknowledge the assistance of ASE interns Connor Dokken (facility setup), Joseph Kleinhenz and Nakul Sridhar (contact angle algorithm and experiment). Finally, I thank my wonderful friends and colleagues: Mohammad Ghazvini, Erfan Rasouli, Logan Strid, Florian Kapsenberg, Bryan Kilgore, Chris Stull, Benn Eilers, David Haley, Hadi Tabatabaee, Mahshid Mohammadi, Saran Salakij and Vishal Patil for all their help and support along the way.

TABLE OF CONTENTS

	<u>Page</u>
1	INTRODUCTION.....2
2	LITERATURE REVIEW.....7
2.1	THE BOILING CURVE 7
2.2	BOILING INCIPIENCE OF DIELECTRIC FLUIDS 11
2.3	SUBMERGED JET IMPINGEMENT 14
2.4	LOCAL ESTIMATION OF BOILING HEAT TRANSFER 18
2.5	ISOLATED BUBBLE- DEPARTURE CHARACTERISTICS AND HEAT TRANSFER..... 24
2.5.1	CONTROLLED ACTIVATION OF NUCLEATION SITES 25
2.5.2	BUBBLE DEPARTURE DIAMETER AND FREQUENCY 27
2.5.3	HEAT TRANSFER MECHANISMS 32
3	OBJECTIVES39
4	EXPERIMENTAL FACILITY AND METHODS.....43
4.1	TEST FACILITY 43
4.2	VISUALIZATION INSTRUMENTATION 49
4.2.1	HIGH SPEED CAMERA SPECIFICATIONS..... 49
4.2.2	IR CAMERA SPECIFICATIONS 51
4.3	SILICON TEST SECTIONS AND MOUNT..... 52
4.3.1	MACROSCALE HEATER TEST SECTION 53
4.3.2	MACROSCALE TEST SECTION MOUNT 59
4.3.3	MICROSCALE HEATER TEST SECTION..... 61

TABLE OF CONTENTS (Continued)

	<u>Page</u>
4.3.4	MICROSCALE TEST SECTION MOUNT 67
4.4	EXPERIMENTAL PROCEDURES 70
4.4.1	IR CALIBRATION..... 70
4.4.2	HIGH SPEED CAMERA CALIBRATION 72
4.4.3	SUBMERGED JET IMPINGEMENT BOILING WITH WATER: MACROSCALE HEATER SUBSTRATE..... 74
4.4.4	SUBMERGED JET IMPINGEMENT BOILING WITH FC-72: MACRO AND MICROSCALE HEATER SUBSTRATES 77
4.4.5	CONDUCTED EXPERIMENTS 80
5	DATA REDUCTION AND ANALYSIS83
5.1	JET FLOW RATE..... 83
5.2	POOL AND JET TEMPERATURES 84
5.3	IR DATA REDUCTION AND ANALYSIS 85
5.3.1	IR DATA ANALYSIS: MACROSCALE HEATER..... 85
5.3.2	IR DATA ANALYSIS: MICROSCALE HEATER 100
5.4	HIGH SPEED DATA REDUCTION..... 109
5.4.1	HIGH SPEED DATA: MACROSCALE HEATER 109
5.4.2	HIGH SPEED DATA: MICROSCALE HEATER..... 110
5.5	THIN FILM SENSOR DATA REDUCTION 115
5.5.1	SENSOR DATA: MACROSCALE HEATER 115
5.5.2	SENSOR DATA: MICROSCALE HEATER..... 118
5.6	UNCERTAINTY ESTIMATES 124

TABLE OF CONTENTS (Continued)

	<u>Page</u>
6	MACROSCALE HEATER RESULTS..... 132
6.1	COMPARISON OF AREA-AVERAGED AND LOCAL BOILING CURVES DURING POOL AND JET IMPINGEMENT BOILING 133
6.1.1	LOCAL VERSUS AREA-AVERAGED BOILING CURVES..... 134
6.1.2	SECTIONALLY-AVERAGED BOILING CURVES..... 137
6.1.3	SECTIONAL VERSUS AREA-AVERAGED BOILING CURVES.... 142
6.2	GLOBAL TRENDS AND SPATIAL VARIATIONS DURING POOL AND SUBMERGED JET IMPINGEMENT BOILING 147
6.2.1	FLUID DI WATER: 20°C SUBCOOLED BOILING..... 147
6.2.2	FLUID FC-72: SATURATED AND 20°C SUBCOOLED BOILING . 162
6.2.3	COMPARISON OF WATER AND FC-72 –AT 20°C SUBCOOLED CONDITIONS 184
6.2.4	MITIGATION OF TEMPERATURE OVERSHOOT 187
7	MICROSCALE HEATER RESULTS194
7.1	MICROSCALE INVESTIGATION OF POOL BOILING..... 194
7.1.1	BOILING INCEPTION- SUBCOOLING EFFECTS 196
7.1.2	VISUALIZATION OF SUBCOOLED POOL BOILING..... 200
7.1.3	BUBBLE DEPARTURE CHARACTERISTICS DURING SUBCOOLED POOL BOILING..... 204
7.1.4	LATENT HEAT CONTRIBUTION TO HEAT TRANSFER DURING POOL BOILING..... 218
7.2	MICROSCALE INVESTIGATION OF JET IMPINGEMENT BOILING 219
7.2.1	INCEPTION OF BOILING IN THE PRESENCE OF JET FLOW 221

TABLE OF CONTENTS (Continued)

	<u>Page</u>
7.2.2 SJIB- BUBBLE DYNAMICS AND SUBCOOLING EFFECTS	224
7.2.3 BUBBLE DEPARTURE CHARACTERISTICS DURING SUBCOOLED SJIB	233
7.2.4 LATENT HEAT TRANSFER DURING SJIB	245
7.3 POOL VERSUS JET IMPINGEMENT BOILING	248
8 CONCLUSIONS AND FINAL REMARKS	253
8.1 SUMMARY	253
8.2 MAJOR CONTRIBUTIONS	258
8.3 LIST OF PUBLICATIONS	259
8.4 RECOMMENDATIONS FOR FUTURE WORK	261
BIBLIOGRAPHY	265
APPENDICES	275

LIST OF FIGURES

<u>Figure</u>	<u>Page</u>
1. Typical pool boiling curve depicting a qualitative dependence of convective heat flux on wall superheat for a controlled heat flux surface	8
2. Bubble ebullition cycle	9
3. Pool boiling curve for a dielectric liquid for a controlled heat flux surface with increasing and decreasing heat flux.....	12
4. Flow field of a submerged jet.....	14
5. Types of artificial nucleation cavities	24
6. Vertical force balance on a bubble departing from the surface	28
7. Mechanisms of heat transfer during (A) Bubble growth (B) Bubble departure (Figure adapted from Kim [62])	34
8. Schematic of experimental facility.....	44
9. Modified test facility for FC-72	47
10. High speed visualization set-up	50
11. Macroscale serpentine heater pattern	54
12. Fabrication sequence for photolithography and metal deposition	56
13. Macroscale silicon test substrate with aluminum thin film heater and voltage sensors	58
14. Macroscale heater surface preparation for mounting.....	59
15. Exploded view schematic of the macroscale test section mount	60
16. Macroscale heater substrate mount: (a) IR viewport and electrical connections; (b) chamfered clamp; (c) assembled test section	60

LIST OF FIGURES (Continued)

<u>Figure</u>	<u>Page</u>
17. Photomask design for the microscale heater and voltage sensors.....	62
18. Estimating the exposure and develop times for the microscale heater pattern (initial trials on glass substrates).....	64
19. Before (a) and after (b) the removal of resist residues (silicon substrate)	65
20. Example of an incomplete metal lift-off and poor film adhesion	66
21. Completed microscale heater	66
22. Schematics of microscale test section mount- top view (left) and sectional front view (right).....	68
23. Microscale test section mount assembly	69
24. Image of the calibration dot grid within a pool of FC-72 at room temperature conditions	73
25. A section of the calibration grid in FC-72 at 10°C and 20°C subcooled pool conditions	73
26. Time-averaged calibration temperature maps of the macroscale heater substrate for three temperatures during calibration with DI water	87
27. A time-averaged and calibrated IR temperature map of the macroscale heater in its original size (256 × 236 pixels). Temperatures in °C.	88
28. Temperature map for the macroscale heater filtered using a top hat filter and cropped to the region of interest. Temperature scale in °C.....	89
29. Energy balance on a (pixel) control volume	90

LIST OF FIGURES (Continued)

<u>Figure</u>	<u>Page</u>
30. Binary template of the macroscale heater. The substrate area corresponding to the serpentine heater (A_s) and the area occupied by the length of heater rings (A_h) are depicted.	92
31. Template of radial locations.....	93
32. Convective heat flux in W/cm^2 for an impinging jet non-boiling condition.....	94
33. Binary representation of the symmetric semi-circular region of the heater geometry	95
34. Filtered temperature in $^{\circ}C$ (a) and convective heat flux in W/cm^2 (b) corresponding to the symmetric semi-circular region of the heater geometry. (Impinging jet non-boiling condition).....	96
35. Comparison of the net input electrical heat flux with area-averaged heat flux values plotted as function of area-averaged temperature difference. The fluid was DI water subcooled by $20^{\circ}C$	99
36. Need for IR image alignment during microscale heater tests	100
37. Instantaneous calibration image cropped to the region of interest.....	101
38. Surface plot of the normalized cross correlation correlation matrix. Location of the best match between compared images is identified by the peak intensity.....	102
39. Crop area selected in the original data image based on the output of the normalized cross correlation	103
40. Calibration and data images overlaid (a) before and (b) after alignment	104
41. Time-averaged calibration temperature maps of the microscale heater substrate for three temperatures during calibration with FC-72. Note: Scale does not correspond to actual temperatures.	105

LIST OF FIGURES (Continued)

<u>Figure</u>	<u>Page</u>
42. Reflections due to the Narcissus effect in the microscale heater images acquired with the IR microlens.	106
43. Calibrated temperature maps of the microscale heater substrate for three temperatures during calibration with FC-72.	107
44. Heated sections of the microscale heater	108
45. Image processing steps for isolated bubble visualization (Example shown for a pool boiling image)	112
46. Plot of bubble diameters over time with departure diameters identified as peaks for a 20°C subcooled pool boiling test at 6.44W	114
47. Sectional areas captured by the macroscale thin film sensors	116
48. Non-boiling condition for $Re_{jet} = 0$ (a) sensor time series (b) calibrated IR map (°C) (c) high speed image of the surface.....	118
49. Sectional areas captured by the microscale thin film sensors	119
50. Un-filtered sensor voltage time series and frequency spectrums for a non-boiling condition (0.04W) during 20°C subcooled pool boiling of FC-72	121
51. Filtered sensor voltage time series (a) and frequency spectrums (b,c) for a non-boiling condition (0.04W) during 20°C subcooled pool boiling of FC-72	122
52. Un-filtered and filtered voltage time series for boiling condition (8.64W) during 20°C subcooled pool boiling of FC-72	123
53. Heater sections (a) and local versus area-averaged boiling curves (b) (Results for DI water subcooled by 20°C, $Re_{jet} = 5161$).....	135
54. Local versus sectionally-averaged boiling curve for pool boiling - heated section H2 (Fig. 53a). results for DI water subcooled by 20°C.	138

LIST OF FIGURES (Continued)

<u>Figure</u>	<u>Page</u>
55. Local versus sectionally-averaged boiling curve for SJIB - heated section H2 (DI water subcooled by 20°C, $Re_{jet} = 5161$).....	140
56. Local versus sectionally-averaged boiling curve for SJIB - heated section H1 (DI water subcooled by 20°C, $Re_{jet} = 5161$).....	141
57. Comparison of sectionally averaged and area-averaged boiling curves for pool boiling with DI water at 20°C subcooling (a) On heated sections (H1, H2 and H3) (b) on unheated sections (UH1, UH2, UH3).....	143
58. Comparison of sectionally averaged and area-averaged boiling curves for SJIB with DI water at 20°C subcooling (a) On heated sections (H1, H2 and H3) (b) on unheated sections (UH1, UH2, UH3)	145
59. Visualization of spatial variations with increasing flux for pool boiling ($Re_{jet} = 0$)	149
60. Visualization of spatial variations with increasing flux for SJIB ($Re_{jet} = 2580$). High speed image (a) IR map (b) and sensor voltage PDF for S_1 (c) and S_2 (d) .	154
61. Pool versus SJIB: thermal distribution on the surface	156
62. Pool versus SJIB – boiling curves for sections H1, H2 and H3.....	160
63. Boiling hysteresis of saturated FC-72 during submerged jet impingement for $Re_{jet} = 5161$	164
64. Saturated pool and jet impingement boiling of FC-72 for increasing and decreasing heat flux conditions.....	167
65. Comparison of saturated and subcooled pool boiling with FC-72.....	169
66. SJIB of FC-72 under saturated and subcooled conditions for $Re_{jet} = 5161$	169

LIST OF FIGURES (Continued)

<u>Figure</u>	<u>Page</u>
67. $Re_{jet} = 7740$ subcooled $20^{\circ}C$ (a) IR temperature map of the surface just prior to CHF at $\sim 22.8W/cm^2$ (b) screen shot of surface undergoing CHF	172
68. Area-averaged boiling curves for submerged jet impingement boiling of FC-72 under (a) saturated and (b) subcooled conditions	174
69. FC-72 saturated pool boiling- radial temperature profiles with increasing heat flux	176
70. Sectional boiling curves for FC-72 (a) saturated (b) subcooled pool boiling	178
71. SJIB of saturated FC-72 $Re_{jet}=5161$ - radial temperature profiles with increasing heat flux.....	180
72. SJIB of saturated FC-72 $Re_{jet}= 7740$ - radial temperature profiles with increasing heat flux.....	181
73. Sectional boiling curves for saturated SJIB FC-72 ($Re_{jet}=7740$).....	183
74. Comparison of Water and FC-72 under $20^{\circ}C$ subcooled pool conditions (a) pool boiling (b) jet impingement boiling $Re_{jet}= 5161$	185
75. Self -cavitating jet nozzle geometry.....	189
76. SJIB with the self-cavitating jet nozzle ($Re_{jet} = 10616$) during increasing and decreasing heat flux conditions.....	190
77. Radial temperature profiles (a) and high speed images of the transition to phase change (b-g) during SJIB with a self-cavitating jet	192
78. Inception of boiling during pool boiling of FC-72 at $10^{\circ}C$ subcooled pool condition (6.9 W). Field of view (5.2 mm x 5.26 mm).....	196
79. Inception of boiling during pool boiling of FC-72 at $20^{\circ}C$ subcooled pool condition (9.3 W). Field of view (5.2 mm x 5.26 mm).....	199

LIST OF FIGURES (Continued)

<u>Figure</u>	<u>Page</u>
80. Visualization time series of a bubbling event at ~6.5W during (a) 10°C and (b) 20°C subcooled pool boiling of FC-72	201
81. Visualization time series of a bubbling event at ~5.8W during (a) 10°C and (b) 20°C subcooled pool boiling of FC-72	202
82. Time variation of bubble departure diameter and departure frequency at ~6.5 W during 10°C and 20°C subcooled pool boiling of FC-72.....	205
83. Time variation of bubble departure diameter and departure frequency at ~5.8 W during 10°C and 20°C subcooled pool boiling of FC-72.....	206
84. Instantaneous calibrated temperature maps and radial temperature profiles of the surface during subcooled pool boiling at 6.5 W	210
85. Instantaneous calibrated temperature maps and radial temperature profiles of the surface during subcooled pool boiling at 5.8 W	211
86. Variation in bubble departure diameters with input power during pool boiling with FC-72	213
87. Variation in bubble departure frequency with input power during pool boiling with FC-72	213
88. Vertical coalescence and multiple bubble generation observed at high power input (10°C subcooled pool boiling of FC-72).....	215
89. Variation in the product $f_d D_b$ with power during subcooled pool boiling of FC-72	217
90. Latent heat contribution during subcooled pool boiling	218
91. Schematic of the flow configuration used for the microscale investigation of jet impingement boiling (not to scale)	220

LIST OF FIGURES (Continued)

<u>Figure</u>	<u>Page</u>
92. Inception of boiling for 10°C subcooled FC-72 in the wall jet region at a distance of 1.5 mm ($3d_{jet}$) from the impingement point (7.47 W)	221
93. Image taken right after the inception of boiling for 20°C subcooled SJIB	224
94. Visualization time series of a bubbling event at 10.05W during (a) 10°C and (b) 20°C subcooled submerged jet impingement boiling of FC-72.....	225
95. Visualization time series of a bubbling event at ~7.4W during (a) 10°C and (b) 20°C subcooled submerged jet impingement boiling of FC-72.....	226
96. Inability of the image processing algorithm to determine sliding bubble diameters	229
97. Visualization of sliding bubbles during SJIB at 7.25W (20°C subcooling). Field of view (3.8 mm x 0.9 mm).....	230
98. Entrainment and recirculation of small vapor bubbles in the jet flow field at 3.7W (10°C subcooled SJIB).....	232
99. Entrainment of a large bubble in the jet flow field at 10.05W in 10°C subcooled SJIB	232
100. Example of multiple off-surface bubble departures in the vicinity of the source	233
101. Time variation of bubble departure diameters at 10.05 W and 8.5 W during 10°C and 20°C subcooled SJIB of FC-72.....	235
102. Variation in bubble departure diameters with input power during SJIB with FC-72	237
103. Example of successive bubble departures of widely different sizes during SJIB	238

LIST OF FIGURES (Continued)

<u>Figure</u>	<u>Page</u>
104. Variation in departure frequencies with power during SJIB (a) evaluated from largest departure diameters (b) evaluated by manual counting of bubble departures.....	240
105. Voltage time series and FFT spectrum of a non-boiling power level (0.1 W) during 20°C subcooled SJIB test	241
106. FFT spectrum of the sensor time series during SJIB	242
107. Instantaneous calibrated surface temperature maps and radial temperature profiles during SJIB	244
108. Latent heat transfer estimates during SJIB (a) evaluated from largest departure diameters (b) evaluated by manual counting of bubble departures	246
109. Pictographic comparison of boiling inception during pool and SJIB boiling at 10°C subcooling	249
110. Departure mechanisms during pool boiling and SJIB.....	250

LIST OF TABLES

<u>Table</u>	<u>Page</u>
1. Matrix of experiments conducted with the macroscale heater.....	82
2. Matrix of experiments conducted with the microscale heater using a regular jet nozzle.....	82
3. Expected temperature drop across the 380 μm thick silicon substrate using a 1-D model at the highest average heat flux	91
4. Uncertainty estimates of measured quantities.....	125
5. Uncertainty estimates for circumferentially averaged quantities.....	128
6. Average bubble departure diameters and corresponding standard deviations for select cases during pool boiling.....	207
7. Average bubble departure frequencies and corresponding standard deviations for select cases during pool boiling.....	208
8. Average bubble departure diameters and corresponding standard deviations for select cases during SJIB	236

LIST OF APPENDICES

<u>Appendix</u>	<u>Page</u>
A. PROPERTIES OF TEST FLUIDS.....	276
B. THIN FILM HEATER FABRICATION PROCEDURES AND PROCESS RECIPES.....	278
C. DETAILED PART DRAWINGS	284
D. ESTIMATION OF NATURAL CONVECTION LOSS (MACROSCALE HEATER)	290
E. MACROSCALE HEATER- IR CALIBRATION CURVES ...	294
F. TOP HAT FILTERING AND CONTROL VOLUME GRID INDEPENDENCE FOR IR MAPS (MACROSCALE HEATER)	300
G. MICROSCALE HEATER- IR IMAGE CALIBRATION	306
H. MATRIX OF EXPERIMENTS	313
I. COPPER VERSUS SILICON - EFFECT OF SURFACE MATERIAL ON JET IMPINGEMENT BOILING OF FC-72315	
J. RADIAL PROFILES OF THE HEAT TRANSFER COEFFICIENT FOR DI WATER (MACROSCALE HEATER)	318
K. SECTIONALLY-AVERAGED BOILING CURVES FOR SUBCOOLED FC-72 ON HEATED REGIONS H1, H2, AND H3 (MACROSCALE HEATER)	323

LIST OF APPENDICES (Continued)

L. CONTACT ANGLE MEASUREMENTS OF WATER ON
SILICON SUBSTRATE327

LIST OF APPENDIX FIGURES

<u>Figure C</u>	<u>Page</u>
1. Circular polycarbonate clamp for macroscale heater test substrate	285
2. Macroscale heater test substrate mount.....	286
3. C-clamps for microscale heater test substrate	287
4. Microscale heater test substrate mount	288
5. Test chamber bottom flange for IR Visualization.....	289
 <u>Figure D</u>	
6. Illustration of IR visualization set-up (a) and comparative illustration of the set-up for evaluating heat loss by natural convection	291
 <u>Figure E</u>	
7. Macroscale heater pixel (98,154) (a) boxed location on IR map (b) corresponding calibration curve for calibration experiment with DI water	295
8. Macroscale heater pixel (148,154) (a) boxed location on IR map (b) corresponding calibration curve for calibration experiment with DI water	296
9. Macroscale heater pixel (69,125) (a) boxed location on IR map (b) corresponding calibration curve for calibration experiment with FC-72	297
10. Macroscale heater pixel (119,125) (a) boxed location on IR map (b) corresponding calibration curve for calibration experiment with FC-72.....	298
11. Macroscale heater pixel (119,175) (a) boxed location on IR map (b) corresponding calibration curve for calibration experiment with FC-72.....	299

LIST OF APPENDIX FIGURES (Continued)

Figure F

12. Temperature maps of the macroscale heater substrate at 66 W/cm^2 in two-dimensional (left) and three-dimensional (right) representation shown for zero, one and two passes of the top hat filter..... 302

Figure G

13. First, second and fourth order calibration curves for a pixel location on the heater 307
14. Comparison of IR temperature maps obtained from first, second, and fourth order calibration fits at each pixel. 308
15. Comparison of first and second order calibration curves for on and off-heater locations 310
16. Calibration curves with temperatures top-hat filtered once 311
17. Calibration curves with temperatures top-hat filtered twice 312

Figure I

18. SJIB of FC-72 on copper and silicon surfaces 317

Figure J

19. Circumferentially averaged profiles of the heat transfer coefficient obtained with DI water at 66 W/cm^2 computed using (a) q''_{elec} (b) $q''_{conv}(r)$ 320

Figure K

20. Sectional boiling curves for 20°C subcooled FC-72 over the heated sections (a) H1 (b) H2 and (c) H3 of the macroscale heater substrate 325

LIST OF APPENDIX FIGURES (Continued)

Figure L

21. Set-up for sessile drop experiment.....	328
22. Droplet shape before and after release	329
23. Change in the profile of a water droplet on the silicon substrate as a function of time.....	329
24. Variation in the average contact angle of a water droplet on a silicon surface with time.....	330

LIST OF APPENDIX TABLES

<u>Table A</u>	<u>Page</u>
1. Thermo-physical fluid properties at atmospheric pressure	277
<u>Table B</u>	
2. Fabrication process for the macroscale heater substrate	279
3. Fabrication process for the microscale heater substrate.....	281
4. Equipment used for substrate fabrication at the OSU EECS cleanroom	283
<u>Table D</u>	
5. Estimated natural convection heat loss for a SJIB test case with saturated FC-72 ($Re_{jet} = 5161$)	292
<u>Table F</u>	
6. Result of increasing control volume dimensions	304
<u>Table H</u>	
7. Matrix of experiments conducted with the macroscale heater with subcooling details	314
8. Matrix of experiments conducted with the microscale heater using a regular jet nozzle with subcooling details.....	314

NOMENCLATURE

Roman

A area [m^2]

A_s heated substrate area [m^2]

A_h area occupied by the heater length [m^2]

c_p specific heat at constant P [J/kg-K]

d diameter [m]

D_b bubble departure diameter [mm]

f_d bubble departure frequency [Hz]

F force [N]

g acceleration due to gravity [m/s^2]

h heat transfer coefficient [$\text{W/cm}^2\text{°C}$]

h_{lv} specific latent heat [J/kg]

H nozzle to surface distance [m]

I	current [A]
k	thermal conductivity [W/m-K]
L_c	characteristic length [m]
Nu	Nusselt number
P	pressure [bar]
Pr	Prandtl number
q	power input [W]
q''	heat flux [W/cm^2]
r	radius [m]
Ra	Rayleigh number
Re	Reynolds number
t	substrate thickness [μm]
t_w	bubble waiting period [s]
t_d	bubble departure period [s]
T	temperature [$^{\circ}\text{C}$]

u velocity [m/s]

V Voltage drop [V]

Subscripts

air air

avg average

b bubble

B buoyancy

cond conduction

concl conduction flux loss

conv convection

d departure

D drag

elec electrical

filter filtered data

fluid fluid

h heater

jet jet

l liquid

L lift

M momentum

net data with conduction losses accounted

pool pool

s substrate

sat saturation

savg sectional average

sp single phase

v vapor

w wetted length

Greek

α thermal diffusivity [m^2/s]

β	volumetric thermal expansion coefficient [$1/^\circ\text{C}$]
δ	thermal boundary layer thickness [mm]
Δ	IR image pixel width [μm]
μ	dynamic viscosity [$\text{N}\cdot\text{s}/\text{m}^2$]
ν	kinematic viscosity [m^2/s]
ρ	density [kg/m^3]
σ	surface tension [N/m]

Abbreviations

Al	aluminum
CHF	critical heat flux
CL	three-phase contact line
DI	de-ionized
FFT	fast Fourier transform
H1	heated section 1 of the macroscale heater
H2	heated section 2 of the macroscale heater

H3 heated section 3 of the macroscale heater

IPA isopropyl alcohol

IR infra-red

MC micro-convection

MAC macro-layer evaporation

MH heated section of the microscale heater

MIC micro-layer evaporation

MS₁ microscale thin film sensor 1

MS₂ microscale thin film sensor 2

NC natural convection

PDF probability density function

RTD resistance temperature detector

S₁ macroscale thin film sensor 1

S₂ macroscale thin film sensor 2

SJIB submerged jet impingement boiling

SL surrounding liquid

TC transient conduction

TLC thermo-chromic liquid crystals

UV ultra-violet

LOCAL HEAT TRANSFER RATE AND BUBBLE DYNAMICS
DURING JET IMPINGEMENT BOILING

1 INTRODUCTION

The progressive trend of enhancing the functionality and speed of integrated circuits while reducing their length scales has resulted in increased levels of heat generation. This advancement towards smaller scale electronics is expected to continue further with number of transistors per unit area doubling approximately every two years as predicted by Moore's Law [1]. Moore's article in 1965 anticipated the consequential increase in heat generation and questioned the capacity of cooling schemes to handle this heat problem. Modern day temperature sensitive electronics require to be maintained at surface temperatures below 85°C for optimal performance and safe operation [2]. Dissipating the high heat fluxes (100 - 1000 W/cm²) produced by these devices while maintaining low surface temperatures, has posed a challenge for thermal management schemes. As a consequence, cooling schemes that are superior to conventional methods like natural and forced convective single phase flows are being explored.

Phase change cooling schemes offer the possibility of removing heat from the system by transforming the coolant from a liquid to a vapor state at a constant saturation temperature. As a result phase change cooling has the potential of achieving high heat transfer rates for small changes in device temperature.

When boiling occurs with the heated surface submerged in a quiescent pool of liquid it is referred to as pool boiling. During pool boiling, natural convection, transient

conduction and the latent heat associated with phase change are the primary contributors to the heat transfer rate.

The addition of a jet flow to a quiescent pool allows for enhanced fluid mixing. When a single phase jet impinges on a heated surface and undergoes phase change, the condition is referred to as jet impingement boiling. If the jet issues into a pool of like fluid and subsequently undergoes phase change, the condition is called submerged jet impingement boiling.

Jet impingement paired with boiling allows for forced convection to act in addition to latent heat transfer. As a result of this enhanced fluid mixing, jet impingement boiling has the potential to extend the limits of the achievable heat transfer rates. As a cooling scheme for electronic devices, jets have the feasibility of being implemented individually or as an array [3, 4] making them attractive candidates for effective cooling of local hot-spots.

Over the years, several means of affecting phase change thermal management have been widely studied. Wolf et al. [5] have provided a detailed summary of the jet impingement boiling literature (until 1993). In more recent times, several other schemes have been investigated. These include technologies such as direct immersion phase change [6], spray cooling [7-9] and microchannel flow boiling [10-12].

The above mentioned phase change liquid cooling methods rely heavily on latent heat of vaporization of the fluid for heat transfer. Thus, a large amount of heat can be

dissipated with a small fluid volume making them accessible schemes for compact electronics. Additionally direct cooling schemes eliminate the need for physical heat spreaders and thereby significantly reduce the associated thermal resistance. Detailed reviews by Mudawar [2] and Bar-Cohen et al., [13] summarize the research developments and application potential of these cooling schemes.

Implementation of phase change liquid cooling technologies to an electronic system needs accommodation for the sensitivity of these electronic devices to stringent surface temperature constraints. For this reason, it is essential to fully characterize the performance of the cooling scheme.

Boiling heat transfer performance is typically quantified in a plot of surface heat flux against the surface excess temperature that drives the heterogeneous phase change, commonly known as a boiling curve. Typically, a single boiling curve that is representative of the spatially averaged heat transfer performance of the phase change scheme is provided. While area-averaged trends provide valuable information on the heat transfer characteristics of the cooling scheme, it is also important to assess local variations in heat transfer rates. In pool boiling, local variation in heat transfer can occur as a result of randomly distributed nucleation sites. Local variations are particularly evident in forced convective flows such as that in a channel flow or in jet impingement, wherein the hydrodynamics and/or local variation in fluid temperature affects local heat transfer rates [14]. In addition, for multi-chip electronics modules the surface consists of multiple heat sources that produce heat at different rates resulting

in local regions of hot-spots [15]. Accounting for the thermal non-uniformities at these local hot-spots is vital to the device design and performance. Such non-uniformities in imposed heat flux and surface temperature are not adequately captured by an area-averaged boiling curve.

While the importance of determining spatially local or sectional representation of boiling heat transfer is clear, such characterization involves evaluation of local values of surface temperature, which necessitates the use of multiple point sensors or the use of quantitative visualization methods. Obtaining the values of heat fluxes corresponding to locally varying surface temperatures has been a challenge limiting most of current literature to area-averaged results over uniform heat flux surfaces.

This thesis presents experiments on pool and submerged jet impingement boiling to illustrate the importance of a spatially local heat transfer analysis. Two scenarios of the heating surface pertinent to electronics cooling are presented by employing thin film serpentine heater geometries deposited on a silicon substrate. The first is a macroscale heater (27.5 mm diameter heater with multiple nucleation sites) that provides a circumferentially uniform but radially non-uniform heat flux distribution to explore the result of spatial variation in imposed heat flux on boiling heat transfer. The second is a microscale heater (1000 μm diameter heater for isolated bubble generation) that simulates boiling at a local hot-spot akin to that of a two-phase spot cooling on an electronic device.

Spatial variation in bubble dynamics and consequent local heat transfer during boiling are documented using thin film voltage sensors along with qualitative and quantitative high speed imaging and infra-red thermography. Local boiling curves are extracted for different radial locations on the macroscale heat transfer surface and quantitatively compared with corresponding area-averaged representations. Bubble ebullition in subcooled FC-72 is visualized with and without a forced convective submerged jet flow to understand the qualitative effects of jet inertia on bubble ebullition and quantify the differences in bubble departure characteristics and latent heat transfer rates.

2 LITERATURE REVIEW

This chapter provides an overview of the present state of knowledge and literature relevant to the work presented in this thesis. The chapter begins with a description of the fundamental concepts of nucleation, boiling heat transfer and the flow field of a submerged impinging jet. Selected relevant studies for area-averaged submerged jet impingement boiling are presented. Previous investigations in the context of area-averaged and spatial characterization of boiling heat transfer are reviewed. Finally, as a step towards understanding boiling heat transfer from basic principles, microscale studies on isolated bubble ebullition and heat transfer from controlled nucleation sites are presented.

2.1 THE BOILING CURVE

Boiling is a mode of phase change heat transfer in which a liquid heated sufficiently beyond its saturation temperature T_{sat} , vaporizes. The temperature difference $(T - T_{sat})$ required to attain boiling is called the incipient wall superheat, where T is the temperature of the surface heating the liquid. The heat flux transferred from the heated surface to the fluid corresponding to this temperature difference can be described by Newton's law of cooling,

$$q'' = h(T - T_{sat}) \quad (1)$$

where q'' is the convective heat flux associated with phase change and h denotes the two-phase heat transfer coefficient.

Boiling on a heated surface submerged in a quiescent pool of liquid is referred to as pool boiling. Nukiyama in 1934 [16] pioneered the investigation of boiling regimes by heating a nichrome wire in a saturated pool of water at atmospheric pressure, thus generating the famous boiling curve (plot of heat flux versus wall superheat). Figure 1 shows a generic pool boiling curve for a heat flux controlled surface and a fluid at saturation conditions along with schematic illustrations of the boiling activity.

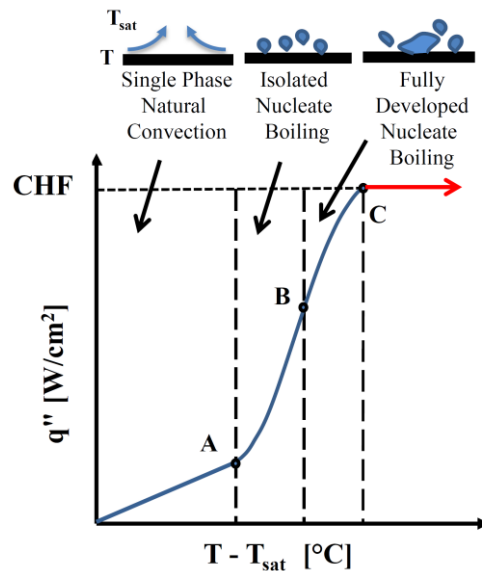


Figure 1: Typical pool boiling curve depicting a qualitative dependence of convective heat flux on wall superheat for a controlled heat flux surface

Of the various regimes distinguished, of particular interest to this study is the nucleate boiling regime. For wall superheats slightly greater than T_{sat} (up to point A in Fig. 1),

heat transfer from the surface to the fluid is dominated by natural convection. When the threshold wall superheat for phase change is achieved (point A in Fig. 1) vapor bubble formation occurs on the surface leading into the nucleate boiling regime. This condition is referred to as the onset of nucleate boiling. The heat flux transferred from the surface even with small changes in surface temperature is found to increase as observed by the change in slope of the boiling curve. This enhancement in heat transfer is attributed largely to the bulk fluid motion induced by the ebullition of bubbles (Fig. 2) namely, the formation (nucleation), growth and the departure of vapor bubbles that occur at specific locations on the heated surface known as nucleation sites. The initial portion of the nucleate boiling regime is called the isolated bubble regime (section A-B in Fig. 1). In this region nucleation sites are few, the bubbles are usually distinct and have negligible interaction with each other.

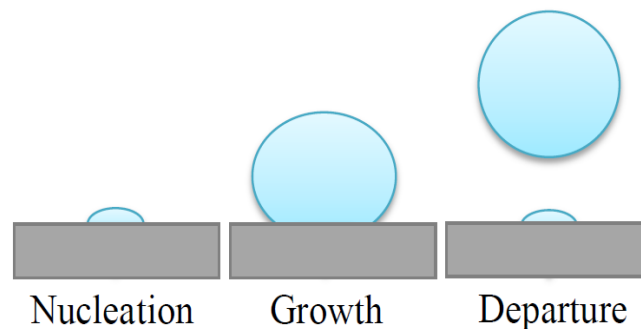


Figure 2: Bubble ebullition cycle

The boiling mechanism is usually that of heterogeneous nucleation in which the vapor trapped in small cavities of the heating surface seed bubble formation and growth. The

amount of wall superheat required to initiate nucleation depends on the surface properties (example the surface material or roughness) as well as the fluid properties.

For a spherical vapor bubble of radius r_b , the Young-Laplace equation (Eq. 2) represents the equilibrium state of the liquid-vapor interface.

$$p_v - p_l = \frac{2\sigma}{r_b} \quad (2)$$

Here p_v and p_l are the pressures of the vapor and liquid phases respectively, σ is the liquid-vapor interfacial tension. This implies that the outward force due to the higher pressure of the vapor trapped in the bubble is offset by the force of surface tension which acts inward and arises due to intermolecular interactions at the interface. The pressure difference on either side of the liquid-vapor interface relates to the wall superheat by the Clausius-Clapeyron equation (Eq. 3).

$$p_v - p_l = \frac{(T - T_{sat}) h_{lv} \rho_v}{T_{sat}} \quad (3)$$

Here h_{lv} is the latent heat of vaporization, and ρ_v is the density of vapor. Using the above equations the wall superheat can be related to bubble radius (Eq. 4).

$$T - T_{sat} = \frac{2\sigma T_{sat}}{h_{lv} \rho_v r_b} \quad (4)$$

As wall superheat is increased beyond point B (in Fig. 1) the nucleation processes enter the fully developed regime (region B to C in Fig. 1) wherein bubbles coalesce to form vapor slugs and/or columns on the heated surface. This widespread vapor

formation near the surface impedes the continuous rewetting of the surface by the bulk fluid causing a reduction in the heat transfer rate. However, the increment in wall superheat retains the upward trend on the boiling curve until point C where critical heat flux (CHF) is attained. CHF represents the maximum obtainable heat flux for boiling heat transfer. The heated surface at this point is engulfed by a vapor blanket that separates the surface from the fluid bulk preventing re-wetting of the surface. Thus the surface experiences a catastrophic increase in temperature that can cause the surface to burn out.

The potential for high heat transfer rates for small changes in device temperature makes nucleate boiling the most desired regime for phase change electronics cooling. In context of the scope of the present study, discussions in boiling trends will be limited to the nucleate boiling regime for a heat flux controlled surface which is of great interest to two-phase electronics cooling.

2.2 BOILING INCIPIENCE OF DIELECTRIC FLUIDS

The dielectric properties of certain fluids like fluorinerts permit direct immersion cooling of electronics. The option of direct contact of liquid coolant with electronics allows for a lower thermal resistance to heat transfer while supporting the cause of compact electronic packaging. In addition to their dielectric nature these fluids are non-toxic, non-inflammable and chemically inert. The low saturation temperatures of these fluids at atmospheric pressure is an added bonus making them ideal candidates for cooling temperature sensitive electronics. Fluorinerts have successfully served as

coolants for applications such as direct liquid immersion cooling [6], single phase forced convective cooling [17] and evaporative spray cooling [7].

While there are several benefits to using dielectric coolants, they are also known to exhibit poor thermal properties when compared with coolants like DI water. Their low surface tensions and hence highly wetting nature necessitates high incipient wall superheats for transition from single phase to nucleate boiling heat transfer. Figure 3 shows the typical pool boiling curve for a dielectric liquid under controlled heat flux conditions. The figure depicts an extended region of single phase (up to point A') at which boiling initiates on the surface.

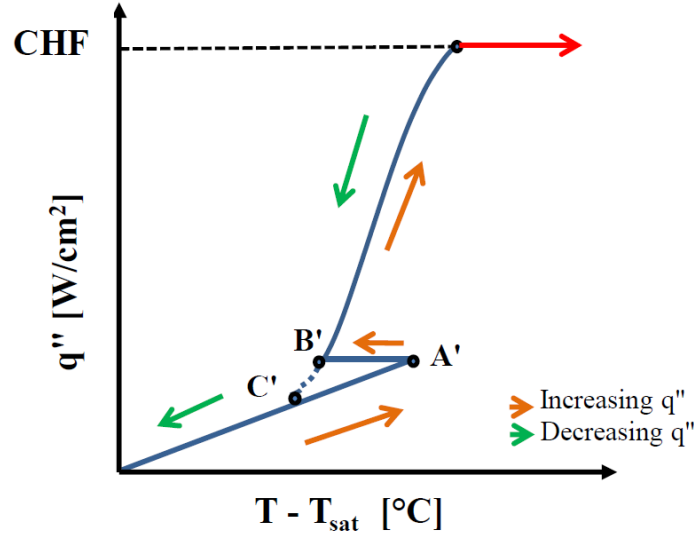


Figure 3: Pool boiling curve for a dielectric liquid for a controlled heat flux surface with increasing and decreasing heat flux

Inception of boiling in highly wetting dielectric liquids at these high wall superheats is typically accompanied by a temperature drop (Fig. 3, A'- B') on the heated surface. As a result of this temperature drop, the boiling trends for these highly wetting fluids obtained for increasing and decreasing heat flux are distinctly different around the region of inception and hence result in a thermal hysteresis (Fig. 3, Δ A'B'C'). These characteristics of high incipient superheat, thermal overshoot and boiling hysteresis severely impede the implementation of dielectric coolants in phase change cooling schemes for temperature sensitive electronics. To utilize these dielectric fluids to their full potential it is essential to quantify their incipience superheats and thermal overshoots along with understanding their cause and consequences in heat transfer.

The effects of surface properties and surface modifications on the boiling incipience of highly wetting dielectric fluids during pool boiling heat transfer have been extensively researched. Marto and Lepere [18] compared the boiling performance of fluorocarbons R-113 and FC-72 at atmospheric pressure conditions on plain and enhanced copper surfaces with fins and cavities. Incipient superheats required for the enhanced surfaces were found to be much less than that for the plain surface. Between the two fluids, FC-72 was reported to have a smaller overshoot with a less severe thermal hysteresis than R-113. The latter fluid demanded incipient superheats almost twice that of FC-72. For the same two fluids, You et.al [19] investigated the role of surface material on boiling incipience during saturated pool boiling. Three electronic material surfaces of silicon, silicon dioxide and aluminum oxide were prepared by sputtering on a platinum heater that provided a uniform heat flux. Probabilistic representation of the incipience data

revealed that incipient wall superheats were substantially affected by the choice of the working fluid while the surface material did not have a significant effect. In agreement with the findings of Marto and Lepere [18], incipience wall superheats in the range of 44.7°C to 74.8°C were reported for R-113 while for FC-72 the superheats ranged from 19.2°C to 50.5°C.

2.3 SUBMERGED JET IMPINGEMENT

Boiling heat transfer in the presence of an impinging jet combines the advantages of latent heat transfer by the nucleating bubbles and the forced convective heat transfer as a result of the impinging jet flow.

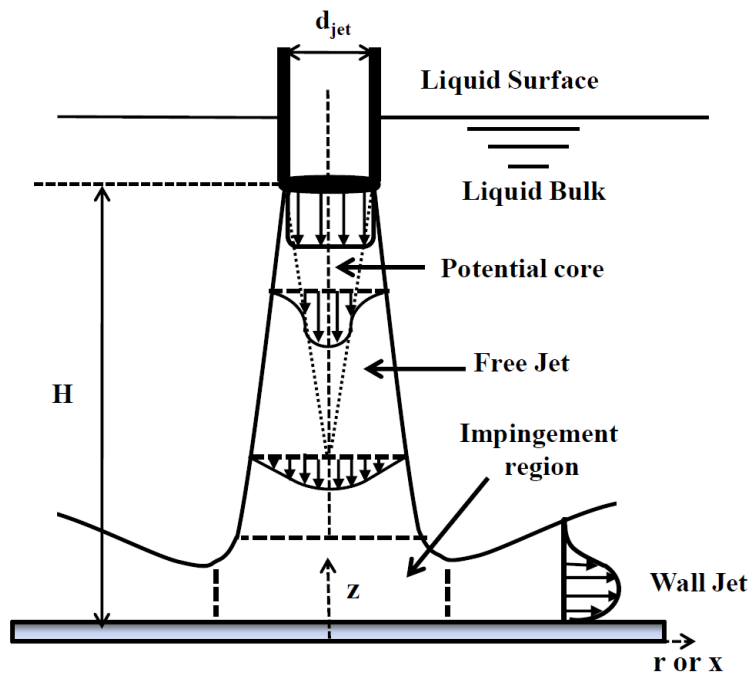


Figure 4: Flow field of a submerged jet

A jet flow that issues into a pool of identical fluid is classified as a submerged jet. Figure 4 provides a schematic illustration of the submerged jet flow structure. The submerged jet in this illustration is represented as an axisymmetric jet emerging from a circular nozzle of inner diameter d_{jet} .

The velocity profile of the jet at the nozzle exit is determined by the characteristics of the upstream flow. For a turbulent flow within the nozzle, the jet emerges into the ambient pool with a turbulent velocity profile. Downstream, the flow field of the submerged jet can be subdivided into three distinct regions (a) the free jet region (b) the impingement region and (c) the wall jet region.

The free jet region exists for jet flows where the exit of the nozzle is located at a height $H \geq 2d_{jet}$ [20]. The name ‘free jet’ implies that the jet is far enough from the impingement surface and hence the flow characteristics of the jet are not influenced by the presence of the surface. In this region, the jet flow is significantly sheared by the ambient fluid resulting in a lateral transfer of momentum. As a consequence of this momentum exchange between the jet and the surrounding fluid, the jet boundaries lose energy and resulting in a broadened velocity profile. The interior region of the jet called the potential core (Fig. 4) remains unaffected by the surrounding momentum transfer and hence this core region retains the initial velocity profile.

With further progression downstream the ambient fluid invades the potential core causing it to disappear. The resulting jet velocity profile has a decreased velocity

component along the jet centerline. The reduction in the jet's axial velocity continues with increasing distance from the exit of the nozzle.

In the impingement region (Fig. 4) the proximity of the jet to the surface causes its velocity to decrease. The deceleration of the jet imposes a high static pressure at the point of contact with the wall, called the impingement or stagnation point. Once impinged, the solid wall forces the jet to turn and accelerate along the length of the wall. An axisymmetric circular jet expands radially along the wall resulting in a distinct circular region of influence. The region of the radially expanding jet flow is called the wall jet region.

The attraction of jet impingement heat transfer lies in the high heat transfer coefficient at the impingement region, where the jet fluid is in direct contact with the surface. Additionally for a submerged jet configuration the momentum exchange between the jet and the surrounding fluid allows for increased fluid mixing improving the resulting heat transfer. The hydrodynamics, local and area-averaged heat transfer performance of single phase axisymmetric submerged jets have been extensively researched in the past [21-23]. For single phase jet impingement over a uniformly heated surface the area-averaged heat transfer coefficient is constant for a given set of flow conditions including the flow velocity, the nozzle geometry and the fluid properties. However, at any given wall superheat, the single phase heat transfer coefficient is expected to increase with increasing jet exit Reynolds number (Re_{jet}) as shown by Ma and Bergles for a study with submerged jet impingement of R-113 [24]. The correlation

recommended by Martin [21] is commonly used to estimate the area-averaged Nusselt number for impingement with a single round nozzle on a uniformly heated surface.

Submerged jet impingement boiling

Jet impingement boiling involves the phase change of a single phase jet upon impingement on a heated surface. Wolf et al. [5] presented a detailed review of the jet impingement boiling investigations conducted until 1993. The review covered the influence of a range of geometric and fluidic parameters on jet impingement boiling heat transfer.

Ma and Bergles [24] conducted experiments under saturated and subcooled conditions with a submerged circular jet of R-113 impinging on a uniformly heated constantan foil. Their study indicated that boiling heat transfer in the fully developed nucleate boiling regime was independent of the jet flow velocity. Ma and Bergles [24] also found that incipience overshoots for R-113 were much higher under saturated conditions compared to subcooled fluid conditions. Under similar test conditions as Ma and Bergles [24], Zhou et al. [25] found the incipient wall superheat to decrease with fluid subcooling irrespective of the jet parameters like the exit velocity and jet nozzle diameter for the fluids R-113 and PF-5052 on a uniformly heated constantan foil. The boiling hysteresis was characterized and attributed to the deactivation of vapor embryos in large surface cavities.

Recently, Cardenas [26] experimentally investigated the area-averaged boiling heat transfer characteristics of a submerged single circular jet on a uniformly heated copper

surface. The effect of geometric parameters such as d_{jet} and surface roughness along with fluidic parameters like pressure, Re_{jet} , fluid (DI water and FC-72) and fluid subcooling on the resulting heat transfer was documented. At a fixed wall superheat, Cardenas [26] reported consistent heat transfer enhancements in the single phase and partially developed nucleate boiling regimes for submerged jet boiling over pool boiling. The heat transfer enhancements were found to increase with increase in Re_{jet} , fluid subcooling and surface roughness for tests with DI water. For tests conducted under a fixed Re_{jet} and saturation temperature, heat transfer coefficients as much as 3.9 times larger were reported for water than for FC-72. With increasing wall superheat the boiling curves for jet impingement cases were found to merge with that for pool boiling. For SJIB of FC-72 on the smooth copper surface Cardenas [26] found no obvious relationship between incipient superheat and the jet Reynolds number. Consistent enhancements in CHF limits were reported with increasing Re_{jet} and increased fluid subcooling. Based on the comprehensive experimental results acquired, a CHF map was generated along with a jet impingement CHF correlation for predicting the maximum heat flux limits during jet impingement boiling.

2.4 LOCAL ESTIMATION OF BOILING HEAT TRANSFER

Area-averaged boiling results for pool and jet impingement boiling are commonly acquired using a heater block with a heating source such as cartridge or thick film heaters and axially located thermocouples. The test surface is placed on the top of this heating block and the sides of the block are thoroughly insulated. A 1-D conduction

model is used to determine the surface temperature and surface heat flux, which in turn provides an area-averaged boiling curve. Such a scheme has been used previously in pool boiling [27], jet and spray impingement boiling [24, 26, 28] and in microchannel flow boiling [29]. While such literature on area-averaged characterization of boiling trends is widely available, the spatial determination of heat transfer performance has been a big challenge for phase change heat transfer studies.

To determine the spatial heat transfer characteristics, multiple point sensors or quantitative visualization methods are needed. These data acquisition techniques are usually expensive to implement and result in a large quantity of data making the analysis cumbersome. That said, the importance of local characterization of boiling heat transfer cannot be ignored especially when applying it to cool micro/nanoscale electronics where spatial variations in temperature may damage the device or compromise its performance. Of particular interest are the flow boiling or jet impingement boiling schemes where the flow hydrodynamics affect the heat transfer in addition to bubble induced mixing.

Spatial heat transfer characteristics in the form of local boiling curves were documented by Wolf et al. in 1995 [14] during free surface (non-submerged) planar jet impingement boiling of 50°C subcooled DI water on a uniformly heated surface. Temperature distribution of the lower side of the heat transfer surface (nickel, chrome, tungsten and molybdenum alloy) was acquired by thermocouples positioned along the stream wise direction of the wall jet. Their experimental results distinctly depicted the

influence of the jet hydrodynamics on single phase and partial boiling regimes with increasing distance along the jet stagnation line. While single phase heat transfer coefficients were higher in regions closer to the impingement point, the corresponding range of wall superheats for the partial boiling regimes shrank due to the proximity with the impinging jet. No appreciable effects were reported for the fully-developed boiling regime with increasing spatial distance from the impingement point or with change in the jet velocity. The spatial and flow velocity independent trends of heat transfer in the fully-developed boiling regime was corroborated by the studies of Zhou and Ma for the case of submerged jet impingement boiling with R-113 on a constantan foil [30]. Here again a thermocouple was used for surface temperature measurement and the jet position was varied for different tests to acquire data at varying locations in the wall jet region. Heat flux estimates were based on area-averaged input electrical flux.

Thermal visualization methods like liquid crystal thermometry or infrared (IR) thermography have been used to determine the transient variations in temperature over entire spatial regions during phase change heat transfer [31, 32]. Even with such high spatial resolution imaging techniques, several past studies on thermal visualization of boiling heat transfer have limited their findings to area-averaged boiling representations. For example, Theofanous et al. [33] used IR thermography at 1kHz to determine area-averaged boiling curves while characterizing pool boiling heat transfer of water on titanium coated sapphire substrate with a spatial resolution of 250 $\mu\text{m}/\text{pixel}$. Calibrated surface temperatures over a 1000 frames were averaged over the

entire imaged heater area to evaluate the surface excess temperatures. These excess temperatures along with the input electrical heat flux were used to generate area-averaged boiling curves over the heater surface. In conjunction with X-ray radiography the nucleation site densities were also predicted. The superheats in regions of active nucleation sites were observed to be comparatively much lower than in the inactive regions. In a similar study, Gerardi et al. [34] employed simultaneous IR and high speed visualization to obtain time and space resolved temperature distribution under nucleating bubbles during pool boiling of water under saturated conditions. A $30 \times 10 \text{ mm}^2$ sapphire substrate was electrically heated using an ITO heater. Heat fluxes were estimated from the measured values of voltage and current during the experimental run. These input electrical heat flux estimates along with the IR temperature maps were used to obtain area-averaged boiling curves over an approximate area of $\sim 5 \times 5 \text{ mm}^2$.

There exist far fewer studies on spatially localized estimation of boiling curves and heat transfer coefficients in literature. Localized RTDs or thin film sensors have been used successfully in the past to obtain spatio-temporal variations in temperature and heat transfer coefficients. In conjunction with high speed imaging, thin film sensors have been used to estimate the contribution of different mechanisms to boiling heat transport under single nucleating bubbles [35, 36]. In one such pool boiling study of single nucleating bubbles from a cylindrical cavity Moghaddam and Kiger [36] illustrated the differences in heat transfer within and outside the bubble contact area

with a plot of heat flux against surface temperature over a section of the heated substrate.

Evaluation of local boiling curves for phase change in microchannel flows has been recently reported [10, 37]. Ozer et al. [37] employed quantitative liquid crystal thermography to obtain local temperature measurements on the upper surface of a microchannel during flow boiling. Simultaneously acquired high speed images aided the determination of bubble size evolution and nucleation site density. A conduction model executed in ANSYS Fluent was used to correct for the local surface heat flux values based on the recorded wall temperatures. Construction of local boiling curves along the microchannel based on the recorded temperatures and estimated values of local heat flux was demonstrated.

Chen and Garimella [10] demonstrated the use of diode temperature sensors to obtain local boiling curves along the length of a microchannel heat sink during flow boiling in the context of identifying the thermal performance impact of flow instabilities in microchannels. Twenty five calibrated diode temperature sensors each embedded in a $2.54 \times 2.54 \text{ mm}^2$ heating element were evenly distributed on a $12.7 \times 12.7 \text{ mm}^2$ substrate housing 60 parallel microchannels. The net heat transferred to the fluid was estimated from the input heat flux by subtracting the heat flux in the absence of the fluid. This net flux and sensor temperatures were used to generate the local boiling and heat transfer coefficient curves along the microchannel. Regions downstream of the channel were found to change phase at lower wall temperatures than upstream of the

channel. Severe fluctuations in the heat transfer coefficients in these regions were indicative of varying flow patterns like bubbly, slug, annular or churn flow. Transition from single phase to pulsating phase change flow in the upstream channel regions was found to occur alongside the onset of flow instabilities leading to an enhanced heat transfer rate. The middle regions of the channel were found to maintain an almost constant heat transfer rate over the entire range of heat fluxes.

For a submerged jet configuration, Dukle and Hollingsworth [38, 39] used qualitative liquid crystal imaging to locate the areas of single phase jet convection and nucleate boiling for a 5°C subcooled R-113 jet impinging on a uniform heat flux surface. Single point temperature measurements were obtained at three locations using RTDs that sensed an area of 2.5 x 1.5 mm². The electrical current required to heat the metallic foil substrate and the voltage drop across each RTD were recorded to evaluate the net thermal energy rate entering the test fluid. Boiling curves at the locations specified by the three RTD in conjunction with the corresponding liquid crystal thermal images were used to isolate regions that were cooled by forced convective jet flow and by phase change heat transport. To the author's knowledge, Dukle and Hollingsworth's [38, 39] study is the only submerged jet boiling heat transfer and qualitative thermal visualization study in literature.

The above past efforts to characterize spatially local heat transfer performance, be it in the form of boiling curves or heat transfer coefficients, support the fact that knowledge

of local heat transfer characteristics is essential to the conceptual understanding and practical implementation of flow boiling heat transfer systems.

2.5 ISOLATED BUBBLE- DEPARTURE CHARACTERISTICS AND HEAT TRANSFER

Characteristics of the boiling surface, such as the presence of cavities, cracks or scratches lead to an earlier incipience of boiling by trapping vapor and providing sites for nucleation. Previous studies [26, 40, 41] have reported an enhancement in overall heat transfer during pool and jet impingement boiling due to increased surface roughness. Boiling being a complex phenomenon depends on several other factors besides the surface such as the fluid, the pressure and the flow conditions to name a few.

A possible way to develop a better understanding of the principles of nucleate boiling is to simplify the process using isolated, artificially controlled active nucleation sites.

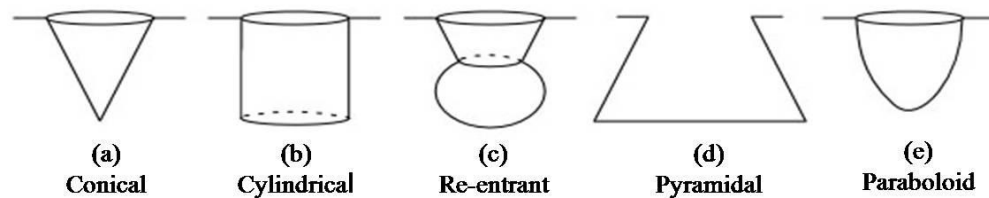


Figure 5: Types of artificial nucleation cavities

Although the need to study isolated bubble nucleation was realized very early, the lack of fabrication precision and technical advancement led to several problems and unsatisfactory results. For example, consider one of the early experimental works in this regard carried out by Preckshot and Denny in 1967 [42]. They studied the ebullition cycle in carbon tetrachloride (CCl_4 , $T_{sat} = 76.7^\circ\text{C}$) from conical and cylindrical cavities (Fig. 5a,b), created with a diamond stylus and a drill respectively, on polished nickel surfaces. The cavities ranged from 5 to 25 μm in diameter. A copper core heater heated the test surface and housed spring loaded thermocouples for recording the surface temperature. Results specific to the geometries studied indicated that steep walled cavities (ratio of depth to diameter > 1) served as the best sites for nucleation owing to efficient vapor entrapment. Wall superheats up to 51.6°C were recorded. However, the poor reproducibility of the surfaces made it difficult to quantify the sensitivity of heat flux measurements to surface properties.

2.5.1 CONTROLLED ACTIVATION OF NUCLEATION SITES

Significant progress in micro-scale machining and micro-fabrication techniques over the last decade has made it easier to create micro-cavities of specific geometry at pre-defined locations, thereby boosting experimental research related to ebullition and heat transfer at isolated nucleation sites.

Shoji and Tagaki [43] fabricated individual conical, cylindrical and re-entrant cavities (Fig. 5a,b,c) (diameters 50 and 100 μm and depth 30 and 50 μm) on a smooth Cu surface. The conical cavity was achieved by pressing a diamond bit using a micro-

hardness meter, the cylindrical cavity was created by micro-electrical discharge machining whereas the re-entrant cavity was the result of combining the two methods. Siedel et al. [44] mechanically indented a 500 μm deep and 180 μm in diameter paraboloidic cavity (Fig. 5e) on a copper plate. More recently, Chang et al. [45] generated a microporous cylindrical cavity (250 μm deep and 300 μm in diameter) on copper over a photolithographically patterned photoresist, chemically etched and coated with micron-sized alumina particles.

Modern-day focus has largely shifted to microchips and integrated circuits for which silicon is the most widely used substrate. Techniques for surface patterning, chemical and dry etching, and the deposition of metal and oxides on silicon are well established. This makes it more convenient for the integration of heaters/sensors and for the design of precisely located and structured micro-cavities. Besides these, silicon is also partially transparent to IR radiation allowing room for thermographic investigations.

Nimkar et al. [46] fabricated an array of pyramidal re-entrant cavities (Fig. 5d) (240 μm square base and 40 μm mouth) using an anisotropic etch for pool boiling studies. Moghaddam and Kiger [47] employed electron beam deposition to fabricate an array of sensors on a silicon chip to record temperatures of the surface. The silicon chip had cylindrical cavities (0.7, 1.3 and 2.4 μm in diameter and 30 μm deep) created by focused ion beam lithography. Hutter et al. [48] micro-fabricated isolated cylindrical cavities (40, 80 and 100 μm deep and 10 μm in diameter) on a silicon wafer by deep etching. Heaters and microsensors were fabricated on the reverse side of the wafer

using photolithography. Qi and Klausner [49] used photolithography and deep reactive ion etching (DRIE) on a silicon substrate to fabricate 45 μm deep cylindrical cavities that ranged from 8 - 60 μm in diameter.

While these modern cavity fabrication techniques have simplified the access to a single nucleating bubble, these processes in most cases still pose a challenge to obtain quantitative spatio-temporal variations in temperature and heat flux at the localized nucleation spot. An alternative approach used for selective activation of nucleation sites is laser activation [50] wherein the power of the laser beam has been used to estimate the flux at the locally heated spot. Spatio-temporal variations in heat transfer under single nucleating bubbles have also been obtained by the use of a microheater array [35, 51-53] where individual heater segments were selectively activated to generate nucleation. In the present work isolated bubbles are generated by the use of a localized serpentine microheater (1000 μm diameter) that simulates a hot-spot on an electronic device.

2.5.2 BUBBLE DEPARTURE DIAMETER AND FREQUENCY

In general, the estimation of latent heat transfer rate during phase change on a heated wall requires the knowledge of the number of active nucleation sites per unit area, the rate at which vapor bubbles are released from the surface and the equivalent volumetric diameter at release. The dynamic force balance of a bubble with its surrounding is essential to determining the bubble's departure characteristics. The diameter of the bubble at departure is numerically estimated by accounting for all the

vertical forces acting on it (Fig. 6), namely, buoyancy (F_B), surface tension (F_σ), liquid drag (F_D), momentum force due to convection around the bubble (F_M), and a lift force due to the wake of the previous bubble (F_L).

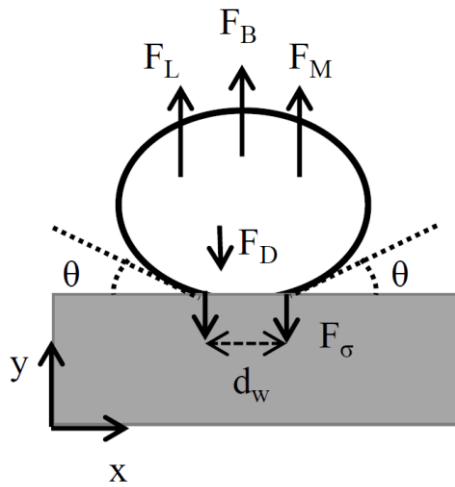


Figure 6: Vertical force balance on a bubble departing from the surface

$$\sum F_y = F_B + F_M + F_L - F_D - F_\sigma \quad (5)$$

Traditionally, the diameter of the bubble at departure (D_b) (capillary length scale) evaluated by balancing the buoyant and surface tension forces (Eq. 6) has been accepted as an appropriate length scale for nucleate boiling [54]. The constant of proportionality in this case depends on the contact angle formed at the liquid-solid-vapor interface line.

$$D_b \propto \sqrt{\frac{\sigma}{g(\rho_l - \rho_v)}} \quad (6)$$

This equation holds for heated surfaces larger than the bubble diameter. For heaters smaller than the bubble diameter a correction factor must be evaluated and applied [55].

Zeng et. al. [56] proposed a numerical model for determining bubble departure diameters based on the premise that at departure surface tension forces vanish, contradicting several earlier correlations and studies that assume buoyancy to be balanced by surface tension forces at departure [45]. Several other numerical correlation for assessing bubble diameters at departure have been proposed in literature and an exhaustive list of correlations has been given by Carey [54].

Experimentally, the departure diameter is usually obtained from high speed images of the bubble detachment process. The time interval between the release of one bubble from a nucleation site and the formation of the next is called the waiting period, t_w . During this period, cooler fluid surrounding the last released bubble rushes toward the nucleation site where residual vapor seeds the growth of a bubble again. The time needed for a bubble to depart from the heated surface once formed is called the departure period, t_d . The bubble departure frequency is thus defined as

$$f_d = \frac{1}{(t_w + t_d)} \quad (7)$$

Clearly, this would depend on how large and at what rate the bubble can grow, which in turn would be affected by the cavity dimensions. Quite contrary to this understanding, Preckshot and Denny [42] found f_d in their data for pool boiling of

CCl_4 to be independent of cavity dimensions as well as the wall superheat. They also noted that the mean diameter of the detached bubble increased with superheat. Chang et al. [45] confirmed this increase in departure diameter with increase in superheat for pool boiling of FC-72 on an isolated cylindrical cavity. However this increase in departure diameter was also accompanied by an increase in f_d . They attributed this observation to the fact that, in the case of isolated cavities the heat from the substrate has no other nucleation sites to activate. As a result all of the available heat goes into nucleating bubbles faster at the single cavity. Higher wall superheats led to vertical coalescence of successive bubbles prior to departure causing a reduction in the departure frequency.

Siedel et al. [44] studied pool boiling of saturated degassed pentane on a paraboloidic cavity indented on a copper disk. The ebullition cycle was recorded by a high speed camera. They found the bubble growth to be very reproducible; however, the bubbles were not perfectly spherical. As a consequence the departure bubble volume estimated from high speed images was chosen as the main parameter. The instantaneous bubble volume and time were non-dimensionalized by the departure volume and total growth time respectively. Independent of the wall superheats the bubble growth rates obeyed the relations $V' = t'^{0.6}$ for $t' > 0.2$ and $V' = 2t'$ for $t' < 0.2$ where V' and t' were taken to be the non-dimensional volume and growth time. Oscillations in the growing bubble were seen to affect the growth of following bubbles. Similar to Chang et al. [45] they found f_d to increase with increasing wall superheat along with vertical coalescence prior to departure at high superheats.

In saturated pool boiling studies of FC-72 on isolated cylindrical cavities etched in silicon, Hutter et al. [48] observed that, irrespective of the cavity depth, the departure diameters increased non-linearly with wall superheat. Temperatures measured by thin film sensors on the back side of the wafer were corrected for conduction losses through the thickness of the silicon substrate to obtain the net wall temperature. The measured f_d attained a maximum value (~ 50 Hz) for high wall superheats (above $\sim 10^\circ\text{C}$). On increasing the system pressure from 1 to 1.5 atm, the authors found that f_d slightly decreased independent of the cavity depth.

Yaddanapudi and Kim [53] deposited a microheater array with 96 Platinum resistance heaters (each measuring $270\ \mu\text{m}$) on a quartz substrate to study heat transfer under bubbles nucleating from a single site with saturated FC-72. Bubble ebullition was recorded at a wall superheat of $22.5\ ^\circ\text{C}$ using a high speed camera from underneath the quartz substrate. The average physical departure diameter over seven bubble cycles was $370\ \mu\text{m}$ which was slightly larger than the size of the heater element used. The corresponding average f_d was found to be ~ 23 Hz. Repeatable bubble departure diameters and frequencies were reported. Demiray and Kim [35] extended the study of Yaddanapudi and Kim [53] to the subcooled regime. A heater array identical in design to that of Yaddanapudi and Kim [53] was used with the individual heater elements shrunk to $100\ \mu\text{m}$. Single bubble visualization experiments were conducted at a wall superheat of about 20°C for pool subcoolings of 4°C and 15°C . Smaller bubble dimensions were observed for a higher subcooling as a consequence of peripheral condensation of the bubble due to the fluid bulk. Typical diameters of the bubbles at

departure were found to be 500 μm and 400 μm for the low and high subcooling respectively. The effect of change in heater dimension on the resulting bubble dimensions was not discussed in this study. However, a later article by the group [52] evaluated the role of heater dimensions on the different forces that become important during the process of bubble ebullition. Through pool boiling experiments with FC-72 and pentane it was found that for heater sizes greater than 2.1 times the capillary length, heat transfer was buoyancy dominated while for a ratio smaller than 2.1 surface tension was a more dominant force. The criteria was found true for liquid subcoolings between 6.6°C to 26.6°C.

2.5.3 HEAT TRANSFER MECHANISMS

Early bubble heat transfer models like that of Forster and Greif [57] attributed heat transfer to the bubble-induced liquid movement. The departing bubbles were treated akin to micro-pumps that pushed hot fluid away from the wall while drawing cold fluid from the bulk towards the heated wall. Following this, several mechanisms were identified that could contribute to heat transfer during bubble growth and departure periods. The following paragraph briefly describes the proposed mechanisms. An illustration of the heat transfer mechanisms is given in Fig. 7.

Micro-layer evaporation (MIC) model, brought forth by Moore and Mesler in 1961 [58], and later verified by Cooper and Loyd in 1969 [59], is based on the premise that an extremely thin layer of liquid between the growing vapor bubble and the heated surface evaporates enhancing heat transfer. Evaporation of this layer also increases the

bubble size. The transient conduction model (TC) by Mikic and Rosenhow [60] suggested that a portion of the superheated liquid layer (twice the bubble departure diameter) is eroded by the departing bubble. This layer is then replenished during the bubble wait period. The net heat removed from the surface is a combination of natural convection and transient conduction, the latter being the dominant mode. A model proposed by Stephan and Hammer in 1994 [61] took into consideration the influence of the liquid meniscus evaporation, occurring at the three-phase contact line (CL) and macro-layer evaporation (MAC) that occurs in the liquid region starting at the edge of the micro-layer extending up to the edge of the vapor bubble. MAC region grows as the bubble radius extends. In addition the perturbation of the liquid in the growing bubble vicinity by micro-convection (MC) and the energy received by the bubble from the surrounding superheated liquid (SL) are also considered important contributors to heat transfer.

The need to develop a composite heat transfer model incorporating the above mentioned mechanisms has encouraged recent studies to adopt advanced techniques of thermal measurement, some of which are reviewed here. An in-depth review by Kim [62] summarizes the advances in this field up to the year 2009.

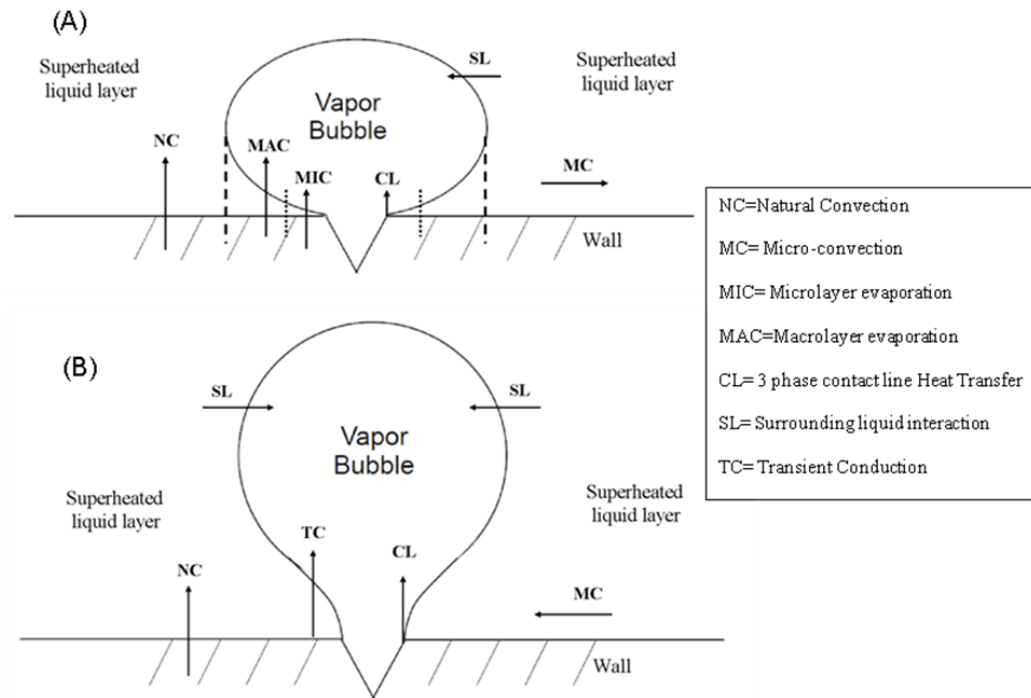


Figure 7: Mechanisms of heat transfer during (A) Bubble growth (B) Bubble departure (Figure adapted from Kim [62])

Kenning and Yan [31] performed wall temperature studies for pool boiling conditions using un-encapsulated thermochromic liquid crystals (TLC) coated on a stainless steel plate. TLCs are known to reflect distinct colors indicative of their temperature when illuminated by white light. Bubble growth was accompanied with a spreading cold spot identified by a drop in wall temperature that was indicative of MIC. Spatial distribution of wall superheat was found to impact MIC.

Demiray and Kim [35] used an array of 96 Platinum resistance heaters (spatial resolution 100 μm) on a quartz wafer to study heat transfer under bubbles nucleating from a single site under subcooled conditions in FC-72. The semi-transparent quartz

substrate allowed high speed visualization of the bubble events from below. These images were compared to the simultaneously recorded temperature data from the sensors in order to estimate the contribution of different mechanisms to the net heat transfer. The bubble equivalent departure diameters were evaluated assuming that all heat transferred by the heater array was converted to latent heat in the bubble. This equivalent diameter was found to be much smaller in comparison to the physical diameter estimated from the high speed images. Hence, it was concluded that the departing bubbles gained maximum energy through their interaction with the surrounding liquid and not from the wall. This implied that micro-layer evaporation and three-phase contact line heat transfer were the smaller contributors when compared with transient conduction and micro-convection that dominated the heat transfer process. It was also noted that during transient conduction the bubble impacted an area corresponding to half its departure diameter unlike that predicted by Mikic and Rosenhow [60].

Moghaddam and Kiger [47] investigated the contributions of MIC, TC and MC during nucleation at a micro-fabricated cylindrical cavity in silicon under saturated conditions with FC-72. The geometry of the cavities was designed in accordance with Hsu's model [63]. An array of thin film sensors (spatial resolution 22 - 40 μm) was employed to assess variations in the heat flux. Thin film heaters were used to maintain the surface at required temperatures. Distinct peaks in the temperature sensor data and heat flux corresponding to stages in the bubble life cycle were identified as the onset of MIC and TC respectively. Heat flux transferred due to micro-convection (MC)

evaluated in the bubble vicinity (immediately outside the bubble contact region) was compared with natural convection (NC) under the same surface temperature conditions by taking advantage of the temperature hysteresis of FC-72. It was found that with increasing wall temperature, all the three mechanisms were enhanced with MC being the most significant. A ratio of the individual heat flux of each mechanism to the total heat flux was used to gauge the relative contribution. At lower wall temperatures transient conduction was seen to be the dominant mode whereas at higher wall temperatures MC was the biggest contributor while MIC made the least contribution. TC clearly occurred prior to bubble departure.

Golobic et al. [64] conducted IR studies (spatial resolution 40 μm , time interval 1ms) to record the wall temperature distribution beneath growing bubbles on a 6 μm thick platinum foil under saturated and subcooled pool conditions on a controlled heat flux surface. Water at atmospheric pressure conditions was used as the test fluid. Their temporal resolution was insufficient for resolving heat transfer details of fast growing bubbles with low residence time. However it was noted that the fast bubbles reached their maximum contact area within 2-3 ms resulting in a uniform drop in the wall temperature in the contacted region. Following this the contact line began receding and the wall temperature was seen to rise again till bubble detachment occurred. The corresponding heat flux showed a characteristic shift from a peak at the center of bubble contact region in the early growth stage of the bubble to a trough with peaks at the edge of the contact area in the latter stage and finally to a peak in the center with troughs at the contact area as the bubble begins to depart. Slow bubbles with long

residence times showed a similar trend with longer departure times. The slow bubble growth was accompanied with some asymmetry in the bubble shape. The authors were unable to correlate their data to existing models.

Wagner and Stephan [65] used an IR camera (spatial resolution 14.5 μm , time interval 1ms) to record wall temperature variations under a bubble nucleating at a single site on a 20 μm thick stainless steel foil during boiling of FC-84 and FC-3284. This was accompanied with high speed visualization to capture the corresponding bubble dimensions. The transferred heat was divided between the evaporation into the bubble and the micro convection. The ratio of the MC to the evaporative heat flux was found to be around 28-30% for the individual fluorinerts tested. This implied that the heat transferred from the wall was small in comparison to that carried away the bubble.

In summary of the literature reviewed in this chapter, it can be said that over the past 50 years a number of macro and microscale studies have investigated the hydrodynamic and thermal mechanisms that govern boiling heat transfer. This includes pool and jet impingement boiling over large uniformly heated surfaces. Effects of surface material, surface geometry and fluid properties on heat transfer enhancement have been investigated. However, information on the spatial variations in local temperatures and heat fluxes during pool and jet impingement boiling heat transfer is scant. Furthermore, most of the literatures available are for heat transfer over uniform heat flux surfaces leaving a gap in knowledge of the result of non-uniformities due to imposed surface heat flux. Documenting these spatial variations

would be of essence to the design and incorporation of pool and jet impingement boiling to temperature sensitive electronics cooling. Recent studies have shifted focus to observing behaviors at isolated nucleation sites to simplify this complex phenomenon of boiling heat transfer. Bubble nucleation, growth and departure behaviors under pool boiling conditions have been documented. The work presented in this thesis aims to gain a better understanding of the spatial variations in heat transfer at the macroscale along with a microscale perspective of nucleation in the presence of a submerged impinging jet.

3 OBJECTIVES

The knowledge of local heat transfer characteristics is essential to the conceptual understanding and practical implementation of boiling heat transfer systems for hot-spot driven electronics cooling. In pool boiling, where there is no imposed forced convection, spatial variations can exist due to the randomly distributed nucleation sites for a uniform heat flux surface. In the context of electronics, additional spatial differences in heat transfer can arise due the presence of localized hot-spots. In the specific case of jet impingement boiling, significant spatial differences in boiling heat transfer can be expected as a result of the forced convective jet flow. The overall goal of this experimental study was to highlight the spatial differences in the bubble dynamics and local heat transfer rate imposed by a forced convective jet flow. To achieve this, pool and submerged jet impingement boiling experiments were conducted on silicon based macro and microscale heaters.

The macroscale heater substrate consisted of a 27.5 mm diameter heated area with multiple nucleation sites. This large scale heater was considered to investigate the differences in global and spatial heat transfer characteristics during boiling with and without a jet flow. A thin film serpentine heater was used to provide a circumferentially uniform but radially varying heat flux distribution on the surface. Such a scenario would be encountered in direct immersion cooling of multi-chip electronics modules, wherein the regions in between the modules are unheated. Voltages from thin film sensors and high speed visualization of the boiling process

were used to qualitatively assess spatial differences during the pool and jet impingement boiling experiments. One of the major spatial differences between pool and jet impingement boiling discussed in literature is the existence of a ring shaped boiling front in the latter case. The jet flow maintains single phase heat transfer within the boiling ring while boiling heat transfer dominates in the regions occupied by the boiling front. It was of interest to quantify and compare the local heat transfer rates in these two distinct regions defined by the boiling front. Infra-red (IR) thermography was used to obtain local temperatures of the heat transfer surface with and without the impinging jet flow. The corresponding local convective heat fluxes were estimated by accounting for axial conduction in the substrate. Local and area-averaged boiling curves were quantitatively compared to highlight the importance of a local heat transfer assessment.

While the large scale heater tests highlight the spatial differences in bubble dynamics, surface temperatures and boiling curves, it was also of interest to characterize the effect of jet inertia at the microscale. In the past, several studies have concentrated on the microscale phenomenon affecting heat transfer during single bubble ebullition in pool boiling. However, the little is known about the microscale ebullition process and the corresponding heat transfer in the presence of an impinging jet. To isolate the influence of the jet inertia and fluid subcooling on bubble ebullition, a microscale pool and submerged jet impingement boiling study was conducted.

Along the lines of the large scale heater a localized serpentine microheater (1000 μm diameter heated area) was designed and fabricated on a silicon substrate to simulate a local hot-spot. The heater was positioned at a radial location of three nozzle diameters from the point of jet impingement in the wall jet region. Bubble dynamics was captured from this microheater in the stagnant pool as well as within the jet flow field using high speed visualization. The bubble diameter at detachment and the corresponding departure frequency during the pool and jet boiling of FC-72 were evaluated from the high speed images. Voltage fluctuations from thin film sensors were used to corroborate the departure frequencies obtained from the high speed visualization. The vapor bubble dimensions and departure frequency were used to assess the net latent heat transfer rate. IR thermography was used to get instantaneous maps of the surface temperature of the microheater.

Overall, the results from this study will aid the local characterization of boiling heat transfer for applications in electronics cooling. Specifically, the methods and results presented could find use in designing cooling modules for devices with multiple heat sources, dissipating heat at different rates. Results from the microheater tests will help characterize the difference in the contribution of latent heat transfer in the wall region of a submerged jet, compared with that for pool boiling.

Parameters Varied

The fluidic parameters that were varied during the macroscale and microscale investigations of pool and jet impingement boiling heat transfer are listed below.

Macroscale heater experiments

The parameters that were varied for the macroscale heater experiments included the jet exit Reynolds number, the fluid subcooling, the heat flux supplied to the surface and the heat transfer fluid. Two heat transfer fluids with very distinct thermo-physical properties were considered in this study, DI water and the dielectric FC-72.

Microscale heater experiments

The microscale heater experiments were conducted at a jet exit Reynolds number of approximately 3128. The parameters that were varied for the microscale heater experiments included the fluid subcooling and the power input supplied to the surface.

4 EXPERIMENTAL FACILITY AND METHODS

This chapter describes the experimental test facility and the equipment used for the jet impingement boiling studies along with the design, fabrication and assembly of the silicon test sections. The key considerations of this setup were to permit both pool and jet impingement boiling studies on a silicon substrate while allowing IR visualization from the rear of the silicon substrate and high speed visualization of the boiling activity from the top. The facility had to be flexible to incorporate testing with two working fluids deionized (DI) water and FC-72 with markedly distinct thermo-physical properties. Details of the experimental procedures and a list of conducted experiments are provided in this chapter. The properties of the test fluids are given in appendix A.

4.1 TEST FACILITY

A simplified schematic of the test facility used for the pool and jet impingement boiling studies is shown in Fig. 8. The facility was built around a central test chamber housing the test section and consisted of (a) jet flow loop (b) pool temperature control loop (c) vapor condensation loop and (d) data acquisition sub-system.

The central test chamber was constructed out of 0.5 inch thick slabs of 316 stainless steel welded together and it measured 25.4 x 19 x 25.4 cm³. To permit high speed flow visualization during the experiments, the chamber was equipped with 1.3 cm thick, 11.8 cm x 11.8 cm clear polycarbonate windows on three faces secured by stainless

steel flanges measuring $14.6 \times 14.6 \times 0.64 \text{ cm}^3$. The top plate of the chamber was removable and supported an inlet plenum for the circular jet nozzle. Detailed part drawings of the test chamber can be found in reference [26].

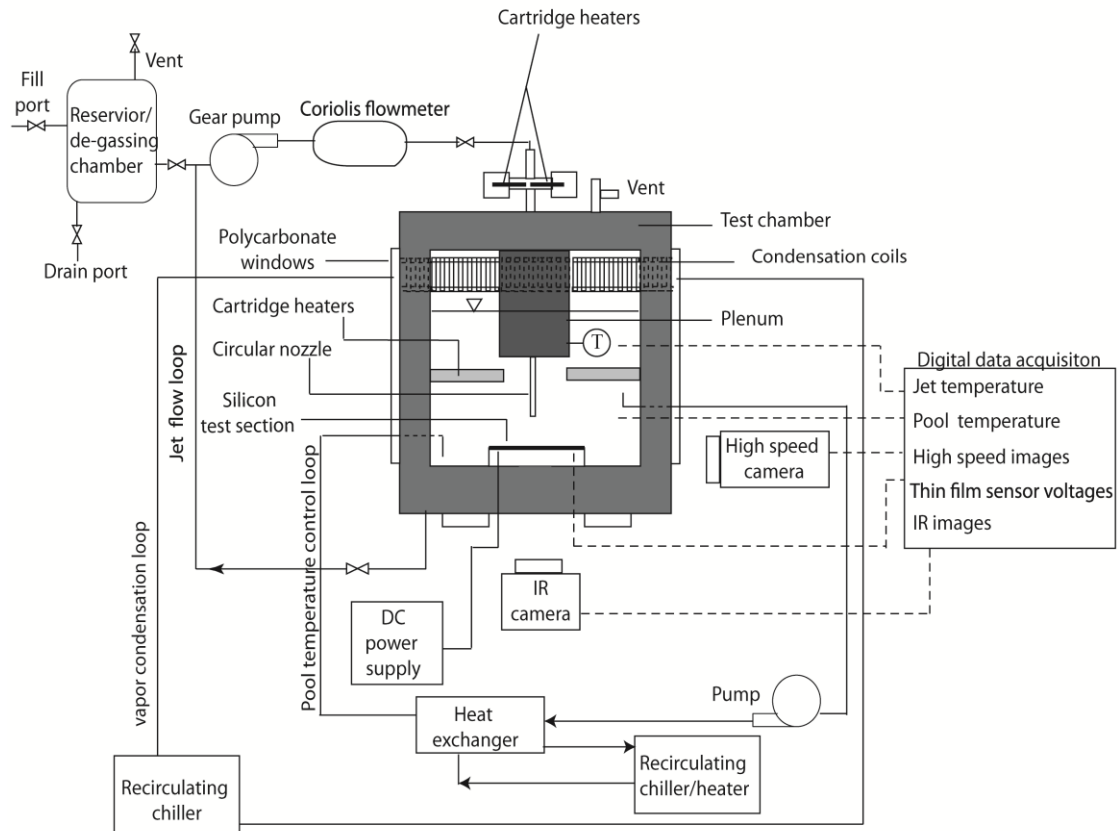


Figure 8: Schematic of experimental facility

The jet flow to the inlet plenum and through the test chamber was recirculated in a loop with a variable-speed gear pump (Micropump, GB-P25JDS-A). The jet mass flow rate was monitored using a Coriolis flowmeter (Micromotion Elite II). The jet temperature was controlled by using two 250-watt cartridge heaters (Watlow, E2A72-BG12H) positioned at the inlet of the chamber top plate. A variac (Superior Electric,

3PN116B) was used to control the power input to the two cartridge heaters. The flow was ejected through a borosilicate glass nozzle (Sutter Instrument) of length 10 cm as a submerged circular jet that impinged on a heated, circular silicon test section. Nozzle inner diameters were varied between 0.5 mm to 1.16 mm based on the different experimental conditions. Glass nozzles were connected to the jet inlet plenum with the combination of a PEEK flangeless nut (Upchurch Scientific-IDEX Corporation, P-230X) and flangeless ferrules (P-200X and P-342X). The 1 mm outer diameter nozzles required an additional sleeve (Upchurch Scientific-IDEX Corporation, F-252X) for support. The inlet plenum allowed for height adjustment of the jet nozzle above the test section. During pool boiling experiments, the flow through the nozzle was turned off. The jet flow line could be easily disconnected from the chamber by the use of Swagelok stainless steel quick disconnects (Stems, SS-QC4-D-400 and bodies, SS-QC4-B-400) along with flexible semi-clear crack-resistant tubing made of Teflon® PFA (McMaster Carr, 51805K73). The remainder of the flow lines in the facility were assembled with 316 stainless steel tubing (Swagelok, SS-T4-S-035-6ME) secured by Swagelok compression fittings. For isolated bubble pool boiling tests with the microscale heater the nozzle was removed completely.

All boiling experiments were performed at atmospheric conditions. The pressure inside the chamber was monitored with a calibrated digital pressure transducer (Omega, PX302-030AV) powered by a precision power supply (Tektronix, PS 5004) with 10 VDC. The pressure recorded at the start of the experiment was used to compute the fluid saturation temperature and hence the required pool temperatures for

the desired test conditions. Required pool temperatures were attained with two 550-watt cartridge heaters (Watlow, G4A-15283) immersed in the pool. The power to these cartridge heaters was modulated by a variac (Staco Energy Products Co., 3PN1010) in combination with a PID controller program in LabVIEW that autonomously adjusted the pool temperature. A data acquisition board (National Instruments, PCI-6221) provided a 5V analog input to the PID controller which in turn controlled a solid state relay (Omega, SSR330DC50) mounted on a finned heat sink (Omega, FHS-7). For subcooled tests with water, a recirculation loop (Fig. 8) was required to maintain the pool subcooling. The loop consisted of a custom made heat exchanger connected to a recirculating heater/chiller (ThermoHaake, C30P) and a vane pump (Teel, 4RM64).

DI water was degassed in an external degassing unit (Fig. 8) that consisted of a 22.7 liter commercial water heater (Rudd, PEP6-1). The water heater was modified to incorporate a vent to the atmosphere and temperature control with a physical PID controller (Omega, CNi3253-DC) connected to a solid state relay (Omega, SSR330DC50) mounted on a finned heat sink (Omega, FHS-7). A T-type thermocouple (Omega, TTSS-18U-12) was installed to read the temperature inside the degassing unit.

For tests with the expensive fluid FC-72, the degassing unit was removed and the degassing was conducted within the test chamber using the immersed cartridge heaters to minimize the fluid volume in use. The modified test facility for FC-72 is shown in

Fig. 9. The oxygen content of the degassed fluid was measured using a dissolved oxygen meter manufactured by Extech Instruments (Model 407510) with a resolution of 0.1 mg/L and an accuracy of ± 0.4 mg/L.

Vapor condensation within the test chamber was made feasible by a sandblasted stainless steel condensation coil located at the top back side of the test chamber. The condensation coil circulated chilled water through an externally connected recirculation chiller (Thermo Scientific, Neslab ThermoFlex5000). For tests with FC-72 loss of fluid to the atmosphere was avoided by using a Graham reflux condenser mounted on the chamber top plate (Fig. 9). Coolant flow in and out of the reflux condenser was regulated by a recirculating heater/chiller (ThermoHaake, C30P).

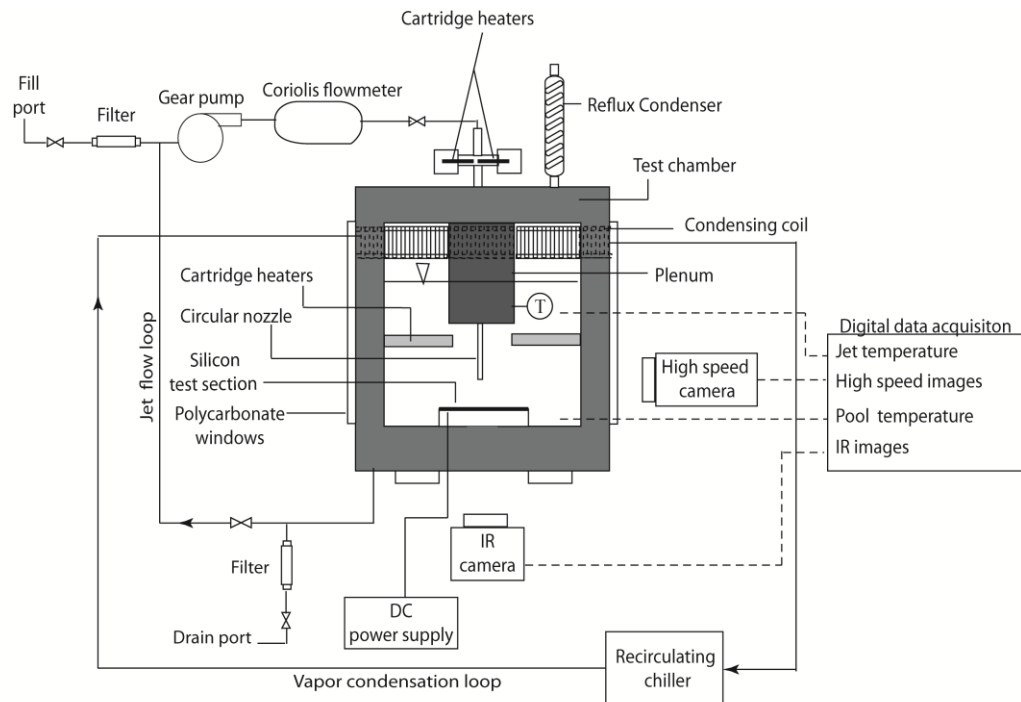


Figure 9: Modified test facility for FC-72

Resistive heating was provided to thin film heaters (see section 4.3) deposited on the silicon test substrate by means of a DC power supply. The power supplies were chosen based on the heat flux required by the fluid in use and the resistance of the deposited heaters. Two dimensionally different thin film heaters deposited on silicon substrates were used in his study. The first consisted of a macroscale heater substrate that heated a 27.5 mm diameter circular area. The second consisted of a microscale heater that heated a 1000 μm diameter circular spot to generate a localized boiling activity. The heater designs and fabrication are described in detail in section 4.3 of this chapter.

A high current DC power supply capable of providing 40V, 165A (American Reliance Inc., Model SPS40-165-K0E7) and a switching mode DC power supply (TENMA, 72-8350) with a maximum specification of 20V, 5A were used for tests with the macroscale heater substrate. Tests with the microscale heater substrate were conducted with a high voltage, low current (60V, 1A) power supply (Agilent, E3617A) owing to the large resistance value of these heaters.

A LabVIEW program was used to record data for the jet, pool and ambient room temperatures, along with the jet mass flow rate, and chamber pressure. Data for the pool and jet temperatures were collected by k-type thermocouples located within the chamber and jet inlet plenum respectively. These k-type thermocouples were connected to a data acquisition board (National Instruments, PCI 6036E) through a terminal block (National Instruments, SCXI-1328) mounted on a 4-slot chassis (National Instruments, SCXI-1000). The output voltage from the pressure transducer

was recorded with a second data acquisition board (National Instruments, PCI-6221) through a signal connector block (National Instruments, CB-68LPR). The same board (National Instruments, PCI-6221) also acquired the jet mass flow rate from the Coriolis flow meter. Temperatures for the PID controller and ambient room conditions were monitored by T-type thermocouples (Omega Engineering). A USB thermocouple input module (National Instruments 9211) was used in conjunction with a USB module carrier (National Instruments, USB-9162) to record the temperatures from the T-type thermocouples.

A second LabVIEW program was used to record voltage drops across sections of the thin film heater during the boiling experiments. Henceforth, these sections will be referred to as thin film sensors. The sensor voltages were recorded using an additional data acquisition device (National Instruments USB-6009) that was connected to the USB port of the computer.

4.2 VISUALIZATION INSTRUMENTATION

High speed imaging and IR thermography were used in this study to qualitatively and quantitatively visualize the phase change process.

4.2.1 HIGH SPEED CAMERA SPECIFICATIONS

High speed visualization of the boiling dynamics during boiling were conducted with a Phantom V310 (Vision Research) camera having a 1280 pixel x 800 pixel inbuilt CMOS sensor and a 20 μm pixel size. The Phantom V310 is capable of recording

images with a maximum speed of 3250 frames per second at full resolution.

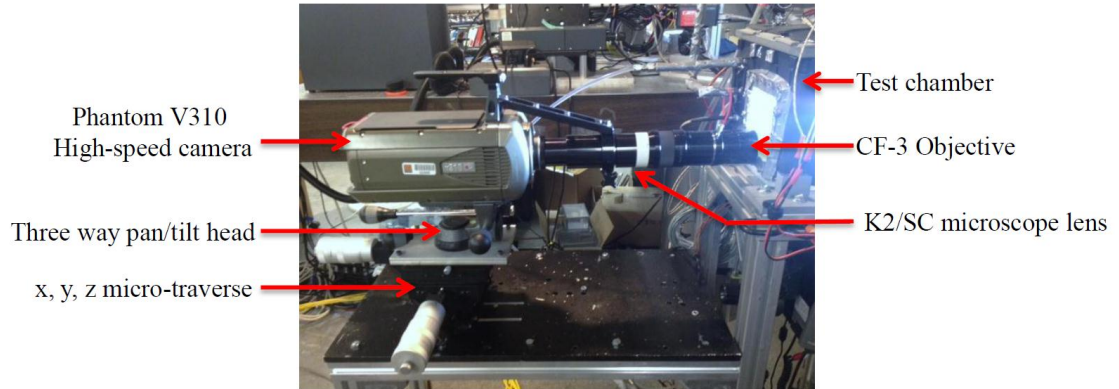


Figure 10: High speed visualization set-up

The high speed camera was mounted on a three way pan/tilt head (GITZO G-1570M) secured to a custom built micro-traverse stage capable of micro-adjustments in the x, y and z directions (Fig. 10). The camera settings were controlled using the Phantom Camera Control (PCC) software provided with the camera.

For tests involving the macroscale heater test section, a 60 mm lens (Nikon, Micro-Nikkor) with an aperture set at F/11 was used to collect the high-speed images. The test surface was illuminated with halogen bulbs diffused by a custom polycarbonate diffuser sheet during the macroscale boiling tests.

Bubble dynamics during the microscale heater tests were observed through a K2/SC microscope lens (Infinity Optics) with CF-3 objective. High-intensity illumination of the test surface was ensured by a 12.7 cm x 12.7 cm densely packed array of 625 white LED's (intensity 17000 mcd) powered by a 5V source. The LED array was designed

by fellow graduate student Florian Kapsenberg [66] and built in-house by undergraduate student Mitchell Daniels.

4.2.2 IR CAMERA SPECIFICATIONS

Thermal visualization of the silicon test surface was conducted with a TVS 8500 IR camera (CMC Electronics). The camera built with a photovoltaic Indium-Antimonide (InSb) focal plane array (FPA) detector possessed 256×256 detecting elements with a field of view of $256 \text{ pixels} \times 236 \text{ pixels}$. The detector was capable of sensing radiation in two mid-range wavelength bands of 3.5 to 4.1 μm and 4.5 to 5.1 μm . Cooled by an integrated Stirling cooler, the camera was suitable for a temperature measurement range of -40°C to 900°C .

The macroscale heater substrate was visualized from its rear side (see Fig. 8) with the IR camera mounted on a custom built stage with vertical (z-direction) adjustment. Images were acquired using a standard 30 mm macro lens at a frequency of 30 Hz. The IR image resolution was estimated for each test based on the known width of the deposited aluminum heaters (described in the next section). Thermal videos from the camera were directly recorded on a computer using an IEEE-1394 FireWire interface.

The microscale heater test section required the IR camera to be used in conjunction with a microscope lens, AVIO TVM-8510U, having a fixed spatial resolution of 10 μm and an estimated focal length of 28 mm. The heater was located at a radial distance of 1.5 mm ($r = 3d_{\text{jet}}$ for a 0.5 mm inner diameter jet nozzle) from the jet impingement point ($r = 0$). To permit IR visualization of the microscale heater at this

radial location the camera mount needed to have the flexibility of adjustment in the x and y directions. To achieve this flexibility, the camera was mounted on a tripod stand with the microscope lens facing upward to image the rear side of the substrate mounted in the test chamber. IR data for the microscale tests were acquired real time at 120 Hz and subsequently transferred onto a computer using the IEEE-1394 FireWire interface.

All communications of the IR camera with the personal computer were conducted via the TVS Viewer software that was provided with the camera. IR videos were first recorded in .tvs format and then converted to images in .IRI format using a feature in the TVS software. The .IRI images were converted to comma-separated-value (.csv) format using PE Professional software (GORATEC Technology) for further processing in MATLAB.

4.3 SILICON TEST SECTIONS AND MOUNT

The test sections for this study were fabricated from 3 inch (76.2 mm) double side polished p-type (111) silicon wafers of thickness 380 μm obtained from Rogue Valley Microdevices. Each wafer had a 2 μm thick thermally grown silicon dioxide layer on either side for electrical isolation and surface protection. The manufacturer specified uncertainties were ± 25 μm for substrate thickness and ± 0.1 μm for oxide film thickness, respectively. The average surface roughness of these substrates was estimated to be 0.87 nm using atomic force microscopy.

Thin film serpentine heaters were fabricated on the silicon substrates using photolithography and metal deposition to provide the heat flux required for phase change along with thin film voltage sensors. The following subsections describe the heater geometries and their fabrication procedures in detail. All microfabrication procedures for the heater test sections were conducted at the clean room facilities (class 1000) at the School of Electrical Engineering and Computer Science (EECS), Oregon State University.

4.3.1 MACROSCALE HEATER TEST SECTION

The macroscale heater pattern (Fig. 11) comprised of three concentric rings where Joule heating was applied while the rest of the silicon surface was unheated. A circular design of heaters was chosen to align with the circular geometry of the jet nozzle adopted in the jet impingement tests. Thus, the geometric center of the heater rings coincided with the stagnation point (point of jet impingement) and is considered as the zero-th radial location ($r = 0$) in these studies. The chosen geometry resulted in a heating profile that was circumferentially uniform but varied with increasing radial locations.

The serpentine heaters, fabricated on the 76.2 mm diameter polished silicon substrate, occupied a circular heating area of diameter 27.5 mm. The silicon substrate serpentine heater dimension was chosen so as to compare the experimental results of the present study with that of a previous study [26] conducted on a 27.64 mm diameter uniformly heated copper surface using the same test facility.

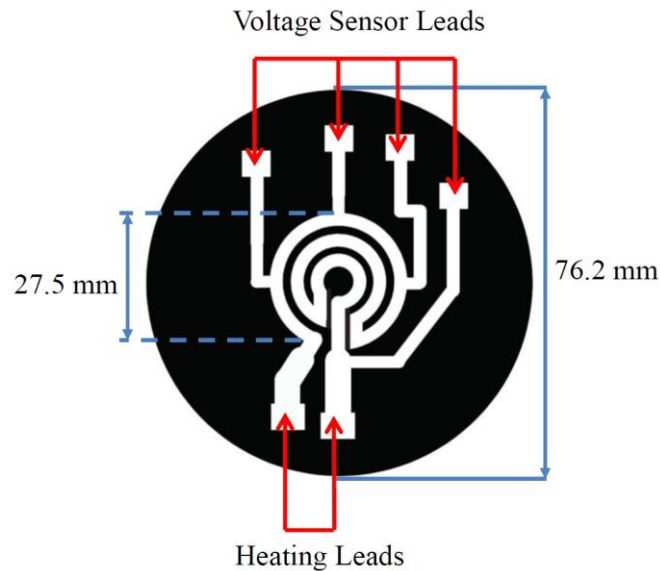


Figure 11: Macroscale serpentine heater pattern

Sensor leads (Fig. 11), drawn out of different sections of the serpentine heater were used to record the fluctuations in voltage caused by variations in the heater resistance with change in temperature. These voltage recordings were particularly useful to isolate regions of boiling activity beyond the onset of boiling. The individual heater rings and sensor leads each spanned a width of 2.5 mm.

Macroscale heater fabrication

The first step to fabricating the heaters involved a thorough cleaning of the silicon wafers. This step plays a key role in providing a good adhesion of the metal heater film on the silicon substrate. Initial test wafers were cleaned with standard cleaning procedures which included rinsing in acetone, isopropyl alcohol (IPA) and de-ionized (DI) water and blow dried. In subsequent trials it was established that a 60 min

ultrasonic rinse in DI water preceding the standard cleaning procedure significantly enhanced the adhesion of the heater film to the substrate. The wafer was then heated at 85°C for one minute on a hotplate to vaporize any remaining liquid.

The heater pattern was transferred on to the silicon substrate using photolithography and subsequent metal evaporation. Figure 12 describes the basic sequence of steps that are involved in this fabrication process. The recipe and process instructions are described in detail in appendix B. Photolithography uses a UV light source (Fig. 12, step A), to transfer a pattern optically from a photomask to a photoresist (light sensitive chemical film) deposited on the substrate to be patterned. Photomasks containing the pattern to be transferred are generally designed in CAD software and subsequently printed on a transparency or a chrome-finished fused silica blank.

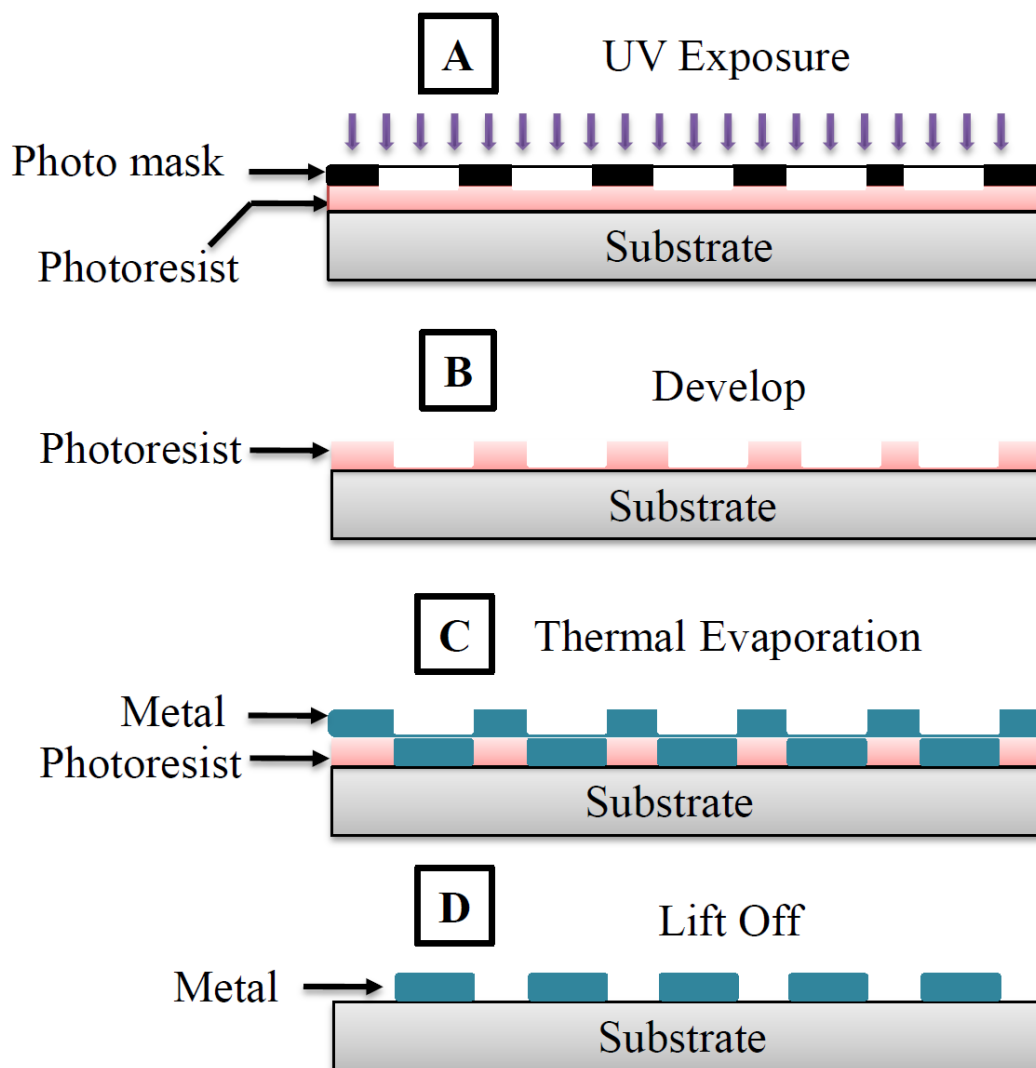


Figure 12: Fabrication sequence for photolithography and metal deposition

The photomask for this study was designed in SolidWorks and printed on mylar. Mylar masks were chosen as they are relatively inexpensive, have a fast turnaround time and are good for feature sizes up to 10 μm . The mylar masks were printed at CAD/ART Services Inc. The heater image in Fig. 11 is representative of the CAD mask used for patterning the macroscale heater.

A layer of positive photoresist Shipley 1818 (MicroChem Corporation) was spin-coated on the silicon substrate, followed by a soft pre-exposure bake on a hot plate. The substrate was then exposed to UV radiation using a Karl Suss contact aligner (Model MJB3) for 23 seconds. Centering of the heater pattern on the substrate was ensured by using an alignment mask that contained complementary features to that of the actual mask (Fig. 11) prior to the UV exposure. Once exposed, a 1: 4 diluted solution of Microposit 351 developer in DI water was used to develop the pattern for about 60 seconds (Fig. 12, step B). The developed resist served as a defining mask for the subsequent metal deposition (Fig. 12, step C).

The heater in this study was made by evaporating a 1.2 μm thick layer of aluminum (Al) film on to the developed photoresist using a Polaron thermal evaporator. In thermal evaporation, the source metal to be evaporated is first placed on a thin holder made of chrome called the boat. The boat with the source metal is mounted horizontally in a vacuum chamber facing the substrate on which the metal is to be deposited. The boat acts as a resistive heater that heats up on the passage of current and thereby melts the source metal placed on it. The molten metal vaporizes and settles on the substrate placed above the boat. The deposition rate of the metal is adjusted by modulating the current through the circuit.

With the Al film deposited, the silicon wafers were immersed in acetone overnight followed by ultrasonication to lift-off the metal from the unwanted regions (Fig. 12, step D). The completed test substrate is shown in Fig. 13.

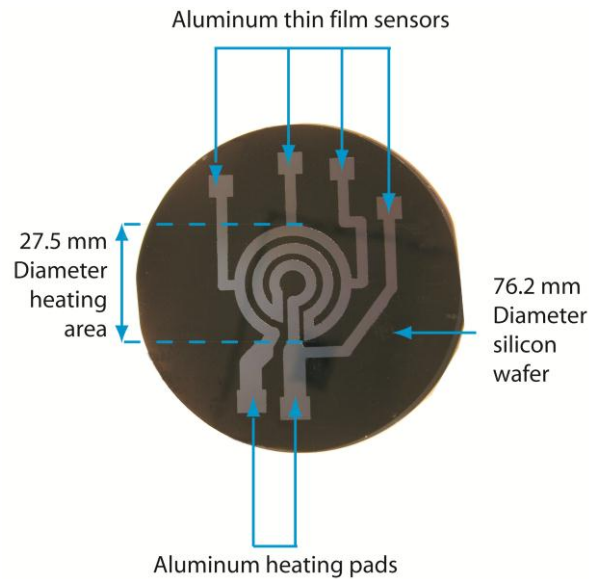


Figure 13: Macroscale silicon test substrate with aluminum thin film heater and voltage sensors

Macroscale heater- surface preparation for mounting

The heater and sensor contact pads were coated with two layers of conductive silver paint (Ted Pella Inc.) to minimize contact resistance (Fig. 14). The silver paint also protected the underlying aluminum thin film from scratches or tears during mounting, clamping or when in contact with the electrical pins. The area occupied by the heater was painted flat black in order to increase the emissivity of the heater side of the wafer for the IR measurements (Fig. 14). The completed heater had a nominal resistance of 3Ω as measured across the heating pads.

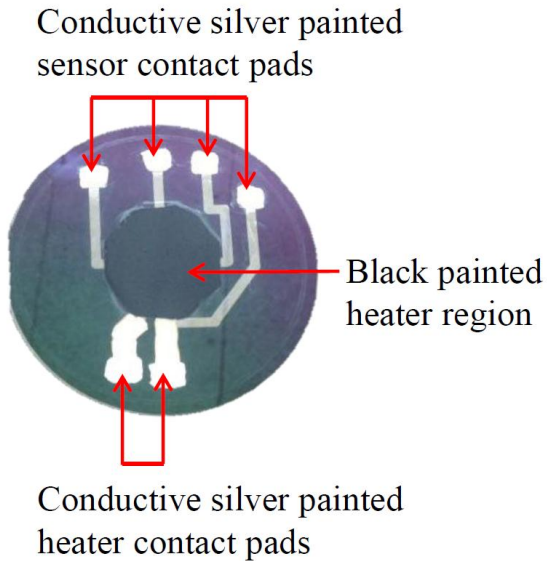


Figure 14: Macroscale heater surface preparation for mounting

4.3.2 MACROSCALE TEST SECTION MOUNT

In order to mount the silicon substrate to the test chamber a holder was custom-designed such that it permitted IR visualization from the rear side of the substrate. For the feasibility of experimenting with two fluids - DI water and FC-72, the silicon substrate was mounted with the blank side of the substrate in contact with the test fluid and the heater side facing the IR camera. An exploded view schematic of the set-up is shown in Fig. 15.

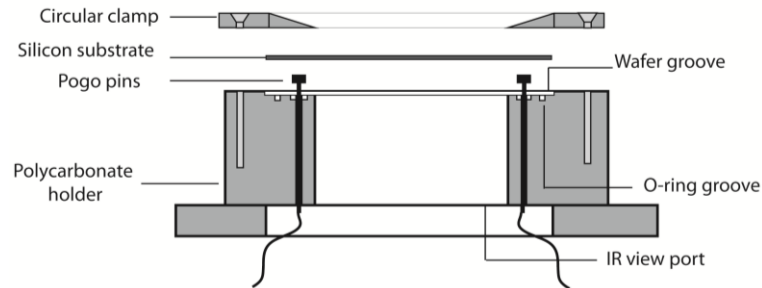


Figure 15: Exploded view schematic of the macroscale test section mount

The 101.6 mm diameter and 34.3 mm tall substrate holder was machined out of gray-tinted translucent polycarbonate rod, rated for a maximum temperature of 115° C (Fig.16a). A 50.8 mm diameter circular viewport allowed unobstructed IR visualization of the 27.5 mm diameter heating area.



(a)

(b)

(c)

Figure 16: Macroscale heater substrate mount: (a) IR viewport and electrical connections; (b) chamfered clamp; (c) assembled test section

The 380 μm thick silicon substrate was clamped down into its groove in the holder with a 6.6 mm thin circular polycarbonate clamp (Fig. 16b). The clamp was chamfered inwards at an angle of 25° to minimize obstruction to the impinging jet flow. A Viton® fluoroelastomer O-ring placed below the substrate provided the necessary seal

to make the mount leak proof. For tests with the low surface tension fluid FC-72, further precautions were required to prevent nucleation from gaps between the silicon wafer and the clamp. This was achieved by placing a thin silicone rubber gasket between the silicon substrate and the clamp plate. Additionally, the circular edge of the clamp was carefully sealed with a ring of high temperature RTV silicone gasket maker that completely eliminated any nucleation at the clamp edge.

Pogo pins fitted into pin sockets with soldering cups were used to make electrical contacts to the thin film heaters and sensors. The pin sockets for the heating leads were soldered to 16 AWG single conductor machine tool wires and banana plugs to interface with the DC power supply. Each sensor pin socket was soldered to two wire strands of an 8-wire shielded coaxial cable to allow data acquisition from multiple sensor lead combinations.

The holder assembly (Fig. 16c) was then mounted into the test chamber with the help of a stainless steel flange. The lip of the polycarbonate mount was pressed against an O-ring on the test chamber to form a seal. Detailed technical drawings of the mount, clamp and the stainless steel flange are given in appendix C.

4.3.3 MICROSCALE HEATER TEST SECTION

Microscale heater tests were conducted to study the bubble dynamics and thermal processes affecting phase change heat transfer at the microscopic level in the presence of an impinging jet. The goal was to design a heater that could generate a local hot spot such that an isolated bubble nucleation can be achieved. Following the lines of

the previously described macroscale heater, the microscale heater was designed to be of a concentric serpentine geometry with two heating leads and four voltage sensing leads. The layout of the heater rings was modified to be symmetric about the y-axis for better uniformity in the heat distribution. The heater was patterned at an off-centered radial location of 1.5 mm ($3d_{\text{jet}}$ for a 0.5 mm inner diameter nozzle) to study the influence of the jet flow on bubble dynamics in the wall jet region. The photomask used for patterning the heater is shown in Fig. 17.

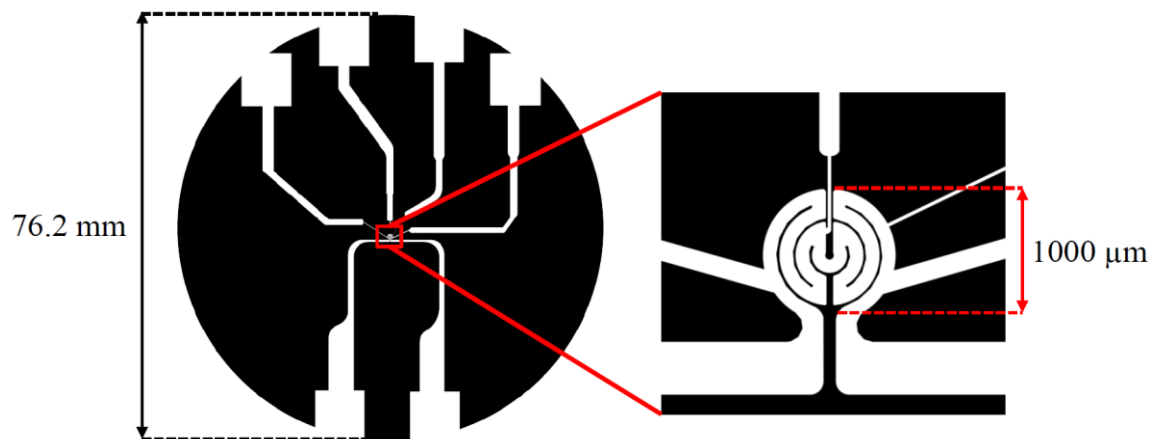


Figure 17: Photomask design for the microscale heater and voltage sensors

The microscale heater was designed to work specifically with the dielectric fluid FC-72, with the heater side in contact with the fluid during the tests. Contact leads for the heater and sensors were extended to the edge of the 76.2 mm silicon substrate to allow sufficient room for the electrical connections without interfering with the incoming jet flow. Literature available on various isolated bubble studies with FC-72 [35, 36, 48, 53] was reviewed to get an estimate of the expected bubble dimensions over a range of

wall superheats (1.3°C to 25°C) and fluid subcooling (0°C - 15°C). These studies reported isolated bubble departure diameters for FC-72 in the range of 300 to 700 μm , resulting in an average bubble departure diameter of 500 μm . The heater diameter was chosen to be 1000 μm which was twice that of average bubble departure diameter determined from the literature search. The choice of a heater size two times larger than the bubble diameter was done to ensure that the nucleating bubble geometries and corresponding heat transfer results were independent of the heater size [52].

The 1000 μm diameter serpentine heater consisted of four 100 μm wide semicircular rings spaced by 25 μm in each half circle about the y-axis. Sensor leads with widths of 100 μm and 22 μm were drawn from sections of the heater rings to capture voltage fluctuations caused by departing bubbles.

Microscale heater fabrication process development

Following similar microfabrication procedures to that described for the macroscale heater photolithography was used to transfer the pattern from a mylar mask onto the photoresist-coated silicon substrates. Shipley 1813 was used as the photoresist for the microscale heater geometry. The significantly smaller feature sizes required substantial process development to accommodate their high sensitivity to the duration of exposure and development. To conserve the silicon substrates initial process trials were first conducted on inexpensive, resist-coated glass substrates. In the beginning, rough estimates of exposure and development durations (12 sec and 25 sec respectively) were chosen in reference with that required for the macroscale heater (23

sec exposure and 60 sec development). Development was conducted in a 1: 4 diluted solution of Microposit 351 in DI water. The resulting feature as examined on an optical microscope (10X zoom) was severely overexposed and overdeveloped (see Fig. 18a). Based on the result the exposure and develop times were reduced to 4 sec and 15 sec respectively.

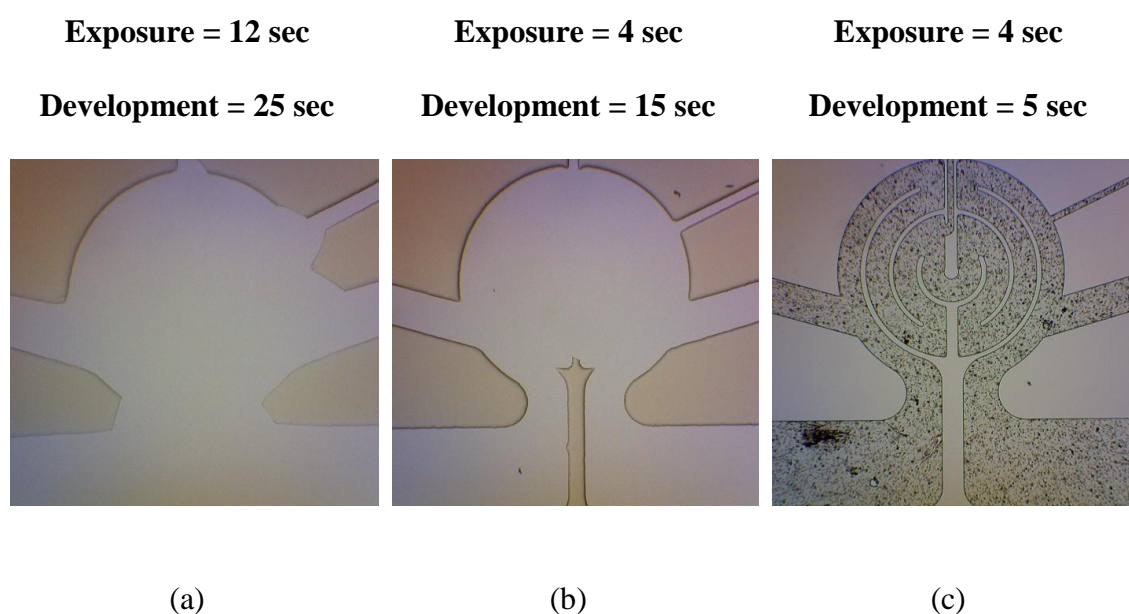


Figure 18: Estimating the exposure and develop times for the microscale heater pattern (initial trials on glass substrates)

The resulting pattern (Fig. 18b) appeared well exposed and sharp at the edges, but clearly overdeveloped between the rings. Retaining the exposure time at 4 sec, the development time was reduced further to generate a distinct heater pattern (Fig. 18c) on the photoresist. Resist residues observed as tiny speckles on the heater regions (Fig. 18 c) indicated that further fine tuning of the develop time was essential, however increasing the development time with a 1: 4 developer dilution caused finer regions with 22 μm features to overdevelop.

As a next step to eliminate resist residues, the dilution of the developer in DI water was increased to 1: 5 to slow down the development rate and have a longer development time. Figure 19 depicts the outcomes before and after increasing the dilution and hence development duration. These images were taken on silicon substrates with Shipley 1813 photoresist.

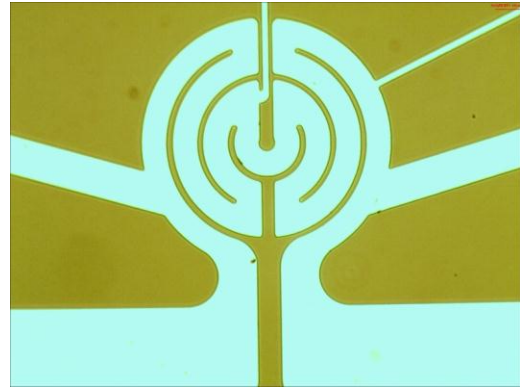
Exposure = 4 sec, Development = 5 sec Exposure = 4 sec, Development = 15 sec

Developer dilution = 1 : 4



(a)

Developer dilution = 1 : 5



(b)

Figure 19: Before (a) and after (b) the removal of resist residues (silicon substrate)

With the exposure and develop times determined, metal deposition was the next step of the process. As a first step of this stage, thermal evaporation used to deposit 40 nm of aluminum followed by a lift-off process similar to that described for the macroscale heater. However two issues surfaced: the adhesion of the film to the substrate was poor and the lift-off procedure was only partially successful. An example of this case is shown in Fig. 20.

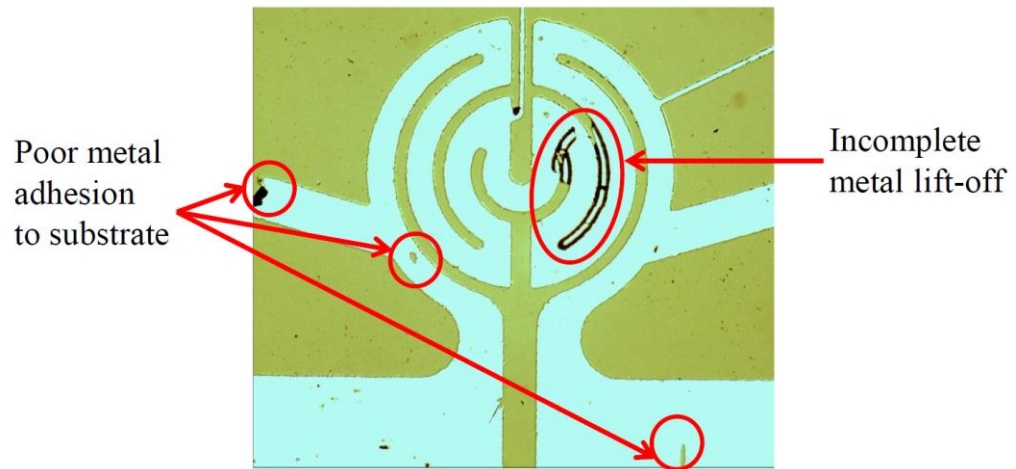


Figure 20: Example of an incomplete metal lift-off and poor film adhesion

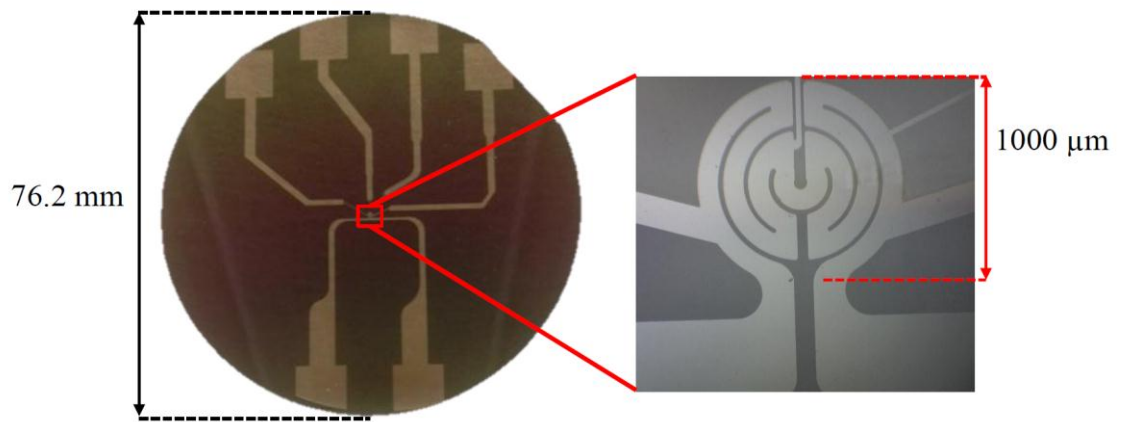


Figure 21: Completed microscale heater

To circumvent the issues of poor adhesion and lift-off, the aluminum was deposited by an electron-beam deposition process. In this process the source metal placed on an iron crucible is melted by accelerating a beam of electrons towards it. The metal vapors rise and settle on the substrate placed above. The electron beam deposition

process offers great control over the film deposition rate allowing for high purity uniform thin films. This process yielded excellent results for the microscale heater thin film. Figure 21 shows an image of the completed 1000 μm heater taken with a ken-a-vision optical microscope.

Microscale heater- surface preparation for mounting

As before, the contact pads were coated with two layers of conductive silver paint (Ted Pella Inc.) to minimize contact resistance. The microscale scale heater was designed for the heater side to be in contact with the test fluid, hence the black paint was not required. The completed heater had a nominal resistance of 193 Ω as measured across the heating pads.

4.3.4 MICROSCALE TEST SECTION MOUNT

Figure 22 shows the top view and sectional front view of the mount designed for the microscale heater substrate. As mentioned in the previous section the microscale heater substrate was mounted in the chamber with the heater side in contact with the dielectric test fluid FC-72. For this set-up, the electrical connections had to be made at the top surface of the silicon substrate within the test chamber. To allow for electrical connections without obstructing the jet flow or the high speed visualization, the heater and sensor leads on the substrate were first extended to the edge of the 76.2 mm silicon substrate.

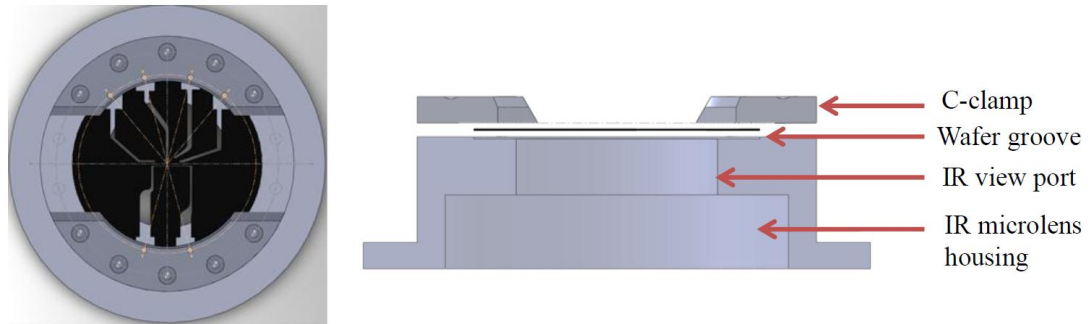


Figure 22: Schematics of microscale test section mount- top view (left) and sectional front view (right)

The 380 μm thick silicon wafer was then seated in a custom-built groove on a 25.4 mm tall and 101.6 mm diameter circular polycarbonate mount. The silicon substrate was clamped down securely with the help of two 6.35 mm tall C-clamps (Fig. 23). The clamps also housed the pogo pins for electrical connections to the heater and sensor contact pads. The tiny pogo pins were press-fit into the body of the clamp at a radial distance of 35.56 mm from $r = 0$, which is the center of the substrate. The gap between the C-clamps allowed sufficient room (38 mm wide passage) for unobstructed high speed visualization of the boiling activity during the experiments. External wiring to the press-fitted pogo pins was achieved by soldering 18 AWG machine tool wires to the solder cup of the pogo pins (Fig. 23). Quick connects were added to the end of these wires for ease of connection within the test chamber. The quick connects allowed hassle free removal of the test mount from the chamber while switching substrates.

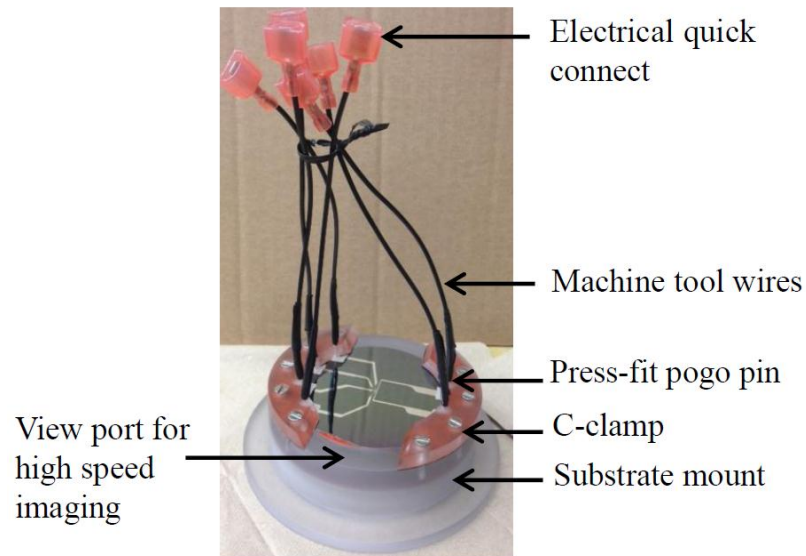


Figure 23: Microscale test section mount assembly

The counter-part electrical quick connects were soldered to onto wires and drawn out of the test chamber through a custom built leak free plug located at bottom wall the chamber. The gaps between the rear side of the silicon and the polycarbonate mount as well as that between the top surface of the silicon and the C-clamps were sealed with a fine layer of high temperature RTV silicone gasket to make the assembly leak free.

The mount provided a 50.8 mm (2 inch) diameter IR viewport on the rear side of the substrate (Fig. 22) for IR visualization. The IR microlens used for test with this substrate had a diameter of 75.7 mm and focal length of 28 mm. The rear end of the mount was widened to a 89 mm diameter to accommodate the IR micro lens. The design of the mount allowed the lens to come as close as 20 mm to the substrate. Detailed part drawings of the clamps and mount can be found in appendix C.

4.4 EXPERIMENTAL PROCEDURES

The following sections describe the calibration and testing procedures adopted during the pool and the submerged jet impingement boiling experiments. All experiments reported in this work were conducted at atmospheric pressure. The procedural differences between the tests with macro and microscale heater, as well as those between tests with DI water and FC-72 have been highlighted where applicable.

4.4.1 IR CALIBRATION

Previous studies by this group have shown that IR thermography requires a detailed calibration of the surface emissivity in order to determine a temperature from a recorded intensity [32, 67, 68].

Following on the lines of these previous studies, an *in situ* pixel-by-pixel calibration of the backside of the silicon wafer for IR thermography was performed prior to each set of tests conducted. The substrate was mounted within the test chamber with the IR camera in the same position as in an actual experiment. Depending on the fluid of choice for the actual experiment (DI water or FC-72), the test chamber was filled with the corresponding test fluid. The test fluids were used for calibration instead of a high temperature fluid like oil to avoid contamination of the test chamber, the test fluid and the silicon surface.

The fluid pool was heated using the cartridge heaters located on the backside of the test chamber. Pool temperature uniformity was monitored by calibrated

thermocouples. The thermocouples used for measuring the pool temperature were calibrated using a NIST-traceable RTD in a well-mixed oil bath. The corresponding thermocouple calibration curves are listed in [26]. No electrical power was supplied to the wafer itself. Calibration was performed for a range of pool temperatures depending on the test fluid used. For water calibration was performed from at six pool temperatures from 29°C to 80°C. For FC-72 which has a saturation temperature of 56°C, calibration data for each set of experiments were acquired at eight to nine temperature points from room temperature to about 54°C. At each steady state condition, pool temperatures and IR images from the rear side of the substrate were recorded simultaneously. It should be noted that because the silicon surface was open to natural convection from the bottom side, the surface temperature was expected to be lower than that of the pool. However, since an *in situ* calibration was performed, natural convection losses also occurred in the actual experimental run. Calculations for losses due to natural convection were nevertheless performed (see appendix D) and verified their insignificance. Hence, it was not deemed necessary to account for natural convection in either calibration or in the actual experiments.

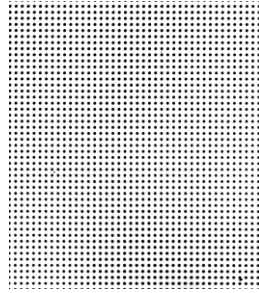
Time-averaged calibration thermal maps were used to determine an appropriate calibration fit for each pixel of the thermal image, using the calibrated pool thermocouple temperatures as a reference. Calibration fits thus obtained for each of the 60,416 pixels were used to obtain calibrated IR thermal maps providing quantitative surface temperature values.

4.4.2 HIGH SPEED CAMERA CALIBRATION

Prior to the start of each experiment a black balance adjustment process was conducted for the high speed camera to account for any pixel offset in the CMOS chip of the camera caused by the chip temperature or any other user-defined image acquisition parameter. The black balance adjustment was done by using the “current session reference” feature available in the Phantom Camera Control (PCC) software.

The high speed imaging of boiling activity with the macroscale heater provided qualitative information whereas the microscale heater experiments required a quantitative assessment of the bubble geometry from the high speed images for computing the evaporative heat flux. Hence a detailed calibration of the high speed camera pixel to physical dimension was conducted for the microscale heater experiments.

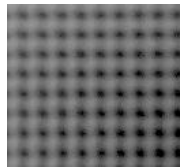
A calibration grid from Edmund Optics was used for the high speed camera pixel calibration. The grid consisted of a 25 mm x 25 mm area filled with circular dots, each measuring 0.0625 mm in diameter and spaced 0.125 mm apart. The calibration grid was attached to the jet plenum and positioned in the stagnant pool of test fluid such that it aligned with the geometric location of the micro heater. Using the Phantom camera at the same location and settings as for the actual experiment, still images of the calibration grid were taken. Figure 24 shows an image of the calibration grid when submerged within the stagnant pool of FC-72 at room temperature conditions.



25°C

Figure 24: Image of the calibration dot grid within a pool of FC-72 at room temperature conditions

Images of the grid in FC-72 were similarly acquired at 10°C and 20°C subcooled pool conditions that were used for the actual tests.



(a) 20°C subcooled pool



(b) 10°C subcooled pool

Figure 25: A section of the calibration grid in FC-72 at 10°C and 20°C subcooled pool conditions

These images were then used for determining the conversion factor from pixel to actual physical dimension. Conversions were determined by counting the number of pixels in x and y directions for a known center to center do spacing using the National Instruments Vision Assistant software. Ten repeated counts were acquired in both x

and y to get an average conversion factor for each test case. The corresponding standard deviation was accounted for in the high speed data uncertainty analysis.

4.4.3 SUBMERGED JET IMPINGEMENT BOILING WITH WATER: MACROSCALE HEATER SUBSTRATE

Submerged jet impingement boiling experiments with DI water were performed at atmospheric pressure under 20°C subcooled conditions using the macroscale heater substrate.

The macroscale heater substrate was thoroughly cleaned with acetone, isopropyl alcohol and deionized water on the plain side - which was to be in direct contact with the fluid. The assembled test section was mounted in the chamber and leak tests were conducted by filling the chamber with DI water. Once leaks were ruled out, a jet nozzle of inner diameter 1.16 mm was fixed to the plenum located in top plate of the test chamber shown in Fig. 8. For this set of experiments the nozzle-to-surface spacing (standoff distance) was kept constant at 3.6 jet nozzle diameters (approximately 4.18 mm). DI water was passed through the nozzle to ensure that there were no leaks from the flangeless nut that was used to affix the nozzle to the plenum. The chamber top plate was lowered using a shop crane, and then aligned and attached to the main test chamber using 4 screws on each wall of the test chamber. An O-ring placed between the top plate and the chamber ensured that this joint was leak free.

A night before the experimental run, the DI water was boiled extensively for several hours inside a modified commercial water heater, which was used as a degassing

chamber. On the morning of the experiment the test chamber was filled with the DI water from the boiler and degassing was repeated for about 2 hours using the cartridge heaters in the chamber. The oxygen content of the degassed water was measured using a dissolved oxygen meter manufactured by Extech Instruments (Model 407510). The oxygen content measurement of the degassed water was lower than the accuracy error of the instrument (± 0.4 ppm). The level of the fluid in the chamber was maintained such that it remained in contact with the condensing coils located at the rear wall of the chamber. This was essential in order to maintain the subcooling of the fluid. The required pool temperature was set on a PID controller that adjusted the pool temperature by controlling the power to the cartridge heaters immersed in the fluid pool. The heated water was continuously recirculated through a heat exchanger by a vane pump to maintain a uniform 20°C subcooling. Approximately two to three hours were allowed for the pool to attain the required temperature and achieve a steady state condition. Thermocouples positioned in the front and the back of the pool continuously monitored the uniformity of the pool temperature.

Three experiments were performed - one of pool boiling and two jet impingement conditions with jet exit Reynolds numbers, Re_{jet} , maintained at 2580 and 5161. For pool boiling experiments, the flow to the nozzle was turned off. For jet impingement experiments, the jet flow was initiated using the gear pump immediately after the chamber was filled. The variable speed controller of the pump together with an inline needle valve was used to set the jet flow to the desired mass flow rate. The temperature of the jet was maintained at the same levels as that of the pool by using

two cartridge heaters located at the inlet of the jet plenum. A thermocouple located within the plenum was used to monitor the jet temperature. Testing was initiated once the pool and the jet had attained steady state.

Beginning from zero power, the current input from the high current DC power supply to the thin film heaters on the silicon surface was incremented in steps of 0.4 A. At each power level, a five to seven minutes wait time was maintained for the system to reach a steady state. Data collection was started once steady state was attained. The upper limit of heat flux was dictated by the voltage limit of the power supply. As a result, critical heat flux (CHF) was not attained in this set of experiments. At each power increment the current indicated by the power supply and voltage measured at the pogo pins in contact with the heater pads were recorded to compute the electrical power input.

High speed videos, IR images, thin film sensor voltages, the jet mass flow rate and the pool and jet temperatures were recorded for each power level during steady state conditions. Illumination for high speed imaging was provided by halogen light sources and a custom polycarbonate diffuser sheet. Plastic covers were carefully placed over the bodies of both the cameras as a precaution against any fluid damage in the event of a leak. The high speed camera was first focused on the nucleating bubbles during a preliminary test run and the ideal recording parameters were determined. These parameters were implemented during the actual tests. IR images were acquired at 30 frames per seconds for a total of 5 seconds. The jet flow rate and pool and jet

temperatures were acquired using a LabVIEW program at the rate of 1 sample per second for 120 seconds. Sensor voltages from two sections of the serpentine heater (described in the next chapter) were acquired using a separate LabVIEW program. A total of 50,000 voltage samples were collected at 24 kHz for each data point.

Finally, at the end of the test day, the DI water in the chamber was drained and discarded. The power supply was switched off and care was taken to unplug the substrate power leads from the supply. The cameras were turned off and the camera lens caps were replaced. The chamber top plate was lifted with the shop crane and the chamber and substrate were dried off with an air blower. The substrate was inspected for any damage and covered with a 125 mm (diameter) x 65 mm (tall) circular glass dish for protection.

4.4.4 SUBMERGED JET IMPINGEMENT BOILING WITH FC-72: MACRO AND MICROSCALE HEATER SUBSTRATES

Overall the testing and data acquisition procedures for FC-72 were the same as that for DI water. However, FC-72 being an expensive fluid was available in a limited quantity. So the initial filling and degassing procedures required slight modifications to accommodate the limited fluid volume. A schematic of the modified test facility for FC-72 is shown in Fig. 9. In this modified facility, the degassing unit and the heat exchanger were removed to minimize the fluid volume during testing. A Graham condenser was added to the chamber top plate to aid the condensation rate. The fluid was filled into the chamber using gear pump and the jet nozzle and thereafter

extensively degassed using the PID controlled cartridge heaters immersed in the test pool. After several hours of degassing, the oxygen content of the degassed FC-72 was measured using a dissolved oxygen meter manufactured by Extech Instruments (Model 407510). The measured oxygen content was on average 2 mg/L (0.13×10^{-4} mole/mole).

Macroscale heater boiling experiments with FC-72 were conducted for both saturated and subcooled pool conditions. For all saturated test cases the fluid height was retained below that of the condensation coils in the chamber. For the subcooled test, the fluid level was raised such that the fluid was in contact with the cooling coils. During pool boiling with FC-72 on the macroscale heater substrate, a variable-speed gear pump recirculated the test fluid in the chamber to maintain uniform temperature. The recirculation occurred near the back wall of the test chamber at an approximate distance of 8 cm from the edge of the silicon substrate. For the jet impingement tests with FC-72, the recirculation caused by the jet flow loop was sufficient for maintaining the uniformity in pool temperatures.

Pool and jet impingement boiling experiments were conducted on the microscale heater substrate using FC-72 under subcooled pool conditions. For imaging the localized microscale bubbling activity generated by the microscale heater accurately, it was important to exclude any source of vibration other than that caused by the jet itself. Consequently, the chiller, the pool cartridge heaters, and pool recirculation were not used during data collection with the microscale heater substrate. The cartridge

heaters were turned off once degassing of the pool was complete and the pool had attained the desired set temperature point. As a result of not using the cartridge heaters or the pool recirculation it was not feasible to maintain the ambient pool at saturation temperature. Hence the microscale experiments could only be conducted for subcooled pool conditions.

The subcooled pool temperature during testing was maintained by adding a silicone rubber heater on the external side of the back wall of the test chamber. The distance of the chamber back wall to the edge of the silicon substrate was about 100 mm and that to the localized microscale heater was about 153 mm. Thus the heater was sufficiently far away from the visualized microscale region to induce any unwanted thermal gradients. The silicone rubber heater was controlled by a Tektronix PS280 DC power supply. The fluid level in the chamber was kept approximately 5 mm above the test surface. Keeping the fluid volume low ensured greater uniformity of the pool temperature. This was important to eliminate any unwanted thermal gradients within the pool fluid that could affect the bubble dynamics. Thermocouples located at the front and back of the pool continuously monitored the pool temperature to check for uniformity. Tests were started once the pool and the jet reached the desired subcooling and no thermal gradients were visible in the live image feed of the high speed and IR cameras. Optimal recording parameters for the high speed images were determined during preliminary test runs and implemented during the actual test. IR images at each power level were acquired real time at 120 frames per second using the IR microlens. Each time the camera recorded a total of 1023 images until the camera buffer was

filled. The images were then transferred to the computer using a FireWire interface. Two sets of 1023 images were recorded for each data point. Pool and jet temperatures, the jet flow rate and the sensor voltages were acquired by the same LabVIEW programs that were used for the macroscale heater tests.

At the end of the testing day, the fluid was drained from the chamber back into the manufacturer-provided storage containers. The power supply was switched off and the substrate power leads were unplugged from the supply. The cameras were turned off. The chamber was kept sealed when not in use to prevent any remnant FC-72 from evaporating.

4.4.5 CONDUCTED EXPERIMENTS

This section summarizes the macroscale and microscale heater boiling experiments that were conducted for this study. Macroscale heater experiments were conducted with two fluids DI water and FC-72. Table 1 provides a list of all experiments completed with the macroscale heater.

With DI water tests were conducted under 20 °C subcooled boiling conditions for one of pool boiling and two jet impingement conditions with jet exit Reynolds numbers, Re_{jet} , maintained at 2580 and 5161. A nozzle of inner diameter 1.16 mm was placed at a height of $3d_{jet}$ above the silicon tests substrate for these experiments. Macroscale heater tests with FC-72 were conducted for saturated and 20°C subcooled conditions with nozzles of three different diameters, two nozzle geometries (cavitating and non-cavitating jet), two H/d_{jet} ratios and for varying Reynolds numbers. Data were

acquired for both increasing and decreasing heat flux conditions to capture the boiling hysteresis of FC-72.

Pool and jet impingement boiling experiments with the microscale heater were performed using the fluid FC-72 for pool subcoolings of 10°C and 20°C. The nozzle used for these microscale heater tests had an inner diameter of 0.5 mm and was placed at height of $6d_{\text{jet}}$ above the silicon surface. Experiments conducted with the microscale heater substrate are listed in Table 2.

Note that Tables 1 and 2 list approximate subcooling values of 10°C and 20°C for ease of comparing the experimental results. Appendix H provides a detailed list of the exact subcooling values for each test case for both the heater geometries.

Table 1: Matrix of experiments conducted with the macroscale heater

Fluid	d_{jet} (mm)	H/d_{jet}	Subcooling (°C)	Re_{jet}	u_{jet} (m/sec)	Nozzle Geometry
Water	1.16	3.6	20	0	0	Regular
				2580	0.81	
				5161	1.6	
FC-72	1.16	3.6	0	0	0	
				5161	1.22	
				7740	1.83	
			20	0	0	
				5161	1.46	
				7740	2.19	
	0.5	6	0	7866	2.23	
				10778	5.92	
	1.10	6	0	10616	5.83	Cavitating
				18416	4.59	Cavitating
			20	18562	5.54	Cavitating

Table 2: Matrix of experiments conducted with the microscale heater using a regular jet nozzle

Fluid	d_{jet} (mm)	H/d_{jet}	Subcooling (°C)	Re_{jet}	u_{jet} (m/sec)	Radial Location (mm)
FC-72	0.5	6	10	0	0	1.5
				3181	1.9	
			20	0	0	1.5
				3128	2.05	

5 DATA REDUCTION AND ANALYSIS

During the pool and jet impingement experiments with the macro and microscale heaters, data were collected in the form of IR thermal images of the test section, high speed images of the boiling activity on the top surface of the silicon, voltage time series from thin film sensors and mass flow rate of the jet along with thermocouple readings for pool and jet temperatures. This chapter discusses the steps implemented for the reduction of the acquired data and the subsequent data analysis. An estimate of errors in measurement is provided with the help of uncertainty analysis.

5.1 JET FLOW RATE

The mass flow rate of the jet (\dot{m}_{jet}) during the jet impingement boiling experiments was monitored by a factory calibrated Coriolis flow meter and recorded using a program in LabVIEW. The measured mass flow rate along with the liquid density (ρ_l) and the inner diameter of the jet nozzle was used to calculate the jet exit velocity (u_{jet}).

$$u_{jet} = \frac{4\dot{m}_{jet}}{\rho_l \pi (d_{jet})^2} \quad (8)$$

The computed jet exit velocity (u_{jet}), liquid density (ρ_l) and liquid viscosity (μ_l), evaluated at the measured temperature, were then used to estimate the jet exit Reynolds number.

$$\text{Re}_{jet} = \frac{\rho_l u_{jet} d_{jet}}{\mu_l} \quad (9)$$

Two fluids, DI water and FC-72, having very distinct thermo-physical properties (appendix A) were used in the present work. The properties for DI water were evaluated at atmospheric pressure and the measured fluid temperature using Engineering Equation Solver[®] (EES) [69]. The properties of the dielectric fluid FC-72 at atmospheric pressure were obtained from its manufacturer 3M [70]. The temperature dependent relationships provided by 3M were used to evaluate the liquid density (ρ_l) and liquid viscosity (μ_l) at the measured fluid temperature.

5.2 POOL AND JET TEMPERATURES

Thermocouples immersed in the front and the back of the pool were used in all experiments to monitor the overall uniformity in pool temperature. The temperature of the jet during the jet impingement experiments was measured by a thermocouple placed within the jet plenum right before its exit into the pool. All temperature readings were acquired at a rate of one sample per second using a LabVIEW program. These temperatures were saved as comma-separated-value (.csv) files directly from LabVIEW.

Pool temperatures recorded during the IR calibration and boiling experiments were averaged to obtain a mean pool temperature value. The mean temperatures of the pool obtained during the IR calibration experiment served as reference for calibrating the simultaneously acquired IR images. The temperatures of the jet and the pool recorded

during the jet impingement boiling experiments were averaged to obtain a mean fluid temperature.

$$T_{fluid} = \frac{T_{pool} + T_{jet}}{2} \quad (10)$$

Overall the recorded jet and pool temperatures were within 0.2 - 0.8 percent of each other. The computed values of T_{fluid} were used to determine the excess temperature of the silicon surface (obtained from IR imaging) over that of the fluid.

5.3 IR DATA REDUCTION AND ANALYSIS

IR visuals of the silicon substrate were acquired for all calibration and boiling experiments presented in this work. All IR videos were first recorded in .tvs format via the TVS Viewer software provided with the IR camera and then converted to images in .IRI format using a feature in the TVS software. Thereafter, each thermal image was converted to a comma-separated-value (.csv) format using the PE Professional software (GORATEC). The csv files contained temperature values for each of the 256 pixels \times 236 pixels in the camera's field of view. All further data processing was done in MATLAB. The IR image processing steps employed for the macro or microscale heater geometries are individually described in this section.

5.3.1 IR DATA ANALYSIS: MACROSCALE HEATER

Several approaches have been adopted to obtain heat flux in IR thermography experiments in literature. IR imaging has been used in literature [33, 34] to obtain time

and space resolved surface temperatures. However the boiling curve heat flux estimates in these studies [33, 34] were based on the measured input electrical flux.

An alternative approach, as presented in this work, is to adopt a two-dimensional conduction analysis to account for the axial conduction in the substrate and thus estimate the net convective heat flux from the recorded temperature maps. This approach has been previously implemented among others by Patil and Narayanan [67] to compute local convective heat transfer coefficients from an impinging air jet, and by Wagner and Stefan [71] for obtaining heat fluxes under single nucleating bubbles. The analysis methods in this study were made versatile to provide both local as well as area-averaged values of temperature and convective heat flux. This approach permitted a quantitative comparison of local and area-averaged boiling curves.

The first task in analyzing the IR data was to determine the calibrated temperature values at all pixel locations in the acquired images. IR data for these tests were acquired at 30 frames per second. At each tested power level and for each calibration temperature, thirty one consecutive thermal images were averaged pixel by pixel to create a time-averaged thermal image. Time-averaged calibration temperature maps of the macroscale heater substrate for three set temperatures during a calibration experiment with DI water are shown in Fig. 26. As described in the experimental procedures, the heater side of the substrate faced the IR camera and the heater region was painted flat black (Fig. 14) for increased surface emissivity. No power was supplied to the heaters during calibration.

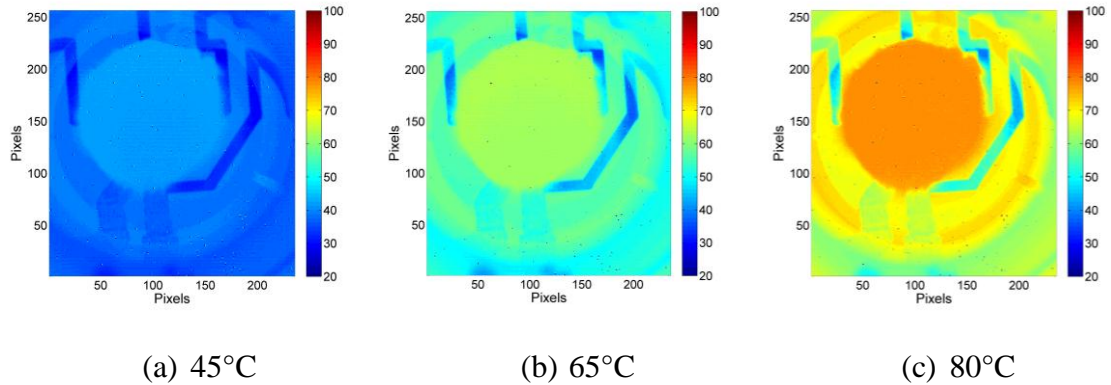


Figure 26: Time-averaged calibration temperature maps of the macroscale heater substrate for three temperatures during calibration with DI water

Each time-averaged calibration IR image was compared with the simultaneously recorded mean pool temperature from the pool thermocouples and accordingly an appropriate calibration fit was determined for each pixel of the IR image. The temperatures obtained from the IR maps were found to vary linearly with increasing pool temperatures and hence a linear (first order) fit was applied to all pixels. The calibration curves for select locations within the black painted heater region for calibration tests with water and FC-72 are given in appendix E. The determined pixel calibrations were applied to all time-averaged experimental IR data to generate calibrated thermal images with quantitative surface temperature values. Figure 27 shows a calibrated time-averaged thermal image of the macroscale heater substrate in its original size (256×236 pixels). The image in Fig. 27 represents an impinging jet non-boiling condition for a test with DI water.

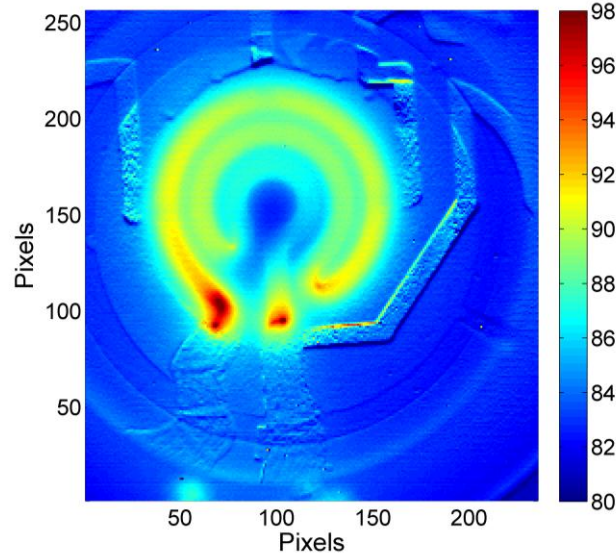


Figure 27: A time-averaged and calibrated IR temperature map of the macroscale heater in its original size (256×236 pixels). Temperatures in $^{\circ}\text{C}$.

All images were cropped from their original size (256×236 pixels) to an area of 150×150 pixels ($\sim 34.5 \times 34.5 \text{ mm}^2$) corresponding to an area slightly larger than that of the heater rings as shown in Fig. 28. As a next step, the calibrated temperature maps were subjected to two-passes of a top hat filter to reduce the uncertainties in the computed conduction heat flux (see appendix F). The top hat filter estimates the temperature value at each pixel ($T_{filter}(i, j)$) based on a weighted average of its neighboring pixels,

$$\begin{aligned}
 T_{filter}(i, j) = & \frac{1}{4}T(i, j) + \\
 & \frac{1}{8}(T(i-1, j) + T(i, j-1) + T(i, j+1) + T(i+1, j)) + \\
 & \frac{1}{16}(T(i-1, j-1) + T(i-1, j+1) + T(i+1, j-1) + T(i+1, j+1))
 \end{aligned} \tag{11}$$

A similar weighted-average filtering of thermal maps has been employed by Dutton et al. [72] to reduce the uncertainties in recorded temperatures using liquid crystal thermometry. Figure 28 represents the cropped and filtered thermal image resulting from this top hat filtering.

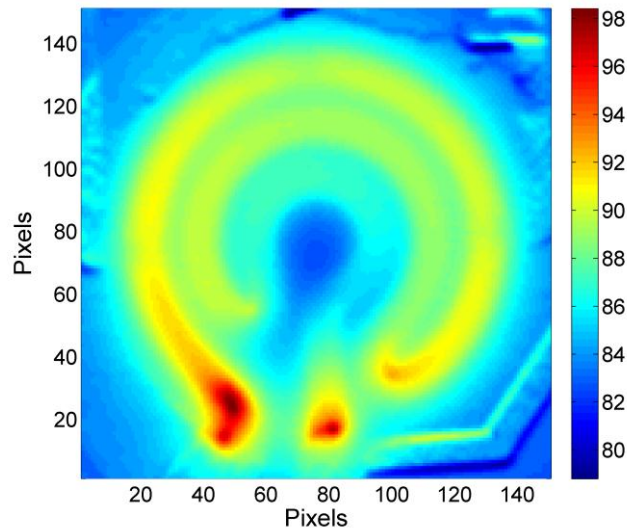


Figure 28: Temperature map for the macroscale heater filtered using a top hat filter and cropped to the region of interest. Temperature scale in °C.

Control volume approach to obtain local heat flux values

For the remainder of the analysis, each pixel was treated as a control volume (Fig. 29), having a square base of width, $\Delta = \Delta x = \Delta y$ and a thickness, $t = 380 \mu\text{m}$, equal to that of the silicon substrate. The value for the pixel width (Δ) was set equal to the IR image resolution determined for each set of experiments from the known width of the deposited heater and sensors. On average $\Delta = 224 \mu\text{m}$ for all the experiments

conducted with the macroscale heater, which is about 1.69 times smaller than the substrate thickness (t). To ensure that $\Delta > t$ would not significantly change the results, calculations for $\Delta = 1.2 t$, were done for a pool boiling test case with DI water at the highest flux. These calculations (appendix F) indicated that the average temperatures for the two cases were within 0.28 percent of each other, owing to the top-hat filtering process on the temperature maps.

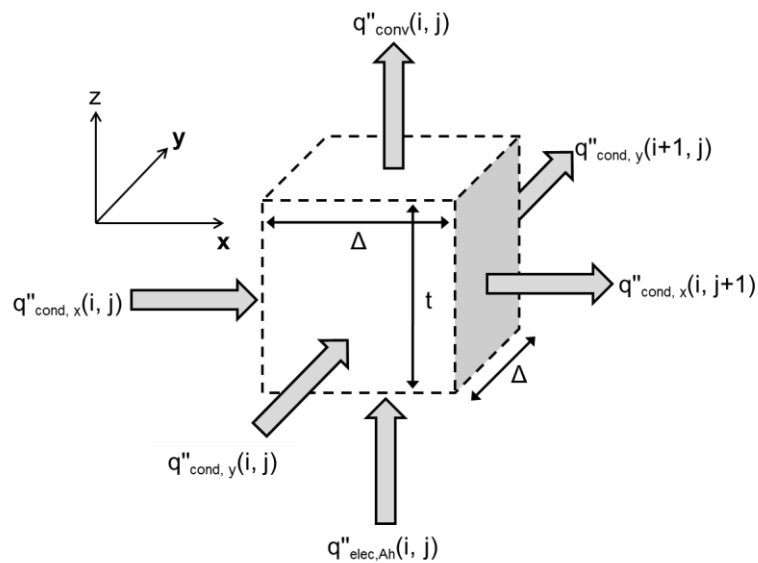


Figure 29: Energy balance on a (pixel) control volume

Accounting for the change in thermal conductivity (k) of silicon with temperature, the two-dimensional conduction heat flux ($q''_{cond}(i, j)$) entering each pixel at the faces of the control volume in the x and y directions, was computed using a central differencing scheme,

$$q''_{cond}(i, j) = - \left(\frac{k(i, j) + k(i, j-1)}{2} \right) \left(\frac{T_{filter}(i, j) - T_{filter}(i, j-1)}{\Delta} \right) \quad (12)$$

The computed conduction heat flux accounts for axial conduction while neglecting the conduction across the substrate thickness. The expected temperature drop across the 380 μm thick substrate estimated using a 1-D analysis is accounted for as a bias error in the uncertainty estimate. Table 3 summarizes the temperature drop across the substrate thickness that can be expected at the highest average heat flux tested for the various experiments conditions with the macroscale heater.

Table 3: Expected temperature drop across the 380 μm thick silicon substrate using a 1-D model at the highest average heat flux

Test	Subcooling ($^{\circ}\text{C}$)	Highest average heat flux (W/cm^2)	Expected temperature drop across the substrate ($^{\circ}\text{C}$)
DI water	20 $^{\circ}\text{C}$	66.5	1.69
FC-72	0	14.9	0.38
FC-72	20 $^{\circ}\text{C}$	19.7	0.50
FC-72 Cavitating Jet	0	10.3	0.26
FC-72 Cavitating Jet	20 $^{\circ}\text{C}$	22.8	0.58

To identify the pixel locations occupied by the serpentine heater, a binary template of the heater pattern was generated in MATLAB using an actual image of the heater substrate. The circular area of the substrate occupied by the serpentine heater geometry is denoted by A_s and the area occupied by the entire length of the rings is denoted as A_h (Fig. 30).

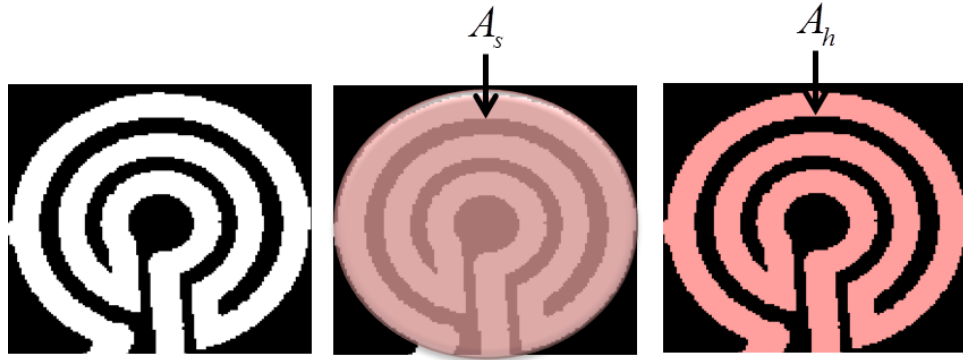


Figure 30: Binary template of the macroscale heater. The substrate area corresponding to the serpentine heater (A_s) and the area occupied by the length of heater rings (A_h) are depicted.

The electrical heat flux, q''_{elec} , was provided at the pixels representing the heater locations in the binary heater template. This value of q''_{elec} over the area A_h , was estimated based on the input voltage (V) measured at the pins in contact with the thin film heaters and the current (I) measured at the power supply.

$$q''_{elec,Ah} = \frac{VI}{A_h} \quad (13)$$

At each (pixel) control volume, an energy balance (Fig. 29) was performed assuming steady state conditions with no energy storage. The convective heat flux, $q''_{conv}(i, j)$, in the pixel locations with the heater was determined as,

$$q''_{conv}(i, j) = q''_{elec,Ah} + \frac{(q''_{cond,x}(i, j) - q''_{cond,x}(i, j+1) + q''_{cond,y}(i, j) - q''_{cond,y}(i+1, j))t}{\Delta} \quad (14)$$

In regions devoid of the heaters, $q''_{conv}(i, j)$ was estimated using the equation above with $q''_{elec, Ah}$ set to zero. The evaluated convective heat flux was subjected to three passes of a three sigma filter followed by a 3-by-3 pixel local averaging at each pixel location to smooth out the data. Defining the centermost pixel of the 150×150 pixels cropped window as $r = 0$, a two-dimensional matrix of radial locations was created as shown in Fig. 31.

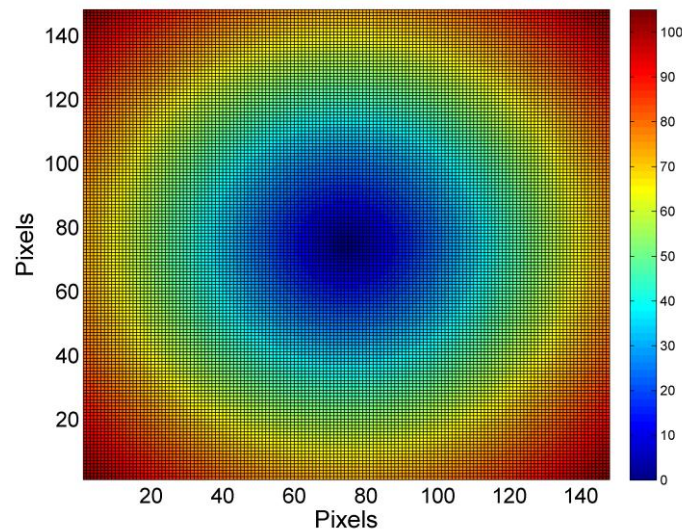


Figure 31: Template of radial locations

The generated radial matrix (Fig. 31) along with the binary heater template (Fig. 30) were used to determine the radial boundary of the macroscale heater. The temperatures and convective heat flux values within this determined radial boundary were retained for further processing. The resulting convective heat flux spatial map within the region of interest is shown in Fig. 32.

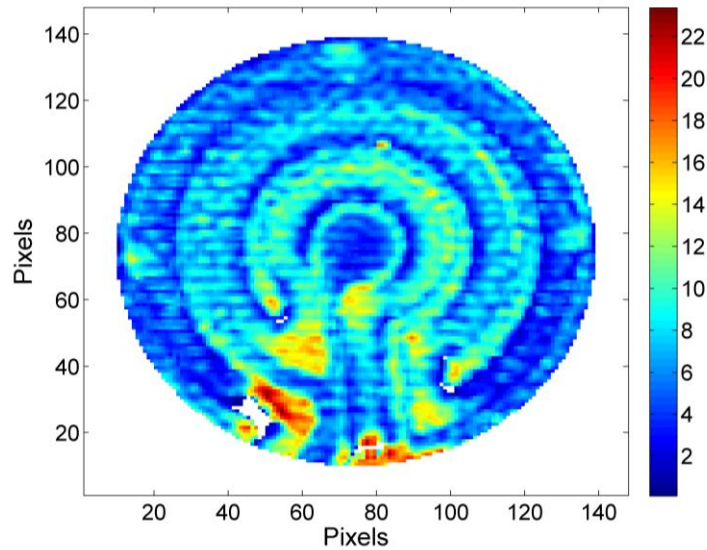


Figure 32: Convective heat flux in W/cm^2 for an impinging jet non-boiling condition.

At this stage of the analysis, boiling curves could be generated for each of the pixel locations within the region of interest using the local pixel temperatures, $T_{filter}(i, j)$ and the computed values of $q''_{conv}(i, j)$. Symmetry afforded by the circular jet and the heater pattern was utilized to present a radially-local assessment of the surface temperatures and the corresponding convective heat flux. The temperature ($T_{filter}(i, j)$) and the flux ($q''_{conv}(i, j)$) were circumferentially averaged for each radial location starting from the impingement point ($r = 0$) to obtain radially local surface temperatures, $T(r)$, and convective heat fluxes, $q''_{conv}(r)$.

To study the trends in the local surface temperature profiles the circumferential averaging of temperatures was restricted to the upper symmetric semi-circular region

of the heaters. This region of the serpentine heater is devoid of heating leads which cause local hot-spots.

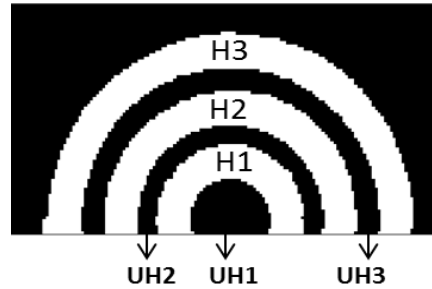


Figure 33: Binary representation of the symmetric semi-circular region of the heater geometry

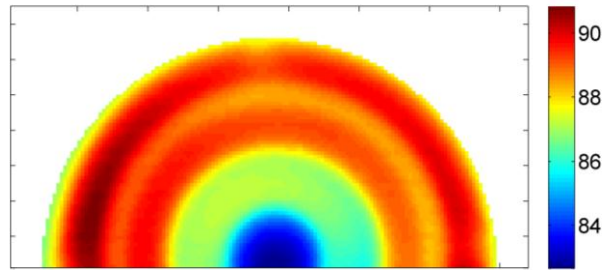
Figure 33 shows a binary representation of the upper semi-circular heater region indicating the specific heated sections (H1, H2 and H3) corresponding to the three heater rings and unheated sections (UH1, UH2, UH3) corresponding to the space between each heater ring for this upper semi-circular section. The filtered temperature map and the convective heat flux corresponding to the symmetric semi-circular region are shown in Fig. 34.

Obtaining the area-averaged temperature and convective heat flux

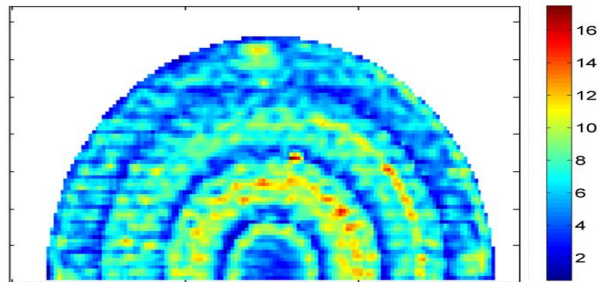
A global estimate of the surface temperature and the convective heat flux was obtained by performing a radially weighted area-average of the circumferentially averaged temperatures $T(r)$ and convective heat fluxes $q''_{conv}(r)$ beginning from the jet impingement point ($r = 0$),

$$T_{avg}(r) = \frac{\{T(r) \cdot (2\pi r \Delta)\} + \{T_{avg}(r-1) \cdot (\pi \cdot (r-1)^2)\}}{\pi r^2} \quad (15)$$

$$q''_{conv,avg}(r) = \frac{\{q''_{conv}(r) \cdot (2\pi r \Delta)\} + \{q''_{conv,avg}(r-1) \cdot (\pi \cdot (r-1)^2)\}}{\pi r^2} \quad (16)$$



(a)



(b)

Figure 34: Filtered temperature in °C (a) and convective heat flux in W/cm² (b) corresponding to the symmetric semi-circular region of the heater geometry. (Impinging jet non-boiling condition)

Estimates of the radial limits (a,b) of each heated section (H1, H2 and H3) and unheated sections (UH1, UH2, UH3) were obtained from the binary representation and

used to compute sectionally-averaged temperatures (T_{avg}) and convective heat fluxes q''_{avg} for the regions of interest.

$$T_{avg}(b-a) = \frac{(T_{avg}(r)_{r=b} \cdot \pi b^2 - T_{avg}(r)_{r=a} \cdot \pi a^2)}{(\pi(b^2 - a^2))} \quad (17)$$

$$q''_{avg}(b-a) = \frac{(q''_{conv,avg}(r)_{r=b} \cdot \pi b^2 - q''_{conv,avg}(r)_{r=a} \cdot \pi a^2)}{(\pi(b^2 - a^2))} \quad (18)$$

To determine the net average electrical heat flux received by the fluid it was important to account for the heat flux leaving the circumferential boundary of the outer ring of the heater substrate area A_s . The conduction flux loss (q''_{concl}) from the substrate area A_s was computed by averaging the conduction flux for the three outer most radial locations on the heater. The net heat flux, $q''_{elec,net}$, was estimated by accounting for this conduction loss.

$$q''_{elec,net} = \frac{VI}{A_s} - q''_{concl,As} \quad (19)$$

With all the local and area-average values computed, boiling curves were generated for various locations and sections of the heater substrate. The boiling curves presented here were subjected to a Locally Weighted Scatter-plot Smoothing (LOWESS) filter that performs a weighted least-squares regression of the data based on a specified span about the excess temperature. This filtering allows for a continuous representation of all raw data. Details of this filtering process can be found in Cardenas et al. [73].

Boiling curve validation

The accuracy of the quantitative results of this visualization study heavily depended on the IR data analysis methods described above. Hence it was essential to validate the convective heat flux output generated by the MATLAB data processing. The validation was performed by comparing the area-averaged convective heat flux obtained from the processed IR maps with the net electrical heat flux supplied to the heater.

The radially weighted, area-averaged temperatures $T_{avg}(r)$ and convective heat fluxes $q''_{conv,avg}(r)$, were used to generate the area-averaged boiling curves over the heated substrate area A_s (Fig. 30). Figure 35 shows the Lowess-filtered [73] area-averaged boiling curves for pool boiling ($Re_{jet} = 0$) and SJIB of DI water (filled symbols) subcooled by 20°C. The x-axis in this plot represents the area-averaged surface temperatures (T_{avg}) in excess of the average subcooled fluid temperature (T_{fluid}). Also plotted for comparison are the values of the net input electrical flux ($q''_{elec,net}$ (open symbols) calculated using Eq. 19) as a function of ($T_{avg} - T_{fluid}$).

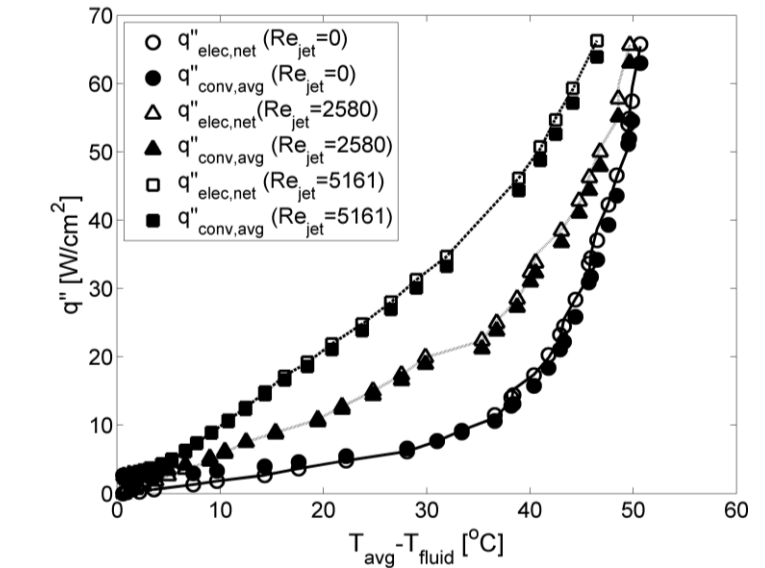


Figure 35: Comparison of the net input electrical heat flux with area-averaged heat flux values plotted as function of area-averaged temperature difference. The fluid was DI water subcooled by 20°C.

Figure 35 shows a reasonably good agreement between the net electrical flux ($q''_{elec,net}$) with the experimentally obtained and analyzed convective heat flux values ($q''_{conv,avg}$). For the two jet impingement tests, the relative difference in the area-averaged heat flux ($q''_{conv,avg}$) and the net electrical flux ($q''_{elec,net}$) was estimated to be in the range of 3 - 4 percent, in the temperature difference range of 20 - 50°C. As a reference, the relative difference between $q''_{conv,avg}$ and $q''_{elec,net}$ for pool boiling ranged from 4 - 10 percent for temperature differences of 20 - 50°C with the larger uncertainties occurring at the lower heat fluxes.

5.3.2 IR DATA ANALYSIS: MICROSCALE HEATER

IR data for the microscale heater tests were acquired at 120 frames per second. At each tested power level and for each calibration temperature, 120 consecutive thermal images of size 256 pixels x 236 pixels were converted to .csv format and imported into MATLAB for processing.

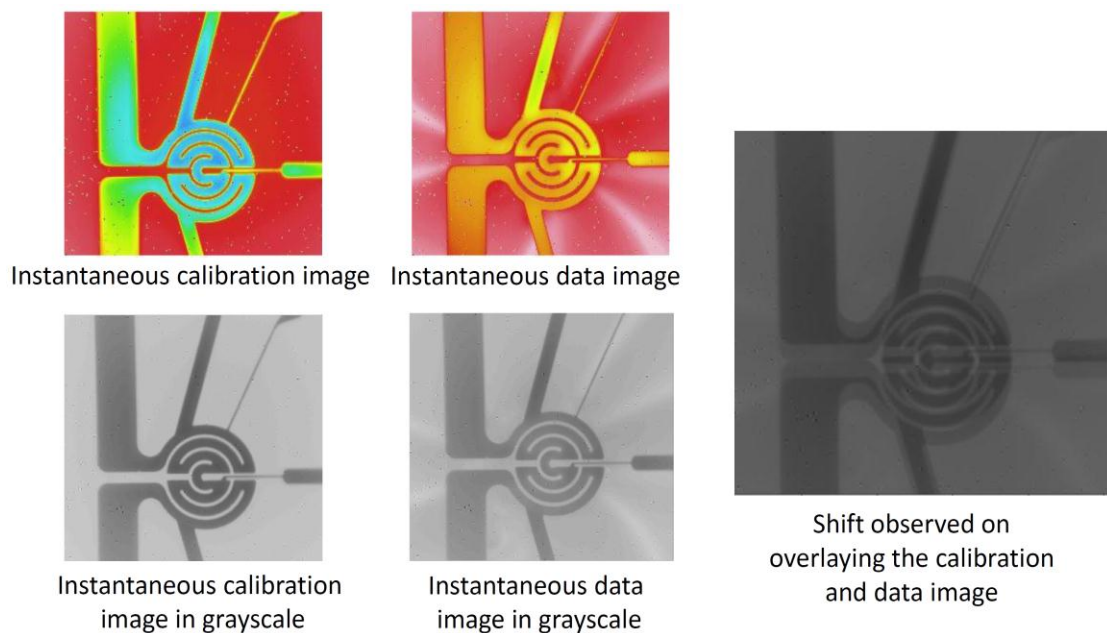


Figure 36: Need for IR image alignment during microscale heater tests

For these tests the IR camera had been mounted on a tripod stand as explained in the previous chapter (see section 4.2.2). The IR camera had an inbuilt Stirling cooler that resulted in vibrations in the camera during data acquisition with the microscope objective. This resulted in the acquired images being mutually off-shifted. An example of the observed shift in the acquired image is shown in Figure 36. Note that these

instantaneous images are for qualitative illustration only, and hence the temperature scale is not shown here. For a meaningful interpretation of results it was imperative to align all the acquired images prior to any further processing. The image alignment procedures adopted for the microscale heater tests are explained below.

Microscale Heater: IR image alignment

Each of the 120 images for each calibration temperature and each tested power level for the pool and jet impingement boiling tests had to be mutually aligned. Image alignment was accomplished by using a normalized two-dimensional cross correlation function in MATLAB. Normalized cross correlation function is a commonly used technique for alignment of images that are off-shifted in either x or y directions.

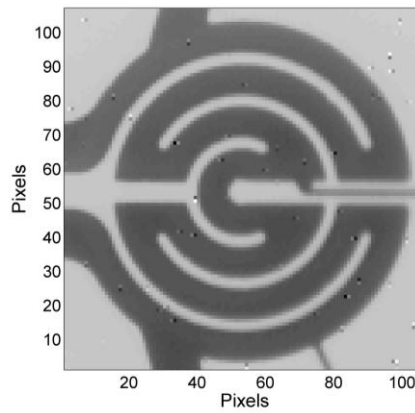


Figure 37: Instantaneous calibration image cropped to the region of interest

Alignment procedures began by importing the first instantaneous IR calibration image of lowest calibration temperature in MATLAB. This calibration image was cropped to

the region of interest. The resulting cropped calibration image is shown in grayscale in Fig. 37.

Treating cropped image as a subset of the originally acquired 256 pixels x 236 pixels image, a normalized cross correlation was conducted between the cropped image and each of the remaining calibration and data images. The cross correlation mapped the cropped image over each section of the 256 pixels x 236 pixels image to find the location of best match. The output of the correlation was a matrix of correlation coefficients, wherein the location of best match has a peak intensity of unity. As an example, the generated matrix and the identified location of the peak intensity is shown as a surface plot in Fig. 38.

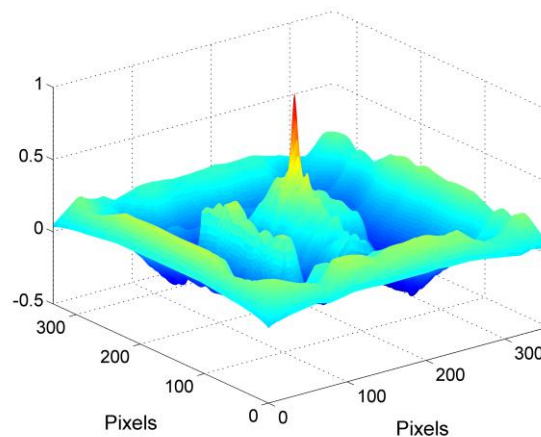


Figure 38: Surface plot of the normalized cross correlation correlation matrix. Location of the best match between compared images is identified by the peak intensity

The output matrix of coefficients has a dimension evaluated as the sum of the number of rows and columns of the two images compared minus one. With this knowledge the co-ordinates of location of best match (peak intensity location) was determined by transforming the co-ordinates from the correlation matrix to the (256 pixels x 236 pixels) image space. The crop area for the aligned images was determined corresponding to the transformed co-ordinates. As verification, the rectangular crop area was overlaid on the data image. The resulting image is shown as a grayscale image in Fig. 39.

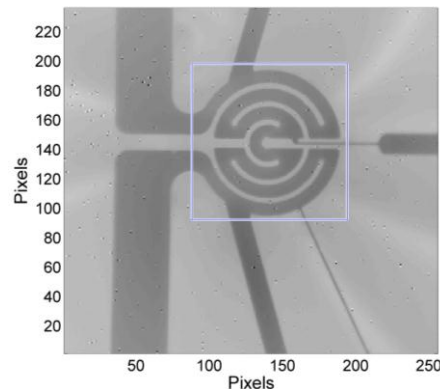


Figure 39: Crop area selected in the original data image based on the output of the normalized cross correlation

The newly aligned and cropped images were overlaid on the first cropped calibration image with which the cross correlation was performed to verify the image alignment. The resulting aligned and overlaid image is shown in grayscale in Fig. 40b. The overall shift between the originally misaligned images (Fig. 36) for this case was evaluated to be 38 pixels in the x-direction and 62 pixels in the y-direction.

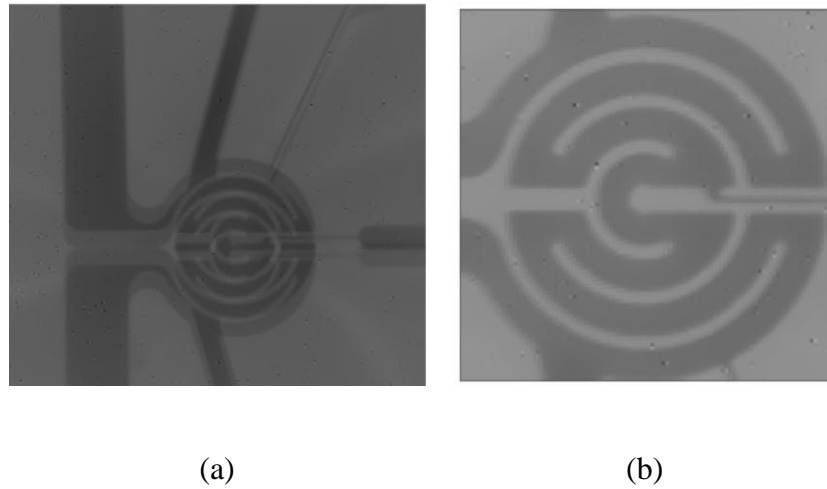


Figure 40: Calibration and data images overlaid (a) before and (b) after alignment

Obtaining calibrated temperature maps

Post-alignment and cropping, the next step was to use the IR temperature maps acquired during calibration experiments to determine appropriate calibration fits for each pixel of the IR images based on the simultaneously acquired pool temperatures. Calibration was performed each time the test surface was changed. Requirement to change the substrate depended on the longevity of the thin film heater. For this set of tests a total of two substrates were used one for pool boiling and the other for jet impingement tests. Correspondingly calibration experiments were conducted once for each test surface. During the calibration experiment IR images and thermocouple data were acquired for eight to nine temperatures in the range of 24°C to 54°C.

A total of 120 successive IR calibration images were first averaged pixel by pixel to create a single time-averaged thermal image for each calibration temperature. Figure

41 shows the time-averaged IR temperature maps of the microscale heater substrate at three calibration temperatures during calibration of the jet impingement test substrate.

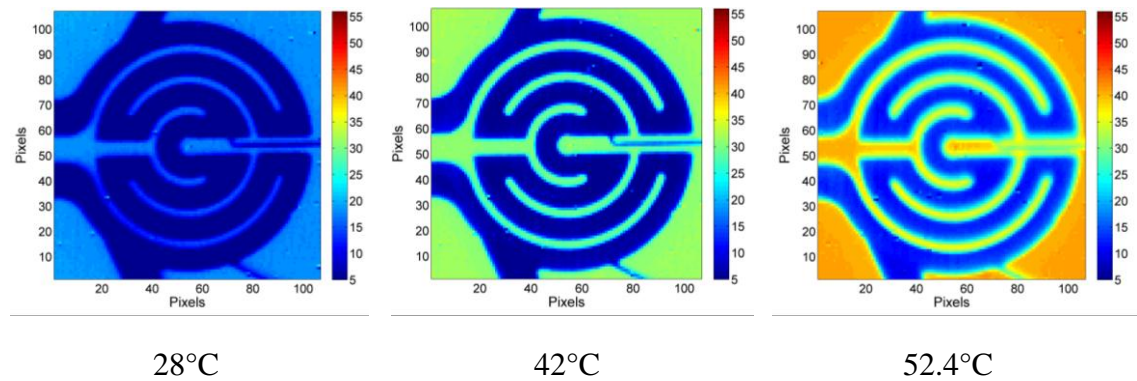


Figure 41: Time-averaged calibration temperature maps of the microscale heater substrate for three temperatures during calibration with FC-72. Note: Scale does not correspond to actual temperatures.

It is to be noted that unlike the macroscale heater, the heater side of the microscale test substrate was directly immersed in the dielectric fluid FC-72. Therefore no black paint was used on the surface during any of the microscale heater experiments. Thus a difference in the emissivity between the heater and non-heater (fluid) regions resulted in low temperature readings in the on-heater locations. The non-heater regions represent a depth weighted average fluid temperature as FC-72 is almost 97% transmissive in the 3-5 μm wavelength range of the camera [70].

A detailed analysis was conducted to determine the appropriate order of the calibration fit for each pixel of the IR image (appendix G). This step was extremely important due to some technical challenges faced in the microscale heater IR image acquisition. For

the microscale test set-up the IR lens imaged the surface through the 380 μm thick silicon substrate and a 2 μm thick oxide layer (present on either side of the silicon wafer). Optical properties widely available for silicon from several manufacturers specify this thickness of substrate to be as much as 50 percent transmissive to IR in the 3-5 μm wavelength range of the IR camera. However it was reported by Krebs [74] that for the same wavelength range (3-5 μm) the 2 μm thick oxide layer can result in as much a 30 percent reflection. In addition microscale image acquisition was extremely sensitive to the positioning of the IR camera. As a result the IR images in several tested cases were affected by the Narcissus effect wherein the IR detector senses unintended reflections from the lens itself [75]. Figure 42 shows an example of the observed reflections in an uncalibrated temperature map acquired during a pool boiling test. For the present work, these 380 μm thick silicon substrates with a 2 μm thick oxide layer were the only ones available. Better estimates of surface temperature with reduced reflection can be achieved in future experiments by obtaining substrates with the appropriate oxide thickness.

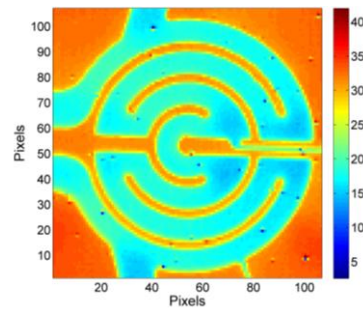


Figure 42: Reflections due to the Narcissus effect in the microscale heater images acquired with the IR microlens.

As a result of the above described issues calibration fits of first, second and fourth order were conducted to determine the best order of fit suited for the acquired data (see appendix G). The curve fit analysis revealed that fits of orders higher than two were unable to predict positive temperatures in regions beyond the calibrated range. Furthermore, second order fit over predicted temperatures in the on-heater locations for temperatures higher than the range of calibration. As a result a linear order fit was chosen for calibration. To obtain better uniformity in temperature values and lower fit error two runs of top-hat filtering (Eq. 11) were conducted prior to applying the linear order fit. Figure 43 shows the filtered and first order calibrated temperature maps for the same three temperatures as shown in Fig. 41.

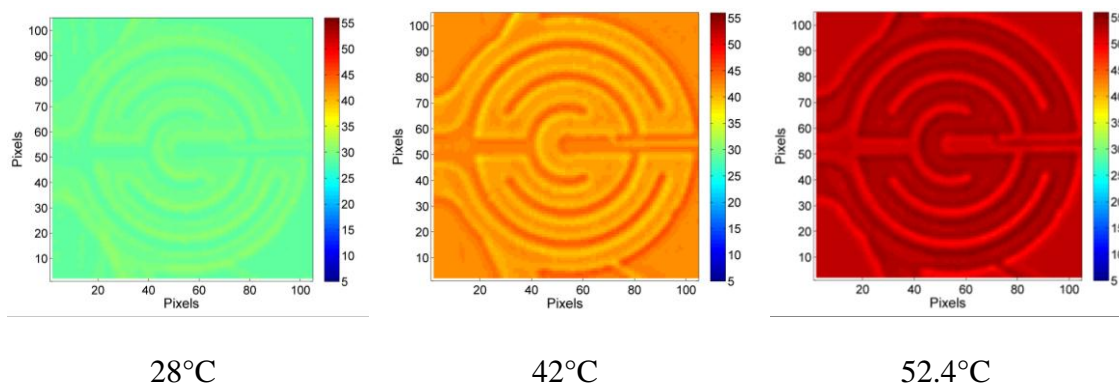


Figure 43: Calibrated temperature maps of the microscale heater substrate for three temperatures during calibration with FC-72.

The instantaneous temperature maps acquired during the pool and jet impingement experiments were processed individually so that the time varying temperature maps could be obtained. All IR maps were filtered with two runs of top-hat filtering as explained for the calibration temperature maps. Linear calibration fits were applied to

each pixel of the IR images to get calibrated temperature maps for each tested condition.

As for the macroscale heater, the serpentine profile of the microheater resulted in alternately heated and unheated sections symmetric about the y-axis. The heated sections of the microscale heater are shown in Fig. 44. The final calibrated instantaneous maps were used to extract radial profiles of the surface temperature for the various power levels tested, at specific time instants.

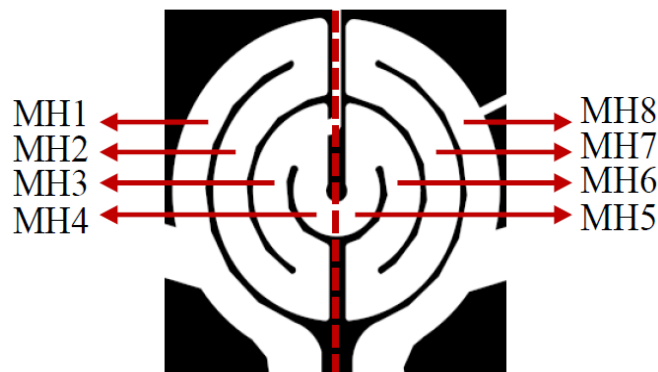


Figure 44: Heated sections of the microscale heater

The voltage measured at the pins in contact with the heater and the correspondingly measured current at the power supply was used to indicate the power input to the system. The recorded input power and the extremely small heated area ($7.85 \times 10^{-3} \text{ cm}^2$) resulted in substantially large values of input heat flux which suggested that significant heat losses occurred in the system that need to be accounted for. This loss could be caused from a combination of conduction in the substrate resulting in heat loss to the subcooled fluid from the un-heated substrate locations and due to natural

convection to the ambient air from the open rear side of the substrate. A computational analysis is currently being conducted by a fellow graduate student to quantify these losses as part of this on-going study. Hence, for the purposes of discussion in this thesis data will be presented in terms of the power input to the system.

5.4 HIGH SPEED DATA REDUCTION

As described in the previous chapter, all high speed images were acquired with a Phantom V310 camera using the manufacturer provided Phantom Camera Control (PCC) software. The images were acquired as videos and saved in a cine file format. The data reduction procedures for tests conducted with each of the heater substrates are described in the following sub-sections.

5.4.1 HIGH SPEED DATA: MACROSCALE HEATER

High speed images collected during the macroscale heater boiling experiments provided qualitative information on the boiling activity taking place on the top (smooth) side of the heater surface. The boiling activity was captured over the entire 27.5 mm diameter heated substrate area for both pool and jet impingement boiling experiments. Images of resolution 1104 x 576 pixels were acquired at 9000 frames per second for tests with DI water while those with FC-72 were recorded at 7401 frames per second with a resolution of 912 x 432 pixels. These images were converted from the cine file format to 12 bit TIFF images using the batch file conversion feature in the Phantom Camera Control (PCC) software and presented as is for qualitative discussions.

5.4.2 HIGH SPEED DATA: MICROSCALE HEATER

The microscale heater boiling experiments with FC-72 resulted in localized boiling activity at the 1000 μm diameter heated area. Images of the bubble dynamics were taken for both pool and jet impingement boiling experiments under subcooled boiling conditions. The primary purpose of these images was to provide quantitative information regarding the bubble departure diameters and departure frequencies so as to compute the net evaporative heat transfer rate.

Ebullition during pool boiling was captured at 7000 frames per second with a pixel resolution of 624 x 704 pixels (5.2 mm x 5.87 mm). For jet impingement boiling experiments, the frame rate was increased to 9000 frames per second and the resolution to 800 x 400 pixels (6.7 mm x 3.3 mm), so as to capture the impact of the jet on the departing bubble trajectories. The acquired images were converted to 16 bit grayscale images in TIFF format using Phantom Camera Control (PCC) software. The TIFF images were subsequently processed using the National Instruments Vision Assistant software to obtain quantitative results for the bubble geometry at departure. Based on the departure conditions at each power level and for each test condition an image processing script was created in the Vision Assistant software. The following paragraphs describe the basic image processing steps that were used for all acquired data images.

The image processing scripts for each test condition sequenced through a series of steps beginning with the identification of the departing bubble in an image. This was

done by a thresholding process in which the pixels occupied by the bubble in the grayscale images were marked on a scale of -32767.5 to 32767.5 assuming them to be brighter than the background. As an example, Fig. 45a shows an image of a bubble at departure during pool boiling at a pool subcooling of 10°C. The corresponding image after the thresholding step is shown in Fig. 45b. For this image the threshold value was set to 128. Pixels identified to be brighter than 128 are shown here in white.

Once the bubble was identified, the images were filtered by a smoothing process that executed a local averaging to smooth regions within the detected bubble contour. This step is depicted in Fig. 45c. The kernel size was kept small (typically a size of 3 kernel was used) to ensure that the smoothing process does not alter the peripheral dimensions of the bubble.

As a next step, the objects identified as the departing bubbles were separated from convection gradients connecting them to the bordering surface using a square or hexagonal structuring element. This step is shown in Fig. 45d. The structuring element size and the number of scan iterations had to be manually adjusted for each script to ensure the removal of narrow isthmuses that connect the bubbles to the image border. All peripheral convection gradients or isolated pixels smaller than an average specified bubble size (for example those observed at the right edge of Fig. 45d) were removed.

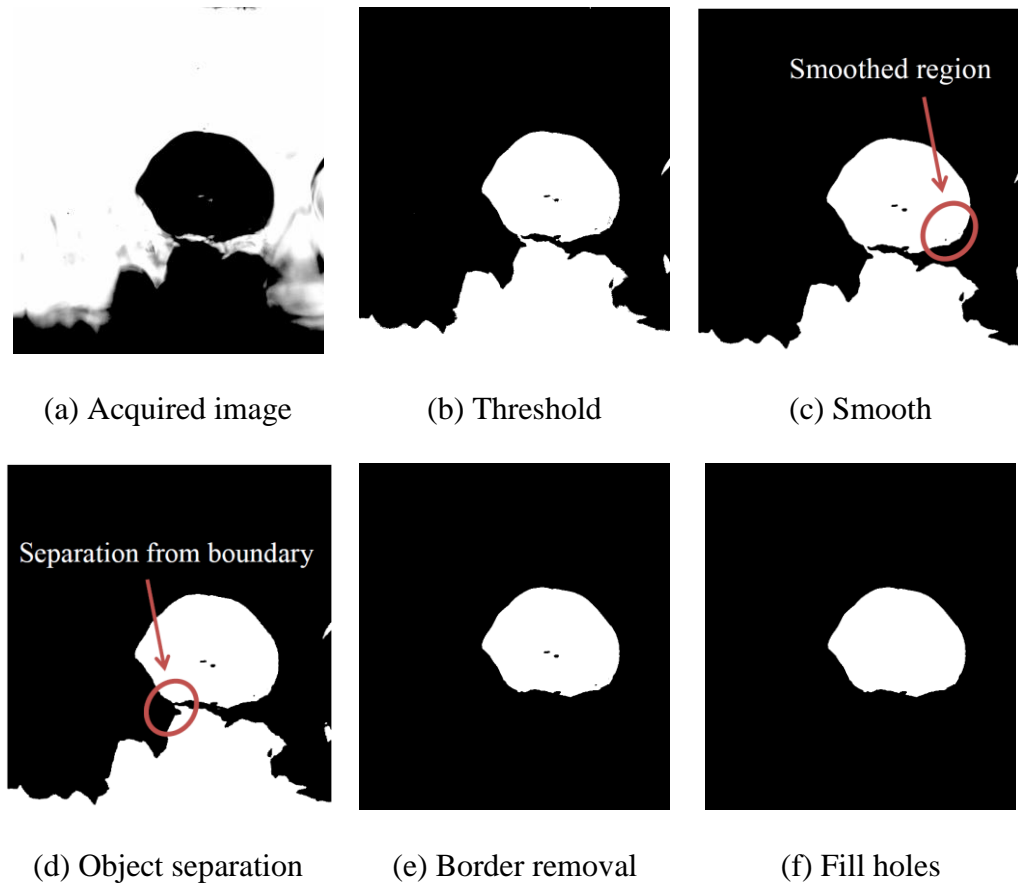


Figure 45: Image processing steps for isolated bubble visualization (Example shown for a pool boiling image)

With the bubble of interest now isolated, the convective gradients connected to the image border were removed leaving the target object in the image. This step is depicted in Fig. 45e. As a final step in the image processing sequence, any small blank patches remaining within the target bubble were filled in to get an estimate of the bubble diameter at departure (Fig. 45f). In addition to the basic steps described above, image masking was used for particular cases with frequent bubble departures (for

example in cases of jet impingement boiling, discussed in detail in sections 7.2.2 and 7.2.3) to selectively process the region of interest (region of bubble departure).

The bubbles obtained with jet impingement at especially low power levels were extremely small and were forced to separate from the source and slide across the silicon surface due to the jet flow. As these bubbles remained attached to the substrate they could not be isolated from the image border (Fig. 96, section 7.2.2). Hence diameters for these sliding bubbles could not be evaluated.

The bubble dimensions for all off-surface departures could be obtained at this stage using the particle analysis feature in the Vision Assistant software. The particle analysis feature estimated the two-dimensional cross-sectional area of the processed bubbles in pixel units. Diameter of the bubble was calculated by the software by equating the estimated bubble cross-sectional area to that of a circular disc. Bubble diameters were extracted as excel (.xls) files from the Vision software and converted to metric dimensions in MATLAB. The pixel to metric conversion factor was determined from the high speed image calibration process described in section 4.4.2. Bubbles diameters were plotted as a function of time (Fig. 46) from the instant of departure until the bubbles disappeared from the recorded image frame. The number of bubble departures was identified by locating the largest (peak) diameter values understanding that as the bubbles proceed in the subcooled pool they would condense and decrease in size. Average departure diameters for each test power level were reported based departure peaks identified over 1 second of acquired data. This allowed

for sufficient number of bubble cycles (typically greater than 20) to get a statistical deviation in reported values.

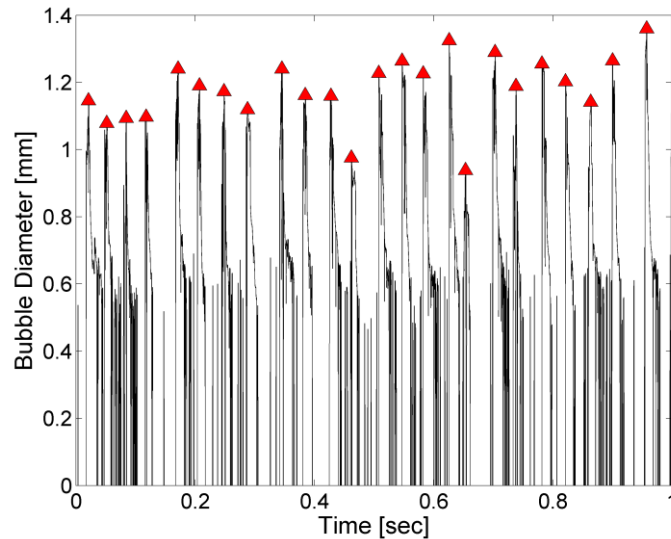


Figure 46: Plot of bubble diameters over time with departure diameters identified as peaks for a 20°C subcooled pool boiling test at 6.44W

Departure frequencies (f_d) of the vapor bubbles were evaluated from the number of departure peaks identified. The time-span for peak to peak comparison (for identifying the maximum diameter value) was adjusted until the final values of the peak locations, and the corresponding departure frequencies were independent of this parameter. The frequencies estimated from the MATLAB codes were additionally verified for select cases by manually counting the bubble departures in the recorded image sets.

5.5 THIN FILM SENSOR DATA REDUCTION

During boiling, bubbles grow and depart from the heated surface, acting as the primary vehicles of heat transfer. As a result the departure of bubbles results in a local temperature drop on the surface [36]. It is common knowledge that resistance is a function of temperature. So, when boiling on a resistive heater, a dip in the local temperature caused by the departing bubbles can be captured as a drop in the corresponding heater resistance value. Likewise, a growing region of vapor would be captured as a rise in resistance. For a fixed current through a resistor, the instantaneous change in resistance can be recorded as a drop in voltage at that instant of time. Thus, voltage variations over sectional heater regions over time are representative of the boiling activity over that area.

Following this concept, the time dependent variations in the thin film sensor voltages were acquired during pool and jet impingement boiling with the macroscale and microscale heater substrates.

5.5.1 SENSOR DATA: MACROSCALE HEATER

During each experimental run, voltages were recorded from two thin film sensors drawn off of the macroscale heater. As seen in Fig. 47, S_1 primarily measured the voltage drop on the heated sections H1 and H2 (two inner rings of the heater) while S_2 provided voltage drop measurements in the outer semi-circular heater section H3 (outermost ring of the heater).

A total of 50,000 samples of sensor voltages were acquired at the steady state of each power level at a rate of 24 kHz using a National Instruments-USB6009 data acquisition system and a LabVIEW program. The data acquisition board limited the voltage readings to a range of $\pm 20V$.

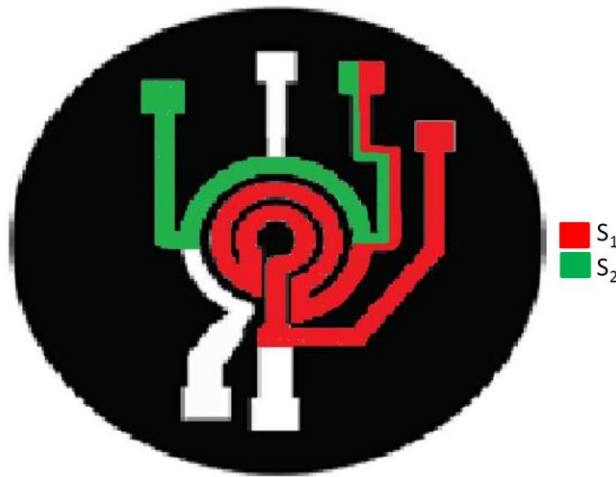


Figure 47: Sectional areas captured by the macroscale thin film sensors

The time series of voltages from each sensor at each power level was analyzed in MATLAB. A series of significant voltage dips were identified in the time series for all macroscale heater tests with DI water. These voltage dips in time were indicative of boiling events. For tests with FC-72 these dips were not captured owing to the fluid properties that resulted in visibly much smaller bubble dimensions than water. As a result the dips produced on the macroscale sensor were too small to be resolved without appropriate signal conditioning.

In order to further interpret these dips in voltage for DI water, a probability distribution function (PDF) of such events was created for both sensors. For each flow

condition, the standard deviation of the voltage series in a non-boiling condition was first determined. Voltage drops having magnitudes of N standard deviations above those of the lowest power non-boiling case in that experimental run were identified as boiling events at the higher power levels. Values of N of 22, 29 and 32 were used for $Re_{jet} = 0, 2580$ and 5161 respectively. The bin size (voltage resolution) for the PDF was fixed at $0.15V$. The PDF, thus formed, described the likelihood of a negative drop in voltage to occur under given experimental conditions.

Prior to associating the observed voltage drops with temperature drops due to boiling events, it was imperative to ensure that the voltage drops were not observed under non-boiling conditions (Fig. 48). Voltage time series for sensors S_1 and S_2 , at a low flux of 0.2 W/cm^2 during pool boiling, is shown in Fig. 48a. The corresponding IR map and high speed snapshot of the heated surface are shown in Figs. 48b and 48c respectively. The IR image is oriented identical to the corresponding high speed image, with the heater leads to the left and the thin film sensors to the right.

In Fig. 48c the stationary bubbles present on the periphery of the surface were remnant from degassing prior to the experiment. It is clear from the images that the low power is insufficient to initiate a boiling event. Hence the random fluctuations seen in the time series is considered indicative of variations due to single phase convection (natural convection), as well as due to noise.

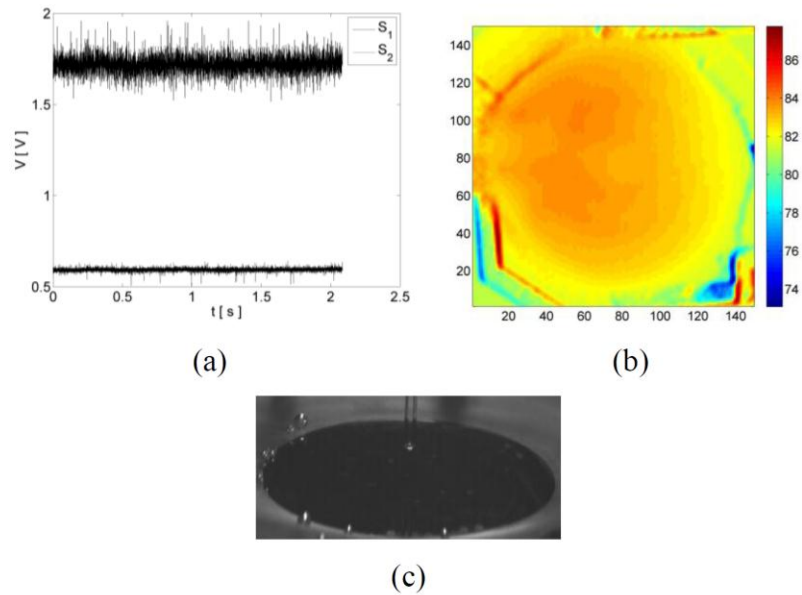


Figure 48: Non-boiling condition for $Re_{jet} = 0$ (a) sensor time series (b) calibrated IR map ($^{\circ}C$) (c) high speed image of the surface

Similar observations were made by observation of the time series at low power levels for SJIB cases. For the jet impingement tests, the variations in voltage at the low power levels could be additionally caused by the forced convection induced by the impinging jet.

5.5.2 SENSOR DATA: MICROSCALE HEATER

Voltage fluctuations representative of bubble departures were acquired from two sensor combinations drawn off of the microscale heater during the pool and jet impingement boiling tests. The two sensors used for the microscale study are shown in Fig. 49. Microsensor MS_1 (shown in red) spanned almost the entire length of the

heater itself, while microsensor MS_2 (shown in green) covered a region marginally larger than one half the full heater length.

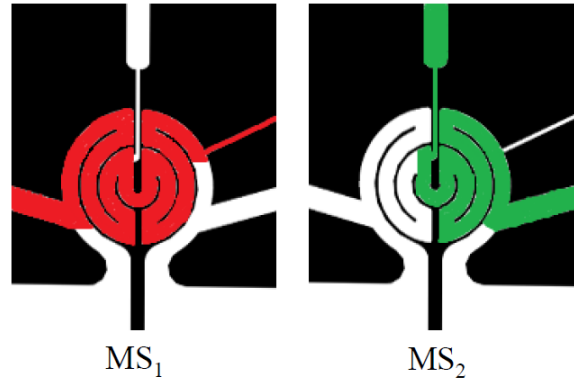


Figure 49: Sectional areas captured by the microscale thin film sensors

The voltage acquisition set-up was identical to that used for the macroscale heater described in section 5.5.1. At each power level 50,000 voltage samples were acquired from the two sensors at frequency of 24 kHz. With increasing power the mean voltage signal acquired from both sensors was found to increase in magnitude. The voltage fluctuations observed about the signal mean with the fluid FC-72 during these microscale heater tests, were of a much smaller magnitude than those with DI water on the macroscale heater. While a distinct periodicity was observed in the voltage signals beyond the onset of boiling, it was necessary to isolate the voltage fluctuations resulting from the boiling activity from those which may be caused due to natural or forced jet convection or noise. Signal processing in the form of a low pass digital filter and a fast Fourier transform (FFT) were implemented to achieve the distinct signal

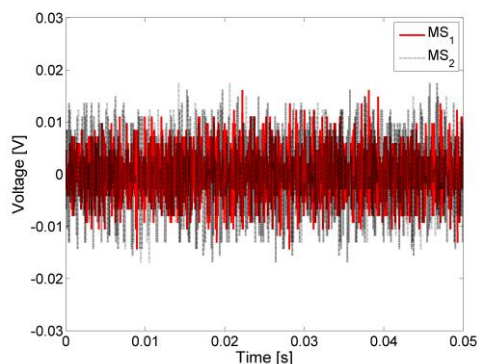
frequency representative of the boiling activity. These procedures are described below with the help of data acquired for a non-boiling and a boiling condition.

Sensor recordings for a non-boiling condition

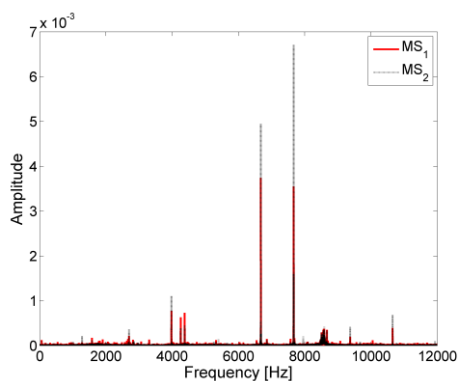
Figure 50 shows the mean subtracted sensor time series and frequency spectrum obtained for a low non-boiling power level of 0.04 W during 20°C subcooled pool boiling of FC-72. Figure 50a shows an instantaneous snap shot of the surface at these test conditions. From the snapshot it is evident that for the low power supplied there was no boiling activity on the surface. The acquired original time series for both microsensors are shown in Fig. 50b. Mean fluctuations of the order of ± 0.1 V were observed for both sensors. Figures 50c and 50d show the frequency spectrum of the two sensor signals on a natural and a log scale respectively. The spectrums were obtained by performing a FFT. The frequency resolution of these spectrums is 0.48 Hz. The FFT frequency spectrums showed significant peaks in the high frequency band from 7000-8000 Hz. Clearly, since no boiling occurred on the surface during this time these peaks corresponded to random fluctuations caused by either natural convection or noise.



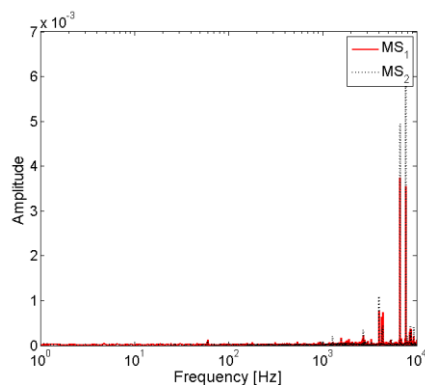
(a) Snapshot of the surface



(b) Unfiltered voltage time series (mean subtracted)



(c) FFT with un-filtered data (frequency axis in natural scale)



(d) FFT with un-filtered data (frequency axis in scale)

Figure 50: Un-filtered sensor voltage time series and frequency spectrums for a non-boiling condition (0.04W) during 20°C subcooled pool boiling of FC-72

From the high speed visuals acquired at 7000 Hz at higher power levels for this pool boiling test case, it was determined that boiling occurred at frequencies well below a 1000 Hz. Following this information, a low pass filter with a cut-off frequency at 1000 Hz was implemented on the mean subtracted time series. The resulting filtered time series is shown in Fig. 51a. The filtered series showed fluctuations less than $\pm 0.5 \times 10^{-3}$

V. The corresponding frequency spectrum shown in Fig. 51b (on the same y-scale as Fig. 50c) clearly depicts the absence of any major peaks for the entire frequency range. The spectrum is also shown on a magnified scale in Fig. 51c where the highest peaks observed had magnitudes less than 1×10^{-4} .

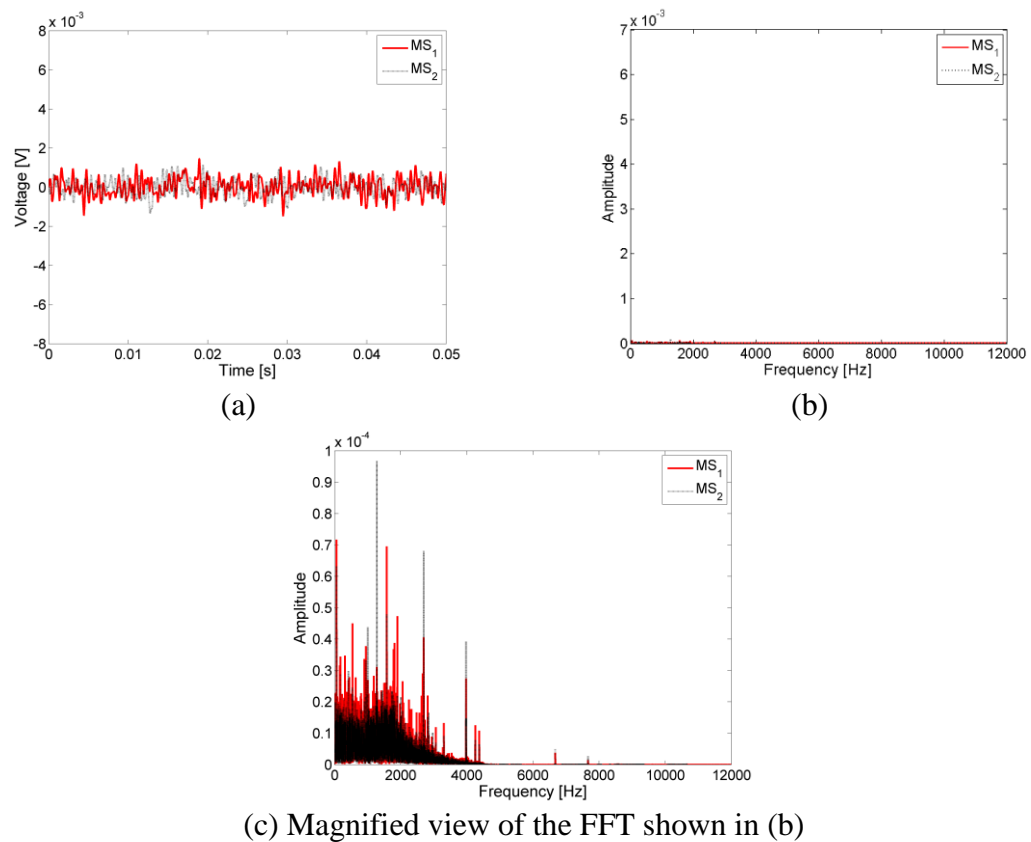


Figure 51: Filtered sensor voltage time series (a) and frequency spectrums (b,c) for a non-boiling condition (0.04W) during 20°C subcooled pool boiling of FC-72

Sensor recordings for a boiling test condition

The same filtering and FFT procedures as described for the non-boiling case were applied to the signals acquired at boiling conditions. Figure 52 shows an example of

the processing steps applied to voltage signals acquired at a power level of 8.64 W during 20°C subcooled pool boiling of FC-72.

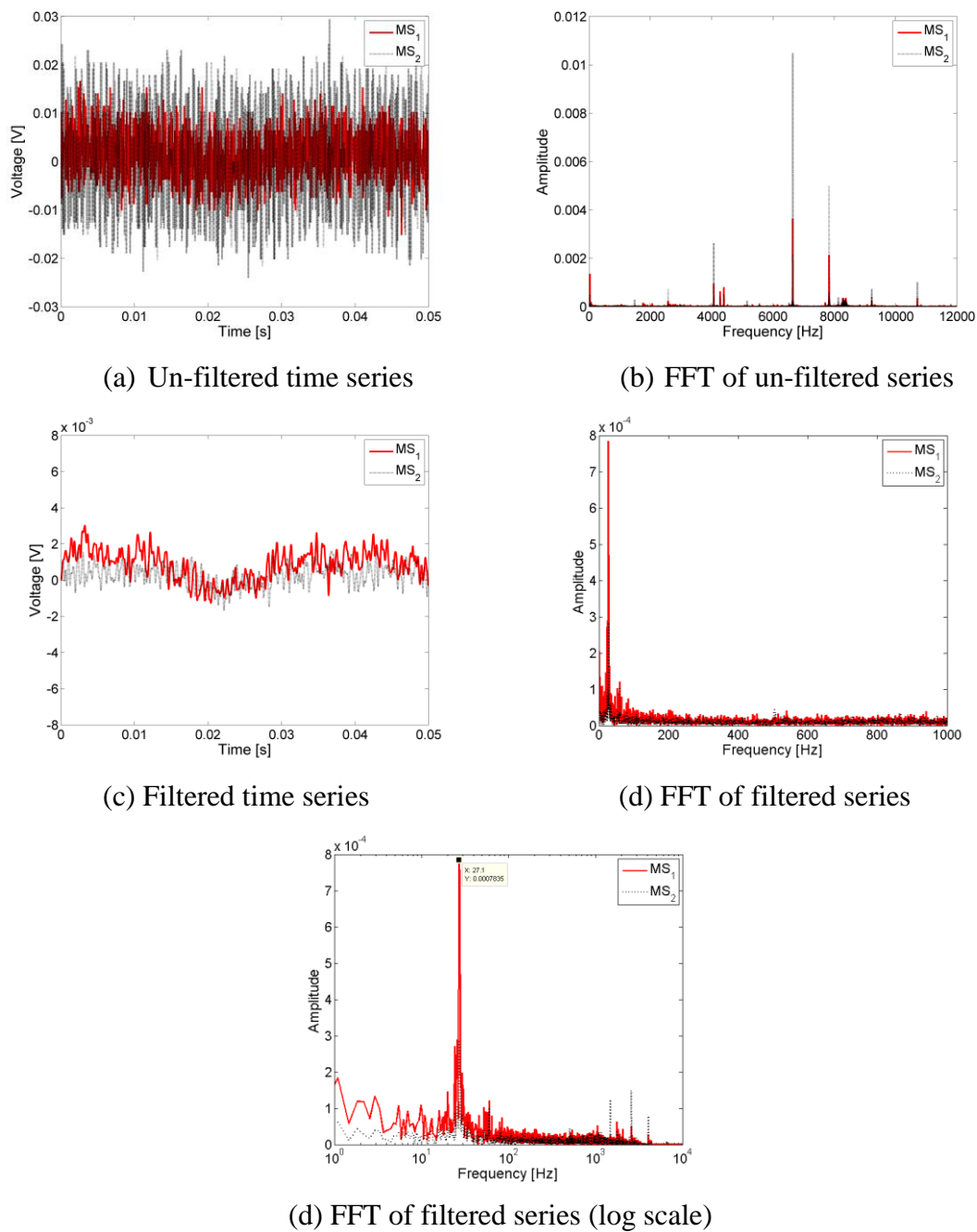


Figure 52: Un-filtered and filtered voltage time series for boiling condition (8.64W) during 20°C subcooled pool boiling of FC-72

The time series shown in Figs. 52a and 52c clearly depict oscillations representative of the boiling activity. These oscillations were not observed for the non-boiling condition voltage time series shown in 51a. The frequency spectrum corresponding to the filtered time series of the boiling case (Fig. 51d) depicted a clear peak at a frequency of about 27Hz indicative of the dominant frequency of the bubble departure for this case. For the jet impingement cases a low pass filter with a cut-off frequency at 2000 Hz was used based on a manual evaluation of frequencies obtained from the high speed images.

5.6 UNCERTAINTY ESTIMATES

This section describes the steps taken to quantify uncertainties in various experimental measurements and the subsequently derived quantities from data analysis. The quantitative experimental measurements included, the pool and jet temperatures, IR thermal images, the jet mass flow rate, the supplied current and voltage, the thin film sensor voltages and the high speed images of bubble ebullition during the microscale heater boiling tests.

Uncertainty in jet flow rate

Uncertainty associated with the reported jet flow rate was computed by a root sum square of the flow meter bias error (manufacturer specified) and the precision error from the recorded data. The overall uncertainty in the reported flow rates is ± 0.94 g/min. The Kline McClintock [76] uncertainty estimate method was used to find the

error propagated in u_{jet} and Re_{jet} based on the temperature and flow rate uncertainties. These values are listed in Table 4.

Uncertainty in sensor voltage measurements

Uncertainty in the time-varying thin film sensor measurements was attributed to the quantization error associated with the data acquisition board. The NI-USB6009 used for acquiring the differential sensor voltages used a successive approximation analog to digital convertor with a manufacturer specified resolution of 14 bit. The USB-6009 was limited to a full scale reading of $\pm 20\text{V}$. The corresponding quantization error estimated for this voltage range was $\pm 1.2\text{ mV}$.

Table 4: Uncertainty estimates of measured quantities

Quantity	Average Uncertainty
Pool Temperature	$\pm 0.6^\circ\text{C}$
Jet Temperature	$\pm 0.6^\circ\text{C}$
Jet Flow Rate	$\pm 0.94\text{ g/min}$
Jet Exit Velocity	$\pm 0.03\text{ m/s}$
Reynolds number	2.2 percent
Sensor Voltage	$\pm 1.2\text{ mV}$
Current	$\pm 0.43\text{ percent}$
Voltage	$\pm 0.58\text{ percent}$

Uncertainty in the supplied voltage and current

As mentioned in the previous chapter, three different DC power supplies were used to power the deposited thin film heaters over the range of tests conducted. The average uncertainty in the current measured with these supplies was ± 0.43 percent. The voltage across the thin film heaters were recorded using a digital multimeter. The average uncertainty the voltages recorded was ± 0.58 percent.

Uncertainty in temperature measurements

Uncertainty in the temperature measurements can result from uncertainty in (a) the thermocouples used to measure the pool temperature during IR calibration (b) IR calibration process and (c) curve fit error associated with the individual pixel calibration curves.

Thermocouples - The bias uncertainty associated with the thermocouples used for measuring the pool and the jet temperatures accounts for error due to calibration of the thermocouples against the NIST standard, NIST standard RTD error, and the thermocouple calibration curve fit error. This value was estimated to be $\pm 0.6^{\circ}\text{C}$. Precision error arises whenever repetitive measurements are taken. The precision error associated with the thermocouples during IR calibration was calculated to be a maximum of 0.03°C . The net uncertainty in the thermocouple measurements was calculated by a root sum square of the thermocouple bias and precision errors, and found to be 0.6°C .

IR image precision - The precision error associated with the IR camera noise was determined using consecutive images spanning one full second of data recorded at each calibration temperature. For the range of macroscale heater experiments conducted the maximum precision error for a pixel temperature (evaluated from 30 consecutive images) was found to be 0.04°C . Similarly for the microscale heater experiments the maximum precision error evaluated using 120 consecutive IR images was found to be 0.038°C .

Calibration curve fit –The curve fit standard error resulting from the linear fit for each image pixel of the macroscale heater was found to have an average value of 0.34°C over all the calibrations conducted. For the microscale experiments the average curve fit error resulting from a linear fit for all pixels in the calibration experiments was 1.2°C (appendix G).

Overall temperature uncertainty - The total uncertainty in the IR temperature measurements was calculated by a root sum square of the net thermocouple uncertainty, the IR precision error and the IR standard curve fit error. The maximum overall uncertainty in the macroscale heater surface temperature using IR thermography was 0.70°C . The overall uncertainty evaluated for the microscale heater surface temperature was about 1.43°C .

Uncertainty in evaluated quantities (Macroscale heater IR image analysis)

Table 5: Uncertainty estimates for circumferentially averaged quantities

DI Water - Pool Boiling ($Re_{jet} = 0$)				
$q''_{elec,Ah}$ W/m ²	Uncertainty Estimate	T(r) [%]	T(r)-T _{fluid} [%]	$q''_{conv}(r)$ [%]
0.34	Average	0.23	33.54	4.16
	Maximum	0.23	55.64	5.58
1.93	Average	0.21	7.48	2.95
	Maximum	0.22	12.58	4.47
7.9	Average	0.18	2.42	2.76
	Maximum	0.20	4.26	6.04
23	Average	0.15	1.51	2.95
	Maximum	0.17	1.96	15.79
29	Average	0.15	1.44	2.88
	Maximum	0.16	1.84	17.97
43	Average	0.15	1.38	2.53
	Maximum	0.16	1.74	12.48
66.5	Average	0.15	1.35	2.14
	Maximum	0.17	1.88	6.60

The Kline and McClintock [76] uncertainty estimate method was used to compute the uncertainties in T_{filter} based on bias and precision uncertainties on measured temperature values. A perturbation uncertainty analysis was done to propagate the uncertainties in T_{filter} , Δ , thermal conductivity, wafer thickness, heater area, T_{fluid} ,

voltage and current, onto the local and the circumferentially averaged quantities. The averaged and maximum uncertainty percent estimates for the circumferentially averaged quantities during pool boiling ($Re_{jet} = 0$) with DI water are listed in Table 5. The uncertainty estimates are given for the range of tested heat flux values.

Uncertainty in high speed image processing (Microscale heater experiments)

Images acquired during the microscale bubbling activity were used to get quantitative values for bubble departure diameters and departure frequencies so as to compute the latent heat transfer rate. Uncertainties in the reported departure diameters result from the various steps in the image processing (see section 5.4.2) and from the calibration procedure (see section 4.4.2) used to convert pixel values to real world dimensions.

Image processing- To estimate the uncertainty resulting from the image processing, bubbles diameters for select cases of pool and jet impingement tests were evaluated by perturbing each user defined parameter of the processing script one at a time while keeping the other parameters at their original value. These user defined parameters that influenced the bubble diameters included the image thresholding, the kernel size for smoothing and the structuring element used for separation of bubble objects from the image periphery. The standard deviation in the final bubble diameter due to the perturbed quantities was evaluated by a root sum square of the individual deviations. This quantity was estimated as $\pm 10.3 \mu\text{m}$ for the pool boiling bubble diameters while the deviation for the diameters of the jet impingement tests was found to be $\pm 14.2 \mu\text{m}$.

Image calibration- Images of a dotted calibration grid (Fig. 25) were acquired at the experimental conditions. These images were used to obtain a pixel to metric conversion factor as explained in section 4.4.2. Uncertainty in the determined conversion factor may result from distortion of the calibration image due to change in fluid density with temperature. An estimate of the calibration uncertainty was achieved by taking the standard deviation of ten repeated measurements of the dot center to center spacing in both x and y directions. The standard deviation due the calibration process was estimated to be $\pm 4.7 \mu\text{m}$.

The overall uncertainty in reported diameters obtained by a root sum square of the above described uncertainties was found to be $\pm 11.2 \mu\text{m}$ for pool boiling and $\pm 14.9 \mu\text{m}$ for the jet impingement boiling tests.

The average departure diameters and departure frequencies were computed in MATLAB. The accuracy of these two values was dependent on the time step chosen to compare the peak diameter values (see section 5.4.2). For pool boiling tests with distinct bubble departures the computed diameters and frequencies were found to be insensitive to small changes (of the order of $\pm 0.14 \text{ ms}$) in the time step. In comparison the jet diameters and frequencies were found to be much more sensitive to changes in the time step (of the order of $\pm 0.11 \text{ ms}$). The standard deviation in the average diameter for a jet case as a result of perturbing the time step for peak comparison was found to be $\pm 8.4 \mu\text{m}$. The corresponding deviation in the average frequency was

about ± 5 Hz where the typical frequencies in the jet impingement cases were in the range of 100-900 Hz.

6 MACROSCALE HEATER RESULTS

This chapter discusses the noteworthy results obtained during boiling experiments with the macroscale heater test substrate (Table 1). The chapter is divided into two main sections.

In the first section, a quantitative comparison between area-averaged and local boiling curves is presented in the context of pool boiling and jet impingement boiling. A simplified interpretation of the spatially varying boiling trends is presented via sectionally-averaged boiling curves wherein sections of like imposed heat flux are analyzed. It is demonstrated that the sectionally-averaged heat transfer representation can substantially simplify the interpretation of data while retaining important information of local heat transfer variation.

The second section describes the origin of the spatial variation in boiling curves. The spatial non-uniformity of nucleation events for pool boiling versus submerged jet impingement boiling (SJIB) is qualitatively depicted with high speed and IR maps of the boiling process. Quantitative corroboration of the spatial non-uniformity is provided with radial temperature profiles and probability density functions obtained from the thin film sensor voltages.

Boiling hysteresis of the highly wetting fluid FC-72 is qualitatively and quantitatively documented with data acquired for increasing and decreasing heat flux conditions. Effects of saturated and subcooled pool conditions on the heat transfer performance of FC-72 are discussed. Spatial differences observed in the magnitudes of thermal overshoot and incipience superheat for FC-72 are described for pool and jet boiling conditions. Boiling heat transfer performance of FC-72 is compared with DI water under 20°C subcooled conditions. The use of self-cavitating jet nozzle geometry for the passive elimination of thermal overshoot in highly wetting fluids like FC-72 is discussed.

6.1 COMPARISON OF AREA-AVERAGED AND LOCAL BOILING CURVES DURING POOL AND JET IMPINGEMENT BOILING

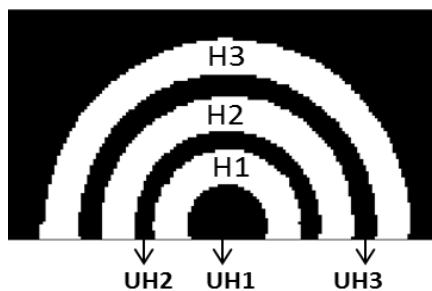
Area-averaged boiling curves can be useful in interpreting the overall heat transfer characteristics of a cooling scheme. Figure 35 in section 5.3.1 discussed the macroscopic behavior of the system as one would expect to see based on available area-averaged literature for pool and jet impingement boiling. Specifically, it is observed that with increasing Re_{jet} , the magnitude of the heat transfer coefficient in the single phase region increases, as denoted by the corresponding increase in slope of the boiling curves. With progressive increase in heat flux both the jet impingement test cases tend to approach pool boiling behavior. Note that since data acquisition was limited by the capacity of the power supply, critical heat flux was not attained in these experiments.

While area-averaged boiling trends provide valuable information on the global phase change characteristics of the cooling scheme, it is also important to assess local variations in heat transfer rates. As emphasized in the introduction of this thesis, spatial differences in heat transfer are extremely important to account for in small scale electronics which require a hot-spot driven thermal management. The following subsections discuss the importance of considering a spatially local heat transfer analysis.

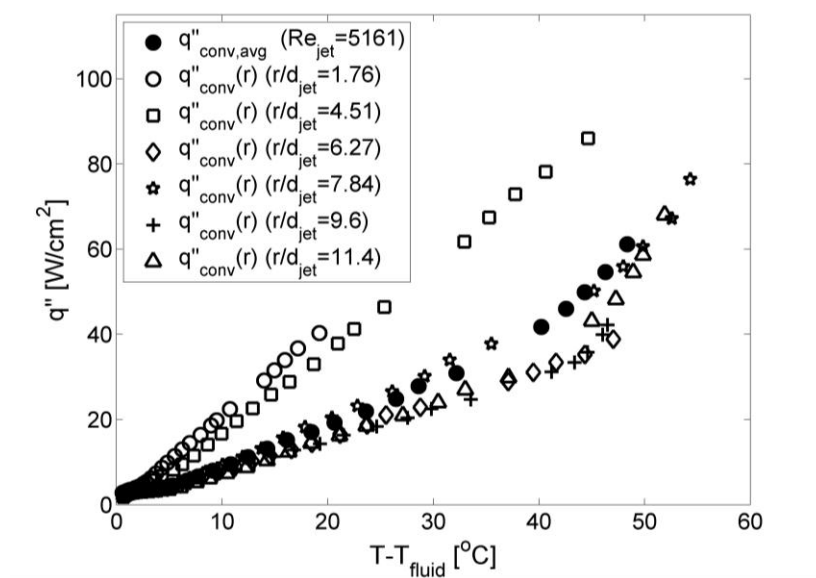
6.1.1 LOCAL VERSUS AREA-AVERAGED BOILING CURVES

The analysis methods adopted in this work provided the feasibility of generating local boiling curves for each pixel location in the domain of interest using the local pixel temperatures, $T_{filter}(i, j)$ and the computed values of $q''_{conv}(i, j)$.

Data interpretation was simplified by opting for a radially-local assessment of the surface temperatures and heat fluxes, in accordance with the circular symmetry of the jet and the thin film heater. Starting from $r=0$ (centermost pixel on the temperature and flux maps), local boiling curves were generated for each radial location on the heated surface using the circumferentially averaged convective heat fluxes $q''_{conv}(r)$ and temperatures $T(r)$.



(a)



(b)

Figure 53: Heater sections (a) and local versus area-averaged boiling curves (b)
(Results for DI water subcooled by 20°C, $Re_{jet} = 5161$)

Figure 53 compares the radially local boiling curves in the presence of a forced convective jet flow ($Re_{jet} = 5161$), to the corresponding area-averaged boiling curve for SJIB of water subcooled by 20°C. The local boiling curves are shown for six different radial locations situated at the center of each heater (H1, H2 and H3 in Fig. 53a) and non-heater section (UH1, UH2, and UH3 in Fig. 53a), along a line of

increasing radii. The corresponding area-averaged curve values ($q''_{conv,avg}$ and T_{avg}) obtained from the radially weighted area-average are denoted here by filled black circles.

The heat transfer trends at each of the radial location depicted here are individually distinct. At radial locations $r = 1.76d_{jet}$ (between $r=0$ and inner heater ring on UH1) and $r = 4.51d_{jet}$ (on H1), that are closer to the jet impingement point, a significantly steep slope in the single phase region of the boiling curve indicative of high heat transfer coefficients (2.42 and 1.87 W/cm² °C respectively) is observed. This can be attributed to the forced convection of the jet that significantly enhances the single phase heat transfer at locations which are close to the stagnation point (point of jet impingement). However, the $q''_{conv,avg}$ severely underestimates the heat transfer coefficient ($h_{sp}=1.22$ W/cm² °C) in this region. In addition, note that these two radial locations retain single phase through the entire experimental run which is not accurately depicted by the area-averaged curve based on the phase change activity occurring in other regions of the test surface. While single phase jet flow dominates heat transfer rate at these locations, the maximum $q''_{conv}(r)$ at the unheated location (UH1) of $r = 1.76 d_{jet}$ is less than one half the maximum value at $r = 4.51d_{jet}$ which is at the center of the first heater ring (H1). This difference in maximum $q''_{conv}(r)$ clearly indicates the consequence of a non-uniform imposed heat flux boundary condition such as that provided by the serpentine heater.

At the location $r = 7.84d_{jet}$ (on H2), a boiling trend more akin to the area-averaged curve is observed. The local values, $q''_{conv}(r)$, at this radial location fall within 0.2 - 20 percent of the averaged values for this experimental run, with the higher differences being exhibited at the larger temperature differences. The single phase heat transfer coefficient at this location is reduced ($h_{sp}=1.29 \text{ W/cm}^2 \text{ }^\circ\text{C}$) when compared with the inner regions and is consistent with the loss in momentum of the radially spreading wall jet. At higher temperature differences, phase change occurs at this location as indicated by a change in slope of the boiling curve.

Further outward from the stagnation point at $r = 11.4d_{jet}$ (on H3) the slope of the single phase region and hence the heat transfer coefficient experience a larger drop ($h_{sp}=1.02 \text{ W/cm}^2 \text{ }^\circ\text{C}$). This is indicative of the diminishing influence of the jet at this large radial distance away from the stagnation point. The area-averaged values over estimate the single phase heat transfer coefficients at these locations, and depict a 4 - 5 $^\circ\text{C}$ lower temperature difference for the onset of nucleate boiling. Thus, an electronic device could easily exceed its limits for safe operation if a cooling system were designed using an area-averaged performance curve.

6.1.2 SECTIONALLY-AVERAGED BOILING CURVES

The previous section clearly indicated that significant differences in the boiling curves exist between an area-averaged representation and a radially-local representation. The differences observed in the boiling trends are caused due to both the flow field set up by the jet as well as the imposed heat flux boundary condition. The intent of this

section is to determine whether averaging over sections with like boundary conditions (for example, uniform heat flux boundary condition in H1, H2 and H3 shown in Fig. 53a) provides an adequate representation of heat transfer performance within these sections or whether it is necessary to have higher spatial fidelity of boiling trends. Sectionally-averaged temperatures (T_{avg}) and convective heat fluxes (q''_{avg}) were determined over the regions with identical imposed boundary conditions.

Figure 54 compares the performance of sectionally area-averaged boiling curves with the local boiling curves within the section H2 (Fig. 53a) during pool boiling of DI water subcooled by 20°C.

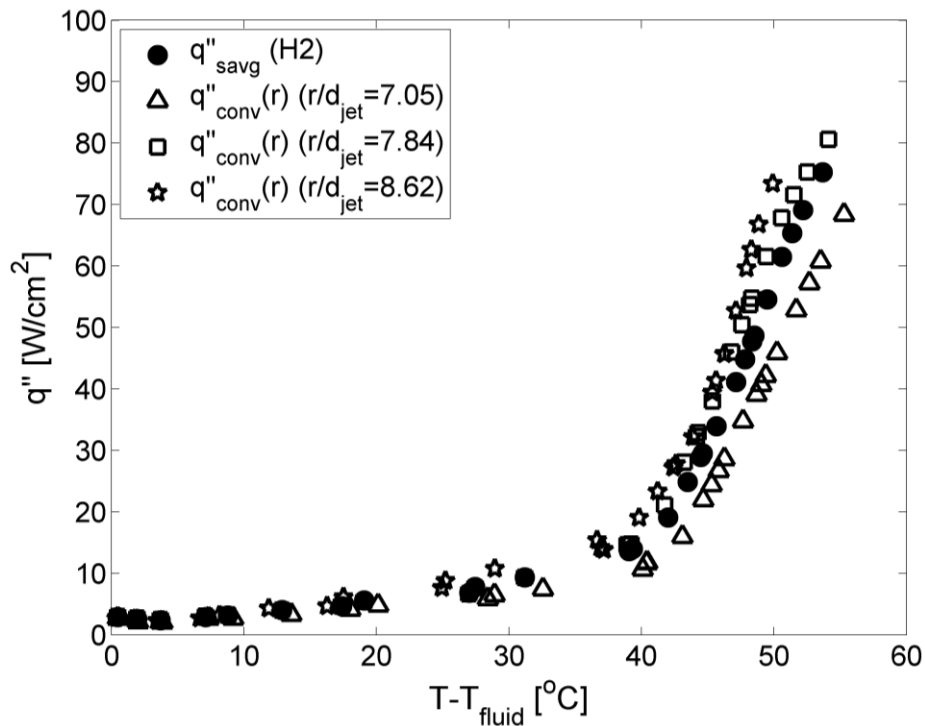


Figure 54: Local versus sectionally-averaged boiling curve for pool boiling - heated section H2 (Fig. 53a). results for DI water subcooled by 20°C.

Negligible differences are observed in the single phase region between the local and sectionally-averaged boiling curves while in the phase change region the curves begin to deviate with increasing heat flux. In the boiling region of the curves, the outer location ($r/d_{\text{jet}} = 8.62$) is seen to have a larger slope in the boiling curve than the inner location ($r/d_{\text{jet}} = 7.05$), indicative of a larger two-phase heat transfer coefficient. Substrate conduction estimates from H2 region at a fixed power input of 440 W (corresponding to the highest flux data in Fig. 54) indicated that the conduction flux out of the inner control volumes towards UH2 region was, on average, 12 percent larger than conduction out towards the UH3 region. Hence, in order to achieve the same convective heat flux as the outer or middle locations, the surface temperature at the inner radial location had to be larger than at other locations within H2. Alternately, for a fixed surface temperature, the inner locations on H2 showed lower convective heat fluxes.

Irrespective of these differences between the local and sectionally-averaged curves, it is seen that the sectionally-averaged data provides a reasonable estimate of the local trends. In the single phase region, the heat transfer coefficient variation between the local data and sectionally-averaged data was on average 8 percent with a maximum of 22 percent deviation from the sectional average for the inner location. In the phase change region of the boiling curve, at a fixed representative heat flux of 60 W/cm^2 , the local temperature differences were on average within 5.3 percent, with a maximum of 5.6 percent deviation from the sectionally-averaged temperature difference for the inner location.

Figure 55 presents the sectionally-averaged and local boiling curves for $Re_{jet} = 5161$ for the same H2 section (Fig. 53a) as that shown for pool boiling in Fig. 54. Similar to the pool boiling case, the inner location at $r/d_{jet} = 7.05$ is seen to have a lower slope in the single phase region of the local boiling curve than does the sectional averaged curve or the outer region of $r/d_{jet} = 8.62$. This result might be seemingly contradictory since in single phase jet impingement, the heat transfer coefficient is larger for locations closer to the impingement point for the H/d_{jet} ratio used in this test ($H/d_{jet}=3.6$). The lower heat transfer coefficient at the inner location in this case is due to the stronger influence of substrate conduction heat loss, than that of the convective jet flow, as explained for pool boiling.

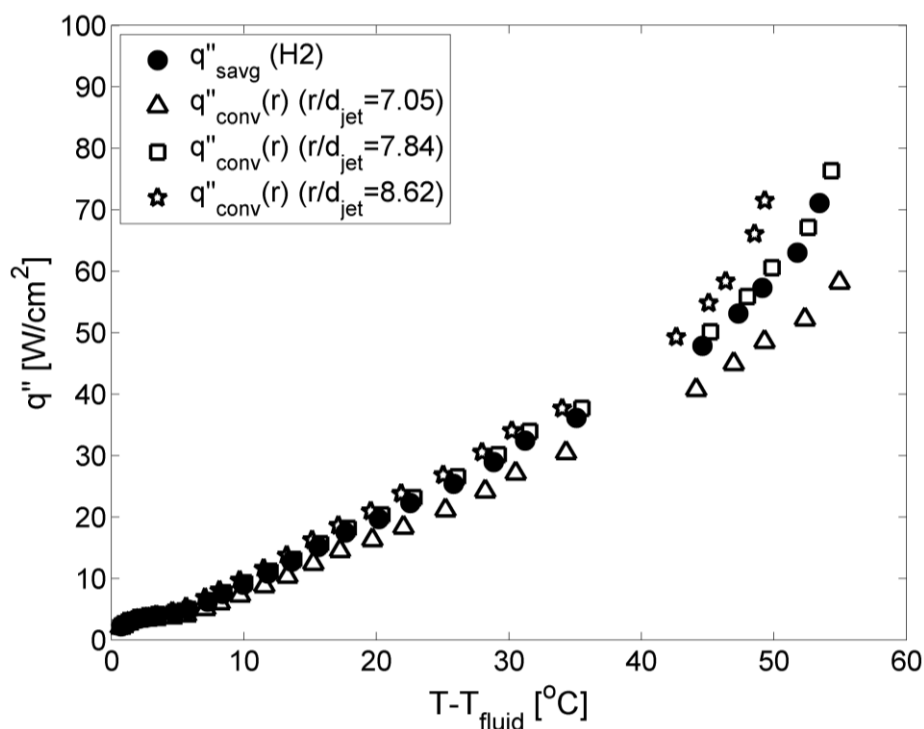


Figure 55: Local versus sectionally-averaged boiling curve for SJIB - heated section H2 (DI water subcooled by 20°C, $Re_{jet} = 5161$)

Figure 56 shows the comparison between sectionally-averaged and local boiling curves for $Re_{jet} = 5161$ on the heated section H1 (Fig. 53a) which is the inner heater ring of the macroscale heater. It is to be noted that within this section, the heat transfer trends are distinctly in single phase regime.

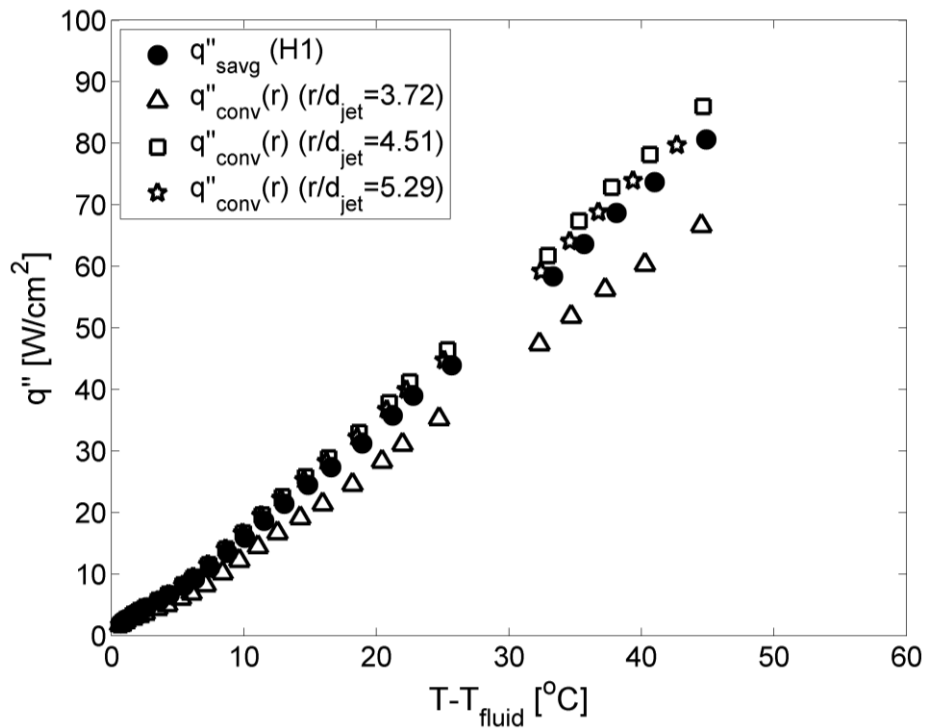


Figure 56: Local versus sectionally-averaged boiling curve for SJIB - heated section H1 (DI water subcooled by 20°C, $Re_{jet} = 5161$)

As with the trends for the H2 section seen in Fig. 55, the heat transfer coefficient in the inner location ($r/d_{jet} = 3.72$) is distinctly lower (by 17.7 percent) than the sectionally-averaged heat transfer coefficient. The reason for the apparent contradiction is much the same as that for the H2 section described above. Substrate conduction estimates from H1 region at a fixed electrical power input of 445 W

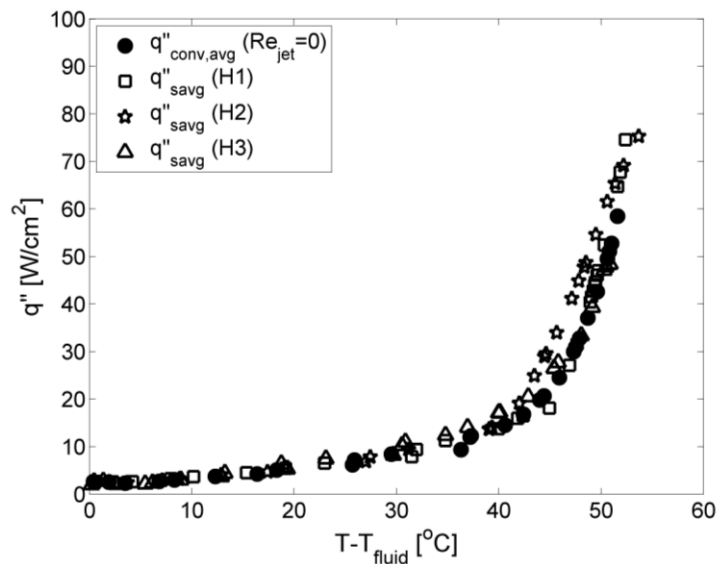
(corresponding to the highest flux data in Fig. 56) indicated that the conduction flux out of the inner control volumes towards UH1 region was, on average, 50 percent larger than conduction flux out towards the UH2 region.

For the present forced convective condition, sectional averaging provides reasonable estimates of boiling trends within the region of like boundary conditions. However, it should be noted that the percentage difference between local and sectionally-averaged data would increase in the case of forced convective flows over large sectional areas.

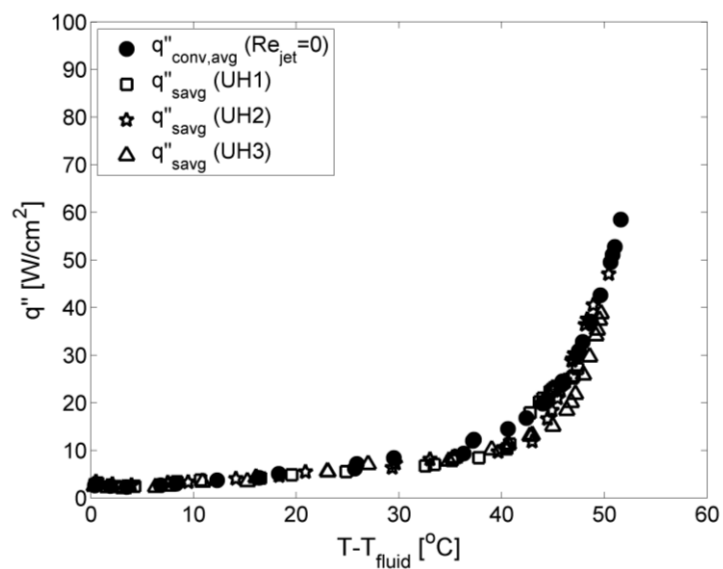
6.1.3 SECTIONAL VERSUS AREA-AVERAGED BOILING CURVES

Following the agreement between sectionally-averaged curves and the local curves within regions of identical imposed boundary conditions, a comparison was made between sectional and area-averaged boiling curves. Results are discussed here for the case of DI water subcooled by 20°C for pool boiling ($Re_{jet} = 0$) and jet impingement boiling at $Re_{jet} = 5161$.

As mentioned previously, in pool boiling there is no forced convective flow to induce spatial temperature variations. However, spatial variation in the surface temperature may be observed due to an imposed non-uniform heat flux. Within each heater ring where electrical heating is supplied (H1, H2 and H3 in Fig. 33), uniformity in the heat flux boundary condition holds while in the unheated substrate regions UH1, UH2, and UH3, there is no imposed heat flux. Figure 57 depict the pool boiling curves computed for locations on and off the serpentine heater rings respectively.



(a)



(b)

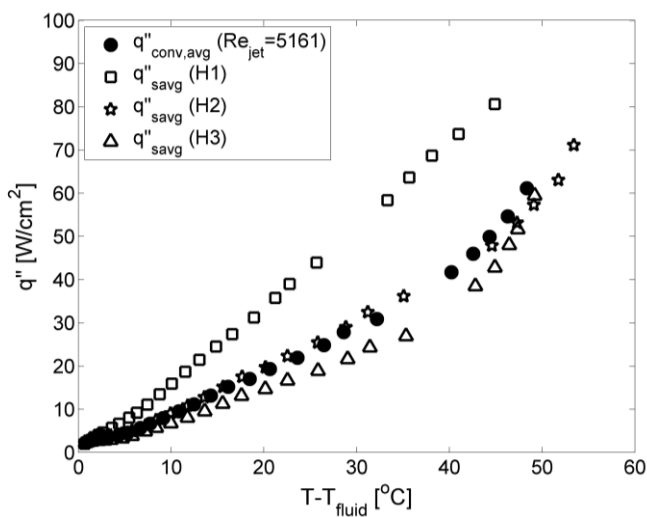
Figure 57: Comparison of sectionally averaged and area-averaged boiling curves for pool boiling with DI water at 20°C subcooling (a) On heated sections (H1, H2 and H3) (b) on unheated sections (UH1, UH2, UH3)

For pool boiling with a non-uniform imposed heat flux, it is shown that trends in boiling curve averaged over regions of like imposed boundary condition provide a more realistic estimate of the local heat transfer conditions when compared with an area-averaged representation of the entire surface. The maximum estimated heat flux in H1 and H2 regions (Fig. 57a) are 25 percent, and 21 percent larger than the estimated area-averaged heat flux respectively. However, the maximum heat flux in the H3 region (Fig. 57a) is observed to lag behind the average by 3 percent. This slight drop in H3 compared with the area-average is attributed to the radially outward conduction losses to the substrate experienced by the periphery of this region.

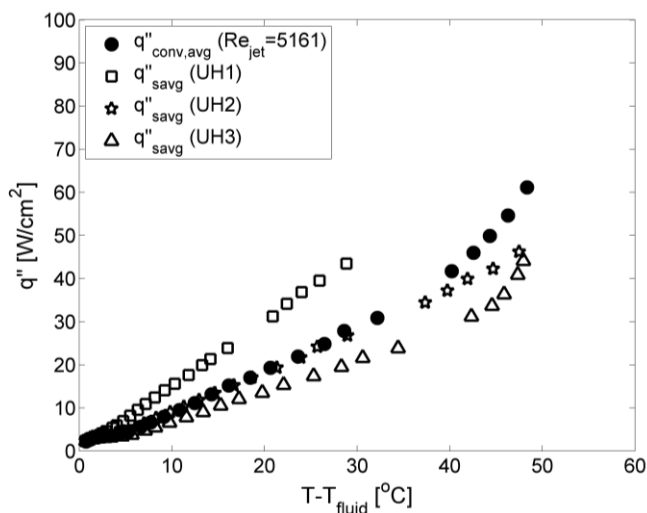
In contrast, sectional averages of the unheated sections (Fig. 57b) are consistently lower than the area-averaged values. The maximum estimated heat flux in UH1, UH2 and UH3 regions are 42 percent, 24 percent and 37 percent lower than the estimated area-averaged heat flux. It should be noted that while differences exist in heat flux magnitudes between sectionally-averaged and area-averaged boiling curves, the trends observed in the temperature difference along the x-axis are not significantly different.

Figure 58 compares sectional and area-averaged trends in the presence of an impinging jet ($Re_{jet} = 5161$) for the heated and non-heated sections of the substrate respectively. Similar to the case of pool boiling, the maximum estimated heat flux in H1 and H2 regions (Fig. 58a) are 27 percent and 15 percent larger than the estimated area-averaged heat flux respectively, while that for H3 is lower by 2.8 percent. The sectional averages of the maximum estimated heat flux in the unheated regions UH1,

UH2 and UH3 (Fig. 58b) are consistently lower than the estimated area-averaged heat flux by 33 percent, 27 percent and 30 percent respectively.



(a)



(b)

Figure 58: Comparison of sectionally averaged and area-averaged boiling curves for SJIB with DI water at 20°C subcooling (a) On heated sections (H1, H2 and H3) (b) on unheated sections (UH1, UH2, UH3)

Figs. 58a and 58b for the jet impingement case clearly depict that in addition to the misrepresented heat fluxes (as seen for pool boiling in Fig. 57), the area-averaged trends fail to capture the large spatial variations in surface temperature induced by the convective flow of the jet. For example, at a fixed representative heat flux of $60\text{W}/\text{cm}^2$, the sectionally-averaged temperature differences on the heated sections H1, H2, and H3 (Fig. 58a) differed from the area-averaged value by 30 percent, 6.8 percent and 1.7 percent respectively.

Another important upshot of such a comparison is that for phase change in the presence of a convective flow, the distinct regions of the single phase and nucleate boiling are lost in the area-averaged representation. These distinct regions of single and phase change flow, which occur during jet impingement partially developed nucleate boiling, are clearly identified with the aid of sectionally-averaged results.

With recent advances in non-intrusive and spatially-resolved thermal imaging, it has become possible to obtain data at several thousand points at once. It is shown here that by a judicious selection of regions that have identical imposed boundary condition as well as small variations in convective flow boundary condition, it is possible to provide sectionally-averaged data that are representative of local variations in heat transfer data. Particular to the cases of pool boiling and jet impingement boiling presented in this section, it has been shown that nine sectionally-averaged curves can adequately represent local variations provided by ~ 7936 local points. Having demonstrated the difference in area-averaged and local boiling curves, we now move

to looking at spatial differences over a parameter space that includes Re_{jet} variation, fluid variation and subcooling variation.

6.2 GLOBAL TRENDS AND SPATIAL VARIATIONS DURING POOL AND SUBMERGED JET IMPINGEMENT BOILING

In this chapter, the global boiling trends and spatial variations are highlighted with increasing Re_{jet} first for DI water at a subcooling of 20°C followed by FC-72 under saturated and 20°C subcooled pool conditions. Spatial non-uniformity of nucleation events during pool boiling and submerged jet impingement boiling (SJIB) are qualitatively and quantitatively discussed. The phase change heat transfer performance of water and FC-72 are compared for pool and jet impingement boiling at 20°C subcooled pool conditions. Finally, a passive means to mitigate the thermal overshoot associated with highly wetting fluids is presented.

6.2.1 FLUID DI WATER: 20°C SUBCOOLED BOILING

For the set of experiments discussed in this section, DI water was used as the working fluid and the jet and pool were subcooled by 20°C. Saturated tests with water at atmospheric pressure were not feasible due to the limitations of the heat exchanger (Fig. 8) that was unable to sustain temperatures higher than 80°C. Experiments without the heat exchanger would have been a compromise on the pool temperature uniformity. Pool boiling and two submerged jet impingement boiling experiments ($Re_{jet} = 2580$ and 5161) were conducted to provide a qualitative and quantitative assessment of the spatial distribution of boiling activity on a non-uniformly heated

surface. Tests with water were conducted for increasing heat flux alone following the results of preliminary tests that indicated an absence of hysteresis for this fluid. Heater surface temperatures were determined using IR thermography. High speed movies of the boiling were recorded and used to interpret the surface temperature contours. Voltage drops from sensors S_1 and S_2 (Fig. 47) were recorded to corroborate the spatial progression of boiling events.

Pool Boiling

Visualization results and sensor data for pool boiling ($Re_{jet} = 0$) with increasing heat flux are shown in Fig. 59. In this figure image set (a) shows the qualitative instantaneous high speed images of boiling activity on the top side of the heated surface. Stationary bubbles, located at the periphery of the disk, remnant from degassing prior to the experiment, are seen in all of the high speed images. Image set (b) shows the calibrated time averaged filtered temperature maps of the back side of the heated substrate. The IR images are oriented identical to the corresponding high speed images presented, with the heater leads to the left. All the IR images have the same maximum and minimum scale for comparison. Sets (c), (d) and (e) depict the voltage time series and PDFs of sensors S_1 and S_2 respectively.

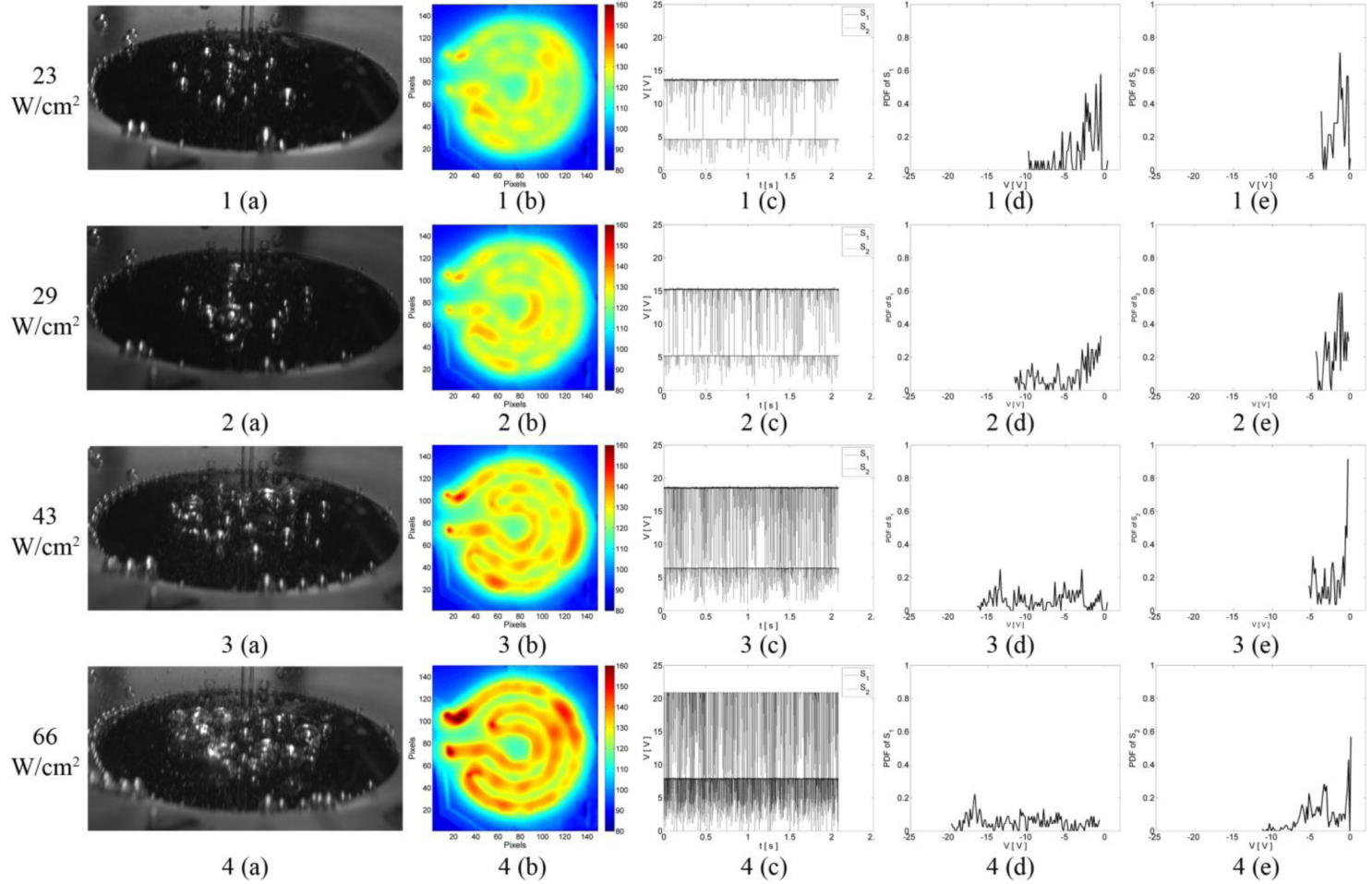


Figure 59: Visualization of spatial variations with increasing flux for pool boiling ($Re_{jet} = 0$)

Pool boiling was found to initiate at the central regions of the heated substrate. With increasing heat flux, bubble density increased substantially and bubbles were seen to nucleate over the entire heated surface (Image set (a)). It should be noted that although the glass nozzle is visible in the images, there was no jet flow under this condition. From the corresponding thermal images (Image set (b)), it is clear that the surface is not at a uniform temperature. Local temperature variations in the range of 130-160°C were observed in the heated regions at the highest heat flux tested (Fig. 59, image 4b). Since heat flux is provided in the concentric rings, the temperature is highest in the regions of the heater rings and heat is diffused axially within the silicon substrate towards the center, in between the concentric heater rings and at the edge of the heated region. Regions of high and low temperatures corresponding to locations of bubbles are also observed in the thermal images in all heater rings and at all power levels. This case of pool boiling is a clear example of how local variation in surface temperatures may be caused by the choice of heater geometry and due to the distributed nucleation activity on the surface.

Images 1c - 4c in Fig. 59 show the voltage time series for sensors S_1 and S_2 plotted for increasing flux levels. Comparisons of the time series shown for the non-boiling condition in Fig. 48, to those shown for the various boiling conditions in Fig. 59 clearly indicate that the sharp dips observed in the voltages are related to the nucleation activity on the surface. The drop in the sensor voltages were an obvious indication of the reduction in the heater resistance and hence the local temperature, caused by the nucleating and departing bubbles. Since sensor S_1 covers a larger region

(heater area) compared with S_2 (Fig. 47), the output mean voltage from this sensor was also larger. At the highest flux (66 W/cm^2), the voltage output from S_1 was pegged at 20 V which was the limit of data acquisition board. However, even at this power level, clear dips in voltage are visible (Fig. 59, image 4c).

The mean voltage from both sensors were found to increase with increasing flux, which is to be expected since the surface temperature (and hence resistance, and voltage for a fixed current) increases with input power. High speed images suggested that the bubble ebullition cycle occurred at frequencies that could be resolved by the high speed camera (i.e., less than 9000 Hz for this test case). The voltage data which were recorded at 24 kHz represent a spatial average (over the sensor area) of multiple bubbling events occurring at an instant in time and as such do not capture the voltage variations during the individual bubble ebullition cycles.

The set of time series of sensors S_1 and S_2 in Fig. 59 indicate that the magnitudes of the voltage dips vary with time. It is also seen that the recorded drops in voltage, significantly increase in magnitude at higher flux levels. This trend is indicative of larger instantaneous reductions in spatially-averaged temperature due to the departure of an increasing number of bubbles from the surface at higher power levels.

Figure 59 image sets (d) and (e) depict the PDFs of the voltage drops with increasing flux for sensors S_1 and S_2 respectively. The area under all PDFs is unity and hence PDFs present a normalized representation of a histogram of voltage drops that can be compared from one power level to the next. At any voltage interval (x-axis of the

PDF), the magnitude of the PDF indicates the likelihood of the voltage drop being in that voltage “bin”. If the voltage drops were indicative of the bubbling events, and the magnitude of the voltage drops were indicative of the number of bubbling events that were occurring at any instant in time, one would expect the PDF plots to be skewed towards more negative voltage bins with increase in power input level. A higher number of boiling events would be indicated by S_1 than S_2 since it covers the inner two rings (larger area) while S_2 covers the outer semicircular section of H3 (Fig.47). Furthermore, at a fixed power level, if bubbles were nucleating across the entire heater surface, the PDFs of S_1 and S_2 would show the same trend of increased probabilities in more negative voltage bins with increased power input.

At 23 W/cm^2 , voltage drops as much as -10V were observed for sensor S_1 (Fig. 59, image 1d) with a significant number of these events occurring at voltage drops less than -3V . PDFs for S_2 at 23 W/cm^2 (Fig. 59, image 1e) were limited to voltage drops less than -4V . At 29 W/cm^2 , the PDF for sensor S_1 (Fig. 59, image 2d) indicated that the majority of the voltage drops still fall within the -0.5 to -3 V range. With increased flux the PDFs for both the sensors shifted towards more negative voltage bins indicating increased boiling activity on the surface. For a flux of 43 W/cm^2 , the PDF of S_1 (Fig. 59, image 3d) depicted a probability for the voltage drops to be in the -10 V to -15 V range. At the highest tested flux (66 W/cm^2) a significant probability of voltage drops being in -14V to -20 V range was observed from the dips in sensor S_1 (Fig. 59, image 4d). The PDF of sensor S_2 (Fig. 59, image 4e) also indicated the occurrence of boiling events in the heater section H3 with a greater number of voltage

drops having magnitudes less than $-5V$. From the presented visual and sensor results it can be concluded that for pool boiling bubbles nucleate and depart from all regions of the serpentine heater.

Jet Impingement Boiling

The series of images 1a - 3a in Fig. 60 depict the high speed visualization of the jet impingement boiling process for $Re_{jet} = 2580$ with progressively higher flux levels. Stationary bubbles were seen at the edge of the polycarbonate clamp in these snapshots. These bubbles were remnants from the pre-experiment degassing. As this location was radially 25.4 mm (1 inch) from the jet impingement point, the influence of the stationary bubbles on the observed boiling could be neglected. For the fixed nozzle-to-surface distance of 3.6 jet diameters considered in this study, a monotonically decreasing heat transfer coefficient is expected during single phase jet impingement with a global maximum at the impingement point.

Bubble nucleation initiated at the periphery of the heated surface (Fig. 60, images 1a - 2a). At these peripheral locations the influence of the wall jet diminishes due to a reduction in its momentum, thereby resulting in higher surface temperatures radially outward from the impingement point (Fig. 60, images 1b - 2b). At a flux of 23 W/cm^2 (Fig. 60, image 1a), occasional bubbles were seen to nucleate and depart from the surface at a certain distance from the jet impingement point.

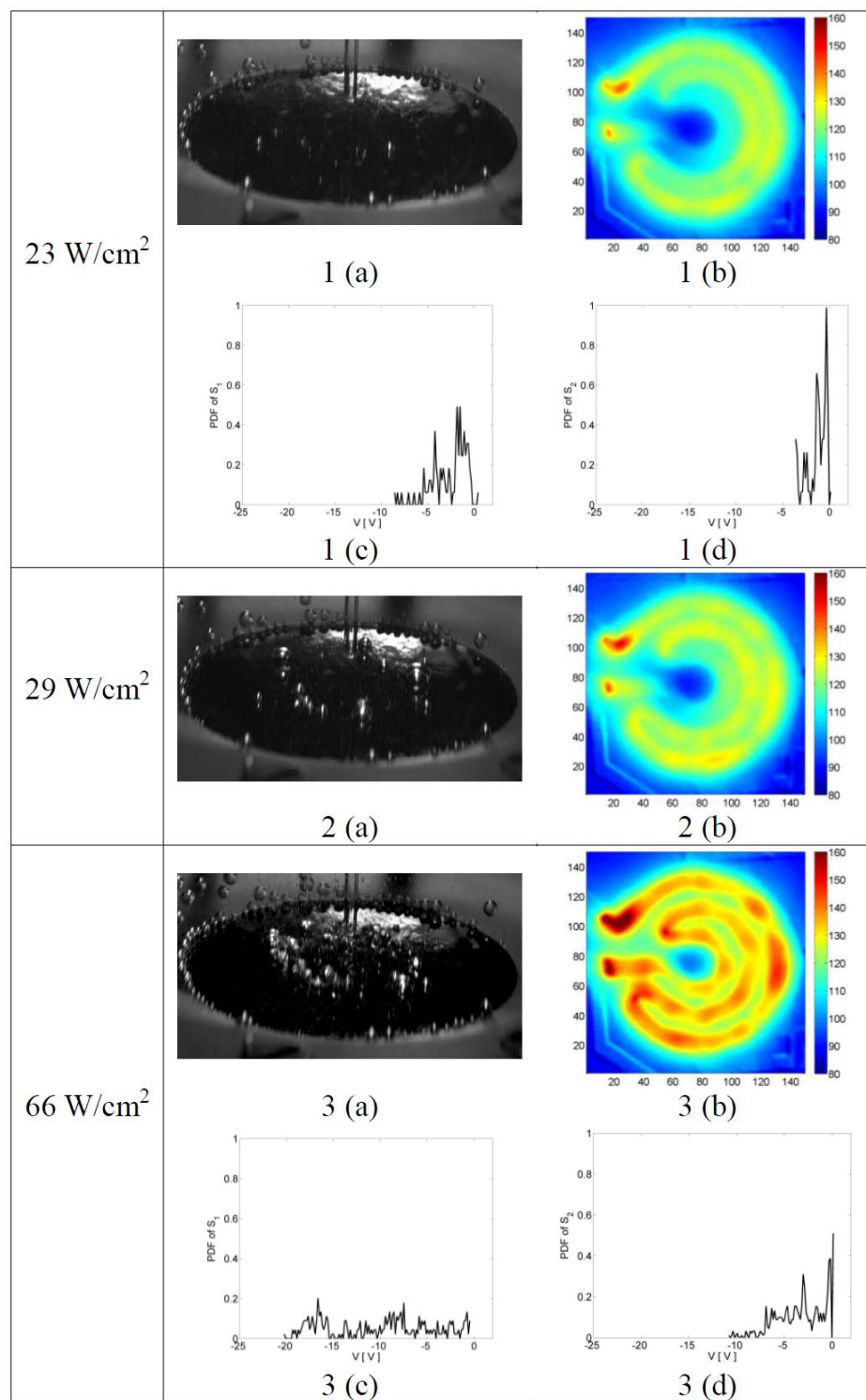


Figure 60: Visualization of spatial variations with increasing flux for SJIB ($Re_{jet} = 2580$). High speed image (a) IR map (b) and sensor voltage PDF for S_1 (c) and S_2 (d)

The PDF of sensor S_1 (Image 1c) for $Re_{jet} = 2580$ at this flux showed much fewer boiling events with lower number of occurrences when compared with pool boiling (Fig. 59, image 1c). The magnitude of the voltage drops observed in S_1 were less than -8.5V. In comparison with sensor S_1 , the probability of events in the vicinity of H3 at this flux of 23 W/cm^2 was much higher as evident in the PDF of sensor S_2 for this case (Fig. 60, image 1d).

With further increase in heat flux to 29 W/cm^2 , boiling activity on the surface increased to form a more distinct ring of bubbles (Fig. 60, image 2a). This ring of bubbles will henceforth be referred to as the boiling front. At the highest tested flux of 66 W/cm^2 (Fig. 60, image 3a), the boiling front developed into a thick ring of bubbles that distinctly progressed inwards towards the impingement point. The inward progression of boiling with increasing flux can be confirmed by observing the diminishing radial influence of the jet in the set of IR images (Fig. 60, images 1b - 3b). The PDFs of sensors S_1 (Fig. 3c) and S_2 (Fig. 3d) for this test case (66 W/cm^2) corroborated the inward movement of boiling events with larger negative voltage drops in the PDF of S_1 ($\sim -20\text{V}$) compared to that of S_2 ($\sim -10\text{V}$). Within the ring of bubbles, single phase convective heat transfer of the jet dominates while boiling heat transfer dominates in the region of the bubbles. This spatial distribution of bubbles on the surface is responsible for the gradual knee in the boiling curve for jet impingement boiling as compared with pool boiling as seen previously in this chapter and observed by Cardenas [26].

Pool versus jet impingement boiling-Thermal distribution

Figure 61 compares the thermal visualization results for pool boiling ($Re_{jet} = 0$) and jet impingement boiling at $Re_{jet} = 2580$ and $Re_{jet} = 5161$, with increasing heat flux. Image sets a – c depict the time-averaged thermal images of the three test cases.

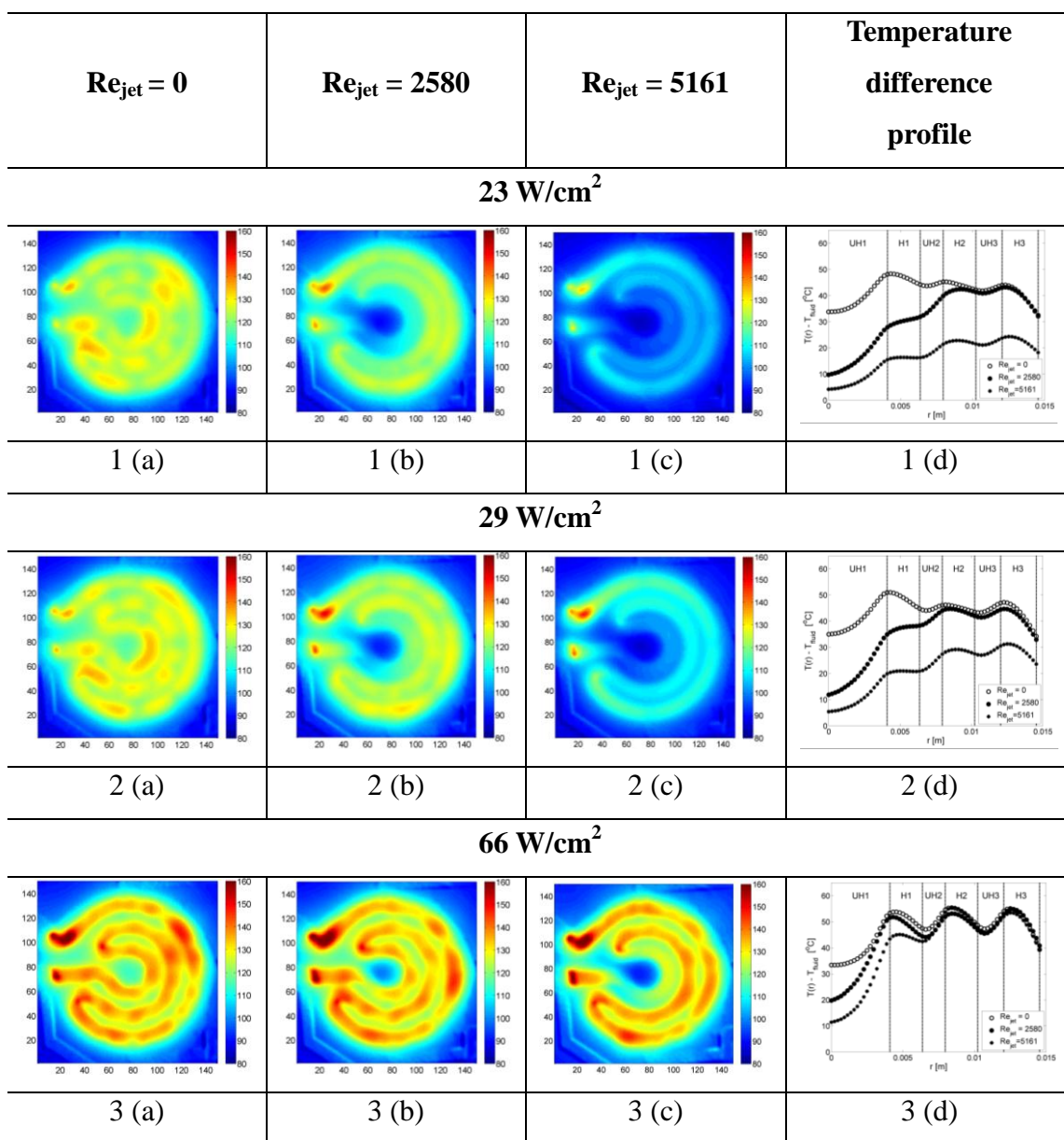


Figure 61: Pool versus SJIB: thermal distribution on the surface

The set of images (d) in Fig. 61 compares the radial temperatures distribution for pool and jet impingement boiling, starting from the point of jet impingement, where $r = 0$. The temperatures along the y-axis in the plots are depicted as the circumferentially averaged temperatures $T(r)$ in excess of the average subcooled fluid temperature, T_{fluid} (Eq.10). For jet impingement boiling, T_{fluid} was taken as the mean of the jet and pool temperatures measured during the experimental run.

The IR thermal maps and the corresponding temperature profiles clearly highlight spatial variation in the thermal distribution, imposed by the concentric heater rings. At each flux level and for each test case, the local temperatures are higher in the regions corresponding to the heated section H1, H2 and H3. For the case of pool boiling where there is no forced convective flow, spatial non-uniformities result as a consequence of the imposed heat flux distribution along with the random spread of boiling activity on the surface. It was discussed in Fig. 59 for $Re_{jet} = 0$ that boiling initiated at the central regions of the heater and progressed outward to occupy a larger area with increasing heat flux. From the temperature profiles at 23 and 29 W/cm² (Fig. 61, images 1d - 2d) it is evident that for pool boiling condition these central regions (in the vicinity of the inner heater ring H1) have the highest temperatures.

At corresponding heat fluxes for jet impingement boiling tests a clear low temperature zone was observed in the regions of UH1 and H1 which are closest to the point of jet impingement. For $Re_{jet}=2580$ it was seen in Fig. 60 that phase change was in its nascent stages at 23-29 W/cm². Nucleation initiated at the periphery of the heated

surface and gradually progressed inwards with increasing heat flux. Correspondingly the temperature profiles for this jet case (Fig. 61, images 1d - 2d) depict a radially increasing trend with the highest temperatures in the outermost heated section H3. At 23 W/cm^2 the temperature profiles for $Re_{jet} = 0$ and $Re_{jet} = 2580$ merged beyond a radial location of 0.009 m (on section H2) indicating the radial limit of the jet influence. As the flux was increased to 29 W/cm^2 , the thermal influence of the jet flow was seen to recede and some circumferential non-uniformities set in at the outer rings of the heaters due to the bubble thermal footprints. The temperature profiles (image 2d) also reflected this receding jet influence as the profiles for $Re_{jet} = 0$ and $Re_{jet} = 2580$ began merging at a lower radius of $r \sim 0.008 \text{ m}$.

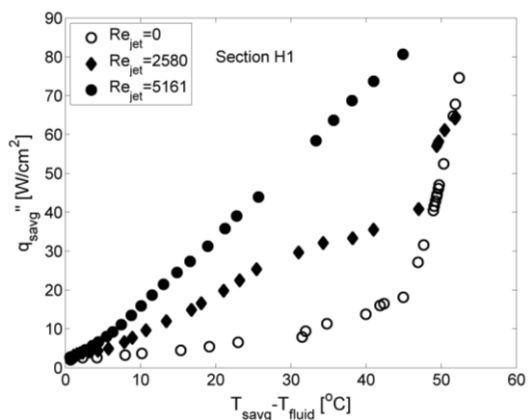
The test case for higher flow rate $Re_{jet} = 5161$ in general followed similar radial trends to the case of $Re_{jet} = 2580$. However the increased jet flow resulted in retaining a large portion of heated area under relatively low temperatures (images 1d – 2d). As discussed in the context of the local boiling curves (Fig. 58), the sections UH1 and H1 remained predominantly in single phase through the tested flux range for this test case.

At the highest flux tested (66 W/cm^2) three distinct bumps on each temperature profile (Fig.61, image 3d), corresponding to the three heater rings, were observed as a result of the non-uniform surface heating. The differences in temperature profiles of pool boiling and $Re_{jet} = 2580$ notably diminished for $r > 0.004 \text{ m}$ while single phase persisted for the $Re_{jet} = 2580$ test case at locations $r < 0.004 \text{ m}$ (UH1). The temperature profile for $Re_{jet} = 5161$ case followed the general trend and merged with

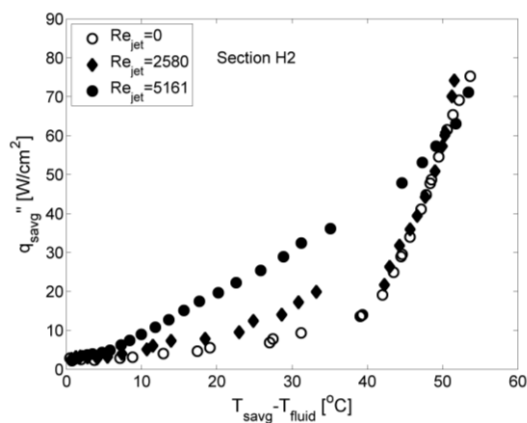
the profiles for $Re_{jet} = 0$ and $Re_{jet} = 2580$ beyond $r \sim 0.006$ m, thereby retaining a larger region under single phase in comparison with $Re_{jet} = 2580$. These observations were supported by the IR maps (images 3a - 3c) and indicated the decreasing spatial influence of the jet and the increasing dominance of boiling over majority of the surface with increasing heat flux.

Pool versus jet impingement boiling – Sectionally-averaged boiling curves

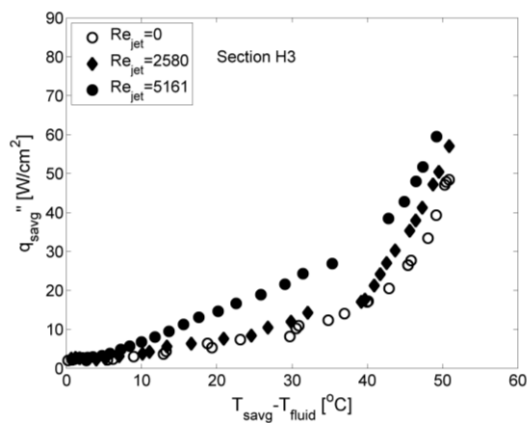
Figure 62 depicts the spatial variations in boiling behavior with increasing radial distance from the impingement point in the form of sectionally-averaged boiling curves. Figure 62a shows the boiling characteristics for heated section H1 spanning $r / d_{jet} = 3.53$ to 5.49 . In the absence of a jet for $Re_{jet} = 0$ (pool boiling), heat transfer in H1 remained in the single phase ($h_{sp} = 0.35$ W/cm²°C) regime up to a temperature difference of $(T_{avg} - T_{fluid})$ of 45°C with large changes in temperature for small changes in the convective heat flux (q''_{avg}). Initiation of boiling was accompanied by a drastic increase in the slope of the boiling curve. Large changes in q''_{avg} were observed for small changes in temperature, as is characteristic of boiling heat transfer. The presence of the jet enhanced the single phase heat transfer ($h_{sp} = 0.92$ W/cm²°C) as indicated by the increase in slope of the boiling curve with increase in Re_{jet} . Note that for $Re_{jet} = 5161$ case section H1 remained in single phase ($h_{sp} = 1.7$ W/cm²°C) for the temperature range tested. Post-initiation of boiling (~48°C), $Re_{jet} = 2580$ replicated the trends for pool boiling ($Re_{jet} = 0$).



(a)



(b)



(c)

Figure 62: Pool versus SJIB – boiling curves for sections H1, H2 and H3

The differences in the boiling trends with Re_{jet} were found to be most pronounced for the section H1 owing to its proximity to the point of jet impingement ($r = 0$). For section H2, ranging from $r/d_{jet} = 6.86$ to 8.82 (Fig. 62b) it was observed that the temperature differences required to initiate phase change dropped by about 8°C for both pool boiling and $Re_{jet} = 2580$ when compared with H1 (Fig. 62a). While there was no significant change in the single phase heat transfer for pool boiling at section H2 ($h_{sp} = 0.34 \text{ W/cm}^2\text{C}$) compared to section H1 (Fig. 62a), the single phase heat transfer rate for the two jet cases ($Re_{jet} = 2580$ and $Re_{jet} = 5161$) declined to $0.5 \text{ W/cm}^2\text{C}$ and $1.04 \text{ W/cm}^2\text{C}$ respectively. The drop in single phase heat transfer rate for the jet cases at section H2 can be attributed to the reduction in momentum of the radially expanding wall jet. The case of $Re_{jet} = 5161$ changed phase at a temperature difference of 47°C which was notably higher than that for $Re_{jet} = 2580$ and $Re_{jet} = 0$. Therefore, it can be concluded that for $Re_{jet} = 5161$, the jet continued to influence the region up to $r/d_{jet} = 8.82$.

For the outermost heated section H3 spanning $r/d_{jet} = 10.4$ to 12 (Fig. 62c), it was seen that the $Re_{jet} = 0$ and $Re_{jet} = 2580$ cases behaved similarly in both single and two-phase regimes. This implied that for the low Re_{jet} case, the jet flow had little or no influence at this radial distance. The single phase heat transfer rate for pool boiling at this location was about $0.34 \text{ W/cm}^2\text{C}$ while that for the $Re_{jet} = 2580$ was about $0.44 \text{ W/cm}^2\text{C}$. For a higher Re_{jet} ($Re_{jet} = 5161$) the slope of the single phase region dropped further ($h_{sp} = 0.77 \text{ W/cm}^2\text{C}$) from that in section H2 ((Fig. 62b) and a clear

transition to phase-change was observed at a temperature difference of approximately 40°C. The three boiling curves approached each other with further advancement in phase change.

6.2.2 FLUID FC-72: SATURATED AND 20°C SUBCOOLED

BOILING

Dielectric coolants are associated with low surface tensions and hence are highly wetting on most surfaces. This wetting nature of dielectric liquids necessitates the need for high incipient wall superheats for the formation of vapor nuclei on the surface. The activation of nucleation sites at these high wall superheats is typically accompanied by a temperature drop on the heated surface. The requisite incipience superheats are unpredictable and often times significantly higher than the fluid saturation temperature. In addition the boiling curve of a highly wetting fluid such as FC-72 obtained with increasing heat flux does not replicate the curve resulting from a decreasing heat flux resulting in a thermal hysteresis. The overshoot, as well as the hysteresis impose severe constraints to the use of these fluids in temperature sensitive applications, where a delayed onset of nucleation could be damaging for the device. The following sections document the overshoot and boiling hysteresis in FC-72 with parametric variations as well as its spatial variation over the surface.

Visualization of Thermal Overshoot and Boiling Hysteresis

Figure 63 depicts the area-averaged boiling curve for the SJIB of saturated FC-72 at a Re_{jet} of 5161. For the experimental conditions tested with FC-72, this Re_{jet} exhibited the largest incipience hysteresis. The x-axis is represented as T_{avg} in excess of the fluid saturation temperature, $T_{sat} = 56^\circ\text{C}$.

With increasing heat flux a very distinct region of single phase was observed with an average heat transfer coefficient of about $0.2 \text{ W/cm}^2 \text{ }^\circ\text{C}$. Interspersed with the area-averaged boiling curve in Fig. 63 are snapshots of the high speed and thermal imaging to additionally depict the spatial variation in the boiling process. Note that the temperature scale for the IR images is shown in excess of the fluid saturation temperature, T_{sat} .

From the high speed image at the low flux level of 1.7 W/cm^2 (inset (a)), it is clear that this power was insufficient to initiate a boiling event. The corresponding IR image depicts the thermal signature of the saturated jet ($\sim 56^\circ\text{C}$) at the impingement point, while the surrounding regions on the substrate are superheated in the range of $\sim 10^\circ\text{C}$ to 20°C . At a heat flux of $\sim 7 \text{ W/cm}^2$ (inset (b)) the high speed image confirmed that the surface was still in single phase. The IR image depicted local wall superheats ($T_{avg} - T_{sat}$) in the range of $\sim 30^\circ\text{C}$ to 45°C . These high surface temperatures fall in the range of electronic device failure for most temperature sensitive applications.

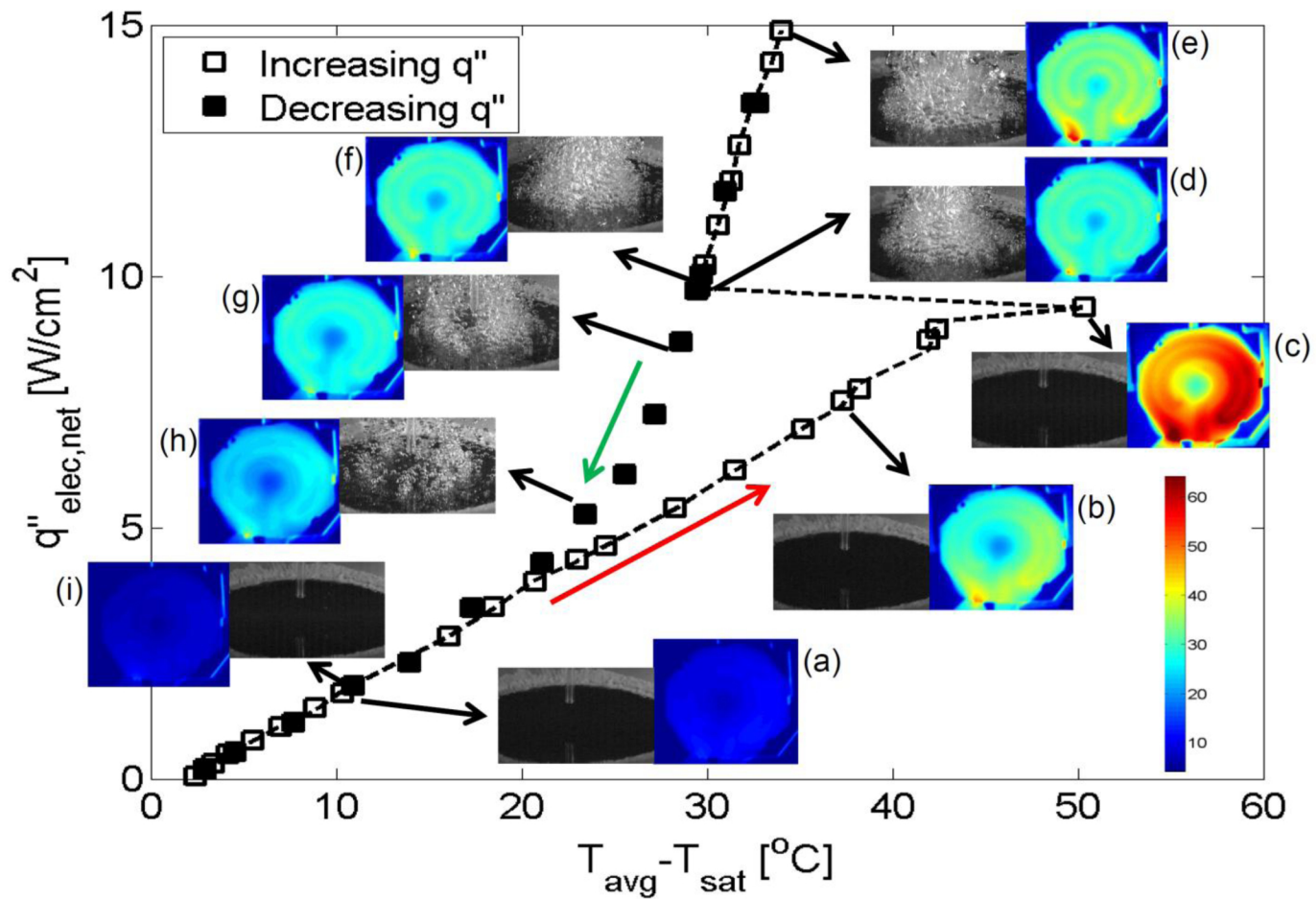


Figure 63: Boiling hysteresis of saturated FC-72 during submerged jet impingement for $Re_{\text{jet}} = 5161$

For this test case, inset (c), representing an input power level of 9.4 W/cm^2 corresponded to the highest wall superheats attained prior to the inception of boiling. Local wall superheats at this flux varied between 35°C to 65°C . Such high local temperatures could easily exceed those attained during critical heat flux (CHF) with these low surface tension fluids. As an example, for a SJIB test of saturated FC-72 ($\text{Re}_{\text{jet}} = 5570$) on a smooth copper surface Cardenas [26] at reported CHF at a flux of 17.5 W/cm^2 and a wall superheat of $\sim 28^\circ\text{C}$. In the present test, ramping up in power was limited by the capacity of the power supply and hence CHF was not attained. However, as seen in Fig. 63 the highest attained heat flux (14.9 W/cm^2) was reasonably close to the CHF observed by Cardenas [26]. The highest flux in this test exhibited an average wall superheat of 34°C which was notably lower than the local superheats attained prior to inception of boiling.

With the surface sufficiently superheated to activate the vapor-trapped cavities, a slight increase in heat flux from 9.4 W/cm^2 to 9.8 W/cm^2 was adequate to drive the process into the fully developed nucleate boiling regime with an explosion of vapor bubbles on the entire surface (Fig. 63, inset (d)). The excessive superheat dominated the ability of the jet to retain a circular boiling front. The onset of nucleation was accompanied by a sudden drop in surface temperature by almost 21°C on an average over the surface. As seen in the corresponding IR map the onset of boiling activity allowed for greater uniformity in the spatial temperatures. The standard deviation in the local wall superheats falls from a value of 6.7°C at 9.4 W/cm^2 (inset (c)) to 2.6°C at 9.8 W/cm^2 (inset (d)) following the onset of phase change. With further increase in heat flux, the

non-uniformities in the local wall superheats, imposed by the serpentine heating profile, gained significance. Figure 63 inset (e) depicts these temperature non-uniformities for the highest heat flux tested $\sim 14.9 \text{ W/cm}^2$. The corresponding high speed visual indicates that at this flux level, the bubbles coalesce at the surface into large vapor slugs.

Reduction in heat flux resulted in a monotonically decreasing curve enclosing an area between the forward and reverse heat flux paths. This area enclosure, referred to as the boiling hysteresis, is indicative of the excess superheat required to initiate boiling as opposed to sustaining the ongoing boiling activity. That is, for a surface with an established nucleate boiling the wall superheat needed to maintain the activity of the nucleation sites is much lower than what was originally required to activate them. From Fig. 63, inset (g) it is evident that with the input flux lowered to about 8.6 W/cm^2 boiling prevails on the surface with a well define ring shaped boiling front. This boiling ring signifies the impact of the jet flow. Further reduction in heat flux lead the process from a fully developed to a partially developed boiling regime with distinct nucleation sites as seen for a flux of approximately 5.3 W/cm^2 in Fig. 63 inset (h). This change from fully to partially developed nucleate boiling occurred due to the deactivation of nucleation sites resulting from a drop in the wall superheat. The boiling curve for the decreasing and increasing fluxes rejoin as the boiling activity on the surface ceases (Fig. 45 inset (i)) and the trend returns to the single phase regime.

Figure 64 shows the boiling curves for saturated pool and submerged jet impingement boiling with increasing and decreasing heat flux levels. Jet impingement boiling is depicted at two flow rates, $Re_{jet} = 5161$ and $Re_{jet} = 7740$. As described in the context of Fig. 63, for each test case the onset of boiling resulted in a temperature drop across the surface. The associated drop in average excess temperatures were approximately 8°C for pool boiling, less than 3°C for the $Re_{jet} = 7740$, while that recorded for $Re_{jet} = 5161$ was nearly 21°C .

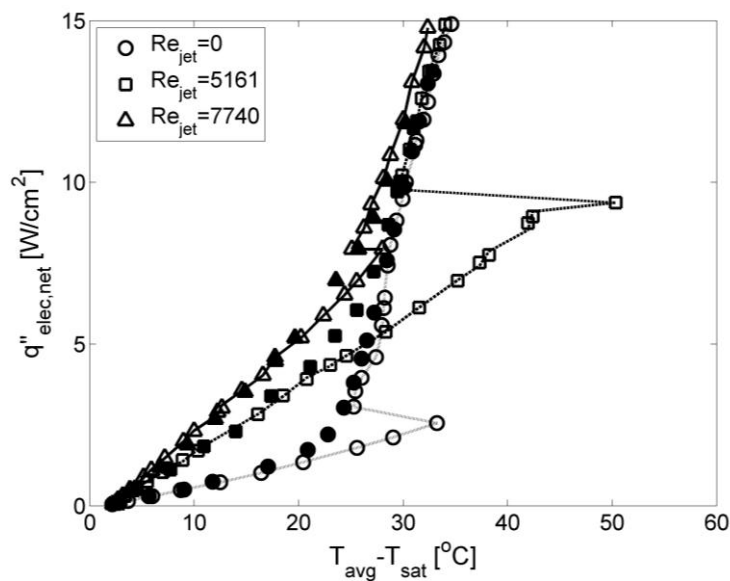


Figure 64: Saturated pool and jet impingement boiling of FC-72 for increasing and decreasing heat flux conditions.

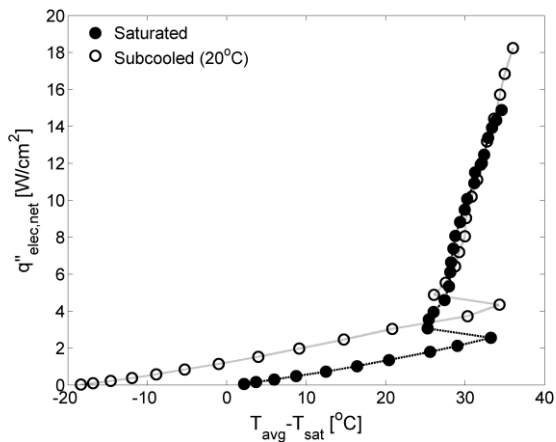
Beyond the onset of nucleation and with progressive increase in heat flux both the jet impingement test cases approached pool boiling behavior as depicted by the merging boiling curves. Hence, the presence of a jet did not additionally contribute to

enhancing the heat transfer rate over that for pool boiling in the fully-developed nucleate boiling regime. However CHF enhancement due to an increase in Re_{jet} has been reported by Cardenas [26].

Similar to the observation in Fig. 63, for decreasing input heat flux the boiling trends for all the tested cases retraced the onward path with the exception of the region of incipience. For each of the test cases, since the surface had an established boiling activity, wall superheats lower than that required for increasing flux were sufficient to sustain the release the vapor bubbles from active nucleation sites. A monotonically decreasing boiling curve with a distinct knee was observed for each case with decreasing heat flux.

Effect of subcooling on global boiling trends

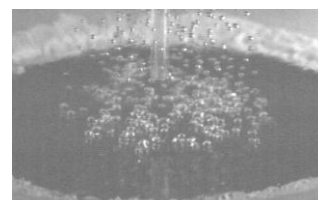
Compared to a saturated pool, a subcooled pool has a larger temperature difference driving the single phase heat transfer that results in an upward shift in the boiling curve in the single phase region. This scenario is depicted for FC-72 during pool boiling in Fig. 65 and during submerged jet impingement boiling in Fig. 66. The single phase upward shift due to fluid subcooling was found to be more pronounced for jet impingement tests (Fig. 66a) where forced convection of the subcooled jet acted in addition to the natural convection to enhance heat transfer.



(a) Pool Boiling

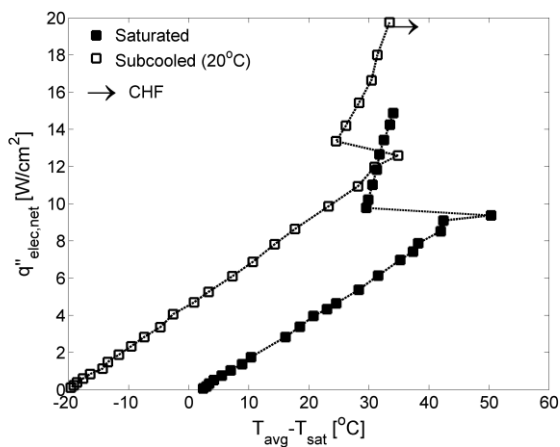


(b) Saturated Pool Boiling at 4W/cm^2



(c) Subcooled Pool Boiling at 4W/cm^2

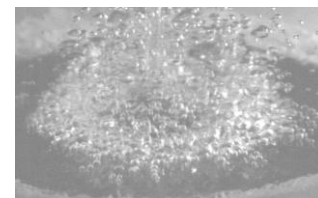
Figure 65: Comparison of saturated and subcooled pool boiling with FC-72



(a) $Re_{jet} = 5161$



(b) Saturated $Re_{jet} = 5161$ at 14.9W/cm^2



(a) Subcooled $Re_{jet} = 5161$ at 20W/cm^2

Figure 66: SJIB of FC-72 under saturated and subcooled conditions for $Re_{jet} = 5161$

The onset of phase change was found to have a negligible influence on the boiling trends for the saturated versus subcooled pool boiling (Fig. 65a). This indicates that nucleate boiling heat transfer severely dominates natural convection in this regime [54]. For cases of jet impingement boiling, differences in the two-phase region were observed based on the inception and spread of the boiling activity on the surface. For example, for $Re_{jet} = 5161$ (Fig. 66a) the slopes for the saturated and subcooled boiling curves after phase change are not the same. The saturated jet with $Re_{jet} = 5161$, required a large superheat for phase change as discussed in the context of Fig. 63. The large superheat at inception resulted in explosive boiling and a drastic drop in surface temperature ($\sim 21^\circ\text{C}$ on average). In contrast for the subcooled jet ($Re_{jet} = 5161$), boiling initiated at the periphery and gradually moved inwards to the impingement point with increasing heat flux. The drop in the area-averaged surface temperature corresponding to the inception of boiling for subcooled $Re_{jet} = 5161$ was about 10.3°C .

In addition to the single phase heat transfer enhancements, the benefits of fluid subcooling have been well documented for the extension of the CHF limits in case of pool boiling [54, 77] and more recently for SJIB with water [26]. The results of the present study support this generally observed trend for extended CHF limits. Even though CHF was not achieved in either case of pool boiling, the images of the boiling activity on the surface can be used to make an interpretive assessment.

Figures 65b and 65c show images of boiling activity at a heat flux of approximately $4\text{W}/\text{cm}^2$ for saturated and subcooled pool boiling respectively. For saturated pool

boiling at 4 W/cm^2 in the two-phase region (Fig. 65b), vapor bubbles coalesced to encompass the entire heater surface. Boiling activity for the image shown is already fully developed. For an identical heat flux, subcooled pool boiling (Fig. 65c) remained in the isolated bubble regime with discrete nucleating sites. A subcooled pool yields smaller vapor bubbles in size that occasionally collapse along the heater surface. As a result of this condensing action, the subcooled boiling activity has a slow progression in the phase change region thereby delaying the occurrence of CHF.

Figures 66b and 66c represent the boiling activities at the highest tested flux for saturated and subcooled jet impingement boiling ($Re_{\text{jet}} = 5161$) respectively. From Fig. 66a it is evident that for the saturated jet, boiling is well into the fully developed regime. The jet is incapacitated to retain a boiling front. CHF was not attained due to the limits of the supply but from the image it is evidently imminent. For subcooled jet impingement it is observed that even at a high heat flux of $\sim 20 \text{ W/cm}^2$, the jet convective flow has a notable region of influence where single phase heat transfer prevails.

It is to be noted that a higher capacity power supply was used for the subcooled tests to probe the CHF limits. A slight increase in flux from $\sim 20 \text{ W/cm}^2$ drove the surface to CHF (Fig. 66a). The occurrence of CHF on the surface was not apparent from the high speed visuals (Fig. 66c), however for a similar experience with a higher jet flow (subcooled test with $Re_{\text{jet}} = 7740$) a qualitative instantaneous snapshot of the transition

to CHF (Fig. 67) was achieved on the TVS Viewer software used to record the IR data, which gave valuable insight.

In Fig. 67b we observe that CHF condition originated at the heater leads and engulfed the rest of the surface. From the IR image of this test case just prior to CHF (Fig. 67a) it is evident that the heater leads corresponded to local hot-spots where temperatures were almost 75°C in excess of T_{sat} .

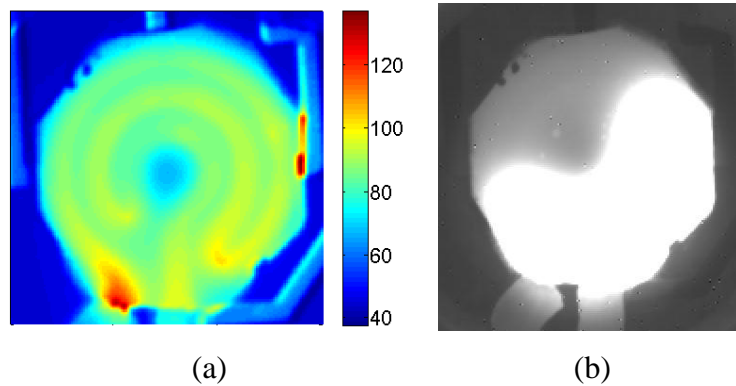


Figure 67: $Re_{jet} = 7740$ subcooled 20°C (a) IR temperature map of the surface just prior to CHF at $\sim 22.8\text{W}/\text{cm}^2$ (b) screen shot of surface undergoing CHF

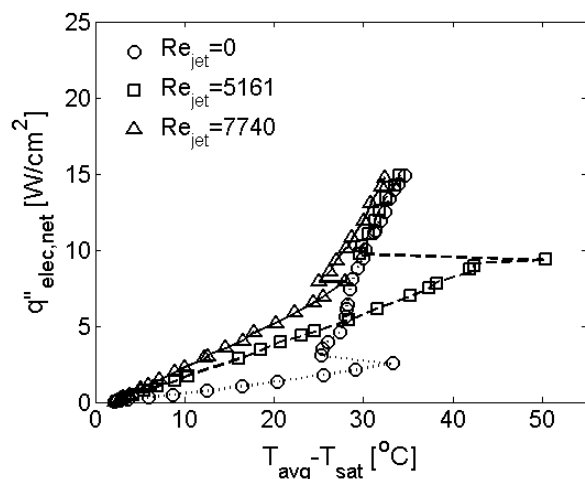
The transition to CHF occurred within a fraction of a second, indicating that the presence of local hot-spots can induce a local CHF condition which in turn subjects the remainder of the surface to attain a premature CHF.

Effect of Re_{jet} and fluid subcooling on incipience superheat and overshoot

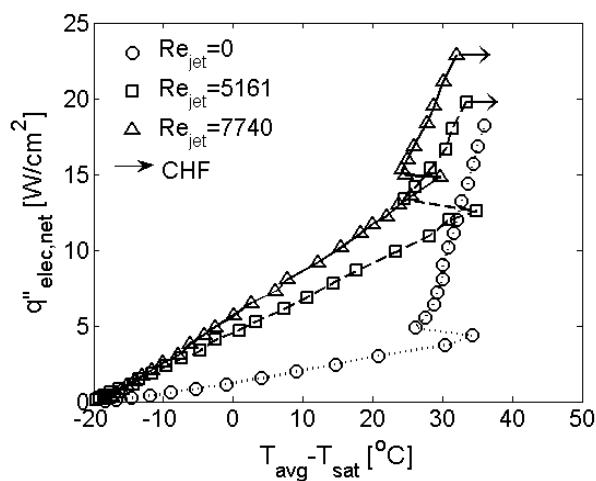
To comprehend the effects of parameters like the Re_{jet} and fluid subcooling on the observed thermal overshoot and incipience superheat in FC-72, pool boiling and SJIB experiments were conducted under saturated and 20°C subcooled pool conditions. The jet Reynolds number, Re_{jet} , was varied keeping H/d_{jet} fixed at 3.6. Jet Reynolds numbers were varied solely by adjusting the jet flow rate. Figure 68 clearly depicts that the magnitude of the single phase heat transfer coefficient increases for both saturated and subcooled boiling with increasing Re_{jet} .

Under saturated boiling conditions, the single phase heat transfer coefficients increased from $\sim 0.05 \text{ W/cm}^2 \text{ }^\circ\text{C}$ for $Re_{jet} = 0$, to about $0.16 \text{ W/cm}^2 \text{ }^\circ\text{C}$ and $0.21 \text{ W/cm}^2 \text{ }^\circ\text{C}$ for $Re_{jet} = 5161$ and 7740 respectively. In comparison for subcooled boiling the single phase heat transfer coefficients increased from $\sim 0.06 \text{ W/cm}^2 \text{ }^\circ\text{C}$ for $Re_{jet} = 0$, to $0.23 \text{ W/cm}^2 \text{ }^\circ\text{C}$ and $0.25 \text{ W/cm}^2 \text{ }^\circ\text{C}$ for $Re_{jet} = 5161$ and 7740 respectively.

It was noted that the increment in the single phase heat transfer coefficient with increasing Re_{jet} was not indicative of an increase in the incipience boiling heat flux in case of FC-72. Under saturated pool conditions (Fig. 68a) the incipient wall superheat for $Re_{jet} = 5161$ was 40% higher than that for pool boiling and almost 56% higher than that for $Re_{jet} = 7740$. The associated drop in average excess temperatures were about 8°C for pool boiling, lower than 3°C for the $Re_{jet} = 7740$, while for $Re_{jet} = 5161$ the recorded drop was nearly 21°C.



(a)



(b)

Figure 68: Area-averaged boiling curves for submerged jet impingement boiling of FC-72 under (a) saturated and (b) subcooled conditions

For tests conducted under subcooled pool conditions (Fig. 68b) the incipient wall superheat for $Re_{jet} = 5161$ was only 1.6% higher than that for pool boiling and about 16% higher than that for $Re_{jet} = 7740$. Thus, for the particular case of $Re_{jet} = 5161$, subcooling reduced the incipient superheat by 36% compared with the saturated test

case. This is in line with the findings of Zhou et al. [25] who found the incipient wall superheat to decrease with fluid subcooling irrespective of the jet parameters like the exit velocity and jet nozzle diameter for tests with highly wetting fluids like R-113 and PF-5052. However, with pool boiling and $Re_{jet} = 7740$ the superheat needed during subcooled tests were 3% and 6% higher than the saturated counterparts respectively. For the subcooled tests the associated drop in average excess temperatures were 8.3°C for pool boiling, 5.1°C for the $Re_{jet} = 7740$ and about 10.3°C for $Re_{jet} = 5161$. Thus, no particular trend in the incipient superheat or temperature overshoot was observed with increasing Re_{jet} over this limited range of saturated and subcooled operating conditions.

Spatial variations during pool boiling of FC-72

Figure 69 shows the radial temperature profiles with increasing heat flux for saturated pool boiling starting from location $r = 0$.

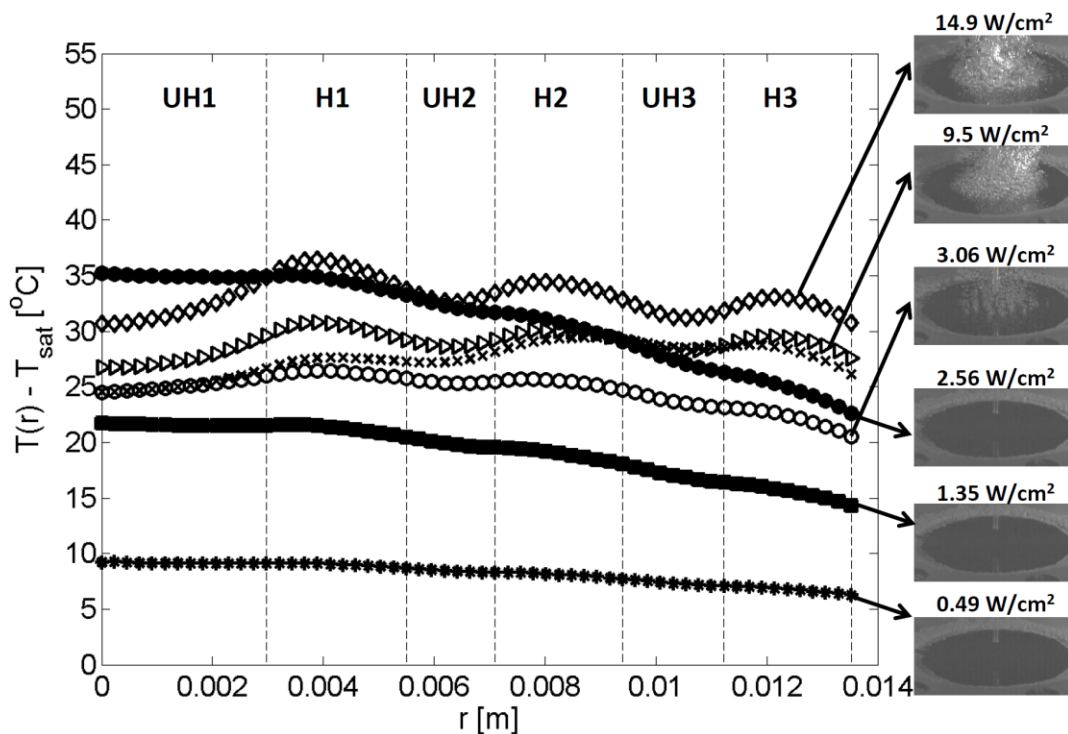


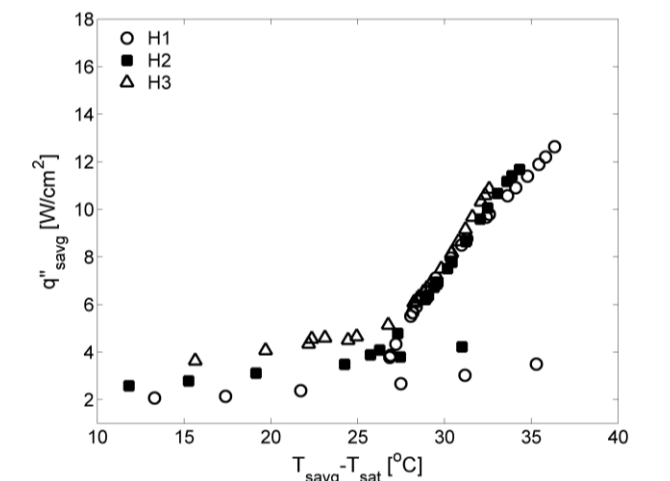
Figure 69: FC-72 saturated pool boiling- radial temperature profiles with increasing heat flux

The temperatures in the y-axis represent the circumferentially averaged temperatures $T(r)$ for each radial location in excess of T_{sat} . The specific heated and unheated sections (Fig. 33) of the surface are indicated along the radial length of the profile. High speed visuals corresponding to the flux levels are provided to associate the thermal trends with boiling activity on the surface. The filled symbols represent flux levels prior to boiling inception while the empty symbols represent those after.

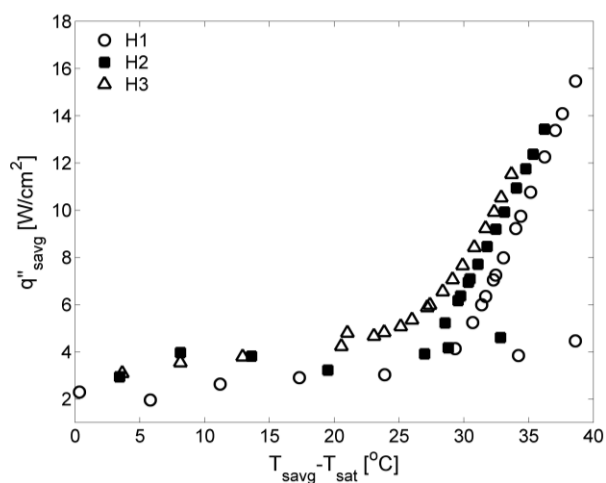
For pool boiling while still in single phase, superheat temperatures were seen to be higher in the vicinity of $r = 0$ (in UH1) and decreased with increasing radial distance.

The observed radial decrease of temperatures in single phase increased for an increase in flux from ~ 0.5 to 2.5 W/cm^2 . These trends are clearly indicated of the dominance of axial conduction over natural convection, with the heat being conducted outward to the cooler regions of the substrate. The profiles are mostly flat over all heated and unheated regions of the substrate, showing no effect of the non-uniform heating profile. Thus, for a fluid with especially low thermal diffusivity such as FC-72, in the single phase region, even a radially non-uniform heating profile such as that generated by a serpentine heater can simulate a uniform heat generation surface.

At the incipient heat flux (2.56 W/cm^2 , filled circles) the incipient superheats are seen to vary from 35°C at $r = 0$ to about 26°C at the edge of H3. The sudden transition to boiling ($\sim 3 \text{ W/cm}^2$, open circles) results in a temperature overshoot over the entire surface with the most excessive drops ($8\text{-}11^\circ\text{C}$) occurring at UH1. In contrast the regions in H3 only experience a drop of about 2°C . The standard deviation in the local overshoots for pool boiling was about 2.7. The high speed images show that boiling initiated in the central regions of heated surface. With boiling heat transfer now dominating the process over conduction, the tapering of temperature profiles radially outward is significantly minimized. With increasing flux and progression to fully developed nucleate boiling, the profiles attain a well-defined shape with three local peaks corresponding to the heater rings.



(a)



(b)

Figure 70: Sectional boiling curves for FC-72 (a) saturated (b) subcooled pool boiling

Figure 70 shows the sectional boiling curves for heated sections H1, H2 and H3 (Fig. 33) during saturated and subcooled pool boiling. In agreement with the saturated pool boiling temperature profiles (Fig. 69), the magnitude of the observed thermal overshoot is highest for section H1 which is closest to $r = 0$, and declines for sections

H2 and H3 which are located at larger radial distances. The trend of overshoots declining with increasing radial distance was consistent for both the saturated (Fig. 70a) and subcooled pool boiling tests (Fig. 70b).

Beyond the onset of nucleation and with increase in heat flux the trends in the boiling curves trajectories were dictated by the progression of boiling activity on the surface. For example, in the context of area-averaged boiling curves for saturated and subcooled pool boiling (Fig. 65) it was shown that at the same supplied heat flux, the saturated test had a rapid progression of boiling with violently coalescing vapor bubbles, while the subcooled test generated distinct nucleating sites with discrete vapor bubbles. As a consequence of these spatial differences in the saturated and subcooled pool boiling activity, the two-phase boiling trends on H1, H2 and H3 were noticeably different. For saturated pool boiling (Fig. 70a) the boiling curves collapsed remarkably well for in the two-phase region indicating fully developed boiling at all regions. While the subcooled tests (Fig. 70b) depicted spatial differences in the boiling trends indicative of isolated nucleation sites on the surface with boiling activity. With increasing heat flux the subcooled boiling curves (Fig. 70b) for all three heated sections approach one another signifying a gradual transition to fully developed boiling.

Spatial variations during SJIB of FC-72

Figures 71 and 72 illustrate the radial temperature difference profiles for saturated SJIB with $Re_{jet} = 5161$ and $Re_{jet} = 7740$ respectively.

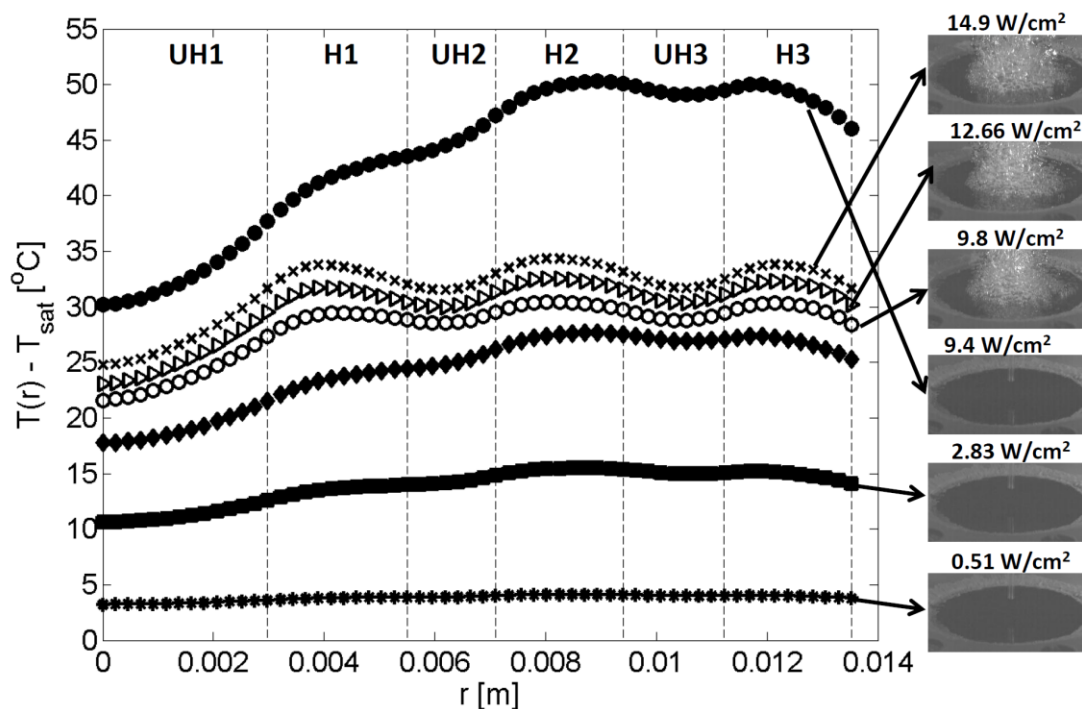


Figure 71: SJIB of saturated FC-72 $Re_{jet}=5161$ - radial temperature profiles with increasing heat flux

In contrast with pool boiling (Fig. 69), the signature of the jet in the vicinity of $r = 0$ is evident from the low temperatures in UH1 at all power levels. For SJIB cases, the forced convection imposed by the jet flow dominates the heat transfer in the single phase regime allowing for heat to be conducted inwards within the substrate towards the regions cooled by the jet. A significant thermal overshoot was observed for the lower Re_{jet} case in contrast with the higher Re_{jet} case. This difference in thermal overshoots can be understood with the help of the temperature profiles and supporting high speed images for each test case.

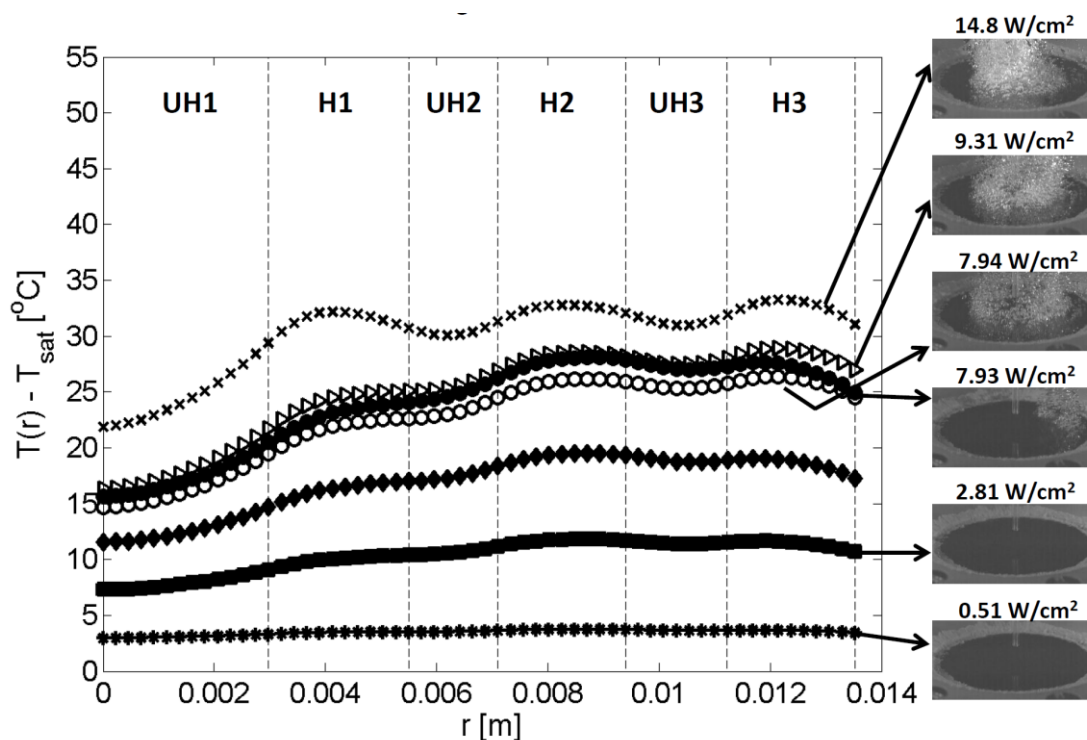


Figure 72: SJIB of saturated FC-72 $Re_{jet} = 7740$ - radial temperature profiles with increasing heat flux

For $Re_{jet} = 5161$ (Fig. 71) substantial incipient superheats were required to initiate boiling. At the highest single phase heat flux of 9.4 W/cm^2 large spatial variations in local wall superheats are observed ranging from (~ 30 - 51°C) with the highest values being in the outermost regions of the heaters (H2 and H3). Local areas on the heated surface reach dangerously high temperature levels which could be a potential cause for local burnout. Transition to boiling directly leads to an explosive fully developed boiling with overshoots ranging from $\sim 8^\circ\text{C}$ at $r = 0$ to $\sim 21^\circ\text{C}$ at select radial locations on H2 and UH3. The standard deviation in local overshoots for this test case was about 4.4°C .

In contrast for $Re_{jet} = 7740$ (Fig. 72), the required incipient superheat (at $7.93\text{W}/\text{cm}^2$) was significantly lower ($\sim 15\text{-}20^\circ\text{C}$) with a standard deviation of 0.4 in the local overshoots. Boiling was found to initiate at distinct locations in the outer regions of the heater where local temperatures were higher. Minor increment in input heat flux by $0.01\text{ W}/\text{cm}^2$ drove the rest of the surface to phase change barring the central regions of the heaters where the jet flow retained its dominance. As a result of the sequential progression of boiling on the surface the associated temperature drops were only of the order of $2\text{-}3^\circ\text{C}$ limited to the regions of UH2, H2, UH3 and a few locations in UH3. Further increase in flux caused the boiling front to move inwards occupying all of the heated substrate area. Figure 73 shows the sectional boiling curves for heated sections H1, H2 and H3 for this case of saturated SJIB ($Re_{jet} = 7740$). Supporting the observation made from the temperature profiles (Fig. 72) for this test case, the sectional curves in Fig. 73 show that the peripheral heater locations H2 and H3 required larger superheats for phase change. Once boiling initiated on the peripheral locations H2 and H3 it allowed for section H1 to have a smooth transition to phase change with an almost non-existent temperature drop. The results of these tests indicate that thermal overshoot is minimized if the progression to phase change is gradual.

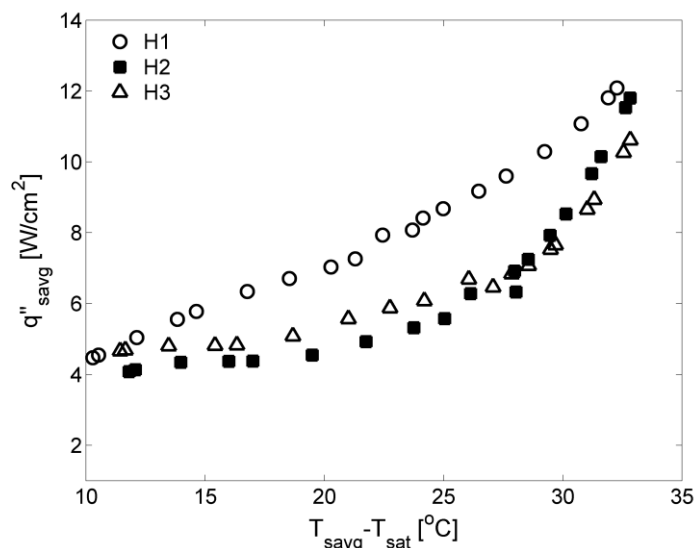
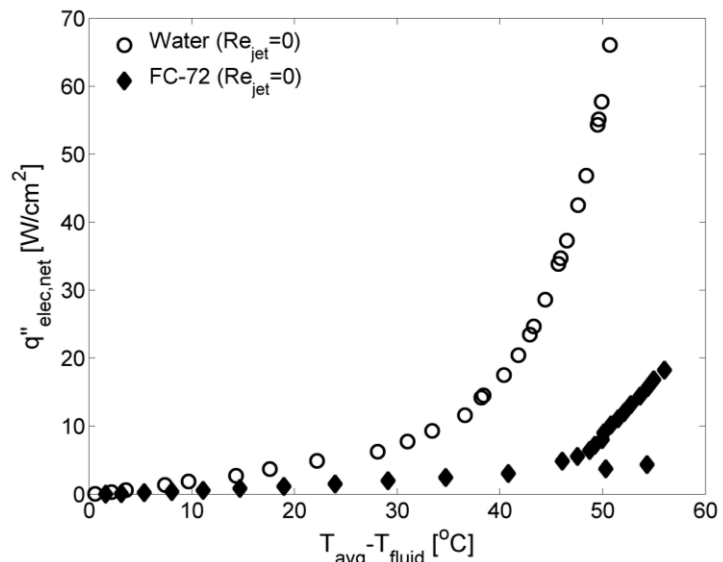


Figure 73: Sectional boiling curves for saturated SJIB FC-72 ($Re_{jet}=7740$)

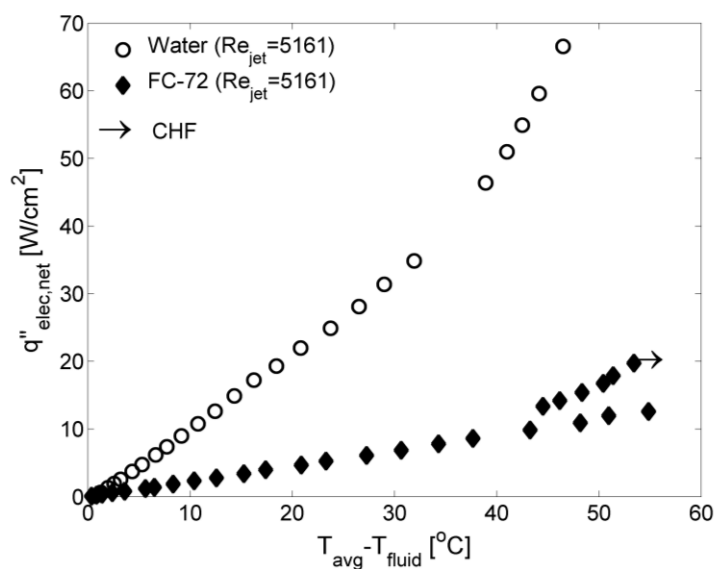
In general, the occurrence of overshoots in fluids like FC-72 is known to be random and unpredictable, however a notable spatial difference is observed in the trends for overshoots between pool boiling and jet impingement boiling. While pool boiling clearly demonstrated highest overshoots in the heated region H1 compared with sections H2 and H3 (Fig. 70), for jet impingement boiling (Figs. 71-73) the region H1 exhibited the least overshoot and highest heat transfer rates owing to its proximity to the jet impingement point. This was found to be consistent for all jet impingement tests under both saturated and subcooled pool conditions. Sectionally-averaged boiling curves for sections H1, H2, and H3 under subcooled boiling conditions are given in appendix K.

6.2.3 COMPARISON OF WATER AND FC-72 –AT 20°C SUBCOOLED CONDITIONS

This section compares the boiling performance of two popular liquid coolants, DI water and FC-72 that were used in this study. The two fluids have quite contrasting thermal properties. Water in addition to being inexpensive and widely available has excellent thermal properties making it the coolant of choice for high heat flux applications. However it has a high saturation temperature and poor dielectric properties that prohibit its use in temperature sensitive or direct liquid cooling applications. Fluorinerts like FC-72 on the other hand have been a popular coolant choice for direct liquid electronics cooling based on their dielectric nature and chemical inertness. In addition, their low saturation temperatures at atmospheric pressure makes them attractive candidates to applications where surface temperatures need to be maintained lower than about 85°C. The advantages associated with using a coolant like FC-72 is severely compromised by its poor thermal properties when compared with water. Owing to these contrasting properties, comparing the phase change thermal performance of these fluids with and without SJIB would be of great value to the electronics community. A comparison of the global boiling trends of these fluids under saturated conditions on a copper surface has been reported by Cardenas [26]. Here these fluids are compared under 20°C subcooled pool conditions.



(a)



(b)

Figure 74: Comparison of Water and FC-72 under 20°C subcooled pool conditions (a) pool boiling (b) jet impingement boiling $Re_{jet}=5161$

Figure 74 compares the area-averaged global boiling trends for DI water and FC-72 with and without jet impingement. Evidently, for a fixed temperature difference, water

exhibits a much higher heat transfer coefficient in for both test cases in all regimes. For pool boiling (Fig. 74a) water had an average single phase heat transfer coefficient of $\sim 0.2 \text{ W/cm}^2 \text{ }^\circ\text{C}$ while that of FC-72 was about $0.05 \text{ W/cm}^2 \text{ }^\circ\text{C}$.

A significant difference was seen in the required incipient superheats of these two fluids. While water transitions to two-phase regime at wall temperatures $\sim 15^\circ\text{C}$ in excess of its saturation temperature, FC-72, owing to its highly wetting nature, required a superheat of 35°C to enter the boiling regime. Thus, even with having a low saturation temperature the appeal of using FC-72 is negatively affected by the requirement of high incipient superheats. A thermal overshoot of almost 8°C is observed for FC-72 during initiation of pool boiling. Once in the nucleate boiling regime the performance of FC-72 declines rapidly as seen from the deviating trends of the two fluids. For the tested range of pool boiling heat fluxes, water resulted in an average two-phase heat transfer coefficient of $0.7 \text{ W/cm}^2 \text{ }^\circ\text{C}$ which was 3.5 times larger than that recorded for FC-72 ($0.2 \text{ W/cm}^2 \text{ }^\circ\text{C}$). For subcooled pool boiling with FC-72 the maximum flux recorded was 18 W/cm^2 , however CHF was not attained.

With an impinging jet ($Re_{\text{jet}} = 5161$, Fig. 74b) the single phase heat transfer coefficients for water and FC-72 enhanced to $0.8 \text{ W/cm}^2 \text{ }^\circ\text{C}$ and $0.23 \text{ W/cm}^2 \text{ }^\circ\text{C}$ respectively. The additional forced convection of the jet delayed the onset of phase change to higher superheats ($\sim 20^\circ\text{C}$) for water; however the superheats required for FC-72 were not much different than the already excessive superheats needed during pool boiling. In the nucleate boiling regime the performance of FC-72 deteriorated

with increasing flux, compared with water. The average two-phase heat transfer coefficients in this case were $1.3 \text{ W/cm}^2 \text{ }^\circ\text{C}$ and $0.3 \text{ W/cm}^2 \text{ }^\circ\text{C}$ for water and FC-72 respectively. It is to be noted that the maximum flux attained for FC-72 with $\text{Re}_{\text{jet}} = 5161$ was 19.7 W/cm^2 , beyond which the surface experienced pre-mature CHF.

6.2.4 MITIGATION OF TEMPERATURE OVERSHOOT

From the experiments conducted with FC-72 it was observed that incipience wall superheats can be large and on occasion even be comparable to or exceed superheats at CHF conditions. In this study, local incipience superheats up to 65°C (Fig. 63) were documented under saturated jet impingement boiling conditions. Although CHF was not achieved for pool boiling conditions in the present study, previous literature on pool boiling with FC-72 have reported incipient superheats as high as 51°C [19].

For new age electronics that operate within a narrow range of temperatures the use of the dielectric liquids as two-phase coolants requires the mitigation or complete elimination of thermal overshoot and boiling hysteresis. As a result, several studies have shifted focus to exploring novel means of overshoot mitigation.

Parker and El-Genk [77] compared pool boiling performance of FC-72 under saturated and subcooled conditions on uniformly heated smooth copper and micro-porous graphite surfaces. Their results showed that the presence of re-entrant type cavities (Fig. 5) on the porous surface aided a timely onset of nucleation in porous graphite owing to the enhanced vapor trapping capabilities of the re-entrant cavity geometry.

The porous surface resulted in complete elimination of temperature overshoot. In comparison, the smooth copper surface exhibited overshoots of 9 -14°C for saturated as well as subcooled conditions. Reduction in temperature overshoot by the use of other novel cavity geometries such as pyramidal re-entrant cavities [78] and zero-angle cavities [79] created by curved surfaces in contact with heated surfaces have also been reported in literature. The application of fluid mixtures having different saturation temperatures [80] towards overshoot mitigation has also been demonstrated.

As explained for Fig. 72, timely nucleation of vapor bubbles at one location can aid the rest of the surface to change phase sooner. This finding is supported by the studies of Bergles et. al.[81] and Bhavnani et. al. [82] wherein bubbles generated from nearby heaters allowed for a timely onset of boiling thus reducing the temperature overshoot on the surface.

A passive means to achieve the same result is by using a self-cavitating jet wherein a concentric collar is added at the end of the circular jet nozzle. This nozzle geometry is shown in Fig. 75. The collar provides an expansion region for the jet flow at the exit of the nozzle. The expansion region provided by the collar and the corresponding pressure drop, result in the generation of a cloud of cavitation bubbles that impinges on the test surface. The impinging bubbles slide over the heated surface providing the liquid –vapor interface required for an early onset of boiling.

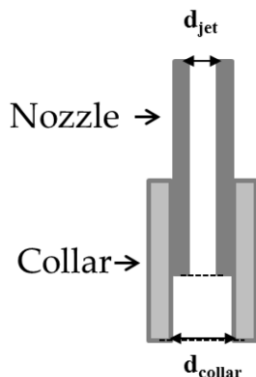


Figure 75: Self -cavitating jet nozzle geometry

This phenomenon was observed as part of ongoing study wherein the goal has been to characterize the resonance characteristics of liquid flow through this nozzle geometry. Cavitation induced bubbles were first observed during the flow of DI water through this nozzle geometry and later confirmed with FC-72. It was established that depending on the fluid temperature cavitation bubbles area generated only above a certain threshold flow velocity. This threshold velocity was found to be much larger for water than FC-72 potentially due to the low surface tension and high vapor pressure of FC-72 compared to water. Tests with the cavitating jet nozzle confirmed that to maintain cavitation through a jet nozzle submerged in an ambient fluid it is extremely critical for the jet and ambient fluid to be of the same temperature. In preliminary tests conducted with cavitating jet nozzle and FC-72, it was found that cavitation ceases to exist for temperature differences larger than $\pm 0.5^{\circ}\text{C}$ between the pool and the jet fluid. The existence of cavitation phenomenon under subcooled pool condition was also confirmed.

The self-cavitating jet used for this experiment consisted of a glass nozzle with outer and inner diameters of 1 mm and 0.5 mm respectively. A glass tube with 1.16 mm inner diameter served as a collar of length 10 mm resulting in a 0.33 mm step height. The nozzle and collar were glued together using aquarium grade silicone sealant. The height of the jet above the surface estimated from the exit of the collar was about $6d_{jet}$ where d_{jet} is the jet nozzle inner diameter. Based on d_{jet} the present test was conducted for $Re_{jet} = 10616$ under saturated pool conditions. With the same test facility used here and for the same test conditions, the area-averaged results for elimination of temperature overshoot by a self-cavitating jet on a smooth copper surface (roughness 33 nm) was reported by Cardenas [26]. The spatial characterization of this overshoot elimination technique is discussed here.

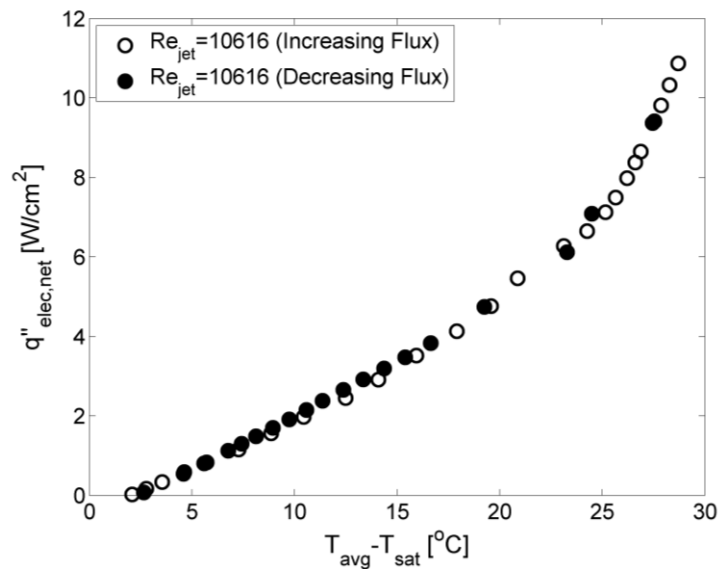
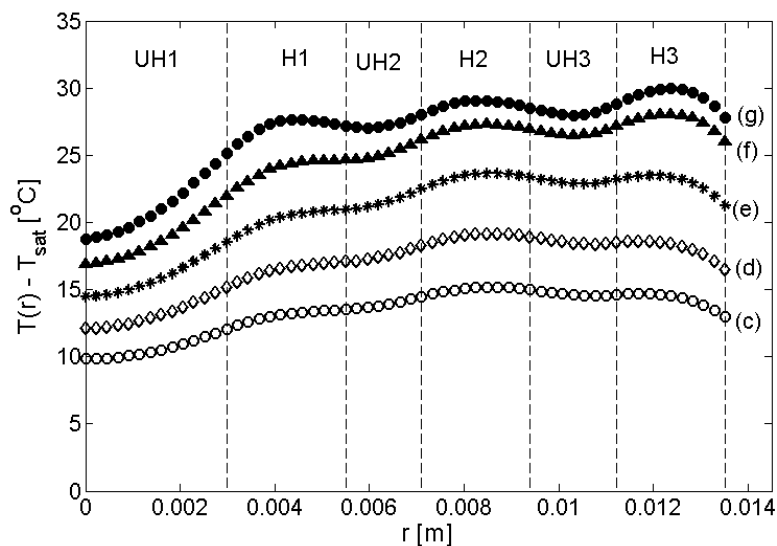


Figure 76: SJIB with the self-cavitating jet nozzle ($Re_{jet} = 10616$) during increasing and decreasing heat flux conditions

Figure 76 shows the boiling curve obtained with the cavitating jet during submerged jet impingement boiling with saturated FC-72. The curve is shown for both increasing and decreasing heat flux conditions. During the single phase a heat transfer rate of $0.28 \text{ W/m}^2\text{C}$ was achieved. Transition to two-phase heat transfer initiated at an average wall superheat of 25°C . The curve depicts a smooth knee in the region of transition from single to two-phase heat transfer. Thus, phase change was achieved with no temperature excursion on the surface. The boiling curves for increasing and decreasing heat flux conditions overlay extremely well validating the elimination of boiling hysteresis.

Figure 77a shows the radial temperature profiles along the surface corresponding to the boiling test described in Fig. 76. The profiles are depicted for increasing heat flux starting at the point of jet impingement ($r = 0$). The associated high speed images with increasing flux are depicted in Figs. 77 (b-c).

Fig. 77b shows the cloud of cavitation induced bubbles impinging on the test surface prior to the start of experiment. No heat was supplied to the substrate at this point. The impinging bubbles can be seen to slide over the test surface, thus acting as a source artificial nucleation sites. With increase in heat flux, boiling initiated at the periphery of the heated surface as seen in Fig. 77(c-d). The corresponding temperature profiles indicate higher temperature in heated sections H2 and H3 in comparison with heated section H1 which is closest to the jet impingement point. No temperature drop was observed at any radial location on the surface.



(a)

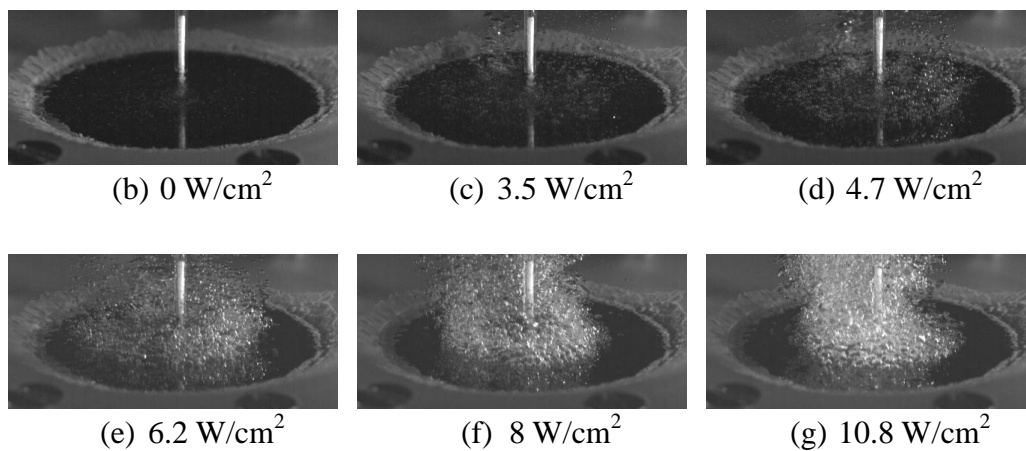


Figure 77: Radial temperature profiles (a) and high speed images of the transition to phase change (b-g) during SJIB with a self-cavitating jet

With further increase in heat flux the boiling front was found to gradually progress inwards (Figs 77 (e-g)) as observed previously in the case for boiling with water (Fig. 60). Thus, the impingement of cavitation bubbles on the surface successfully eliminated any possibility of a nucleation explosion on the surface. The scattering of cavitation induced bubbles provided the much needed liquid-vapor interface thus,

allowing the activation of surface cavities at much lower wall superheats compared to a regular jet nozzle.

In conjunction with the tests conducted by Cardenas [26] on a copper surface, the above tests with silicon confirmed the elimination of temperature overshoot independent of the nature of the test surface and were reported in [83]. Boiling trends of the two surfaces for both cavitating and non-cavitating jet conditions clearly depicted that copper being of a higher surface roughness (33 nm) required much lower incipient superheats when compared with the much smoother silicon (roughness 0.89 nm). The performance of a regular jet nozzle on the two surfaces is discussed in appendix I. These observations indicate that the passive elimination of thermal overshoot has an important role to play in temperature sensitive electronics applications which are commonly based on silicon chips.

7 MICROSCALE HEATER RESULTS

This chapter presents an investigation of pool and jet impingement boiling from a microscale hot-spot. The latent heat transferred from a heated surface to a fluid during boiling is dependent on the nucleation, growth and departure characteristics of vapor bubbles. Boiling in the presence of a jet would involve significant hydrodynamic and thermal interaction between the jet and the nucleating bubbles. The goal of this part of the study was to highlight the qualitative and quantitative differences in the bubble dynamics, departure characteristics and latent heat transfer with and without jet impingement.

Pool and jet impingement boiling results for the dielectric fluid FC-72 are presented for pool subcoolings of 10°C and 20°C. All experiments presented in this section were conducted at atmospheric pressure. Qualitative comparisons are made using the series of instantaneous high speed images acquired during experiments. Quantitative results in the form of bubble departure diameters, frequencies, and latent heat transport are presented for the two subcoolings with change in input power.

7.1 MICROSCALE INVESTIGATION OF POOL BOILING

Over the past years, a number of studies have investigated bubble nucleation, growth and departure behaviors under pool boiling conditions along with the latent heat transfer resulting from the determined bubble geometries [35, 36, 48, 51, 53]. In general, the estimation of boiling heat transfer from a heated wall requires the

knowledge of the number of active nucleation sites per unit area, the rate at which vapor bubbles are released from the surface and the bubble diameter at release. For a large heated substrate area, the onset of boiling results in several active nucleation sites as seen from the high speed images presented earlier in this thesis. Studies such as that of Theofanous et. al [33] and Gerardi et. al [34] have used such large heated areas to determine the nucleation site density during pool boiling. Several recent studies have shifted focus to documenting hydrodynamics and heat transfer at isolated nucleation sites/artificial cavities during pool boiling to simplify this complex phenomenon [35, 36, 44, 48, 64]. The results of single bubble studies [44, 45, 48] among several others; indicated that bubble departure diameters increase with increasing wall superheat; however the impact on the resulting departure frequency is still in question.

In the present study, the inception and departure characteristics of vapor bubbles in a subcooled pool of FC-72 were obtained by the use of a 1000 μm heater that simulated a local hot-spot on the silicon substrate. The following section presents qualitative and quantitative results obtained for bubble ebullition during pool boiling of FC-72 at subcoolings of 10°C and 20°C. All high speed images for pool boiling were acquired with the same field of view (5.2 mm x 5.87 mm) for a physical comparison of bubble sizes. All the images shown here for pool boiling have been cropped down to 5.2 mm x 5.26 mm to eliminate reflections on the silicon substrate.

7.1.1 BOILING INCEPTION- SUBCOOLING EFFECTS

The series of images in Figure 78 qualitatively depict the onset of phase change during pool boiling of FC-72 at 10°C subcooled pool conditions. Boiling initiated at an input power of 6.9 W for this test condition. Images were captured at 7000 frames per second and the time stamps corresponding to each instantaneous image are provided.

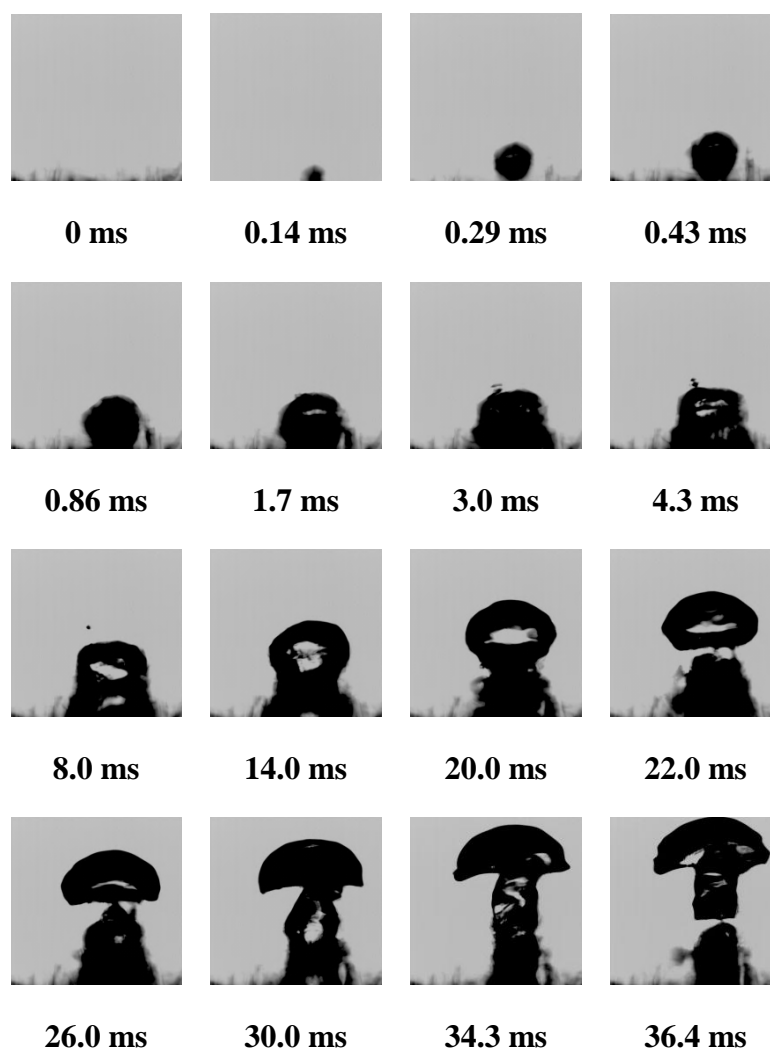


Figure 78: Inception of boiling during pool boiling of FC-72 at 10°C subcooled pool condition (6.9 W). Field of view (5.2 mm x 5.26 mm).

The images in the top row of Fig. 78 depict four consecutively acquired snapshots during the initiation of boiling. From Fig. 78, it can be noted that phase change initiated at single location on the heated surface with the emergence of a vapor embryo in about 0.14 ms once the surface was sufficiently superheated. A drastic increase in bubble size can be observed in the first 0.43 ms (top row, of Fig. 78) immediately after the phase transition. This initial growth rate is presumably aided by the presence of the thermal boundary layer that develops adjacent to the bubble due to conduction from the wall to the surrounding liquid. The thickness of the boundary layer may be approximated as $\delta = k_l/h_{sp}$ where k_l is the liquid thermal conductivity, and h is the convection heat transfer coefficient. Using the single phase convective heat transfer coefficient for FC-72, obtained previously in this work with the macroscale heater substrate ($h_{sp}=0.05 \text{ W/cm}^2\text{°C}$), the boundary layer thickness was found to be approximately 0.1mm. The initial growth stages of the bubble result in a fairly spherical shape as dictated by the surface tension forces. With progress in time the bubble growth in the vertical direction was seen to slow down and a lateral dilation of the bubble occurred until about 8 ms. This reduction in vertical growth could be attributed to the condensation of the bubble at its upper periphery in its attempt to expand into the subcooled fluid bulk. Buoyant forces were found to take effect once the bubble had gained sufficient volume, resulting in the gradual rise of the bubble and the formation of a neck along the line of contact. Departure finally occurred at 22 ms with the bubble geometry assuming a hemispherical appearance flattened at the bottom and dome shaped at the top. Hemispherical deformations of vapor bubbles

departing into a subcooled bulk have confirmed by the numerical simulations of Pan et al. [84] for flow boiling in a vertical channel. In accordance with their findings, the vapor dome advancing into the subcooled fluid gradually transitions to a concaved geometry under the cumulative influence of buoyancy, drag, surface tension and the local inertial forces caused by the condensation at the bubble periphery.

The departure of the first vapor bubble in this case left behind a substantial vapor volume at the hot-spot that induced successive bubble growth in less than 6 ms. The rapid succession of bubbles resulted in vertical coalescence (with the bubble that departed at 22 ms) forming a vapor mushroom. The merging of bubbles continued for a little more than 10 ms as the nucleation site continued to feed the previously departed bubble. After a total duration of 10.4 ms the coalesced vapor mushroom was seen to finally depart from the source. The average bubble departure diameters for this test case were found to be 2.3 mm which was 1.3 times greater than the diametric span of the thin film heater. The corresponding departure frequency was 26.3Hz. It is to be noted that the images shown in Fig. 78 were acquired during preliminary tests. For the actual test run for this subcooling, boiling occurred at an in power of 7.6 W with an average bubble departure diameter of 1.69 mm and a departure frequency of 30.7 Hz.

Figure 79 depicts the onset of phase change during pool boiling of FC-72 at a higher pool subcooling of 20°C. Compared with the low subcooling case (Fig. 78), the inception of boiling at a higher subcooling required an approximately 1.3 times greater input power of 9.3 W.

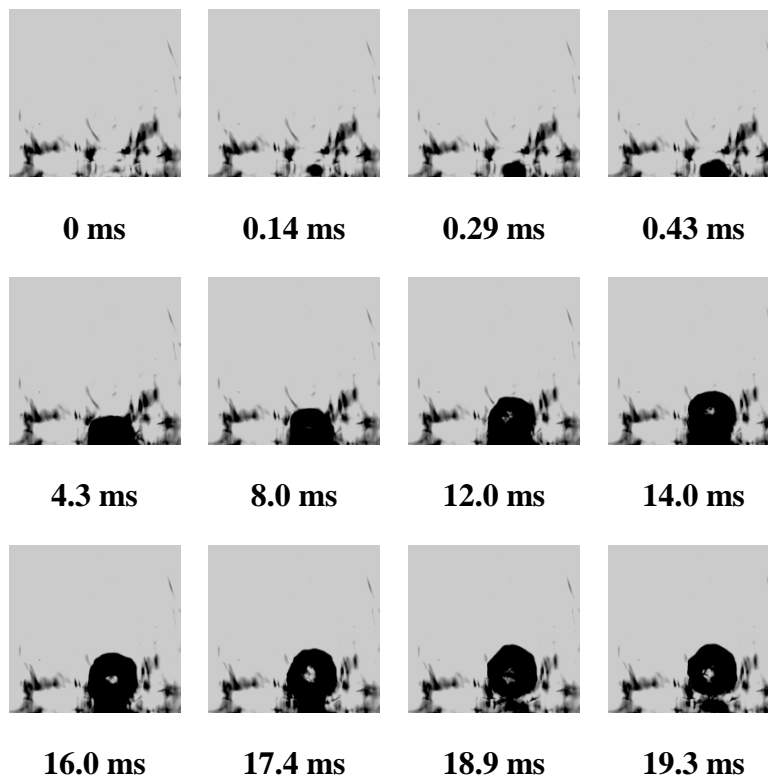


Figure 79: Inception of boiling during pool boiling of FC-72 at 20°C subcooled pool condition (9.3 W). Field of view (5.2 mm x 5.26 mm).

Here again the first four images represent consecutive snapshots of the initial growth stage of the first vapor bubble. In contrast to the low subcooling case (Fig. 78), the bubble's initial growth appeared to be much slower in first 0.43 ms. With increase in time, a steady rate of growth was observed with the bubble geometry being notably spherical. Both these observations (slower growth rate and spherical geometry) are characteristic of a higher subcooling where the thermal gradient between the heated surface and subcooled bulk limits the height of the saturated thermal layer in the vicinity of the bubble. As a result, a notable surface area of the bubble is exposed to the subcooled fluid for condensation at the bubble periphery. In addition lateral growth

of the bubble is impeded. Thus, smaller and more spherical bubble geometry is enforced. At each time step, the bubble dimensions were distinctly smaller than those observed at corresponding stages of growth for the lower subcooling (Fig. 78). The formation of a neck along the surface contact line began at 16 ms with the bubble finally departing at 19.3 ms. The average bubble departure diameters evaluated for this power level beyond onset was 1.67 mm. As observed in these images bubble deformations due to the drag forces from the surrounding liquid at departure were minimal owing to surface tension along with the small surface area of the bubbles.

7.1.2 VISUALIZATION OF SUBCOOLED POOL BOILING

This section discusses the qualitative effects of fluid subcooling on the bubble geometry during pool boiling of FC-72. The qualitative observations are discussed at fixed input power levels for the two tested pool subcoolings of 10°C and 20°C.

Figures 80 and 81 represent a series of snapshots during a bubbling event at an input power ~6.5 W and ~5.8 W respectively, for the two pool subcoolings tested. Images are shown at time intervals of 6 ms before and after the instant of bubble departure (shown at 12 ms). The data presented were acquired while decreasing input power.

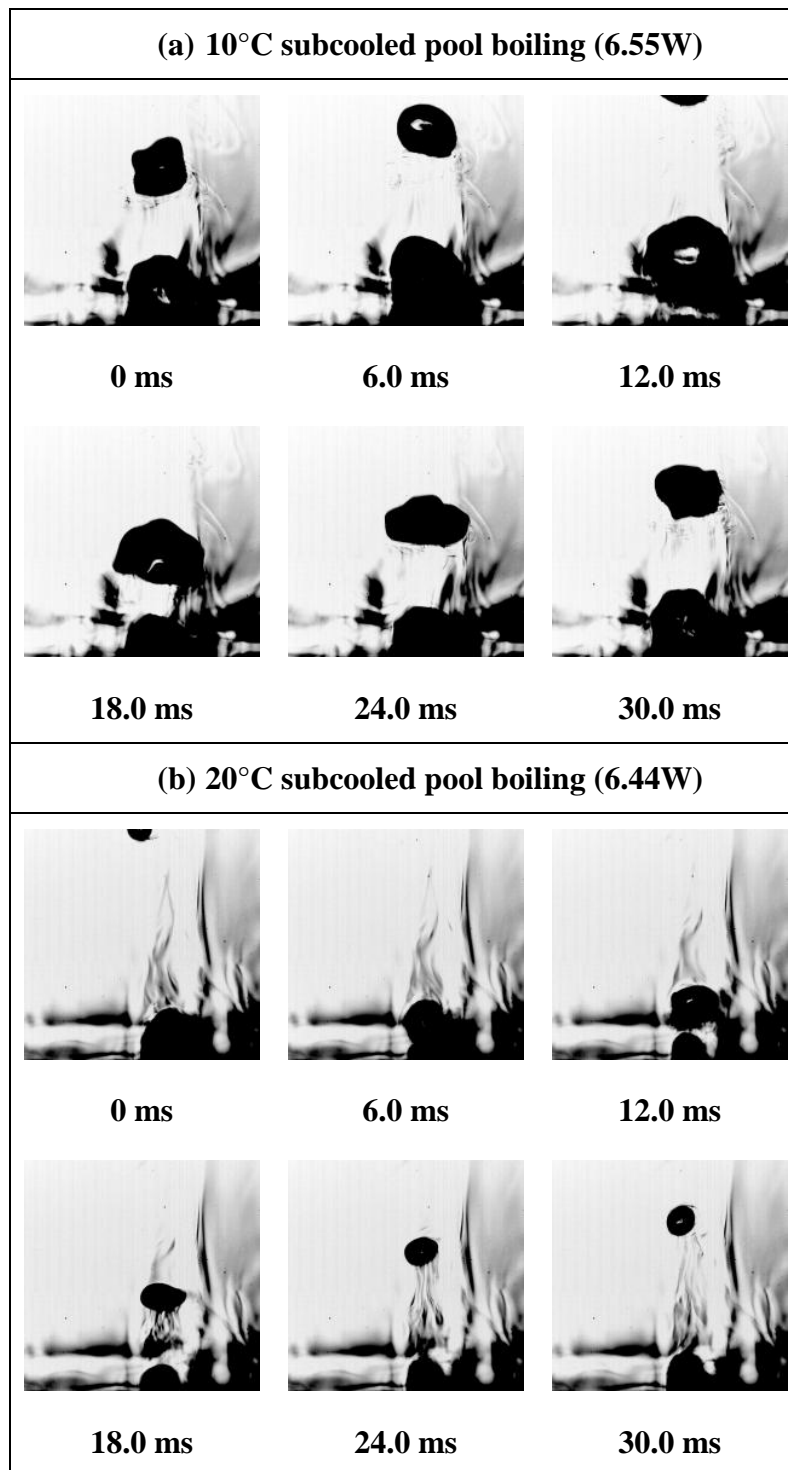


Figure 80: Visualization time series of a bubbling event at $\sim 6.5\text{W}$ during (a) 10°C and (b) 20°C subcooled pool boiling of FC-72

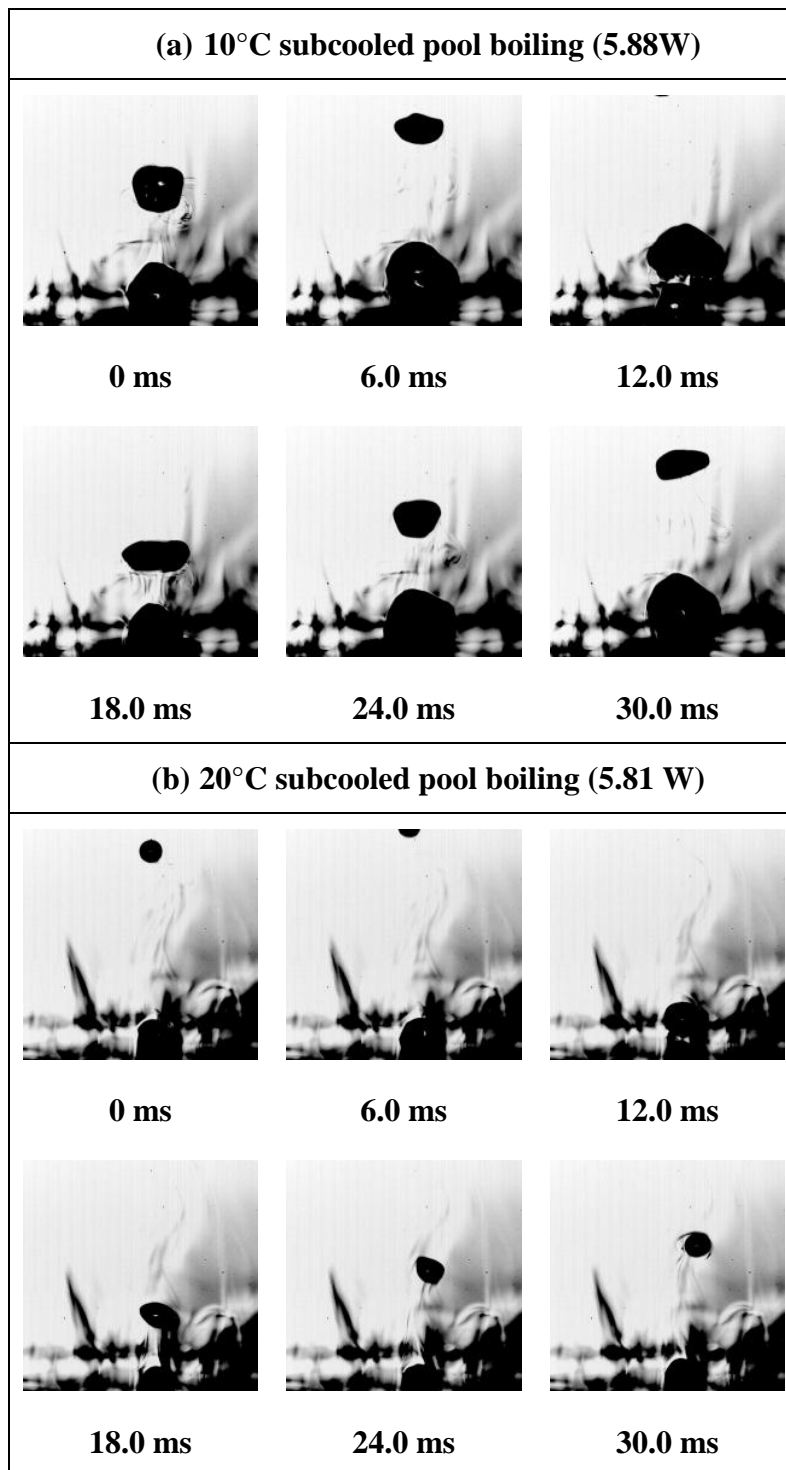


Figure 81: Visualization time series of a bubbling event at $\sim 5.8\text{W}$ during (a) 10°C and (b) 20°C subcooled pool boiling of FC-72

At both the power levels shown, a lower pool subcooling (Figs. 80a and 81a) resulted in bubbles of significantly larger dimensions than the corresponding higher subcooling (Figs. 80b and 81b). The average bubble departure diameters evaluated at the two power levels indicated that increasing the pool subcooling by a factor of two resulted in a reduction in bubble diameter by a factor of about 1.6.

For the larger bubbles at a low subcooling of 10°C (Figs. 80a and 81a), significant distortions were observed in the bubble shape during growth, departure and subsequent movement in the subcooled pool. The larger surface area of the bubbles resulted in a higher rate of condensation post departure as evident from the rapid shrinking of the bubble seen between 12-30 ms (Figs. 80a and 81a). Aided by surface tension, bubbles try to attain a spherical geometry as they rise (as seen in Fig. 80a).

The higher subcooling of 20°C (Figs. 80b and 81b) preferentially yielded bubbles of spherical contour during growth, departure and for the majority of the flow duration in the subcooled bulk. In comparison with the 10°C subcooling, minor geometric distortions were observed during the period of bubble rise. This can be attributed to the smaller surface area (due to an increase in the surface tension) resulting in lower condensation rates. From the convective flow patterns seen in these images (Figs. 80b and 81b) it is evident that the smaller bubbles in the highly subcooled case demonstrated a tendency to rotate about the horizontal axis. This indicates that post departure as bubble dimensions get smaller, Marangoni forces caused by local temperature gradients in the vicinity of the bubble gain dominance and influence the

bubble trajectory. On decreasing input power from ~6.5 W (Fig. 80) to ~5.8 W (Fig. 81), a corresponding decrease in the bubble dimensions was observed at both subcoolings. A drop in power by 0.67 W at 10°C subcooling induced a drop of about 152 μm on the evaluated average bubble departure diameter, while a drop of 0.63 W at 20°C subcooling affected a 113 μm reduction in the average departure diameter.

7.1.3 BUBBLE DEPARTURE CHARACTERISTICS DURING SUBCOOLED POOL BOILING

Quantitative results for bubble departure characteristics and latent heat transfer are presented in this section. At first the effects of pool subcooling on bubble departure diameter and departure frequency are discussed at fixed input power levels. This is followed with a discussion of trends observed for varying input power levels.

Figures 82 and 83 compare the time variance of the bubble diameters (D_b) and frequencies (f_d) at departure conditions at ~6.5 W and ~5.8 W for the two subcoolings tested. The frequency spectrum obtained from the thin film sensors corresponding to each test case are also shown for a comparison. The qualitative high speed images for these power levels were discussed in section 7.1.2.

Each data point in the bubble departure time series represents an individual bubble departure event (Figs. 82a, 82b, 83a and 83b). In general, the evaluated departure diameters showed reasonable consistency barring a couple of outliers. Table 6 lists the average bubble diameters at departure and the corresponding standard deviations for the cases depicted in Figs. 80-83.

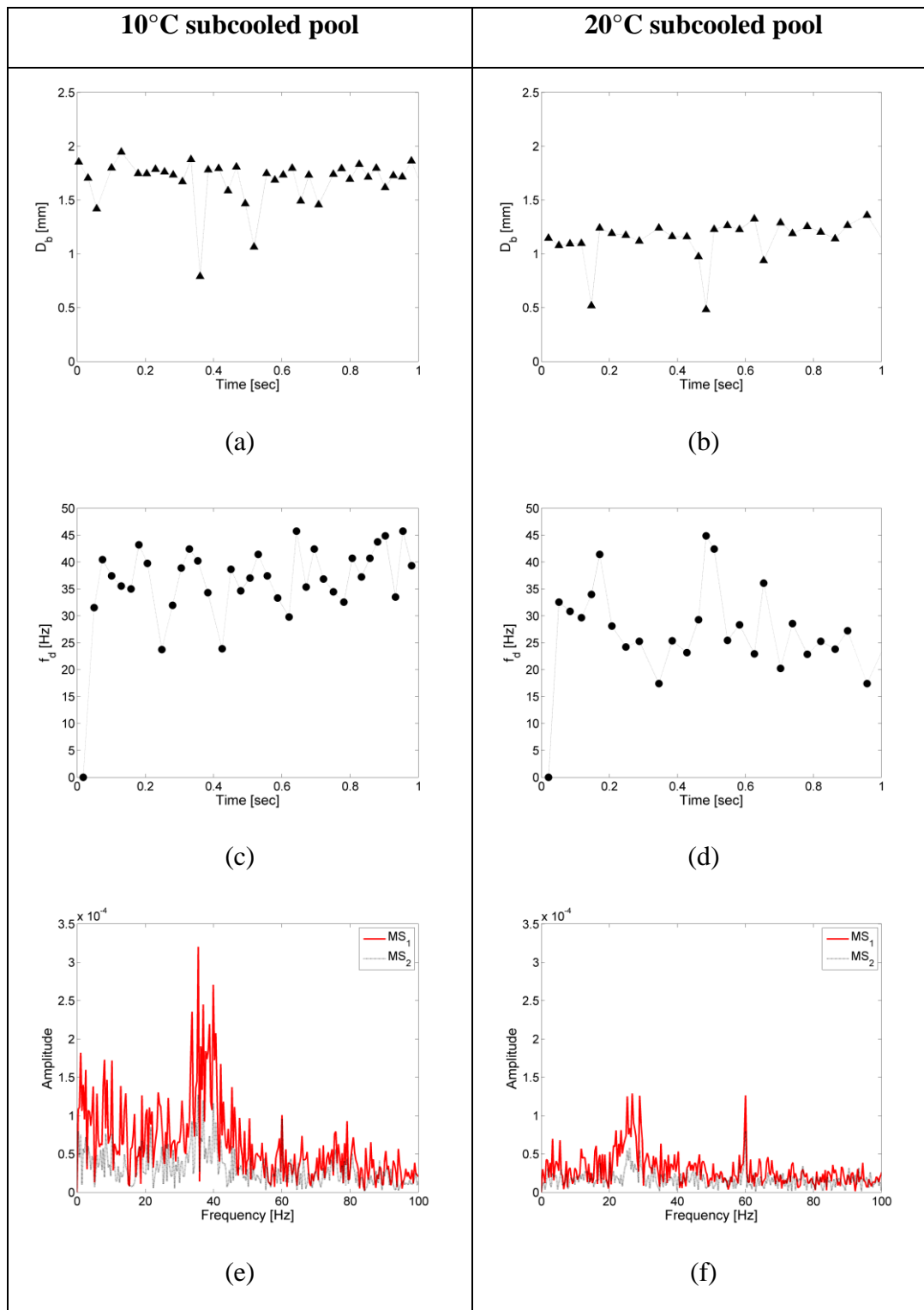


Figure 82: Time variation of bubble departure diameter and departure frequency at ~ 6.5 W during 10°C and 20°C subcooled pool boiling of FC-72

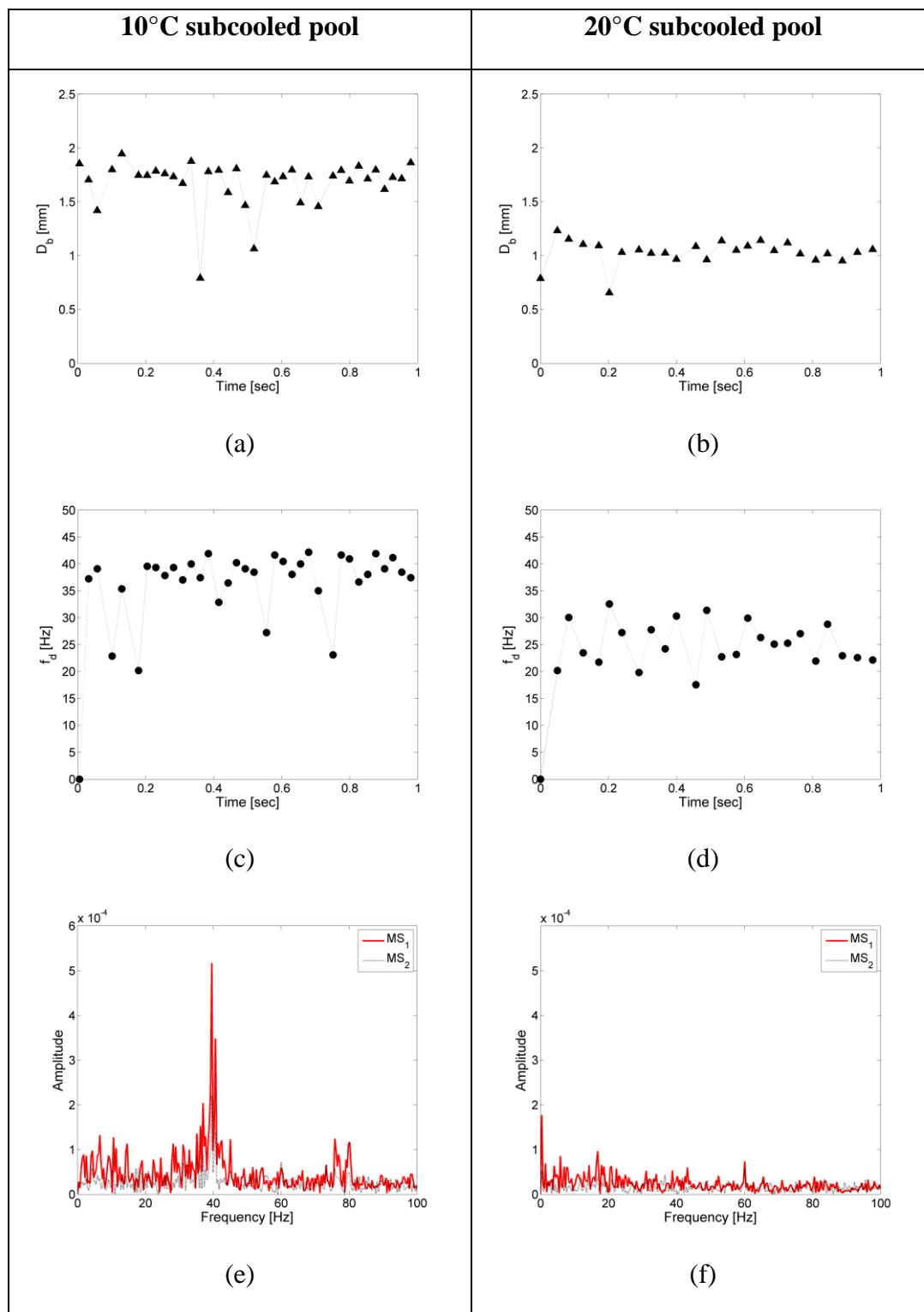


Figure 83: Time variation of bubble departure diameter and departure frequency at ~ 5.8 W during 10°C and 20°C subcooled pool boiling of FC-72

Table 6: Average bubble departure diameters and corresponding standard deviations for select cases during pool boiling

Power Input [W]	10°C subcooled pool		20°C subcooled pool	
	D_b [mm]	Standard Deviation [mm]	D_b [mm]	Standard Deviation [mm]
6.5 W	1.83	0.20	1.13	0.19
5.8 W	1.68	0.19	1.02	0.15

The evaluated diameters corroborate the visual observations discussed in the context of the qualitative images (Figs. 80- 81), which are (i) increasing the pool subcooling significantly reduced the resulting bubble dimensions at departure, and (ii) with decrease in power (over this limited range) the average bubble departure diameters were found to decrease irrespective of the subcooling.

In addition to the above findings it was observed that the low fluid subcooling test resulted in bubbles of diameters larger than the 1000 μm (1 mm) heater while the values of D_b at the higher subcooling of 20°C were comparable to the diameter of the heater over this limited range of input power. An investigation by Raj and Kim [52] on the heater size effect on bubble dimensions in FC-72 indicated that for heater lengths smaller than $\sim 2.1D_b$, pool boiling is dominated by surface tension as opposed to buoyancy. This implies that for heaters smaller than the bubble, the growth of the bubble would be limited by the heater allowing surface tension forces to dictate the bubble geometry. For heaters larger than the bubble they found the bubble geometry to

stretch vertically owing to increased evaporation. This criteria was validated by Raj and Kim [52] for fluid subcoolings up to 26.6°C. In the tests presented here such vertical stretching of bubbles was not observed confirming that we were indeed in the surface tension dominated mode owing to heater sizes smaller than the bubbles.

Figures 82c, 82d, 83c and 83d depict the time series of the frequency corresponding to the successive bubble departures shown in Figs. 82a, 82b, 83a and 83b. From the figures shown at both power levels it is evident that overall, the larger bubbles (corresponding to the low subcooling) yielded higher departure rates. The non-uniformly spaced bubble departures are reflected as notable fluctuations in the corresponding frequency time series. The average departure frequencies for the four test cases shown in Figs. 82c, 82d, 83c and 83d are listed in Table 7.

Table 7: Average bubble departure frequencies and corresponding standard deviations for select cases during pool boiling

Power Input [W]	10°C subcooled pool		20°C subcooled pool	
	f_d [Hz]	Standard Deviation [Hz]	f_d [Hz]	Standard Deviation [Hz]
6.5 W	37.4	5.2	27.8	7.0
5.8 W	37.5	4.3	25.4	4.2

Figs. 82e, 82f, 83e and 83f show the sensor-area-averaged frequency spectrums obtained from the thin film voltage sensors at the corresponding power levels. The signals acquired at the two power levels for 10°C subcooled test (Figs. 82e and 83e)

depict a distinct peak frequency of about 38 Hz which is in agreement with the mean frequencies obtained from the visualization data. The high amplitude corresponding to these peaks can be explained as an influence of the large bubble dimensions at this subcooling that leave a distinct signature at departure. In contrast, for the 20°C subcooled pool boiling (Figs. 82f and 83f) the peaks observed were not as amplified owing to the reduced bubble dimensions at departure. However, at 6.5W (Fig. 82f) a clear set of three peaks were observed at 28.93 Hz, 26.73 Hz, 25.27 Hz giving an average frequency of 27 Hz which is in support of the frequency attained from the high speed visualization. An additional peak was observed at 60 Hz which could be due to thermal fluctuations in the heater vicinity. This peak was found to recur at 5.8W (Fig. 83f) with reduced amplitude for the 20°C subcooled pool boiling test. At this heater power a small peak was observed at 17 Hz which was lower than the frequency of 25.4 Hz evaluated from the high speed images.

A quantitative assessment of the wall heat flux or the average surface superheat corresponding to the boiling conditions discussed above could not be made due to the technical issues faced with the IR image acquisition and subsequent analysis (see section 5.3.2 for details). However, the instantaneous calibrated temperature maps and radial temperature profiles can be used to make a comparative interpretation of the local superheat on the heated surface. Figures 84 and 85 show the instantaneous calibrated temperature maps and the corresponding radial temperature profile for the 10°C and 20°C subcoolings tested at the two power levels discussed in Figs. 80-83. The horizontal line across the IR maps represents the radial line along which the

temperature profiles were extracted. The horizontal red line along the temperature profiles indicates the saturation temperature of the test fluid FC-72. High temperature peaks are observed on all maps and profiles shown corresponding to the heated sections of the heater depicted previously in Fig. 44. Thus, the peaks are a representation of the non-uniformity in the heating profile.

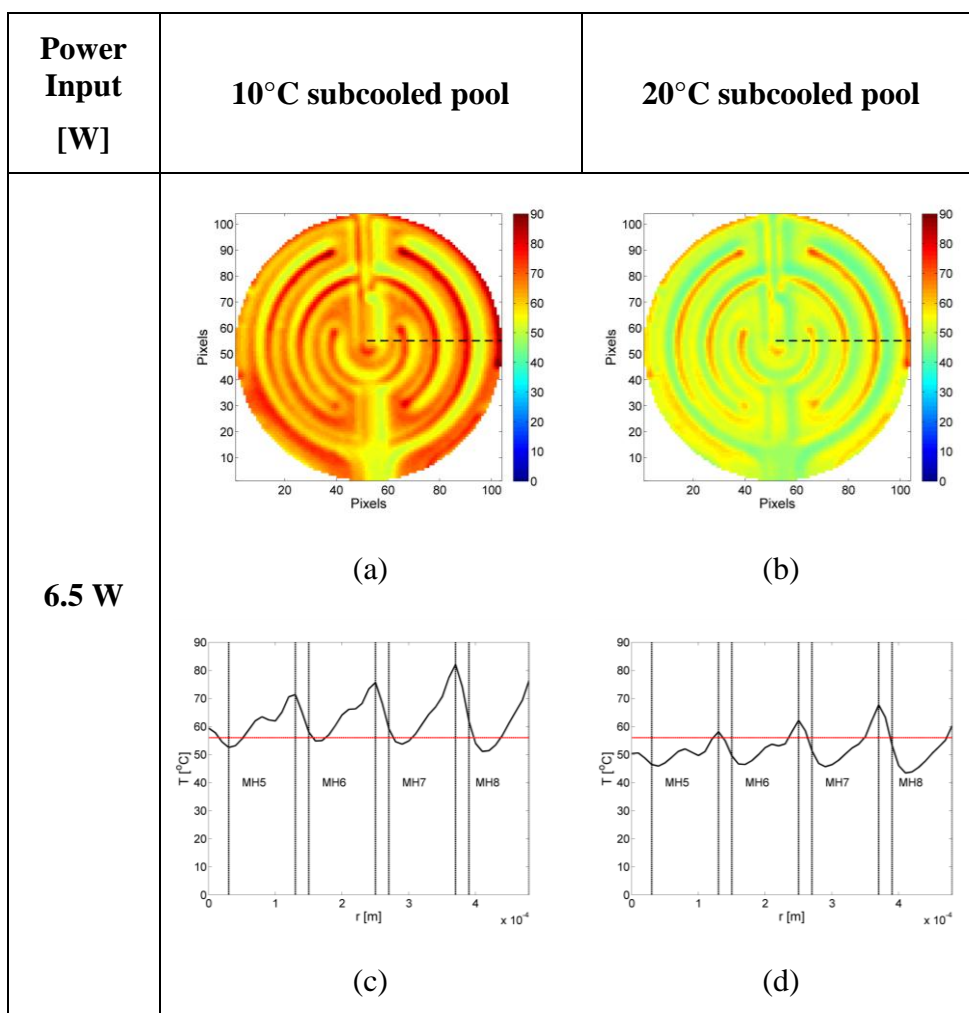


Figure 84: Instantaneous calibrated temperature maps and radial temperature profiles of the surface during subcooled pool boiling at 6.5 W

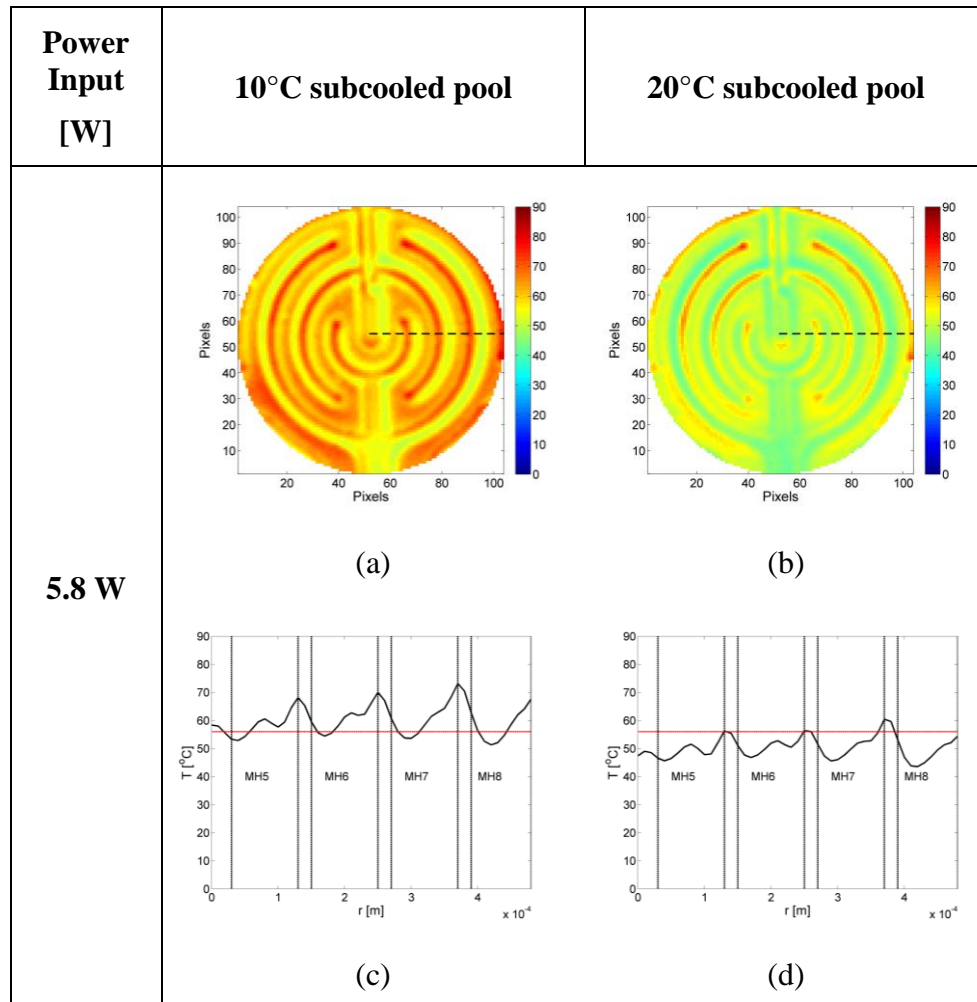


Figure 85: Instantaneous calibrated temperature maps and radial temperature profiles of the surface during subcooled pool boiling at 5.8 W

Additional spatial variations in temperature resulted as a consequence of the unwanted reflections captured by the camera (see section 5.3.2). As discussed in the description of the experimental set-up, no black paint was applied to the heater side for the microscale heater experiments and the heater was in direct contact with the fluid. Hence the regions intermediate to the heater sections represent a depth-weighted average fluid temperature.

The temperature profiles clearly indicate that select locations on the heated sections exceeded the fluid saturation temperature by an amount sufficient enough to sustain boiling. At a given power input the profiles for the 10°C subcooling demonstrated much higher superheats in comparison with the 20°C subcooling profile. For instance at 6.5W the 10°C subcooling profile (Fig. 84c) indicated local temperature peaks 18°C-25°C in excess of the saturation temperature, while the corresponding profile for the 20°C subcooling (Fig. 84d) showed temperature peaks in the range of 2°C-16°C in excess of the saturation temperature. A similar observation was made for a decrease in power to 5.8W where the 10°C subcooling profile (Fig. 85c) depicted peaks from 5°C-15°C above saturation while the 20°C subcooling profile (Fig. 85d) was merely a few degrees (3°C-5°C) over saturation at select locations. For the latter case (20°C subcooling at 5.8 W) several locations were noted to be below the fluid saturation and this corresponds to the last power level before the end of boiling activity on the surface for this test case. The reduction in power input was found to induce greater uniformity in the distribution of the temperature peaks for both tested subcoolings.

Trends in departure characteristics for varying input power levels

Figure 86 depicts the variation in bubble departure diameters with input power for the 10°C and 20°C subcoolings tested.

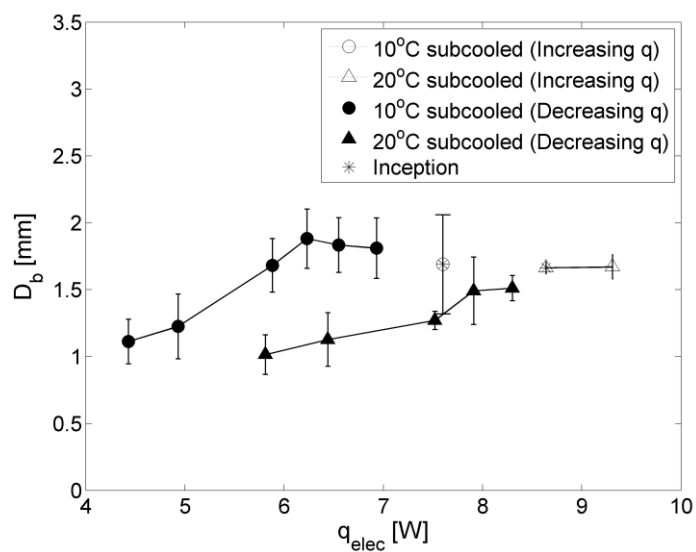


Figure 86: Variation in bubble departure diameters with input power during pool boiling with FC-72

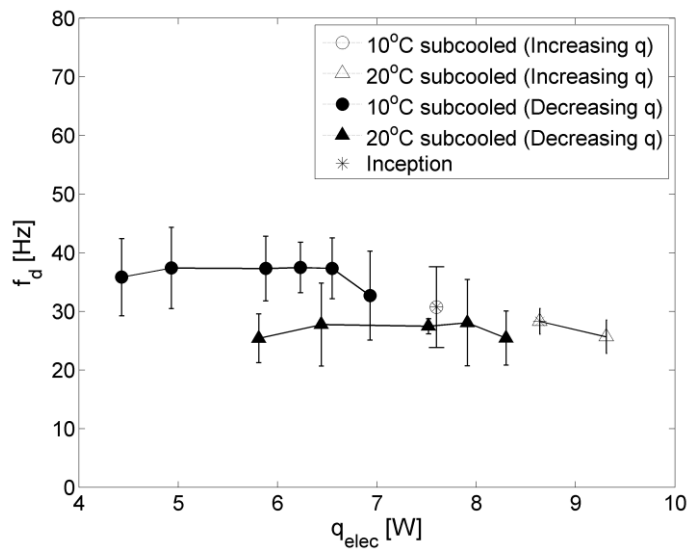


Figure 87: Variation in bubble departure frequency with input power during pool boiling with FC-72

Diameters are plotted for decreasing input power (filled symbols) conditions and select points (open symbols) for the increasing power beginning at inception. The departure frequencies corresponding to the D_b shown in Fig. 86 are plotted as a function of power input in Fig. 87. Each data point represents an average value at the specified power input over departures for a minimum of 20 successive bubbles. The standard deviation in the values is indicated by error bars.

Over the ranges of 4.4W-6.5W for the 10°C subcooled test and 5.4W-7.9W for the 20°C subcooled test, the diameter values at departure were found increase linearly with input power. The corresponding frequencies depicted consistent values (~ 37.3Hz at 10°C subcooling and 27.4 Hz for 20°C subcooling) independent of the change in input power. While the increase in departure diameter with increasing power is expected due to a corresponding increase in the wall superheat, the trends in departure frequency with increasing power have been in question in past literature. The power independence of frequency observed at low power levels in the present study are in line with the findings of Preckshot and Denny [42] who observed similar trends with CCl_4 on an indented copper surface. However, studies on single cavities such as that of Chang et al.[45] with FC-72 or Siedel et al. [44] with n-pentane have reported increasing frequencies with increasing wall superheat for bubbles in the isolated boiling regime during saturated pool boiling. For tests with saturated FC-72, Hutter et. al. [48] reported that their measured f_d attain a maximum limit for high superheats (greater than ~10°C).

Along a line of decreasing power input, the values of D_b (Fig. 86) were seen to be limited at an upper bound value. For the decreasing heat flux conditions, the maximum diameter value attained for the 10°C and 20°C subcoolings at departure were 1.9 mm and 1.5 mm respectively. The minor variation observed for the 10°C subcooled data above a power of 6.5W were within the range of deviation specified by the error bars. During 4°C and 15°C subcooled pool boiling studies of bubble ebullition on a quartz substrate Demiray and Kim [35] found bubble departure diameters to fall in the range of 0.37 to 0.5 mm. In comparison bubble diameters almost twice as large were observed in the present study.

The departure frequencies corresponding to the higher range of input power (above 6.5W for the 10°C subcooled test and above 7.9W for the 20°C subcooled test) were seen to decline. For their studies with FC-72 on a single cavity Chang et al.[45] found the decline of frequencies to occur at high wall superheats synchronously with vertical coalescence. Similar observations were made in the 10°C subcooled test conducted for this work.

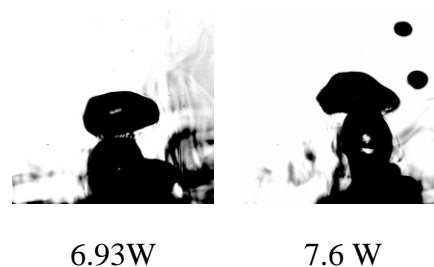


Figure 88: Vertical coalescence and multiple bubble generation observed at high power input (10°C subcooled pool boiling of FC-72)

Figure 88 shows snapshots of two bubbling instants during the 10°C subcooled pool boiling test where vertical coalescence occurred for a high power input. In addition to the coalescence, the high heat input resulted in the generation of multiple active nucleation sites and therefore multiple bubble events.

Among the few studies that have investigated bubble departure characteristics of FC-72 under subcooled conditions Moghaddam [85] reported $D_b \sim 0.64\text{-}0.74$ mm for a subcooling range of about 4-5°C during pool boiling on a silicon surface with a cylindrical cavity. The corresponding frequencies at departure were of the order of 130-146 Hz with the frequencies decreasing with increasing D_b .

A variety of correlations for predicting bubble departure diameters can be found in previous literature that account for the effects of parameters such as supplied heat flux, wall superheat, subcooling, liquid and vapor densities, and surface tension to name a few. A detailed list of these correlations are presented in Carey [54]. In the context of the present study, the effects of fluid subcooling, heat flux and wall superheat on the latent heat transfer are of primary interest. However, comparing the present data to these bubble diameter correlations would require the specific knowledge of wall superheat and/or the supplied heat flux. Since the quantitative assessment of these parameters from the collected data is currently ongoing and needs more work correlations for departure diameter are not compared here.

The relation between the departure diameter and departure frequency is another subject of keen interest to heat transfer studies as they are important for estimating the

latent heat transport by vapor bubble formation. An early relation proposed by Jacob and Fritz suggested that D_b is inversely proportional to f_d and their product remains constant. This was supported by the results of Moghaddam [85] during saturated pool boiling tests with FC-72 using a single cavity. For similar conditions Hutter [86] found the product of $f_d D_b$ to increase almost linearly with wall superheat. On similar lines Zuber's correlation [54] predicted that the product of $f_d D_b$ follows a constant relationship given by

$$f_d D_b = 0.59 \left[\frac{\sigma g (\rho_l - \rho_v)}{\rho_l^2} \right]^{(1/4)} \quad (20)$$

For the boiling conditions tested in this work, the values predicted by Eq. 20 are about 0.28 mm/s. The product of $f_d D_b$ obtained from the subcooled pool boiling results of the present study are shown in Fig. 89.

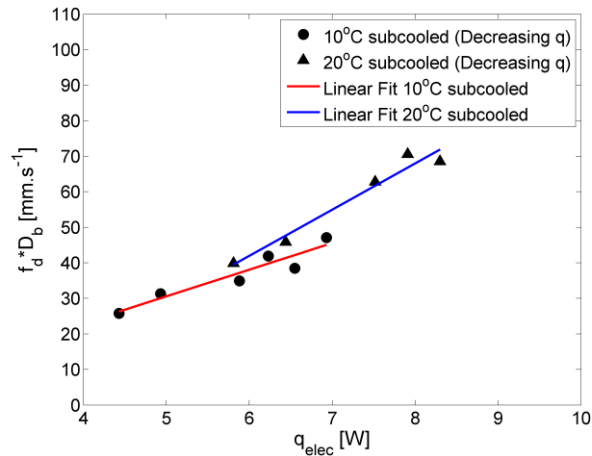


Figure 89: Variation in the product $f_d D_b$ with power during subcooled pool boiling of FC-72

The trends observed clearly depict that the product $f_d D_b$ varies almost linearly with increasing input power following the trends observed by Hutter [86] and is not a constant as predicted by Eq. 20.

7.1.4 LATENT HEAT CONTRIBUTION TO HEAT TRANSFER DURING POOL BOILING

The primary intent of the isolated bubble studies was to estimate and compare the latent heat transport from the surface due the generation and release of vapor bubbles for pool boiling versus jet impingement boiling. This evaporative heat transfer rate can be computed from the measure bubble departure characteristics using Eq. 21.

$$\dot{q}_{evap} = f_d \rho_v \left(\frac{1}{6} \pi D_b^3 \right) h_v \quad (21)$$

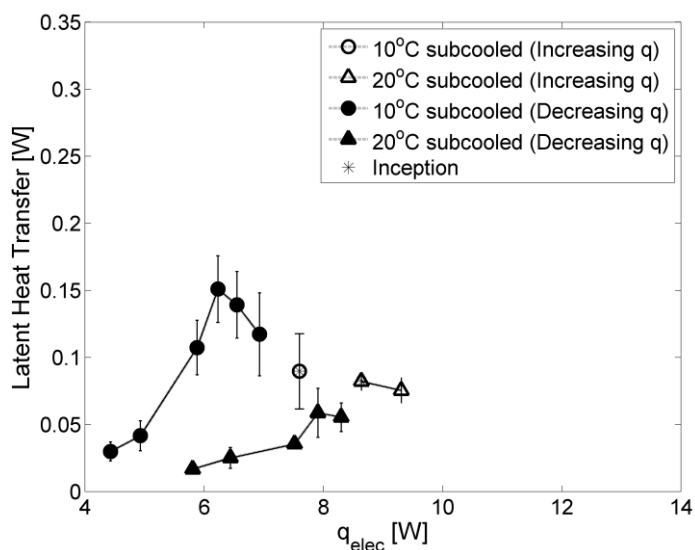


Figure 90: Latent heat contribution during subcooled pool boiling

The latent heat transport for the subcooled pool boiling tests conducted in this study are shown in Fig. 90 as a function of the input power. From the trends it is evident that evaporative heat transport increased along a line of increasing heat input corresponding to the increase in departure diameters observed earlier for these test cases in Fig. 86. The increase in latent heat transport for each case was seen to continue up to the point D_b reached its maximum limits and the f_d were almost constant. The maximum values of the latent heat transport obtained for the conducted tests were 0.15 W and 0.058 W for the 10°C and 20°C subcooled pool boiling conditions respectively. Evidently, owing to larger bubble diameters at departure and simultaneously larger f_d , the lower subcooling of 10°C achieved a higher evaporative heat transport. Corresponding with the saturation in bubble growth and decline in departure frequencies, the evaporative heat transfer rate was also seen to drop.

7.2 MICROSCALE INVESTIGATION OF JET IMPINGEMENT BOILING

In comparison with pool boiling, little attention has been paid to the effects of a forced convective jet flow on the bubble ebullition characteristics. The present study investigates the influence of a submerged jet flow on bubble ebullition characteristics within a subcooled pool of FC-72. Bubble ebullition is generated using the same 1000 μm serpentine heater geometry as used for the pool boiling studies discussed earlier in this chapter. Figure 91 shows a schematic of the flow configuration used for the microscale heater submerged jet impingement boiling tests.

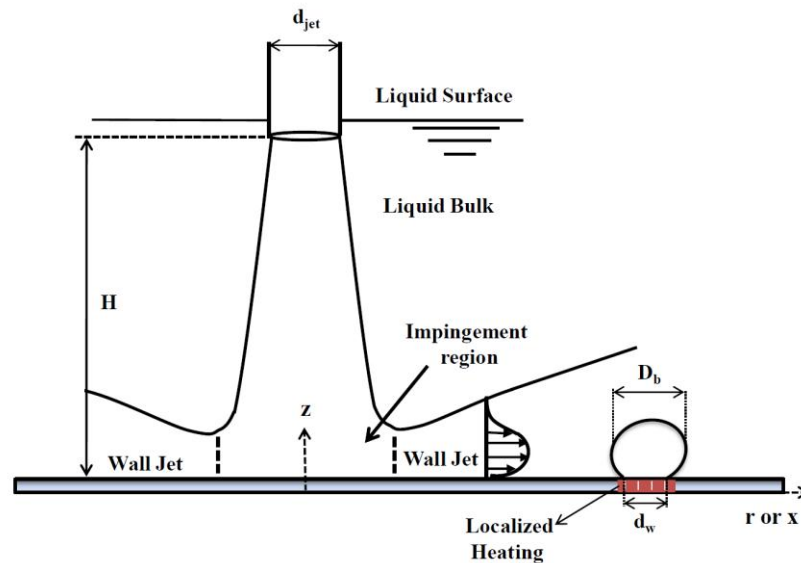


Figure 91: Schematic of the flow configuration used for the microscale investigation of jet impingement boiling (not to scale)

A jet nozzle of inner diameter 0.5 mm was positioned at a height of $6d_{jet}$ above the impingement surface. The microheater that simulated a local hot-spot was positioned at a fixed radial location of 1.5 mm ($3d_{jet}$) from the impingement point, along the path of the radial wall jet. Tests were conducted at a jet Reynolds number of about 3128 for pool subcoolings of 10°C and 20°C . Similar to the discussion for pool boiling, at first qualitative observations from the visualization of the SJIB tests are discussed followed with description of the bubble departure characteristics and latent heat transport in the presence of jet flow. Finally, comparisons of the heat transfer results from pool and jet impingement boiling are made to highlight the salient observations. All high speed images for SJIB were acquired with the same field of view (6.7 mm x 3.3 mm) for a physical comparison of bubble sizes. The images shown here for SJIB have been

cropped down to 4.9 mm x 2.7 mm (unless specified otherwise) to eliminate reflections on the silicon substrate.

7.2.1 INCEPTION OF BOILING IN THE PRESENCE OF JET FLOW

The net momentum force due to convection around a vapor bubble is typically considered as one among the various forces that determine the release geometry and generation frequency of vapor bubbles [66]. This momentum force gains significance in the presence of an impinging jet flow where the radially spreading wall jet encounters nucleation sites and vapor bubbles along its path.

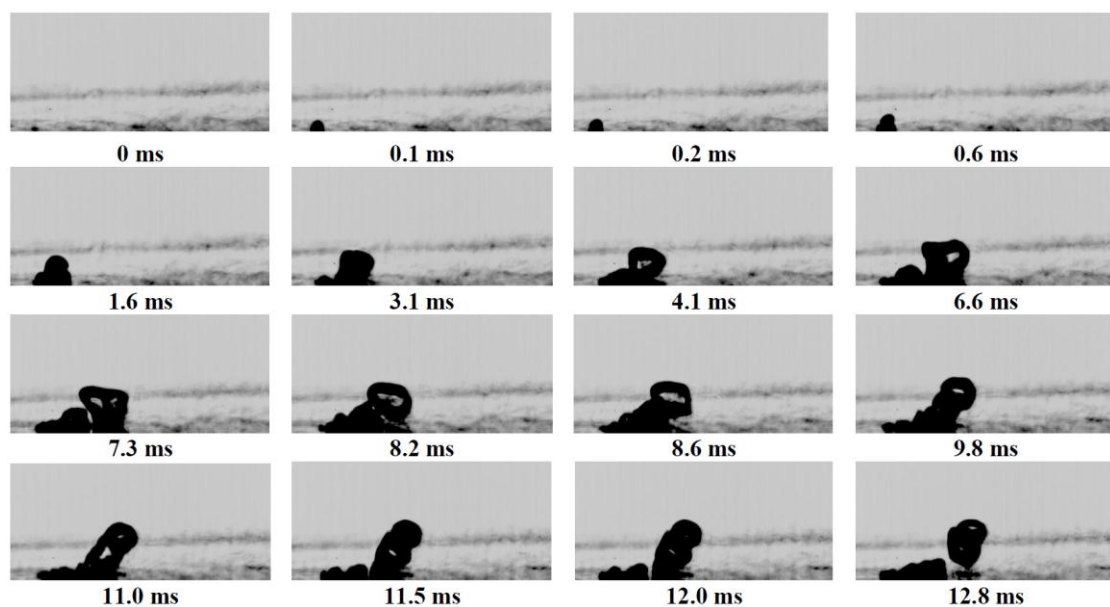


Figure 92: Inception of boiling for 10°C subcooled FC-72 in the wall jet region at a distance of 1.5 mm ($3d_{jet}$) from the impingement point (7.47 W)

Figure 92 depicts the inception of boiling in the presence of a forced convective jet flow during pool boiling for 10°C subcooled FC-72. Nucleation was initiated at a

single site on the heated surface in less than 0.1 ms as seen the images in the top row (left corner). An input power of 7.47 W was required to initiate boiling in this case. The bubble nucleus at 0.6 ms was observed to be much smaller in size compared to that seen for pool boiling (Fig. 78) at an earlier time step of 0.29 ms during inception. This implies that the growth rate of the vapor bubble was significantly impeded due to condensation. The role of the subcooled pool in limiting the thermal boundary layer thickness in the vicinity of the growing bubble was discussed in the context of pool boiling. The addition of a subcooled jet flow along the heated surface is expected to exaggerate this effect by severely thinning down the the thermal layer. As an estimate the thermal layer thickness evaluated for a SJIB test with FC-72 at a higher Re_{jet} of 5161 was about 0.02 mm. This would be an under estimated thickness as the Re_{jet} used in these microscale heater tests is much lower (~ 3128). However since previous macroscale heater tests with FC-72 were not conducted at this low Re_{jet} an exact estimate of the boundary layer thickness could not be provided. As a result of the reduced thickness of the thermal layer, condensation of the growing vapor bubble by the subcooled bulk was much more enhanced during the SJIB than for pool boiling.

As an additional effect of jet flow during boiling, the growing bubble was sheared to the right (Fig. 92, 0.6 ms to 4.1 ms) forced by the incoming wall jet (see configuration in Fig. 91). The restrictions imposed by the wall jet and the subcooled pool compelled the bubble to stretch along the length of the surface. Upon gaining sufficient volume and being additionally pushed by the wall jet, the bubble laterally separated from the source along the wall and subsequently attempted to lift-off from the surface (Fig. 92,

7.3 ms-8.2 ms) due to buoyancy. At this stage the forces of surface tension were seen to play an important role in retracting and reattaching the departing bubble to the source as seen in the image at 8.2 ms. This implies that surface tension can exceed the momentum forces exerted by the jet. The reattachment resulted in the formation and subsequent growth of a vapor slug at the source location (Fig. 92, 8.6 ms). The elongation and simultaneous condensation by the subcooled bulk continues with the vapor slug angled to the right influenced by the jet flow up to about 11 ms. With sufficient volume gained, the slug was once again forced by the jet to separate from the source along the length of the wall leading to its final departure at 12.8 ms.

An important information gained by these images is that the cumulative effect of the jet momentum and surface tension may result in multiple separations (along the surface) and departures (from the surface) of the same bubble. This process in effect can contribute to a higher heat transfer rate during jet impingement boiling where each departure from the surface results in the transfer of some portion of heat to the ambient fluid.

For the higher subcooling of 20°C although the instant of inception was not captured on camera the images taken subsequently showed that the fluid subcooling and additional jet flow cause the bubbles to separate along the length of the wall with almost negligible bubble departures into the pool. An image of this condition is shown in Fig. 93. Inception occurred at 8.3W which was a higher input power than that required for 10°C SJIB.

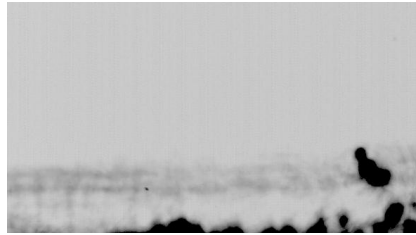


Figure 93: Image taken right after the inception of boiling for 20°C subcooled SJIB

7.2.2 *SJIB- BUBBLE DYNAMICS AND SUBCOOLING EFFECTS*

This section presents the qualitative effects of fluid subcooling and jet induced forced convection on the bubble geometry and dynamics during SJIB of FC-72. The qualitative observations are discussed at select input power levels with the acquired visualization results.

Figures 94 and 95 represent a series of snapshots during SJIB at input powers of ~10 W (during increasing power input) and 7.4 W (during decreasing power input) respectively for the two subcoolings of 10°C and 20°C tested. Images are shown at time intervals of 2.4 ms.

Subcooling effects on the bubble geometry followed similar trends to that of pool boiling (Figs. 80 and 81) wherein a lower pool subcooling (Figs. 94a and 95a) resulted in bubbles of significantly larger dimensions than the corresponding higher subcooling (Figs. 94b and 95b).

Significant differences in the bubble dynamics between pool and jet impingement boiling were observed as a result of the jet flow.

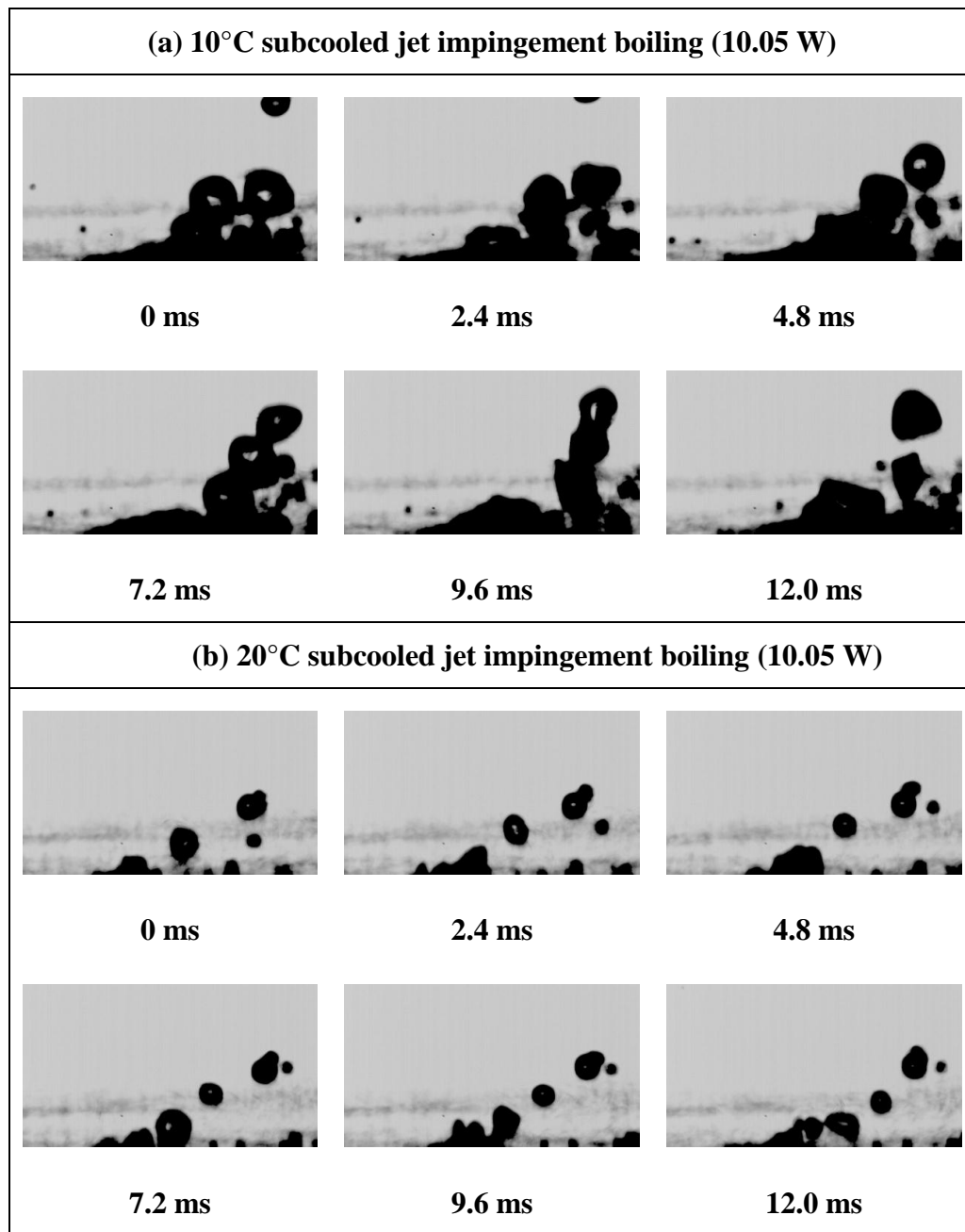


Figure 94: Visualization time series of a bubbling event at 10.05W during (a) 10°C and (b) 20°C subcooled submerged jet impingement boiling of FC-72

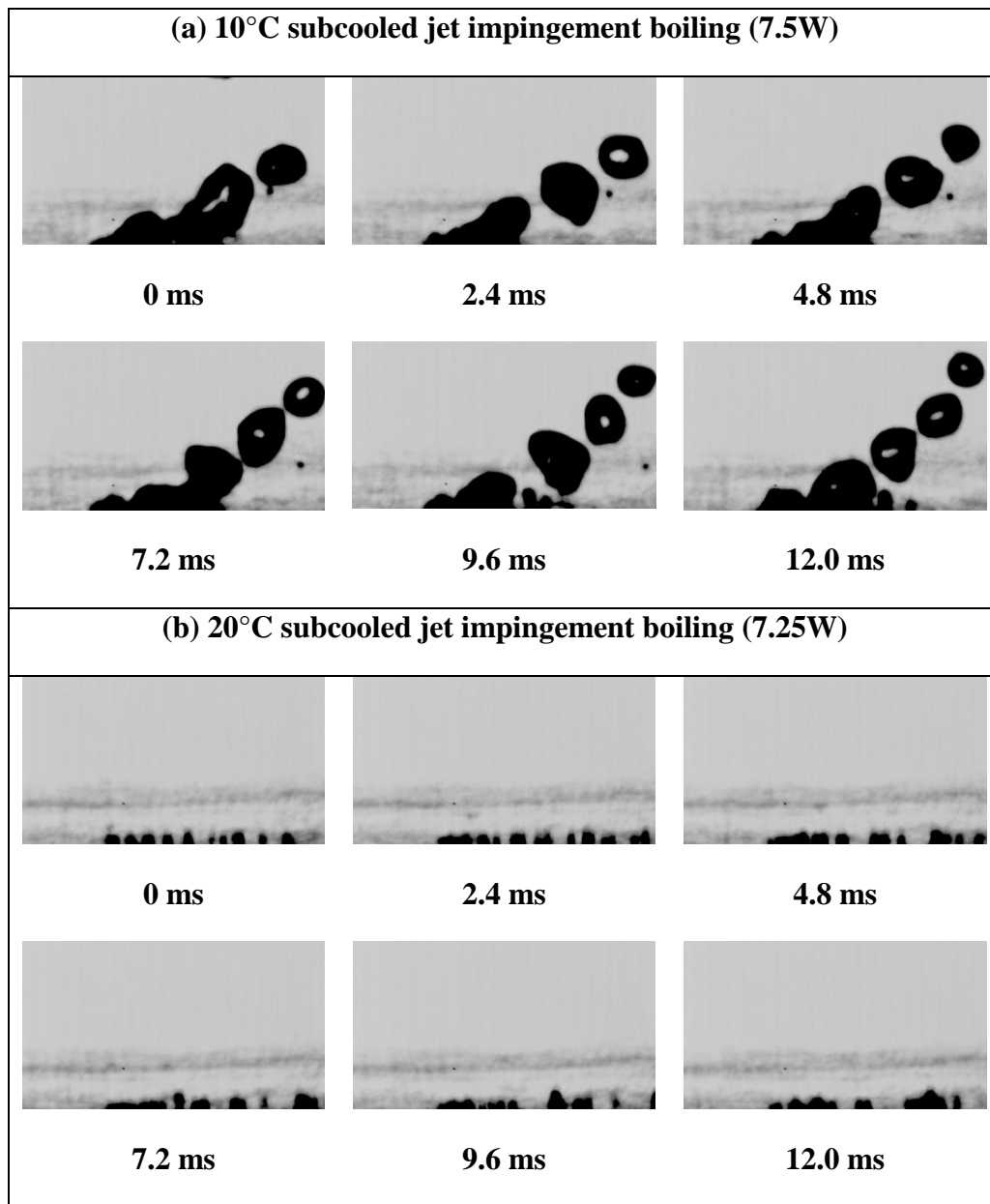


Figure 95: Visualization time series of a bubbling event at $\sim 7.4\text{W}$ during (a) 10°C and (b) 20°C subcooled submerged jet impingement boiling of FC-72

The first most evident difference observed from the visualization was that the jet flow caused the bubbles to grow and depart from a location off-shifted from the original source. The incoming wall jet sheared the vapor growing at the source to a film along

the wall and thereby resulting in an off-shifted bubble growth. Directed by the jet flow patterns bubble growth and departure assume an angular direction as seen in Figs. 94a, 94b and 95a.

The second important observation was the dual mechanism of bubble separation from the source, the first being the traditional departure from the heated surface, while the second was the lateral separation of miniscule bubbles along the length of the surface. These two mechanisms are very distinctly seen to coexist in Fig. 94b at a higher subcooling of 20°C. Notable differences in the range of bubble diameters was observed owing to fragmentation by the jet, coalescence with other bubbles in the pool or based on the mechanism of release from the source. The bubbles that depart were observed to be of much larger dimensions compared to the ones separated along the wall (example in Fig. 94b). The separated bubbles were found to maintain their miniscule sizes and no growth was found to occur along the surface post separation barring those due to later bubble mergers. The remainder of the surface gained heat by conduction within the substrate. This conducted heat was possibly just sufficient to create a thin thermal boundary layer along the surface wherein the miniscule separated bubbles retained their dimensions without collapsing from condensation (Fig. 94b, 95b).

Based on the largest observed departure diameters the average D_b at a high power input of 10.05W for 10°C SJIB was ~1.03 mm while that for a lower power of ~7.4W during decreasing heat flux conditions was ~ 1.02 mm. Thus, the change in power did

not affect the bubble departure diameters significantly. A comparison of the images during 10°C SJIB at the two power levels (Fig. 94a, 95a). At 10.05 W (Fig. 94a) shows that the high power was sufficient to result in substantial vapor slugs in both the angular and lateral (along the surface) directions. In contrast images at ~7.4W (Fig.95a) clearly depicts that the reduction in power almost eliminated any lateral bubble separation without altering the departing bubble dimensions at this 10°C low subcooling. In addition the departing bubbles were large enough to sustain shearing forces of the jet and prevent a transition to sliding along the wall. The average departure diameters evaluated from the angular detachment of the bubbles from the source slug is not much affected as a consequence.

For SJIB at a higher subcooling of 20°C the average D_b was about 0.57 mm (Fig. 94b). In this case the bubbles were much smaller due to condensation compared to the 10°C subcooled test. As a result, even at this high power of 10.05 W a steady stream of departing bubbles were seen to be forced along the wall (for example in Fig. 94b at 7.2 ms and 12 ms). Correspondingly, a decrease in power (Fig. 95b) had quite the contrasting effect compared to the low subcooling case. Bubbles departures from the surface were now completely eliminated and boiling was restricted to bubble separation and sliding along the wall (Fig. 95b). An assessment of separated sliding bubble diameters was not feasible owing to the image processing algorithm that currently removes objects attached to the wall to eliminate the source. To estimate these diameters further development of the image processing algorithm will be required in continuing studies. An example of the inability of the processing algorithm

to capture the diameters of the sliding bubbles is shown in Fig. 96. An additional complexity in obtaining bubble diameters for the jet cases was the simultaneous occurrence of angular departures and sliding bubble separation. As a result only the bubble departures from the surface were evaluated using the algorithm procedures described in section 5.4.2.

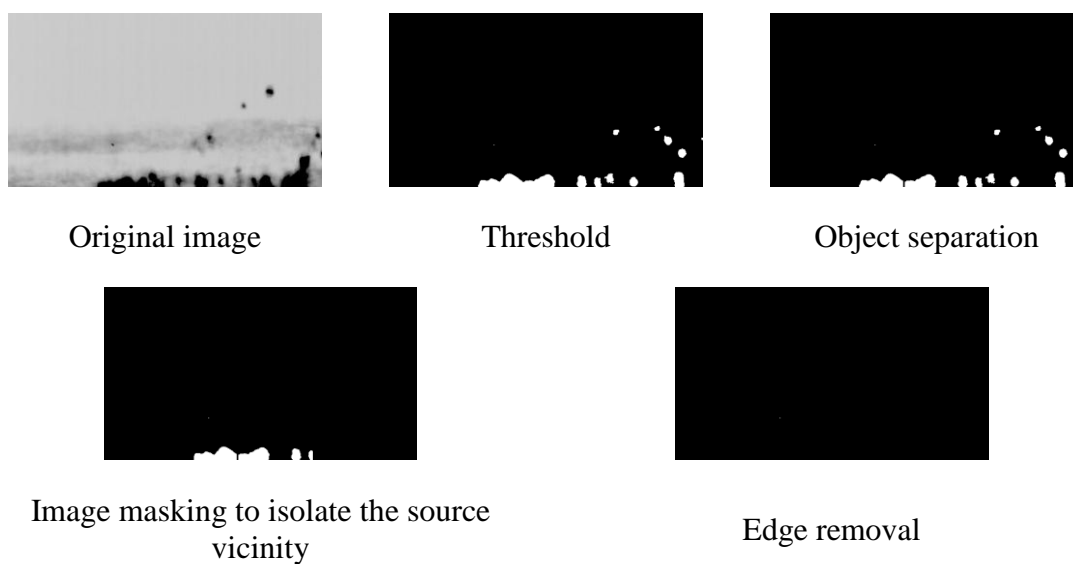


Figure 96: Inability of the image processing algorithm to determine sliding bubble diameters

Sliding bubble heat transfer is a subject of keen interest to two-phase heat transfer studies. The sliding action of bubbles has the scope to enhance the heat transport by providing an additional outlet for heat transfer between the surface and the fluid bulk besides phase change and natural /forced convection. Sliding bubbles in heat transfer have been investigated in previous literature during pool boiling [87] and reported during flow boiling in vertical channel [88]. The thermal fields under sliding bubbles

have been investigated using liquid crystal thermography by Kenning and Bustnes on inclined plates [89]. In this study the visualized sliding bubbles were generated during boiling heat transfer by a local hot-spot in combination with an impinging jet flow. Figure 97 depicts a magnified view of the visualization of sliding bubbles generated from the bubbling source and sheared along the surface by the incoming wall jet for the same case depicted in Fig. 95b.

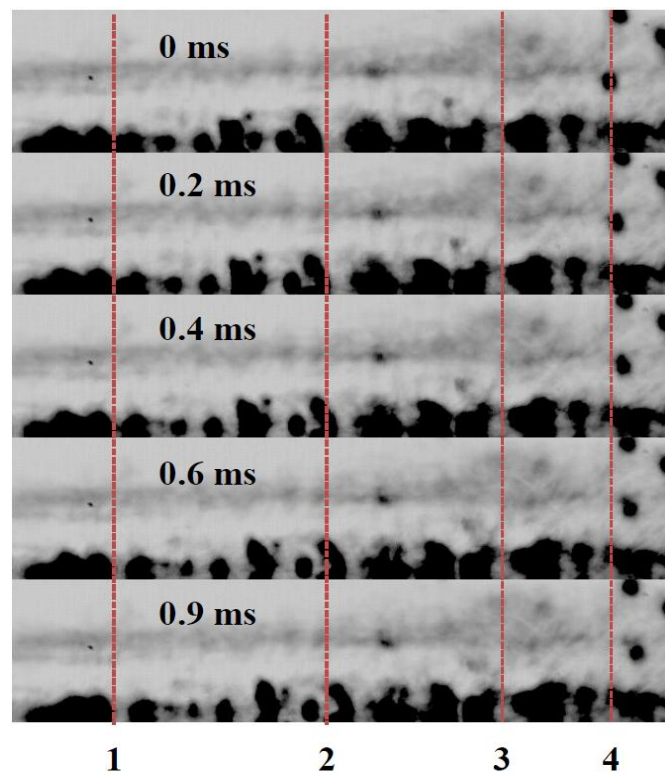


Figure 97: Visualization of sliding bubbles during SJIB at 7.25W (20°C subcooling).
Field of view (3.8 mm x 0.9 mm).

In this image series, the bubble source is located to the left. The edge of the source is indicated by the line marked at point 1. By following the line along point 1 it can be seen clearly that for this case bubble separation from the source occurs within 0.4 ms.

Bubbles generated are pushed along the wall by the jet flow. The shearing action of the jet can be observed along the line marked at point 2 where a taller bubble is caused to bend in a trying to balance the forces of surface tension and fluid momentum. Lines points 3 and 4 indicate that even at this distance from the source (~greater than 2 mm) and from the point of impingement (~ greater than 3.5 mm), the jet exerts a notable influence. Between point 3 and the right edge of the images, the transition of the jet flow direction is distinctly observed. Between points 3 and 4 bubbles continue sliding along the surface, while beyond point 4, the surface bubble is almost unaffected. However a rightward movement in the bubbles floating above the surface is observed. This indicates that from this point on the flow begins to turn upward in an attempt to recirculate.

Recirculation caused by the jet flow field can additionally contribute to heat transfer by entrainment of bubbles in the jet flow field. Figure 98 shows an example of entrainment of tiny bubbles in the jet flow. In these images the extremely small vapor bubbles are seen to lift-off from the surface under the influence of the jet flow and return towards the surface after an almost 360° recirculation with the jet flow. Similar entrainment was also observed for larger bubbles as shown in Fig. 99. The image series show a fairly large bubble return (left edge of the image) to the source location. The bubble impacts the surface and subsequently departs. Thus, mechanisms such as sliding and bubble entrainment induced by jet flow can significantly enhance heat transport in the isolated bubble boiling regime.

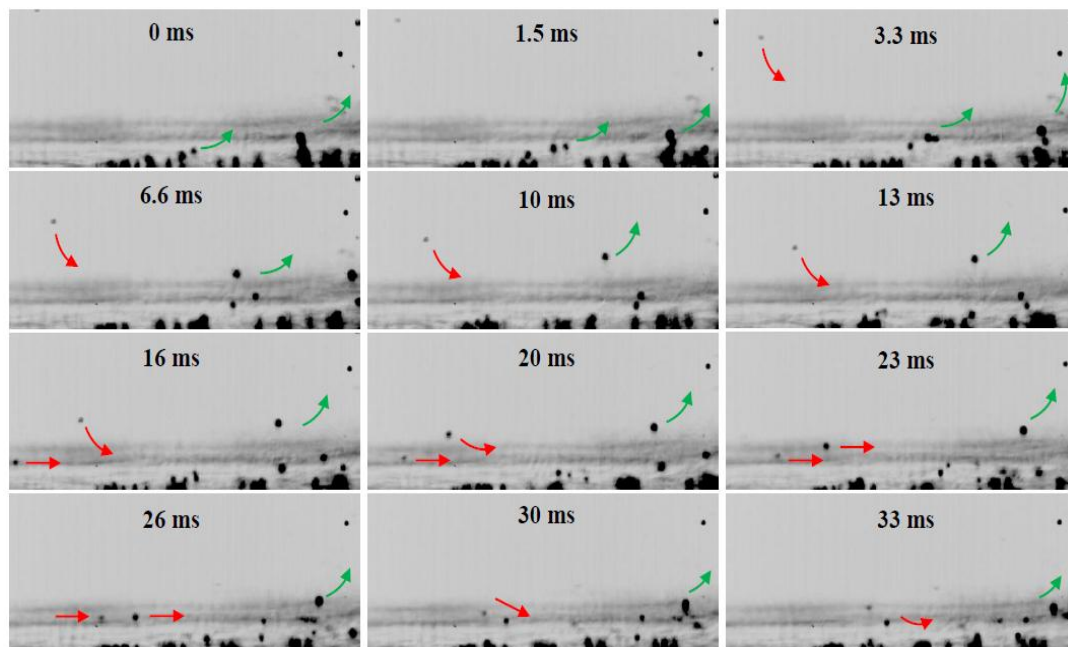


Figure 98: Entrainment and recirculation of small vapor bubbles in the jet flow field at 3.7W (10°C subcooled SJIB)

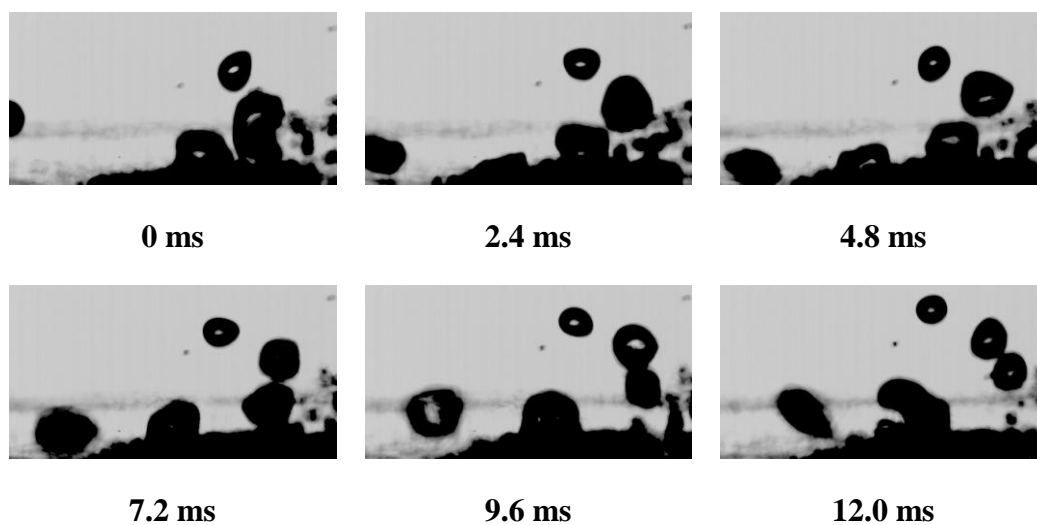


Figure 99: Entrainment of a large bubble in the jet flow field at 10.05W in 10°C subcooled SJIB

7.2.3 *BUBBLE DEPARTURE CHARACTERISTICS DURING SUBCOOLED SJIB*

Quantitative results for bubble departure characteristics and latent heat transfer during subcooled submerged jet impingement boiling are presented in this section. Bubble departure diameters and frequency variation with time and input power are discussed at select power levels followed with a discussion of trends observed for varying input power levels at fluid subcoolings of 10°C and 20°C.

Departure diameters during subcooled SJIB

As seen from the various images of the microscale SJIB phenomena (Figs. 94-99), boiling in the presence of a jet resulted in multiple bubbles in the vicinity of the source. The bubbles resulted as a cumulative effect of various factors such as entrainment, coalescence, and lateral bubble separation to name a few. In addition there were occasions of multiple departures at the same instant (Fig. 100) in the vicinity of the source where the departure diameters could be largely different.

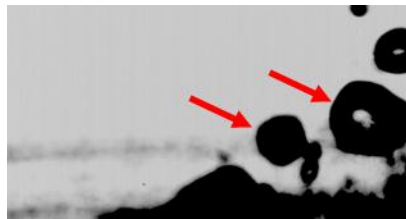


Figure 100: Example of multiple off-surface bubble departures in the vicinity of the source

An added effect of the jet was that departures occurred from a vapor slug sheared substantially by the jet. Hence the location of departures could vary in successive images. The above scenarios of SJIB added significant complexity to the image processing for SJIB. As a result of these issues only the largest bubble departure diameters measured at the steady state of each power level in the immediate vicinity of the source were used to interpret the departure characteristics.

Figure 101 shows the time variance of the maximum bubble departure diameters (D_b) during SJIB. The diameters are plotted at 10.05 W and ~8.5 W for the two subcoolings tested and represent the largest bubble diameters observed for the off-surface departures. The separation diameters of the sliding bubbles were not obtained as explained in Fig. 96.

At each power input (Fig. 101) a comparison of the D_b between the two subcoolings clearly depicts that a higher subcooling resulted in significant reduction of bubble dimensions at departure in comparison with the diameters seen for a low subcooling. For each power level, the average D_b was evaluated over a minimum of 20 largest bubbles. Table 8 lists the average values of D_b at select input power levels along with their corresponding standard deviation.

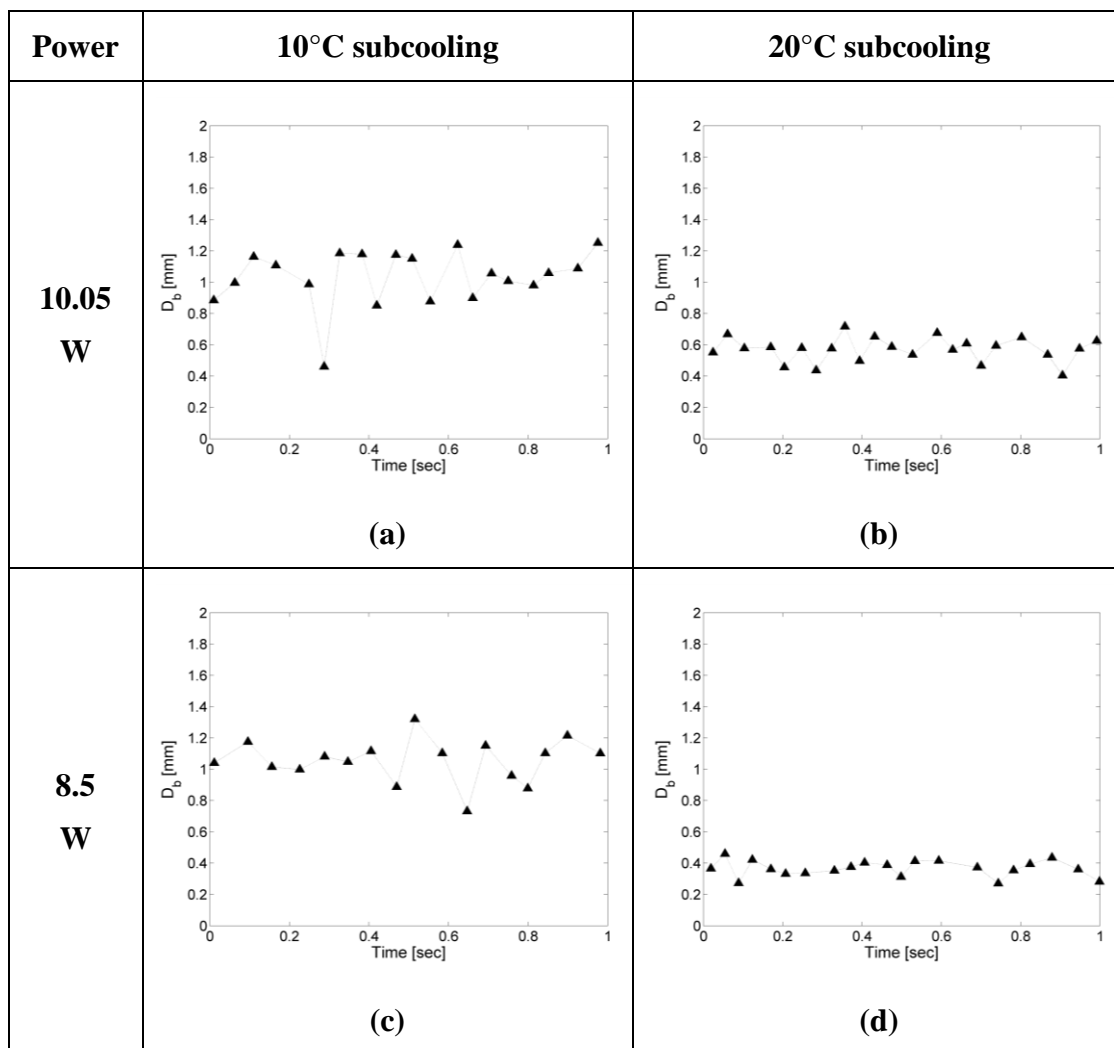


Figure 101: Time variation of bubble departure diameters at 10.05 W and 8.5 W during 10°C and 20°C subcooled SJIB of FC-72

From the evaluated D_b in Table 8, it is evident that the departure diameters at a 10°C subcooling were consistently higher than the corresponding 20°C subcooling values at all the three power levels shown. At 10.05 W, an increment in subcooling by a factor of 2 result in a reduction of D_b by a factor of 1.8. At a lower power level of 8.5W the D_b was reduced by a factor of 2.9. No value of D_b was obtained for the 20°C

subcooled case at ~7.4 W. As explained in Fig. 95 the boiling activity in this case was reduced to that of sliding bubbles and hence no off-surface bubble departures were observed in the vicinity of the source

Table 8: Average bubble departure diameters and corresponding standard deviations for select cases during SJIB

Power Input [W]	10°C subcooling		20°C subcooling	
	D_b [mm]	Standard Deviation [mm]	D_b [mm]	Standard Deviation [mm]
10.05 W	1.03	0.18	0.57	0.079
8.5 W	1.05	0.14	0.36	0.052
7.4 W	1.02	0.15	-	-

Reduction in power at 10°C subcooling had negligible effects on the D_b at these high power inputs indicating the bubble departure diameters had obtained their maximum attainable limit for the given fluid conditions. This scenario was depicted qualitatively in Figs. 94 and 95 where a reduction in power for this low subcooling ceased the generation of sliding bubbles without affecting the departure dimensions. In contrast for the higher subcooling of 20°C a reduction in power from 10.05W to 8.5 W resulted in D_b diminished by a factor of 1.47.

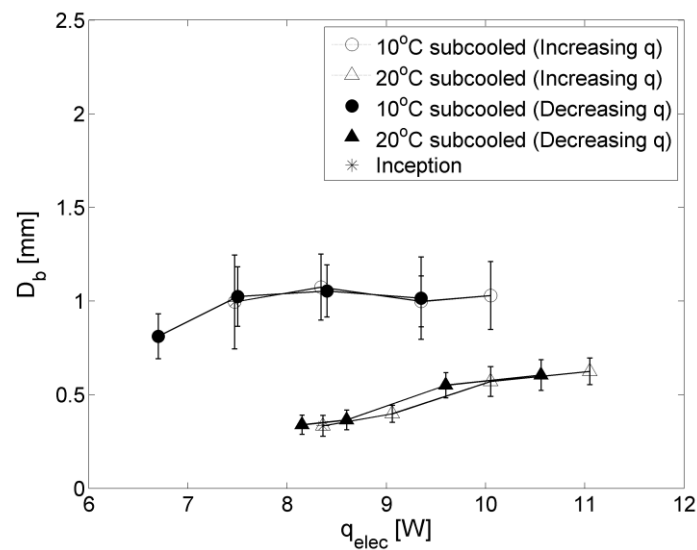


Figure 102: Variation in bubble departure diameters with input power during SJIB with FC-72

Figure 102 depicts the variation in largest observed bubble departure diameters with change in input power during subcooled SJIB. Trends observed in D_b during increasing input power conditions agreed well with those evaluated for decreasing power. The values obtained for corresponding increasing and decreasing power inputs were within 0.01-0.02 % of each other for the range of power inputs depicted in Fig. 102. In general, the bubble off-surface departure diameters were observed to increase at lower power levels and saturate at a maximum value for higher power inputs. The peak value in D_b with change in input power was attained for relatively lower power levels at a low subcooling of 10°C compared with the higher subcooling of 20°C. As previously discussed in the context of Table 8, the evaluated D_b were consistently

higher at a 10°C subcooling than the corresponding 20°C subcooling values at all power levels tested.

Departure frequencies during SJIB

Obtaining departure frequencies during SJIB was significant challenge owing to the same reasons as described earlier for bubble departure diameters (Fig. 100). Frequencies had to be obtained from the number of recorded departure diameters. However the complexity of having multiple simultaneous departure events limited the work here to reporting only the largest observed diameters at departure. In addition there were occasions of successive departures where the following bubble was smaller than the first or vice versa. In such a case, tracking the bubble diameters and assuming the bubble diameter at departure to be the maximum value before condensation in the bulk would be incorrect.

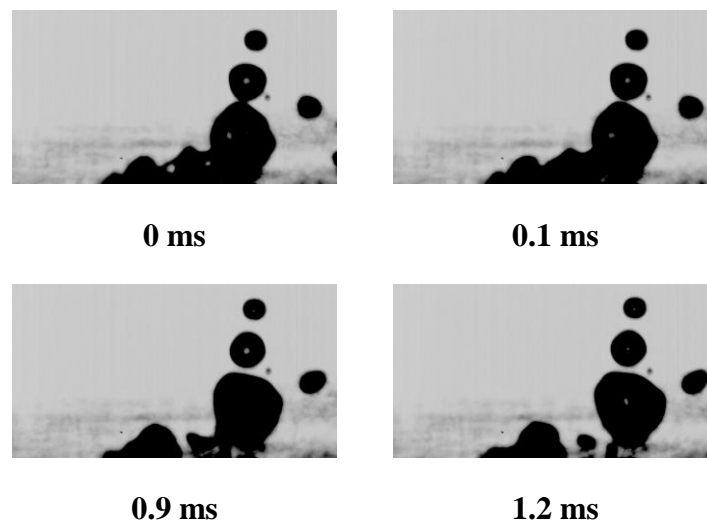
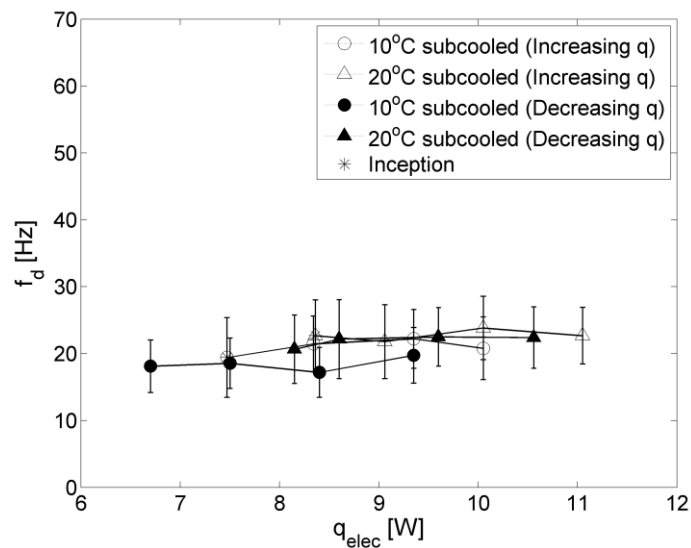


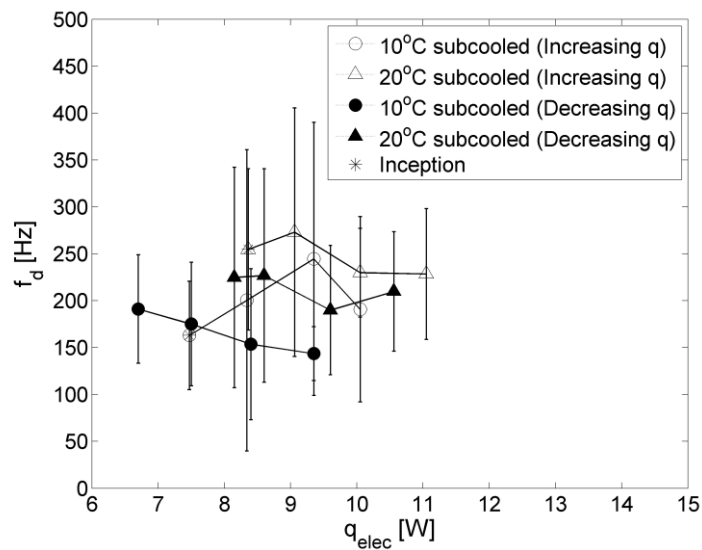
Figure 103: Example of successive bubble departures of widely different sizes during SJIB

Interpreting a frequency from only the largest observed diameters would clearly be an under prediction of the actual SJIB scenario where the jet flow enforces rapid fragmentation of the randomly sized vapor bubbles from the source as seen in Fig. 103. As an example, Fig. 104 compares the frequencies obtained from the image processing (Fig. 104a) of the largest departure diameters (plotted in Fig. 102) with frequencies evaluated from the manually counted bubble departures in (Fig. 104b). It is evident from the two plots that the frequencies evaluated by the two methods differ by an order of magnitude. The manually counted frequencies include the off-surface departures of a minimum of 15 bubbles of irrespective of diameter. As a result the manual frequencies are much higher and are a more realistic estimate of the actual boiling events during SJIB.

Irrespective of the method of frequency determination, no specific trends were observed in the variation of frequencies with change in input power. However the frequencies observed for the higher subcooling using either method appeared to be marginally larger than those determined for the lower subcooling. The standard deviations in the evaluated frequencies are plotted along with the data points as estimate of the variation in values at each power. The deviations observed for the manually counted frequencies (Fig. 104b) are significantly larger than those from the image processing algorithm (Fig. 104a). This is expected since the real-time departures were distributed over a wider range for bubbles of various sizes.



(a)



(b)

Figure 104: Variation in departure frequencies with power during SJIB (a) evaluated from largest departure diameters (b) evaluated by manual counting of bubble departures

It is feasible that at each power level, the net departure frequencies be classified as a summation of departure frequencies due to bubbles of distinct sizes. Such an approach for image processing is currently under investigation as part of this ongoing study. However some support of this idea might be gained by inspecting the frequency spectrum obtained from the sensor voltages for specific power levels of the jet impinging boiling tests. At first the voltage time series and frequency spectrum of a non-boiling test case for jet impingement was inspected. Figure 105 shows the filtered voltage time series and the corresponding filtered frequency spectrum for a 20°C subcooled SJIB test at a non-boiling power level of 0.1W. From the two plots it is obvious that no significant voltage fluctuations or peaks were observed at this low power level. Three minor peaks were observed in the frequency spectrum which might be the resultant of the forced convection due to the impinging jet flow.

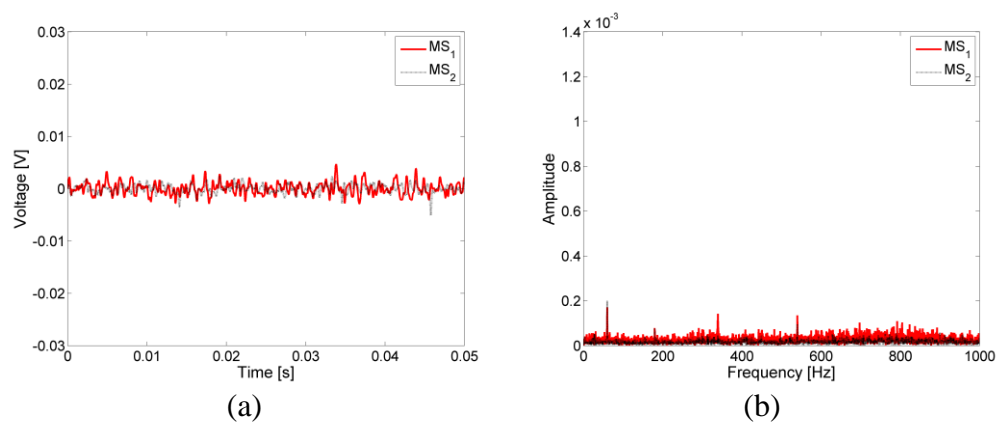


Figure 105: Voltage time series and FFT spectrum of a non-boiling power level (0.1 W) during 20°C subcooled SJIB test

Figure 106 shows the filtered FFT frequency spectrum obtained for the two fluid subcoolings during SJIB tests at power levels of 10.05 W and 8.5 W.

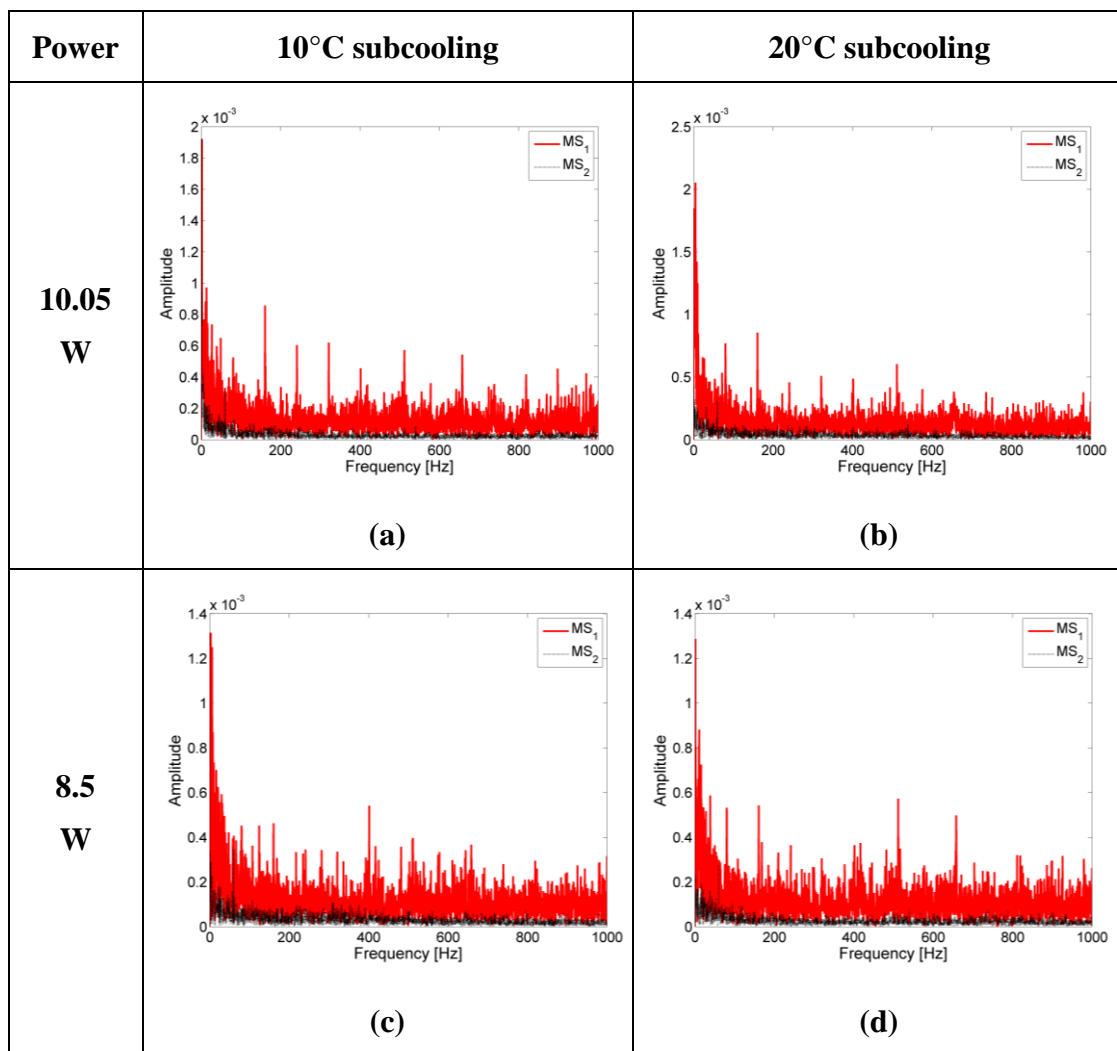


Figure 106: FFT spectrum of the sensor time series during SJIB

The frequency spectrum for all the four test conditions, clearly depict several dominant peaks in the range of 0-1000Hz which were not observed for lower non-boiling power levels (see example in Fig. 105). For both subcoolings, a clear drop is

observed in the peak magnitudes with the reduction in power. The peaks observed among all the four spectra shown in Fig. 106 are larger by an order of magnitude from those observed during bubble departures in pool boiling (Figs. 82 and 83). From the dominant frequency peaks observed in Fig. 106 it can be established that the manually counted departure frequencies shown in Fig. 104b indeed provide a more realistic estimate of the bubble departure frequencies during SJIB.

Surface temperature profiles

Figure 107 depicts the thermal maps and radial temperature profiles of the silicon microheater surface obtained during the subcooled SJIB tests at input power levels of 10.05W and 8.5W. The thermal maps for SJIB showed almost negligible effects of unwanted reflections.

The thermal maps and temperature profiles (Fig.107) show fairly uniform thermal distributions on the surface barring those resulting from the serpentine heater geometry. As for pool boiling, the line through the IR maps represents the radial line along which the temperature profile was extracted. The straight line through the temperature profiles reflects fluid saturation line.

Corresponding to the bubble diameters observed for these power levels (see Table 8) it was observed that the lower subcooling (Fig.107a,c) which had larger values of average D_b also depicted larger wall superheats. This observation was in agreement to that seen in pool boiling (Fig. 84).

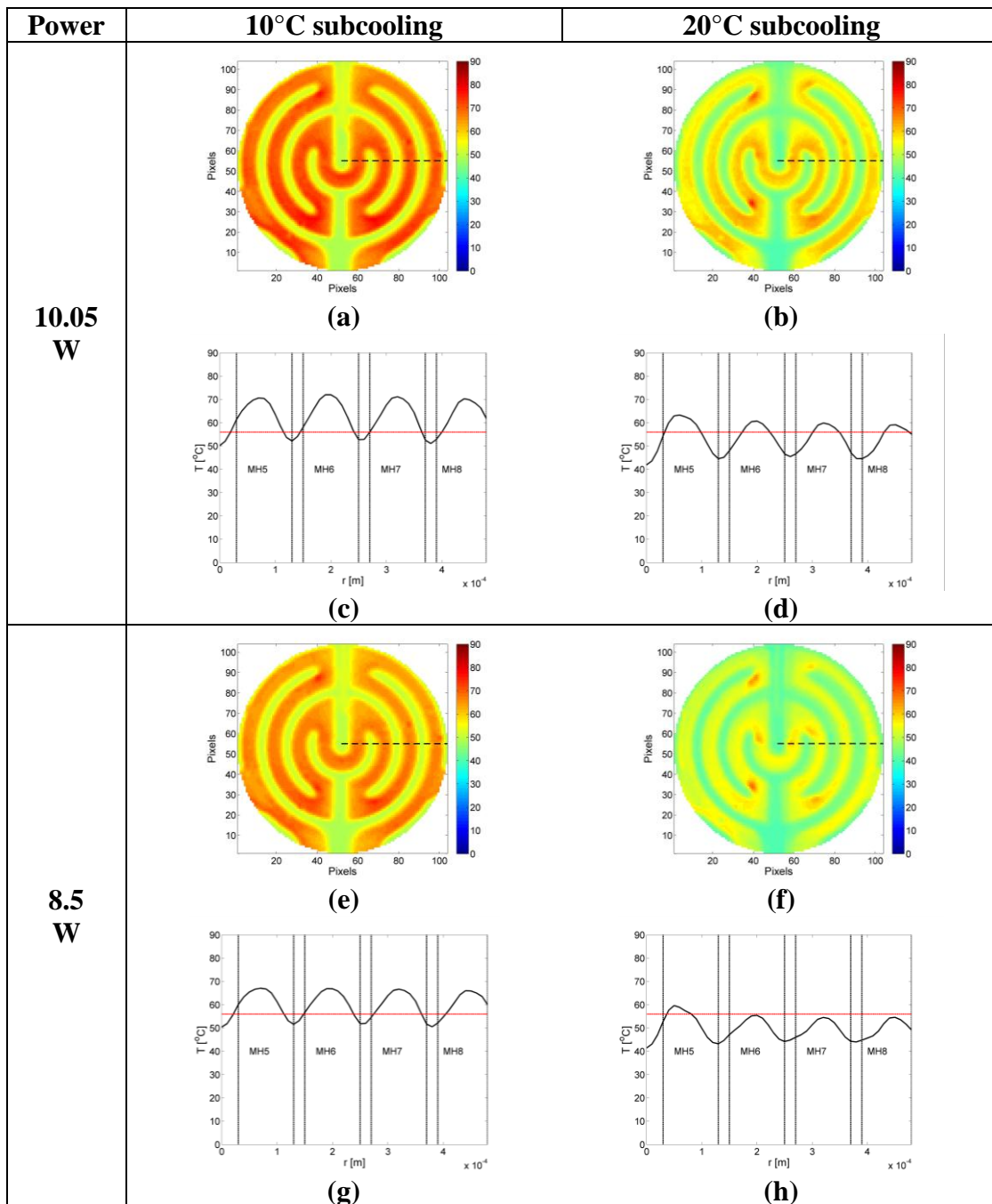


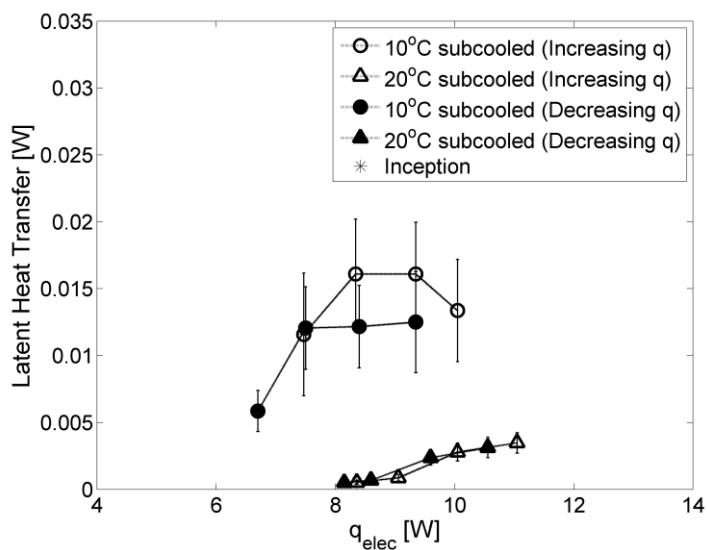
Figure 107: Instantaneous calibrated surface temperature maps and radial temperature profiles during SJIB

Superheats as high as 15°C were observed at all the on-heater locations for the low subcooling at 10.05 W (Fig.107a,c) while the higher subcooling showed a superheat of ~5-8°C at select locations on the heater regions (Fig.107b,d). A drop in power by 1.5 W caused a 5°C drop in superheats for the low subcooling (Fig.107c,g). The decrease in 1.5 W power at 20°C subcooling resulted in temperatures well below the saturation line (f) barring the heated region of MH5 which still retained a superheat of ~ 2-3°C (Fig.107h). However the thermal map (Fig. 107f) for the latter case shows local spots where temperatures are in excess of 70°C which are sufficient to sustain boiling at this power level.

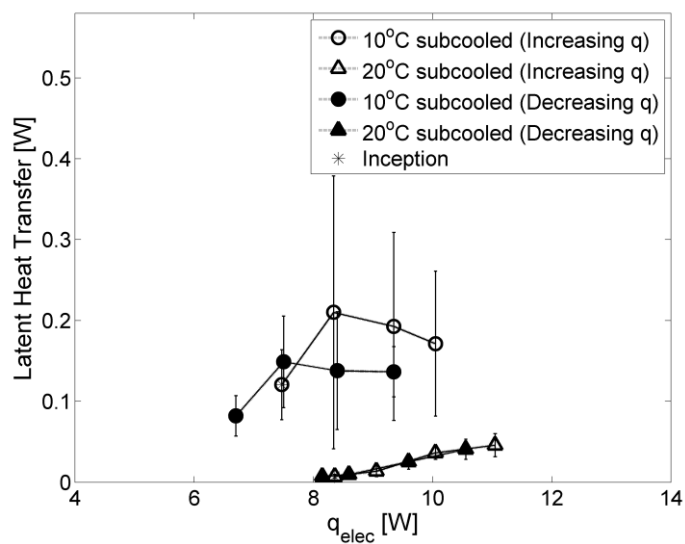
7.2.4 LATENT HEAT TRANSFER DURING SJIB

Figure 108 shows the two estimates of the latent heat transfer evaluated based on the two estimates of bubble departure frequencies discussed in Fig. 104 using the largest measured bubble diameters shown in Fig. 102.

While in Fig. 108a the used values of D_b and departure frequency correspond with each other, it has been established earlier in this section that these frequencies under predict the number of actual departures occurring on the surface. Hence the evaluated latent heat values in Fig. 108a are also an under estimation of total latent heat transfer rate. However this plot gives an estimate of the heat transfer resulting from the largest observed bubble departure for each of the tested heat flux and subcooling conditions.



(a)



(b)

Figure 108: Latent heat transfer estimates during SJIB (a) evaluated from largest departure diameters (b) evaluated by manual counting of bubble departures

In Fig. 108b the values of D_b and departure frequency used for calculating the latent heat transfer do not directly correspond with each other as the frequencies were obtained by manual counting of departures. These frequencies were shown previously to be much higher (by an order of magnitude) than those evaluated by the image processing. As a result the latent heat values shown in Fig. 108b over predict the evaporative heat transfer.

Based on the above reasons it is only appropriate to observe the qualitative trends in latent heat transfer with increase in input power. Qualitatively it is observed that irrespective of the method of frequency determination, the latent heat transfer contribution during the highly subcooled test increases with input power and approaches a limit guided by the plateau in departure diameters as seen in Fig. 102. The latent heat values for this high subcooling test were consistently lower than the corresponding values for the low subcooling. The latent heat estimates for the 10°C low subcooling test show a trend of increasing at low power input until a maximum limit is attained beyond which the heat transfer rate is seen to fall. The maximum limit for this case is again dictated by the limits attained by the bubble departure diameters as no significant change in departure frequencies was observed with change in power. The values obtained for the increasing and decreasing heat input were found to agree well for the high subcooling test, however large differences were observed in the computed values for the low subcooling at high power inputs.

7.3 POOL VERSUS JET IMPINGEMENT BOILING

This section revisits the major trends observed during the microscale investigations of subcooled pool and SJIB and highlights the salient differences between the two modes of heat transfer.

Inception

To begin with the inception of boiling with and without the presence of an impinging jet was captured at an identical subcooling of 10°C. Boiling initiated at a slightly higher power input of 7.47 W for SJIB compared to pool boiling which occurred at 6.9 W. In both cases boiling initiated at an isolated spot; however the progression of boiling thereafter was immensely impacted by the mode of convection prevalent in the ambient pool. Figure 109 compares a series of images for pool boiling and SJIB. The snapshot for both modes at ~1.6 ms clearly shows that at similar time span after inception the bubble growth rate for pool boiling was noticeably higher than that for SJIB. A major difference in the two modes of boiling was the location and direction of bubble departure. While bubbles always departed along the vertical for pool boiling (22 ms), the presence of a jet sheared the bubble to force departure at an angular direction (8.2 ms). The time stamps indicate that much shorter duration was required for a departure during SJIB.

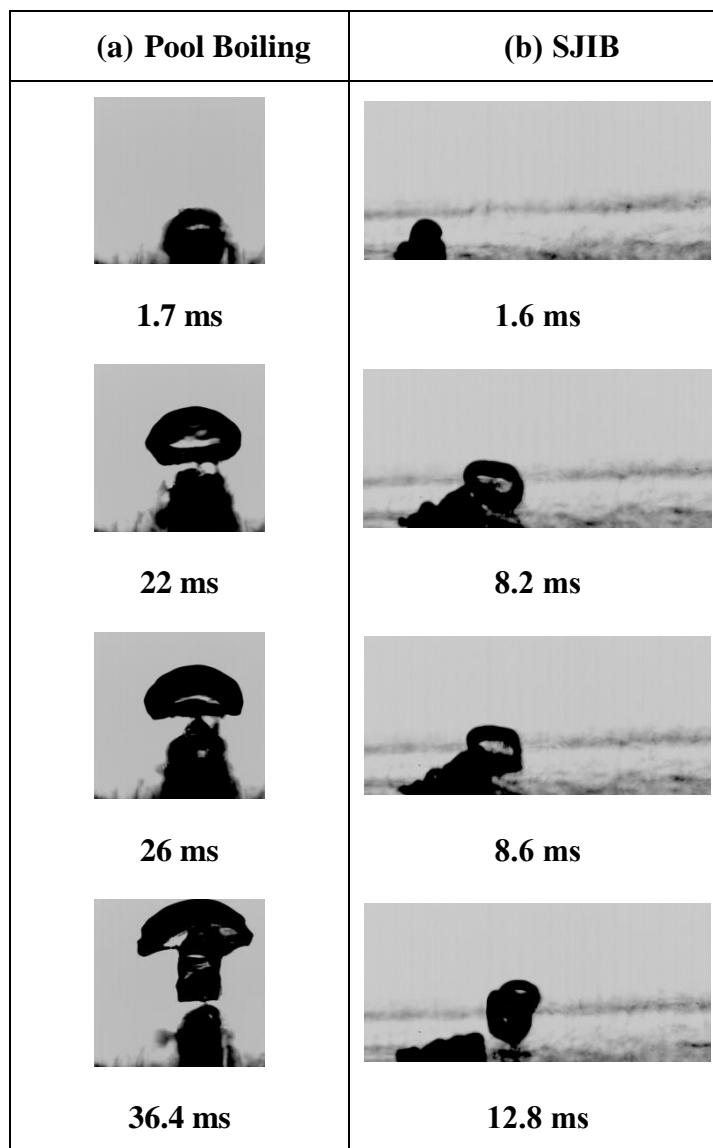


Figure 109: Pictographic comparison of boiling inception during pool and SJIB boiling at 10°C subcooling

Similarities observed in the two modes at this low subcooling included bubble coalescence and secondary departures of the initial bubbles post-merger. The bubble dimensions observed in SJIB are significantly smaller at all times during the ebullition

cycle indicating that bubble condensation was significantly enhanced due to forced convection.

Bubble departure mechanisms, characteristics and entrainment

Figure 110 depicts the distinct differences observed in the departure mechanisms for pool and SJIB.

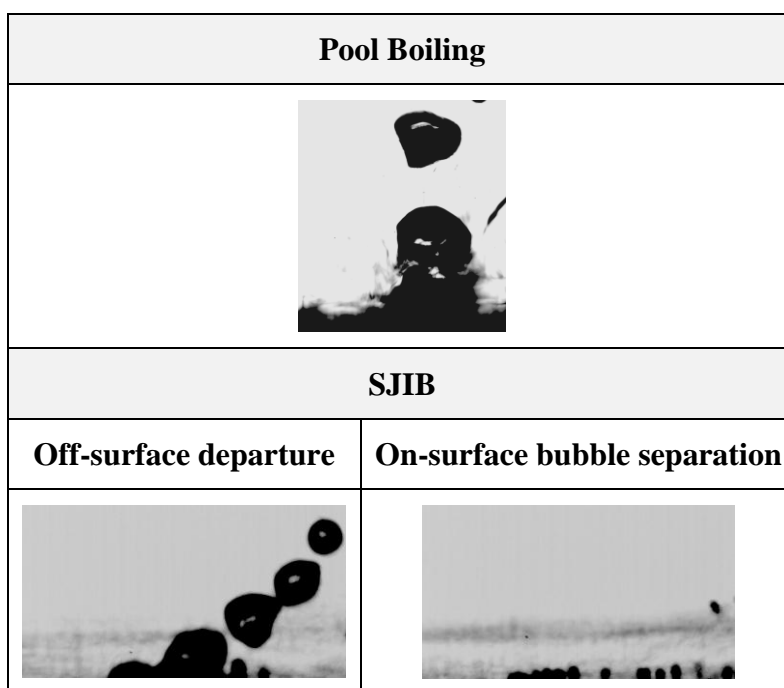


Figure 110: Departure mechanisms during pool boiling and SJIB

As mentioned earlier in pool boiling bubbles were seen to have a vertical direction of departure from the source on the surface. Bubble geometry in this case was found to be affected by forces due to buoyancy, surface tension, effects of peripheral condensation, local temperature gradients, and fluid motion caused by the growth and subsequent movement of the bubble itself. For SJIB all of the above forces acted in

addition to the fluid momentum imposed by the jet leading to enhanced condensation and significant shearing of the source. As a result of this jet inertia two modes bubble release from the source were observed. The first were off-surface departures similar to pool boiling but different in the direction of release. These off-surface departures were angled due to the momentum force of the jet. A second mode of bubble release was the separation of sliding bubbles that travelled along the heated surface. This mode of sliding bubble heat transfer was seen to co-exist with off-surface departures at high power levels while at low power levels and high subcooling they were found exist independent of off-surface departures as seen (Fig. 110).

In general, the departure diameters evaluated for both pool and SJIB increased with increasing input power at low power inputs but were found to saturate at a maximum value toward the higher input powers. The largest departure diameters evaluated from the high speed images for SJIB at fluid subcoolings of 10°C and 20°C were found to be smaller than that for the corresponding pool boiling tests by a factor of 1.6 and 2.3, respectively. No significant trends were noted in frequency with change in power especially for low power inputs. However a dip in frequency was noted at higher power inputs during both pool and SJIB which could be attributed to bubble coalescence at these higher heat inputs as reported in previous pool boiling literature [45]. While pool boiling departure frequencies were typically in the range of 35-45Hz an accurate assessment of the departure frequency during SJIB was not achieved owing to the simultaneous occurrence of multiple departure of widely varying diameters (see section 7.2.3). Frequency spectrum from the thin film sensors indicated

the existence of multiple dominant frequencies in the range of 0-1000 Hz with peak amplitudes higher than that observed during pool boiling. Irrespective of the fluid subcooling, the latent heat transfer rate achieved at a fixed input power from the off-surface bubble departures during SJIB was found to be smaller in comparison with pool boiling. At a subcooling of 20°C and a power input of 8.6 W, manual estimation of SJIB off-surface departure frequencies and the corresponding bubble departure diameters obtained from the code were used to obtain a realistic estimate of the latent heat transfer rate from departed bubbles during SJIB. The results indicated that the latent heat transfer rate obtained from pool boiling at a corresponding input power of 8.3 W and 20°C subcooling was as much as 1.5 times greater than that seen during SJIB. This can be attributed to the larger bubble diameters at departure during pool boiling.

An additional effect of jet inertia over pool boiling was the observation of bubble entrainment in the jet flow. This phenomenon was discussed for the entrainment of small and large bubbles in Figs. 98 and 99. It was shown through these images that recirculated bubbles can return to impact and re-depart from the surface. Such added mechanisms of bubble, surface and bulk fluid interaction have the potential to enhance the rate of heat transfer from the heated surface.

8 CONCLUSIONS AND FINAL REMARKS

The present chapter summarizes the salient results obtained from this study. This is followed with lists of the notable scientific and technological contributions and publications achieved from this work. In the end, recommendations are provided for future work.

8.1 SUMMARY

An experimental study for the local characterization of pool and submerged jet impingement boiling heat transfer was presented. The primary intent of the study was to highlight the importance of considering a local heat transfer analysis of boiling heat transfer schemes for applications in temperature sensitive electronics cooling.

Local variation in pool boiling heat transfer can result due to randomly distributed nucleation sites. The integration of forced convective flows such as that in a channel flow or in jet impingement can exaggerate the local variation in heat transfer rates due to involved hydrodynamics and consequent variation in surface and fluid temperature. For multi-chip electronics modules non-uniformities can also occur in the form of local hot-spots due to the local fluctuations in the surface temperatures or the heat flux.

To investigate the local differences in bubble dynamics and the resulting heat transfer rates in the above mentioned scenarios, qualitative and quantitative visualization

experiments of pool and submerged jet impingement boiling were conducted on a silicon surface. Two thin film serpentine heater geometries were designed and deposited on the silicon substrate to provide the heat flux required for phase change. The first was a macroscale heater (27.5 mm diameter heater with multiple nucleation sites) that highlighted the effect of spatial variations in imposed heat flux on boiling heat transfer by providing a circumferentially uniform but radially non-uniform heat flux distribution. The second was a microscale heater (using a 1000 μm heater for isolated bubble generation) that simulated boiling at a local hot-spot similar to that of a two-phase spot cooling on an electronic device.

The spatial non-uniformity of nucleation events for pool boiling versus jet impingement boiling was qualitatively depicted with high speed and IR thermal images of the boiling process on the macroscale heater substrate. Radial temperature profiles extracted from the IR thermal maps and PDFs of voltage drops obtained from thin film sensors quantitatively corroborated the non-uniformity of nucleation events in different sections of the heated surface.

A quantitative comparison between area-averaged and radially-local boiling curves was presented for experiments conducted with the macroscale heater substrate. A simple control volume analysis was established that accounted for axial conduction in the silicon substrate to evaluate the local convective heat fluxes corresponding to the local surface temperatures obtained from the IR maps. Area-averaged representation of the heat flux and temperatures were acquired by means of radially-weighted

average. As a validation of the evaluated convective heat fluxes, it was shown that the net input electrical heat flux varies within 4 to 10 percent of the area-averaged results. The inability of the area-averaged boiling curve to represent the spatial variations in boiling heat transfer was demonstrated by comparisons with the circumferentially-averaged local boiling curves at different radial locations on the surface.

Sectionally-averaged representations of boiling curves were presented wherein sections of like imposed heat flux were analyzed. It was shown that if the sections are chosen such that they contain similar boundary conditions and are relatively small, sectional averaging can adequately represent local trends for both pool boiling and jet impingement boiling. It was demonstrated in this work that such a sectionally-averaged heat transfer representation can substantially simplify the interpretation of data while retaining important information of local heat transfer variations over the heated surface.

A single circular submerged jet configuration was used to delineate the radial influence of the convective jet flow on boiling heat transfer for two liquid coolants with distinct thermo-physical properties, DI water and the dielectric FC-72 on the macroscale heater substrate. The distribution of wall superheats imposed by the impinging jet flow was illustrated by comparing radial temperature profiles during pool and jet impingement boiling. Qualitative and quantitative visualization images and sensor results were used to confirm that in contrast with pool boiling bubble nucleation initiated at the periphery of the heated surface during SJIB where the

influence of the jet momentum was minimal. With increasing heat flux, the boiling front was shown to progress inwards toward the point of jet impingement. The SJIB temperature profiles at locations corresponding with the boiling activity at a given flux were seen to merge with that for pool boiling. While no boiling hysteresis was observed for DI water, significant boiling hysteresis of FC-72 was documented under saturated and subcooled fluid conditions with results for increasing and decreasing heat flux conditions. It was demonstrated that in contrast with pool boiling, thermal overshoots during jet impingement boiling for a highly wetting fluid like FC-72 are highest in regions farthest from the impingement point. The proficiency of a passive self-cavitating jet nozzle geometry in eliminating the thermal overshoot in highly wetting fluids like FC-72 at all radial locations was established. The existence of self-cavitation with the modified nozzle geometry was verified under subcooled pool conditions.

Tests were conducted with the microscale heater substrate to comprehend the effects of jet inertia on bubble departure characteristics in the wall jet region. Pool boiling and SJIB experiments were conducted at 10°C and 20°C subcooled conditions for FC-72.

Boiling was generated at a 1000 μm locally heated spot located at a radial distance of three jet diameters (1.5 mm) from the point of jet impingement. Qualitative high speed visualization indicated the co-existence of two modes of bubble release during jet impingement boiling (a) off-surface bubble departures and (b) bubble separation from the source resulting in sliding bubbles over the surface. Additional differences

introduced by the jet flow on the ebullition processes between pool boiling and SJIB included significant reduction in bubble dimensions due to enhanced condensation, and angular direction of the off-surface bubble departures. Similarities observed in the ebullition processes between pool boiling and SJIB at a low subcooling included multiple departures of the same bubble due to the combined effects of bubble coalescence and surface tension, while at a high subcooling bubble dimensions were found to be notably smaller and bubble geometries were more spherical. The effect of jet flow on the entrainment of small and large bubbles was pictographically depicted.

Quantitative results indicated that bubble departure diameters for pool and jet impingement boiling increase and saturate at a maximum value with increasing power. At fixed subcoolings of 10°C and 20°C the largest departure diameters for jet impingement boiling were found to be smaller than the corresponding pool boiling test by a factor of 1.6 and 2.3, respectively. No notable trends were observed in the corresponding departure frequencies. However frequencies were noted to drop marginally at higher heat fluxes (especially for pool boiling) due to bubble coalescence. The simultaneous or successive occurrence of multiple bubble departures during SJIB, with largely disparate diameters posed severe complexity in obtaining accurate estimates for off-surface bubble departures. However upper and lower limit estimates of frequencies were obtained by accounting for the time spans between the largest bubble departures in the image processing and by manually counting the departures, respectively. The two methods of frequency estimation differed by an order of magnitude with the manually counted results being greater (in range of 150-

300 Hz). The frequency spectra obtained from the thin film sensor voltages clearly depicted multiple peaks in the frequency range of 0-1000 Hz confirming that the manually counted frequencies were more realistic estimates. Latent heat transfer rates were acquired for pool and jet impingement boiling from the evaluated bubble diameters and corresponding frequencies at departure. The general trends indicated that a lower subcooling resulted in a greater latent heat transport for both pool and SJIB while pool boiling displayed consistently higher latent heat transfer rates than SJIB at a given power and subcooling. For a fixed power level (~8.5 W) and at a subcooling of 36°C, pool boiling resulted in a 5.7 times larger latent heat transfer rate compared with SJIB rates evaluated based on the manually counted frequencies.

8.2 MAJOR CONTRIBUTIONS

The notable scientific and technological contributions from the work presented in this thesis are listed below.

- Characterization of spatial variation in boiling activity, temperature distribution and convective heat flux during pool and jet impingement boiling using high speed imaging, IR thermography and thin film voltage sensors
- Quantitative comparison of local, sectional and area averaged boiling curves
- Documentation of spatial non-uniformities in boiling heat transfer due to a non-uniform heat flux profile imposed by a serpentine heater geometry

- Qualitative and quantitative visualization of thermal overshoot and boiling hysteresis in dielectric FC-72 during jet impingement boiling
- Characterization of spatial variation in thermal overshoot and incipience superheats for FC-72 during saturated and subcooled pool and submerged jet impingement boiling
- Verification of local mitigation of thermal overshoot in FC-72 using a passive self-cavitating jet geometry
- Demonstration of isolated bubble ebullition in subcooled FC-72 using a microscale thin film serpentine heater in simulation of a surface local hot-spot
- High speed visualization of the inception of phase change during pool and submerged jet impingement boiling under subcooled conditions
- Documentation of jet flow induced sliding bubbles and bubble entrainment
- Quantification of bubble geometries, frequencies at the corresponding latent heat transfer at bubble departure for pool and submerged jet impingement boiling

8.3 LIST OF PUBLICATIONS

The results and methods accomplished through this work have been in part communicated in the form of a journal article, conference proceedings and posters as listed below.

- Mani, P.; Cardenas, R.; Narayanan, V., “Comparison of Area-averaged and Local Boiling Curves in Pool and Jet Impingement Boiling”, 2012, International Journal of Multiphase Flow, Volume 42, pp. 115–127.
- Mani, P.; Cardenas, R.; Narayanan, V., “Submerged Jet Impingement Boiling on a Polished Silicon Surface”, 2011, ASME InterPACK 2011-52042, Portland, OR, USA.
- Mani, P.; Narayanan, V., “Thermal and Flow Visualization of Submerged Jet Impingement Boiling with FC-72”, ASME HT 2012-58384, Puerto Rico, USA.
- Cardenas, R.; Mani, P.; Narayanan, V.; Dokken, C., “On the Elimination of Temperature Overshoot during Jet Impingement Boiling of Highly Wetting Fluids”, ECI 2012-1466, Lausanne, Switzerland.

Poster presentations

- ‘Submerged Jet Impingement Boiling on a Polished Silicon Surface’, ASME InterPACK Conference, Portland, OR, USA (2011). (Awarded 3rd position in the Thermal Management category).
- ‘Thermal Overshoot and Boiling Hysteresis with FC-72’, ASME Summer Heat Transfer Conference, Rio Grande, Puerto Rico, USA (2012).

8.4 RECOMMENDATIONS FOR FUTURE WORK

The microscale pool boiling and SJIB results presented in this thesis require continued investigations to improve the accuracy of the quantitative results and gain a better understanding of the thermal process that affect microscale boiling heat transfer. While significant information on the effects of jet inertia and bubble departure characteristics was accomplished from the experiments presented herein, there were several technical challenges faced that need more work. The recommendations for strengthening this work are segregated in terms of the changes required in the experimental set-up and the additional work required for improving the image analysis. Lastly, some suggestions for further investigations are provided.

Experimental set up and data analysis

For this quantitative visualization study, IR and high speed imaging are the two primary methods of data acquisition, however problems were faced in the IR data acquisition (Narcissus effect, tripod camera mount) and high speed data analysis (complexity of bubbles generated during SJIB). To combat these issues the following are recommended

- (a) The sturdy z-stage used for the macroheater tests is recommended for re-use in the microheater set-up with the addition of an x-y traverse. This added flexibility in the x-y directions would allow room for further investigation at different radial locations on the test surface with greater stability and ease in camera positioning.

- (b) The use of a proper thickness of an anti-reflective coating on the silicon substrate is recommended to minimize the reflections observed in the IR images during the microscale study.
- (c) A synchronization of IR and high speed cameras along with sensor data acquisition board is recommended for real time comparison of boiling events. Since pool boiling events were observed at ~40 Hz it might be possible to capture the local temperature variations during bubble ebullition.
- (d) For these microscale tests, the presently used chamber measuring 25.4 x 19 x 25.4 cm³ is much larger than required. The use of a miniaturized transparent-walled test chamber is highly recommended. This will help to minimize the fluid in use, save time in pool degassing and achieve a greater uniformity in pool temperatures during experiment. Transparent walls would permit a visualization of the boiling activity from more than one side allowing for a volumetric estimate of spherical and non-spherical bubble geometries. Additionally an x-y traverse adjustment to the chamber top-plate is required to align nozzle to heater with high precision.

Data Analysis

- (a) Significant amount of time was invested in manual conversion of each IR image over the various tests from .IRI to .csv format for image processing in MATLAB. Hence a suitable program for the batch conversion of IR images is required.

- (b) The IR image alignment code use currently only accounts for shifts in the x and y directions. If the current set-up with a tripod is continued for experiments then a method of accounting for rotational adjustments of the camera in addition to the x-y adjustments is suggested.
- (c) High speed image processing algorithm needs further development to account for the multiple departures occurring simultaneously or successively during SJIB. The varying sizes of bubble departures needs to be accounted for. A bubble tracking algorithm will be useful to isolate bubbles of distinct radii that depart simultaneously during SJIB. The net departure frequency and latent heat transfer needs to be evaluated by a summation of the individually recorded departure events for jet boiling.
- (d) An additional high speed image processing algorithm needs to be developed to account for the heat transfer due to the sliding bubbles.

Proposed investigations

The following studies are suggested for continuation for this work.

- (a) For a highly conductive substrate such as silicon being heated at a single spot, the present experiments demanded large power inputs. The corresponding estimates of latent heat transfer rates from the high speed were extremely small indicating that a significant amount of heat was lost through the substrate to the subcooled fluid or ambient air. A heat loss analysis needs to be conducted for the present set-up with the aid of IR temperature maps of the surface acquired

during actual experiments to obtain estimates for the convective heat transfer during boiling.

- (b) With the synchronization of IR and high speed imaging a quantification of the transient heat transfer can be gained for pool boiling conditions where departure frequencies were found to be $\sim 40\text{Hz}$. In addition this will aid in the quantification of equivalent bubble departure diameters from heat flux maps of the surface during pool boiling conditions.
- (c) The effect of heater size on the bubble dimensions during growth and departure for pool and SJIB must be investigated.
- (d) The effect of varying jet Reynolds number and radial location of the heat source (wall jet versus impingement region) needs to be characterized.
- (e) Heat transfer enhancements due to sliding bubbles and entrained bubbles can be investigated with the help of bubble tracking algorithms.
- (f) The use of a single cavity etched in silicon for the isolated bubble generation may be explored. Cavities would help in minimizing bubble generation in multiple sites at high superheats.

BIBLIOGRAPHY

- [1] G. E. Moore, "Cramming more components onto integrated circuits (Reprinted from Electronics, pg 114-117, April 19, 1965)," *Proceedings of the Ieee*, vol. 86, pp. 82-85, Jan 1998.
- [2] I. Mudawar, "Assessment of high-heat-flux thermal management schemes," *Ieee Transactions on Components and Packaging Technologies*, vol. 24, pp. 122-141, Jun 2001.
- [3] A. J. Robinson and E. Schnitzler, "An experimental investigation of free and submerged miniature liquid jet array impingement heat transfer," *Experimental Thermal and Fluid Science*, vol. 32, pp. 1-13, Oct 2007.
- [4] P. Tie, Q. Li, and Y. M. Xuan, "Investigation on the submerged liquid jet arrays impingement cooling," *Applied Thermal Engineering*, vol. 31, pp. 2757-2763, Oct 2011.
- [5] D. H. Wolf, F. P. Incropera, and R. Viskanta, "Jet Impingement boiling," *Advances in Heat Transfer*, vol. 23, pp. 1-132, 1993.
- [6] S. H. Bhavnani, G. Fournelle, and R. C. Jaeger, "Immersion-cooled heat sinks for electronics: Insight from high-speed photography," *Ieee Transactions on Components and Packaging Technologies*, vol. 24, pp. 166-176, Jun 2001.
- [7] J. H. Kim, "Spray cooling heat transfer: The state of the art," *International Journal of Heat and Fluid Flow*, vol. 28, pp. 753-767, Aug 2007.
- [8] I. Mudawar, D. Bharathan, K. Kelly, and S. Narumanchi, "Two-Phase Spray Cooling of Hybrid Vehicle Electronics," *Ieee Transactions on Components and Packaging Technologies*, vol. 32, pp. 501-512, Jun 2009.
- [9] T. A. Shedd, "Next generation spray cooling: High heat flux management in compact spaces," *Heat Transfer Engineering*, vol. 28, pp. 87-92, Feb 2007.
- [10] T. L. Chen and S. V. Garimella, "Local heat transfer distribution and effect of instabilities during flow boiling in a silicon microchannel heat sink,"

International Journal of Heat and Mass Transfer, vol. 54, pp. 3179-3190, Jul 2011.

- [11] W. L. Qu and I. Mudawar, "Thermal design methodology for high-heat-flux single-phase and two-phase micro-channel heat sinks," *Ieee Transactions on Components and Packaging Technologies*, vol. 26, pp. 598-609, Sep 2003.
- [12] W. L. Qu, S. M. Yoon, and I. Mudawar, "Two-phase flow and heat transfer in rectangular micro-channels," *Journal of Electronic Packaging*, vol. 126, pp. 288-300, Sep 2004.
- [13] A. Bar-Cohen, M. Arik, and M. Ohadi, "Direct liquid cooling of high flux micro and nano electronic components," *Proceedings of the Ieee*, vol. 94, pp. 1549-1570, Aug 2006.
- [14] D. H. Wolf, F. P. Incropera, and R. Viskanta, "Local jet impingement boiling heat transfer," *International Journal of Heat and Mass Transfer*, vol. 39, pp. 1395-1406, May 1996.
- [15] R. Mahajan, C. P. Chiu, and G. Chrysler, "Cooling a microprocessor chip," *Proceedings of the Ieee*, vol. 94, pp. 1476-1486, Aug 2006.
- [16] S. Nukiyama, "Maximum and minimum values of heat transmitted from metal to boiling water under atmospheric pressure," *J.Japan Soc. Mech. Eng.*, vol. 37., pp. 367-374 1934.
- [17] K. W. Tou, G. P. Xu, and C. P. Tso, "Direct liquid cooling of electronic chips by single-phase forced convection of FC-72," *Experimental Heat Transfer*, vol. 11, pp. 121-134, Apr-Jun 1998.
- [18] P. J. Marto and V. J. Lepere, "Pool Boiling Heat-Transfer from Enhanced Surfaces to Dielectric Fluids," *Journal of Heat Transfer-Transactions of the Asme*, vol. 104, pp. 292-299, 1982.
- [19] S. M. You, Bar-Cohen, A., Simon, T. W., "Boiling Incipience and Nucleate Boiling Heat-Transfer of Highly Wetting Dielectric Fluids from Electronic Materials," *IEEE Transactions on Components Hybrids and Manufacturing Technology*, vol. 13, pp. 1032-1039, 1990.

- [20] N. Zuckerman and N. Lior, "Jet Impingement Heat Transfer: Physics, Correlations and Numerical Modeling," *Advances in Heat Transfer*, vol. 39, pp. 565-629, 2006.
- [21] H. Martin, "Heat and Mass Transfer between Impinging Gas Jets and Solid Surfaces," *Advances in Heat Transfer*, vol. 13, pp. 1-60, 1977.
- [22] R. Viskanta, "Heat-Transfer to Impinging Isothermal Gas and Flame Jets," *Experimental Thermal and Fluid Science*, vol. 6, pp. 111-134, Feb 1993.
- [23] D. W. Zhou and C. F. Ma, "Radial heat transfer behavior of impinging submerged circular jets," *International Journal of Heat and Mass Transfer*, vol. 49, pp. 1719-1722, May 2006.
- [24] C. F. Ma and A. E. Bergles, "Jet Impingement Nucleate Boiling," *International Journal of Heat and Mass Transfer*, vol. 29, pp. 1095-1101, Aug 1986.
- [25] D. W. Zhou, C. F. Ma, and J. Yu, "Boiling hysteresis of impinging circular submerged jets with highly wetting liquids," *International Journal of Heat and Fluid Flow*, vol. 25, pp. 81-90, Feb 2004.
- [26] R. Cardenas, "Submerged Jet Impingement Boiling Thermal Management," PhD, School of Mechanical, Industrial and Manufacturing Engineering, Oregon State University, Corvallis, 2011.
- [27] B. J. Jones, J. P. McHale, and S. V. Garimella, "The Influence of Surface Roughness on Nucleate Pool Boiling Heat Transfer," *Journal of Heat Transfer-Transactions of the Asme*, vol. 131, pp. -, Dec 2009.
- [28] R. H. Chen, L. C. Chow, and J. E. Navedo, "Effects of spray characteristics on critical heat flux in subcooled water spray cooling," *International Journal of Heat and Mass Transfer*, vol. 45, pp. 4033-4043, Sep 2002.
- [29] W. L. Qu and I. Mudawar, "Flow boiling heat transfer in two-phase micro-channel heat sinks - I. Experimental investigation and assessment of correlation methods," *International Journal of Heat and Mass Transfer*, vol. 46, pp. 2755-2771, Jul 2003.
- [30] D. W. Zhou and C. F. Ma, "Local jet impingement boiling heat transfer with R113," *Heat and Mass Transfer*, vol. 40, pp. 539-549, May 2004.

- [31] D. B. R. Kenning and Y. Y. Yan, "Pool boiling heat transfer on a thin plate: Features revealed by liquid crystal thermography," *International Journal of Heat and Mass Transfer*, vol. 39, pp. 3117-3126, Oct 1996.
- [32] D. Krebs, V. Narayanan, J. Liburdy, and D. Pence, "Spatially resolved wall temperature measurements during flow boiling in microchannels," *Experimental Thermal and Fluid Science*, vol. 34, pp. 434-445, May 2010.
- [33] T. G. Theofanous, J. P. Tu, A. T. Dinh, and T. N. Dinh, "The boiling crisis phenomenon - Part I: nucleation and nucleate boiling heat transfer," *Experimental Thermal and Fluid Science*, vol. 26, pp. 775-792, Aug 2002.
- [34] C. Gerardi, J. Buongiorno, L. W. Hu, and T. McKrell, "Study of bubble growth in water pool boiling through synchronized, infrared thermometry and high-speed video," *International Journal of Heat and Mass Transfer*, vol. 53, pp. 4185-4192, Sep 2010.
- [35] F. Demiray and J. H. Kim, "Microscale heat transfer measurements during pool boiling of FC-72: effect of subcooling," *International Journal of Heat and Mass Transfer*, vol. 47, pp. 3257-3268, Jul 2004.
- [36] S. Moghaddam and K. Kiger, "Physical mechanisms of heat transfer during single bubble nucleate boiling of FC-72 under saturation conditions-I. Experimental investigation," *International Journal of Heat and Mass Transfer*, vol. 52, pp. 1284-1294, Feb 2009.
- [37] A. B. Ozer, A. F. Oncel, D. K. Hollingsworth, and L. C. Witte, "A method of concurrent thermographic-photographic visualization of flow boiling in a minichannel," *Experimental Thermal and Fluid Science*, vol. 35, pp. 1522-1529, Nov 2011.
- [38] N. M. Dukle and D. K. Hollingsworth, "Liquid crystal images of the transition from jet impingement convection to nucleate boiling .1. Monotonic distribution of the convection coefficient," *Experimental Thermal and Fluid Science*, vol. 12, pp. 274-287, Apr 1996.
- [39] N. M. Dukle and D. K. Hollingsworth, "Liquid crystal images of the transition from jet impingement convection to nucleate boiling .2. Nonmonotonic distribution of the convection coefficient," *Experimental Thermal and Fluid Science*, vol. 12, pp. 288-297, Apr 1996.

- [40] A. K. Das, P. K. Das, and P. Saha, "Nucleate boiling of water from plain and structured surfaces," *Experimental Thermal and Fluid Science*, vol. 31, pp. 967-977, Aug 2007.
- [41] B. J. Jones, J. P. McHale, and S. V. Garimella, "The Influence of Surface Roughness on Nucleate Pool Boiling Heat Transfer," *Journal of Heat Transfer-Transactions of the Asme*, vol. 131, Dec 2009.
- [42] G. W. Preckshot, and Denny, V.E., "Explorations of Surface and Cavity Properties on the Nucleate Boiling of Carbon Tetrachloride," *The Canadian Journal of Chemical Engineering*, vol. 45,, pp. 241-6, 1967.
- [43] M. Shoji and Y. Takagi, "Bubbling features from a single artificial cavity," *International Journal of Heat and Mass Transfer*, vol. 44, pp. 2763-2776, Jul 2001.
- [44] S. Siedel, S. Cioulachtjian, and J. Bonjour, "Experimental analysis of bubble growth, departure and interactions during pool boiling on artificial nucleation sites," *Experimental Thermal and Fluid Science*, vol. 32, pp. 1504-1511, Sep 2008.
- [45] Y. S. Chang, K. H. Jeong, H. J. Lee, Y. P. Lee, and H. Y. Kim, "Behavior of thermal bubbles formed from a single nucleation site," *Journal of Mechanical Science and Technology*, vol. 24, pp. 415-420, Jan 2010.
- [46] N. D. Nimkar, S. H. Bhavnani, and R. C. Jaeger, "Effect of nucleation site spacing on the pool boiling characteristics of a structured surface," *International Journal of Heat and Mass Transfer*, vol. 49, pp. 2829-2839, Aug 2006.
- [47] S. Moghaddam and K. Kiger, "Physical mechanisms of heat transfer during single bubble nucleate boiling of FC-72 under saturation conditions-II: Theoretical analysis (vol 52, pg 1295, 2009)," *International Journal of Heat and Mass Transfer*, vol. 52, pp. 6061-6061, Dec 2009.
- [48] C. Hutter, D. B. R. Kenning, K. Sefiane, T. G. Karayiannis, H. Lin, G. Cummins, and A. J. Walton, "Experimental pool boiling investigations of FC-72 on silicon with artificial cavities and integrated temperature microsensors," *Experimental Thermal and Fluid Science*, vol. 34, pp. 422-433, May 2010.

- [49] Y. S. Qi and J. F. Klausner, "Heterogeneous nucleation with artificial cavities," *Journal of Heat Transfer-Transactions of the Asme*, vol. 127, pp. 1189-1196, Nov 2005.
- [50] I. Golobic and H. Gjerkes, "Interactions between laser-activated nucleation sites in pool boiling," *International Journal of Heat and Mass Transfer*, vol. 44, pp. 143-153, Jan 2001.
- [51] J. G. Myers, V. K. Yerramilli, S. W. Hussey, G. F. Yee, and J. Kim, "Time and space resolved wall temperature and heat flux measurements during nucleate boiling with constant heat flux boundary conditions," *International Journal of Heat and Mass Transfer*, vol. 48, pp. 2429-2442, Jun 2005.
- [52] R. Raj and J. Kim, "Heater Size and Gravity Based Pool Boiling Regime Map: Transition Criteria Between Buoyancy and Surface Tension Dominated Boiling," *Journal of Heat Transfer-Transactions of the Asme*, vol. 132, Sep 2010.
- [53] N. Yaddanapudi and J. Kim, "Single Bubble Heat Transfer in Saturated Pool Boiling of FC-72," *Multiphase Science and Technology*, vol. 12, pp. 47-63, 2000.
- [54] V. P. Carey, *Liquid-vapor phase-change phenomena: An introduction to the thermophysics of vaporization and condensation processes in heat transfer equipment*, 2nd ed.: Taylor and Francis, 2008.
- [55] F. P. Incropera, D. P. Dewitt, T. L. Bergman, and A. S. Lavine, *Fundamentals of Heat and Mass Transfer*, 6th ed.: John Wiley and Sons, 2007.
- [56] L. Z. Zeng, J. F. Klausner, and R. Mei, "A Unified Model for the Prediction of Bubble Detachment Diameters in Boiling Systems .1. Pool Boiling," *International Journal of Heat and Mass Transfer*, vol. 36, pp. 2261-2270, Jun 1993.
- [57] H. K. Forster, Greif, R., "Heat transfer to a boiling liquid - mechanisms and correlations," *J. Heat Transfer* vol. 81 1959.
- [58] F. D. Moore, Mesler, R.B., "Thement of rapid surface temperature fluctuations during nucleate boiling of water measure," *AICHE J.*, vol. 7, pp. 620-624, 1961.

- [59] M. G. Cooper, Lloyd, A.J.P., "The microlayer in nucleate boiling," *Int. J. Heat Mass Transfer* vol. 12, pp. 895-913, 1969.
- [60] B. B. Mikic, Rohsenow, W.M., "A new correlation of pool boiling data including the effect of heating surface characteristics," *J. Heat Transfer* vol. 9, pp. 245-250, 1969.
- [61] P. Stephan and J. Hammer, "A New Model for Nucleate Boiling Heat-Transfer," *Warme Und Stoffubertragung-Thermo and Fluid Dynamics*, vol. 30, pp. 119-125, Nov 1994.
- [62] J. Kim, "Review of nucleate pool boiling bubble heat transfer mechanisms," *International Journal of Multiphase Flow*, vol. 35, pp. 1067-1076, Dec 2009.
- [63] Hsu.Y.Y, "On the Size Range of Active Nucleation Cavities on a Heating Surface " *J. Heat Transfer*, vol. **84**, pp. 207-216., 1962.
- [64] I. Golobic, J. Petkovsek, M. Baselj, A. Papez, and D. Kenning, "Experimental determination of transient wall temperature distributions close to growing vapor bubbles," *Heat and Mass Transfer*, vol. 45, pp. 857-866, May 2009.
- [65] E. Wagner and P. Stephan, "High-Resolution Measurements at Nucleate Boiling of Pure FC-84 and FC-3284 and Its Binary Mixtures," *Journal of Heat Transfer-Transactions of the Asme*, vol. 131, Dec 2009.
- [66] F. Kapsenberg, "Lateral Fluid Motion in Nucleate Boiling Through Asymmetric Surface Structures," M.S., School of Mechanical, Industrial and Manufacturing Engineering, Oregon State University, Corvallis, 2011.
- [67] V. A. Patil and V. Narayanan, "Spatially resolved heat transfer rates in an impinging circular microscale jet," *Microscale Thermophysical Engineering*, vol. 9, pp. 183-197, Apr-Jun 2005.
- [68] V. A. Patil and V. Narayanan, "Application of heated-thin-foil thermography technique to external convective microscale flows," *Measurement Science & Technology*, vol. 16, pp. 472-476, Feb 2005.
- [69] S. A. Klein, "Engineering Equation Solver," ed, 2010, pp. F-Chart Software.
- [70] 3M, "Fluorinert Electronic Liquid F C-72, 3 M Specialty Materials," 2000.

- [71] E. Wagner and P. Stephan, "High-Resolution Measurements at Nucleate Boiling of Pure FC-84 and FC-3284 and Its Binary Mixtures," *Journal of Heat Transfer-Transactions of the ASME*, vol. 131, pp. 121008-1-121008-12, Dec 2009.
- [72] T. W. Dutton, L. R. Pate, and D. K. Hollingsworth, "Imaging of Surface-Tension-Driven Convection Using Liquid Crystal Thermography," *Journal of Heat Transfer-Transactions of the ASME*, vol. 132, Dec 2010.
- [73] R. Cardenas, Mani, P., Narayanan, V., "Sub-Atmospheric Mini-Jet Impingement Boiling of Water under Saturated and Subcooled Conditions," in *ASME/JSME 8th Thermal Engineering Joint Conference*, Honolulu, Hawaii, USA, 2011.
- [74] D. Krebs, "A Technique for Spatially Resolved Wall Temperature Measurements in Microchannel Heat Sinks Using Infrared Thermography " M.S., School of Mechanical, Industrial and Manufacturing Engineering, Oregon State University, Corvallis, 2008.
- [75] G. M. Carlomango, "Infrared thermography in heat transfer," in *Handbook of flow visualization*, ed Washington DC: Hemisphere Publishing Corporation, 1989, pp. 531-553.
- [76] S. J. Kline, McClintock, F. A., "Describing Uncertainties in Single-Sample Experiments," *Mechanical Engineering*, vol. 75, pp. 3-8, 1953.
- [77] J. L. Parker and M. S. El-Genk, "Enhanced saturation and subcooled boiling of FC-72 dielectric liquid," *International Journal of Heat and Mass Transfer*, vol. 48, pp. 3736-3752, Aug 2005.
- [78] S. H. Bhavnani, C. P. Tsai, R. C. Jaeger, and D. L. Eison, "An Integral Heat Sink for Cooling Microelectronic Components," *Journal of Electronic Packaging*, vol. 115, pp. 284-291, 1993.
- [79] S. J. Reed and I. Mudawar, "Elimination of boiling incipience temperature drop in highly wetting fluids using spherical contact with a flat surface," *International Journal of Heat and Mass Transfer*, vol. 42, pp. 2439-2454, Jul 1999.
- [80] P. J. C. Normington, M. Mahalingam, and T. Y. T. Lee, "Thermal Management Control without Overshoot Using Combinations of Boiling

Liquids," *IEEE Transactions on Components Hybrids and Manufacturing Technology*, vol. 15, pp. 806-814, Oct 1992.

- [81] A. E. Bergles, Kim, C. J., "A Method to Reduce Temperature Overshoots in Immersion Cooling of Microelectronic Devices " presented at the InterSociety Conference on Thermal Phenomena in the Fabrication and Operation of Electronic Components: I-THERM '88, Los Angeles, CA , USA 1988.
- [82] S. H. Bhavnani, S. E. Balch, and R. C. Jaeger, "Control of incipience hysteresis effects in liquid cooled electronics heat sinks," *Journal of Electronics Manufacturing*, vol. 9, pp. 179-190, Jun 1999.
- [83] R. Cardenas, P. Mani, V. Narayanan, and C. Dokken, "On the Elimination of Temperature Overshoot during Jet Impingement Boiling of Highly Wetting Fluids," presented at the ECI 8th International Conference on Boiling and Condensation Heat Transfer, Lausanne, Switzerland, 2012.
- [84] L. M. Pan, Z. W. Tan, D. Q. Chen, and L. C. Xue, "Numerical investigation of vapor bubble condensation characteristics of subcooled flow boiling in vertical rectangular channel," *Nuclear Engineering and Design*, vol. 248, pp. 126-136, Jul 2012.
- [85] S. Moghaddam, "Microscale study of nucleation process in boiling of low surface tension liquids," PhD, Department of Mechanical Engineering, University of Maryland, College Park, 2006.
- [86] C. Hutter, "Experimental pool boiling investigation of FC-72 on silicon with artificial cavities, integrated temperature micro-sensors and heater," PhD, School of Engineering, The University of Edinburgh, Edinburgh, 2009.
- [87] G. Sateesh, S. K. Das, and A. R. Balakrishnan, "Analysis of pool boiling heat transfer: effect of bubbles sliding on the heating surface," *International Journal of Heat and Mass Transfer*, vol. 48, pp. 1543-1553, Apr 2005.
- [88] R. Situ, Y. Mi, M. Ishii, and M. Mori, "Photographic study of bubble behaviors in forced convection subcooled boiling," *International Journal of Heat and Mass Transfer*, vol. 47, pp. 3659-3667, Aug 2004.
- [89] D. B. R. Kenning and O. E. Bustnes, "Liquid crystal studies of sliding vapour bubbles," *Heat and Mass Transfer*, vol. 45, pp. 867-880, May 2009.

APPENDICES

APPENDIX

A. PROPERTIES OF TEST FLUIDS

Table A 1: Thermo-physical fluid properties at atmospheric pressure

	Water (P = 1.01 bar)	FC-72 (P = 1.01 bar)
T_{sat} [°C]	100 ^A	56 ^B
ρ_l [kg/m ³]	997.1 ^{A,#}	1680 ^{B,#}
ρ_v [kg/m ³]	0.5974 ^{A,*}	13.27 ^{A,*}
μ_l [kg/m-s]	8.90x10 ^{-4A,#}	6.43x10 ^{-4 B,#}
σ [mN/m]	71.97 ^{A,#}	10 ^{B,#}
h_{lv} [kJ/kg]	2256.7 ^C	88 ^{B,#}
c_p [J/kg-K]	4183 ^{A,#}	1100 ^{B,#}
k_l [W/m-K]	0.5948 ^{A,#}	0.057 ^{B,#}
Pr	6.26 [#]	12.40

A. EES [69]	* Evaluated at T_{sat}
B. 3M FC-72 datasheet [70]	# Evaluated at 25 °C
C. Carey [54]	

APPENDIX

B. THIN FILM HEATER FABRICATION PROCEDURES AND PROCESS RECIPES

Table B 1: Fabrication process for the macroscale heater substrate

Step	Process	Instructions	Time/Speed
1.	Substrate Cleaning	Immerse substrate in a 125 mm x 65 mm glass dish with DI water.	
		Ultrasonic Rinse	60 min
		Rinse with acetone, IPA, DI water and blow dry.	
		Dehydrate on hotplate at 85°C.	2 min
2.	Spin Coater Preparation	Line the spinner bowl with Al foil and mount the 2 inch substrate chuck.	
		Place substrate on the chuck.	
3.	Spin Photoresist	Using the graduated pipette dispense 1 ml of the positive resist S1818 on the center of the substrate. Start spin.	30 sec / 3000 rpm
4.	Soft Bake	Dehydration bake on hotplate at 85°C.	2 min
5.	Aligner Preparation	Turn on the aligner power, lamp, nitrogen flow, compressed air flow and vacuum. Level the substrate stage and check if the stage is centered.	Lamp warm up 10 min
6.	Mask Preparation	Clean the alignment mask and the photomask by blow drying on both sides. Attach each mask to a 4 inch x 4 inch clear glass with Kapton tape.	
7.	Alignment	Secure the alignment mask to the mask holder. Place the substrate on its stage, slide the stage into position and lock it. Raise stage to bring the mask and wafer in contact.	
		Align the edge of the wafer to the edge of the mask to ensure centering. Lower and slowly unlock stage without disturbing the wafer position.	

Table B 1: Fabrication process for the macroscale heater substrate (continued)

Step	Process	Instructions	Time/Speed
8.	Exposure	Secure the photomask to the mask holder. Slide the substrate stage in to position and lock it. Raise the stage to bring the mask and wafer in contact.	
		Set the exposure time and hit EXPOSE on the aligner panel.	23 sec
9.	Develop	In a 125 mm x 65 mm glass dish prepare a 1:3 diluted solution of Microposit 351 developer in DI water.	
		Immerse the substrate in the solution while continuously mixing (shaking) the solution.	30 sec
		Remove substrate from the solution and rinse thoroughly with DI water. Blow dry. Inspect the pattern.	
10.	Thermal Metal Evaporation	Vent chamber and secure the substrate to the holder with Kapton tape. Add clips of Al metal to the source boat.	
		Evaporate 1.2 μm of Al. Vent the chamber and remove the substrate.	
11.	Lift off	Immerse the substrate in acetone and cover the dish with Al foil.	Overnight
		Ultrasonicate the substrate 125 mm X 65 mm glass dish with acetone. Check for a clean pattern. Rinse immediately with acetone, IPA and DI water. Blow dry.	5 sec
12.	Contact pad Preparation	Coat a layer of silver paint on each contact pad. Let it dry	60 min
		Coat a second layer of silver paint on each contact pad. Let it dry	60 min

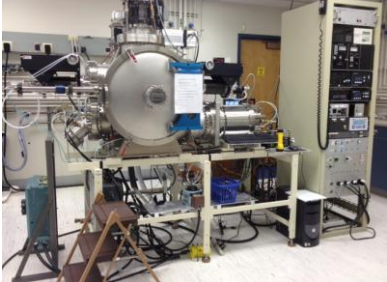
Table B 2: Fabrication process for the microscale heater substrate

Step	Process	Instructions	Time/Speed
1.	Substrate Cleaning	Immerse substrate in a 125 mm X 65 mm glass dish with DI water.	
		Ultrasonic Rinse	60 min
		Rinse with acetone, IPA, DI water and blow dry.	
		Dehydrate on hotplate at 85°C.	2 min
2.	Spin Coater Preparation	Line the spinner bowl with Al foil and mount the 2 inch substrate chuck.	
		Place substrate on the chuck.	
3.	Spin primer	Using the graduated pipette dispense 1 ml of the MCC Primer to cover the full substrate. Let it stand.	20 sec
		Start the spin.	30 sec / 3000 rpm
		Dehydrate on hotplate at 115°C.	2 min
4.	Spin Photoresist	Replace the substrate on the spin coater chuck. Using the graduated pipette dispense 1 ml of the positive resist S1813 on the center of the substrate. Start spin.	30 sec / 3000 rpm
5.	Soft Bake	Dehydration bake on hotplate at 115°C.	2 min
6.	Aligner Preparation	Turn on the aligner power, lamp, nitrogen flow, compressed air flow and vacuum. Level the substrate stage and check if the stage is centered.	Lamp warm up 10 min
7.	Mask Preparation	Clean the mask by blow drying on both sides. Attach mask to a 4 inch x 4 inch clear glass with Kapton tape.	

Table B 2: Fabrication process for the microscale heater substrate (continued)

Step	Process	Instructions	Time/Speed
8.	Exposure	Secure the photomask to the mask holder. Slide the substrate stage in to position and lock it. Raise the stage to bring the mask and wafer in contact. Align the wafer edge with the edge of the mask.	
		Set the exposure time and hit EXPOSE on the aligner panel.	4 sec
9.	Develop	In a 125 mm X 65 mm glass dish prepare a 1:4 diluted solution of Microposit 351 developer in DI water.	
		Immerse the substrate in the solution while continuously mixing (shaking) the solution.	15 sec
		Remove substrate from the solution and rinse thoroughly with DI water. Blow dry. Inspect the pattern in the optical microscope.	
10.	E-beam Metal Deposition	Vent chamber and secure the substrate to the holder with Kapton tape. Add clips of Al metal to the source crucible.	
		Evaporate 1.2 μm of Al. when done, vent the chamber and remove the substrate.	
11.	Lift off	Immerse the substrate in acetone and cover the container with Al foil.	60 sec
		Ultrasonicate the substrate 125 mm X 65 mm glass dish with acetone. Check for a clean pattern. Rinse immediately with acetone, IPA and DI water. Blow dry.	5 sec
12.	Contact pad Preparation	Coat a layer of silver paint on each contact pad. Let it dry	60 min
		Coat a second layer of silver paint on each contact pad. Let it dry	60 min

Table B 3: Equipment used for substrate fabrication at the OSU EECS cleanroom

Equipment Name	Purpose	Image
<p style="text-align: center;">Sonicator (Branson 5510)</p>	<p style="text-align: center;">Substrate cleaning, Metal lift-off</p>	
<p style="text-align: center;">Spin coater (Headway Research Inc.)</p>	<p style="text-align: center;">Photoresist spin coating</p>	
<p style="text-align: center;">Photo aligner (Karl SUSS MJB3)</p>	<p style="text-align: center;">Photolithographic transfer of pattern to the substrate</p>	
<p style="text-align: center;">Polaron thermal evaporator</p>	<p style="text-align: center;">Aluminum thin film deposition</p>	
<p style="text-align: center;">Electron beam deposition system</p>	<p style="text-align: center;">Thin film deposition</p>	

APPENDIX

C. DETAILED PART DRAWINGS

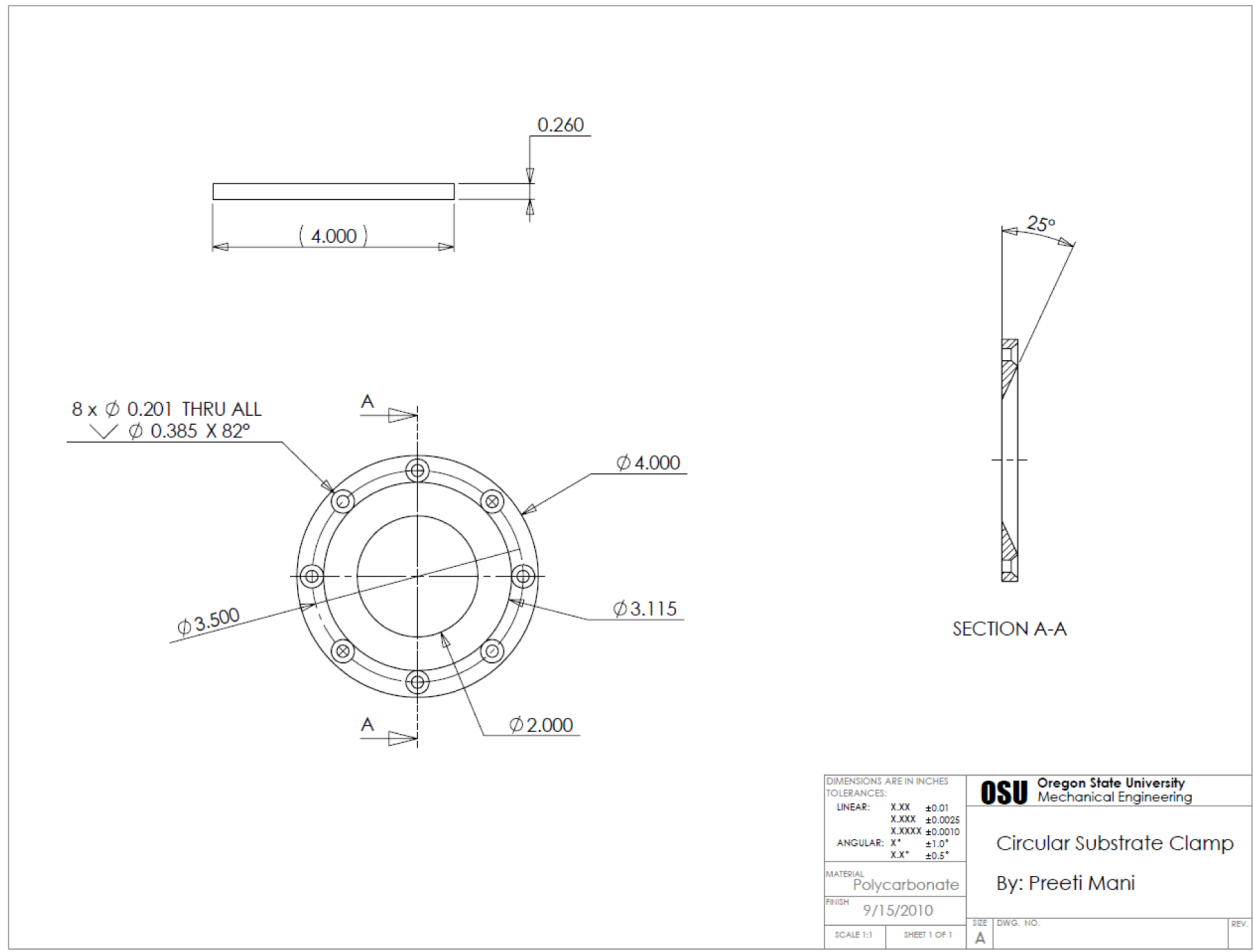


Figure C 1: Circular polycarbonate clamp for macroscale heater test substrate

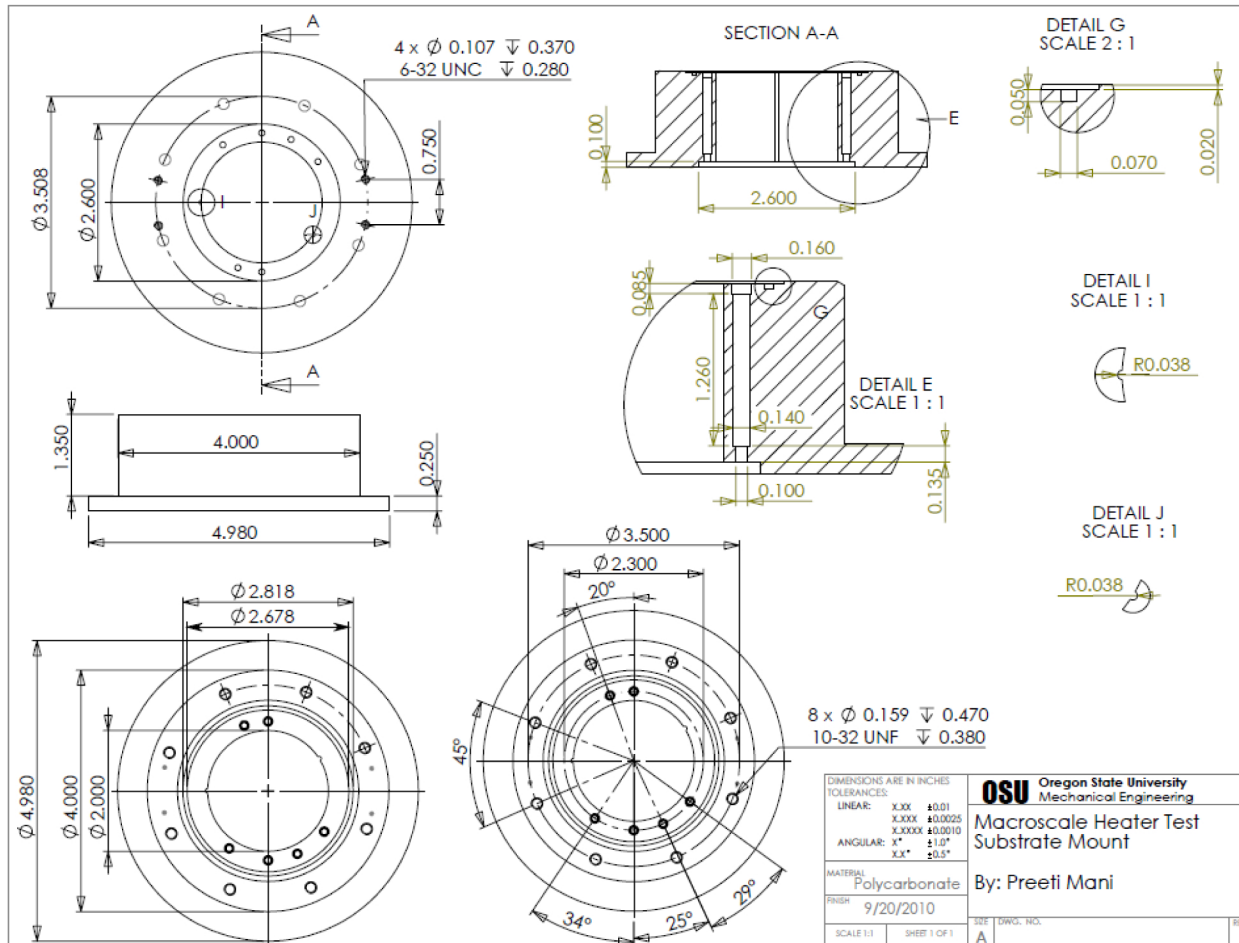


Figure C 2: Macroscale heater test substrate mount

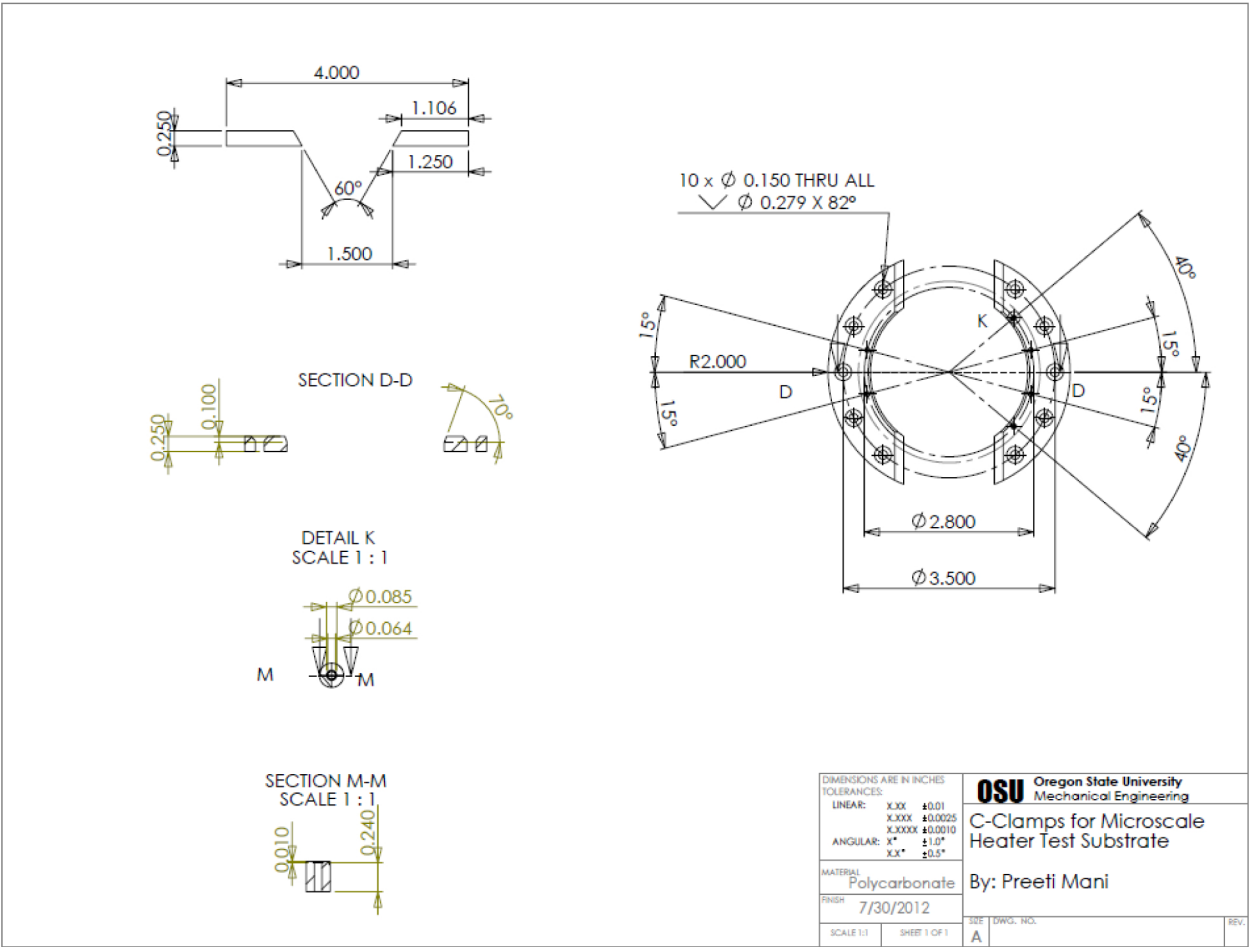


Figure C 3: C-clamps for microscale heater test substrate

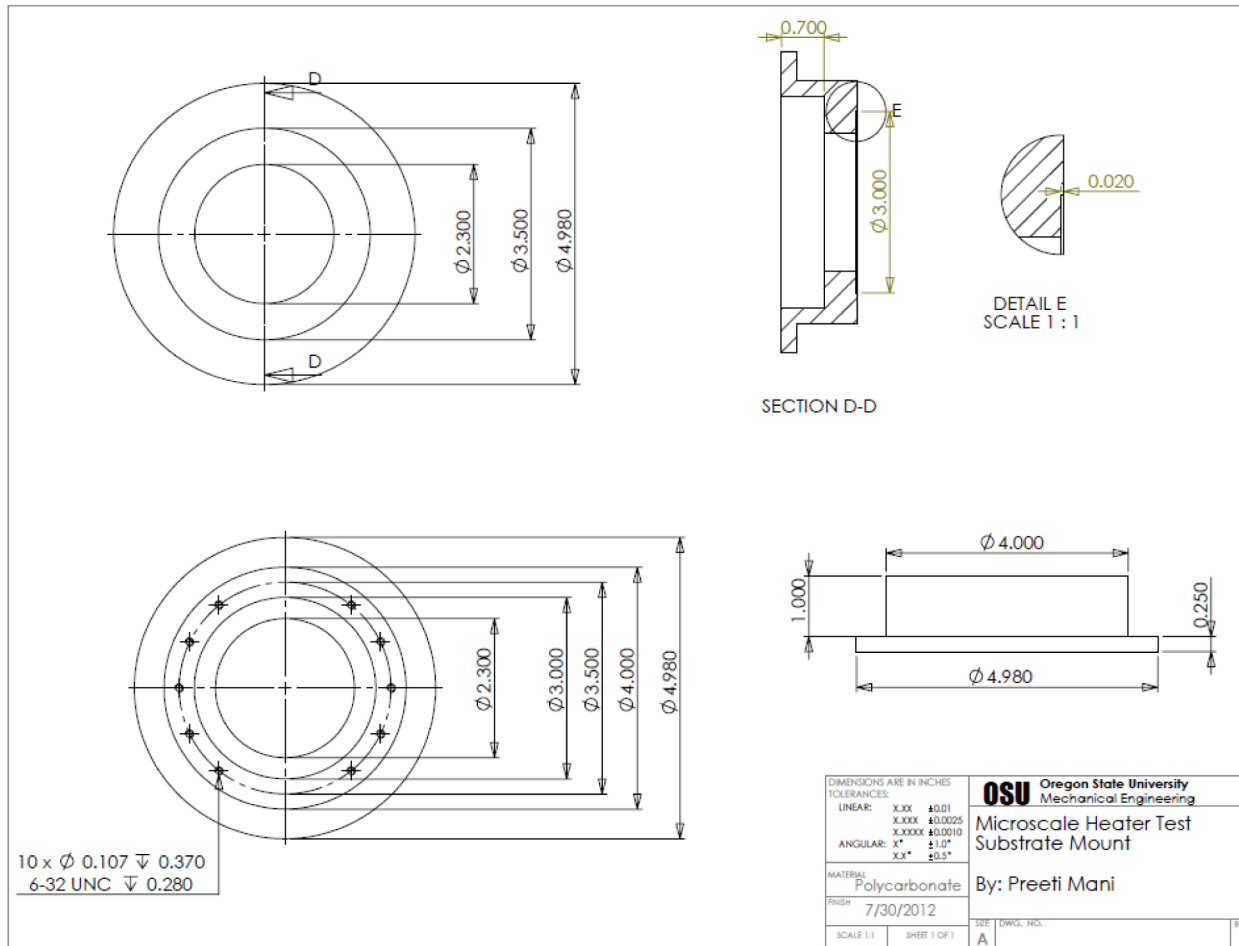


Figure C 4: Microscale heater test substrate mount

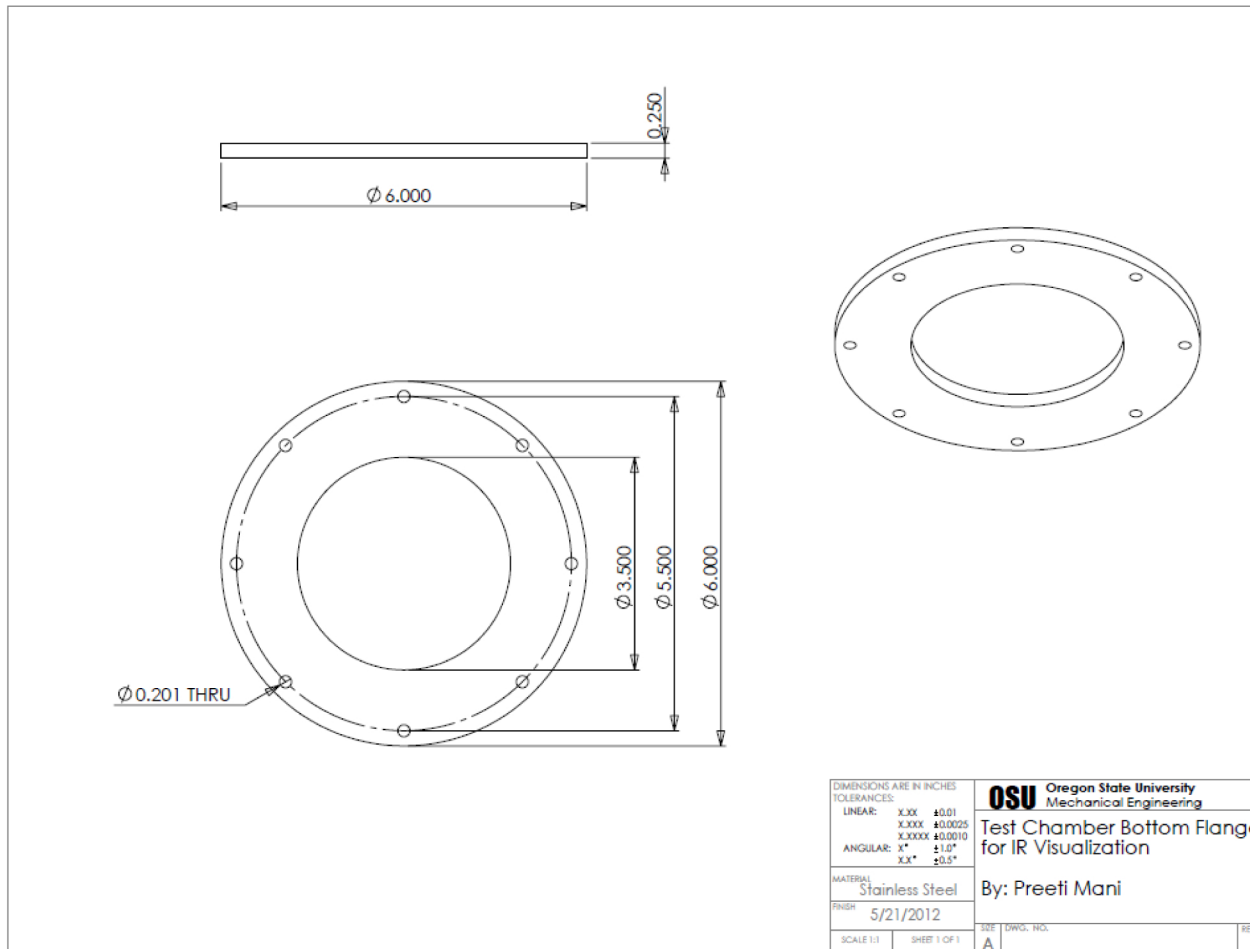


Figure C 5: Test chamber bottom flange for IR Visualization

APPENDIX

D. ESTIMATION OF NATURAL CONVECTION LOSS (MACROSCALE HEATER)

The macroscale heater tests were conducted on silicon substrates that had one face (top side) immersed in the heat transfer fluid while the heater side (rear side) was open to ambient air to permit IR visualization. Figure D 1a shows an illustration of this set-up. Of the 76.2 mm silicon substrate, a circular area of 50.8 mm diameter was exposed to air. It was therefore necessary to evaluate the heat lost to the ambient air due to natural convection.

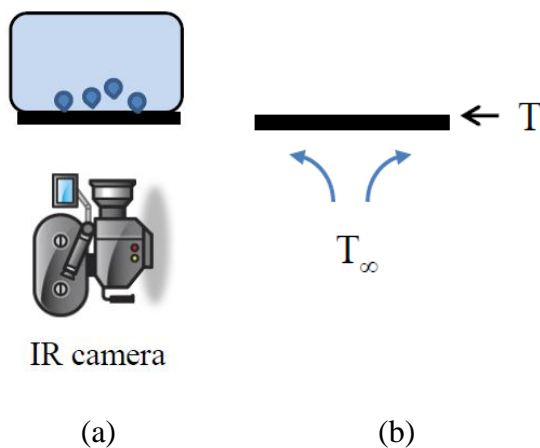


Figure D 1: Illustration of IR visualization set-up (a) and comparative illustration of the set-up for evaluating heat loss by natural convection

Figure D 1b shows a comparative illustration of the IR visualization set-up of the macroscale heater to a rear side heated surface open to natural convection by ambient air. For the purposes of this heat loss calculation, the recommended correlation for the average Nusselt number (\overline{Nu}_{Lc}) [55] for the lower surface of a hot plate was used.

$$\overline{Nu}_{L_c} = 0.27 Ra_{L_c}^{1/4} \quad (10^5 \leq Ra_{L_c} \leq 10^{10})$$

Here L_c is the characteristic length of the plate defined as the ratio of the exposed plate area to the exposed plate perimeter and $Ra_{L_c} = ((g\beta(T - T_\infty)L_c^3) / \nu\alpha)$ is the Rayleigh number estimated over the length L_c . Fluid properties for air were obtained from Engineering Equation Solver [69]. The average wall temperatures measured by the IR thermography during macroscale heater tests were used along with the ambient air temperature measured during the day of the respective experiments to estimate the net flux lost to the ambient by natural convection.

$$q''_{NC} = \frac{(\overline{Nu}_{L_c} k_{air})}{L_c}$$

The net loss computed for a set of average wall temperatures during a SJIB test with saturated FC-72 at $Re_{jet} = 5161$ are listed below in Table D 1. The average ambient temperature for this test was 26°C.

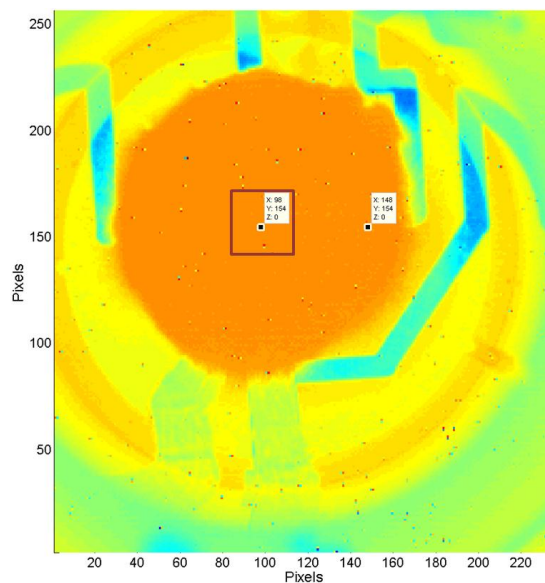
Table D 1: Estimated natural convection heat loss for a SJIB test case with saturated FC-72 ($Re_{jet} = 5161$)

$T = T_{avg}$ (°C)	\overline{Nu}_{L_c}	q''_{NC} (W/cm ²)
58.09	76.14	5.05×10^{-4}
64.90	79.89	6.42×10^{-4}
74.49	84.42	8.46×10^{-4}
85.58	88.87	1.09×10^{-3}

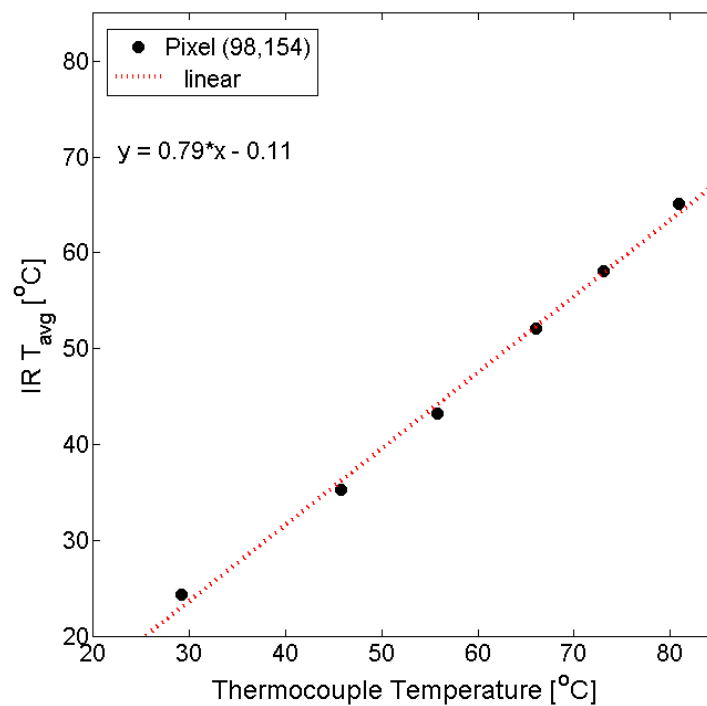
From the above values for flux loss due to natural convection it is evident that the losses are insignificantly small. Such calculations were performed for all test cases as a confirmation of the low natural convective heat loss. On the basis of the above calculations and the fact that natural convective losses would occur both during calibration and actual experiments, these losses were not accounted for.

APPENDIX

E. MACROSCALE HEATER- IR CALIBRATION CURVES

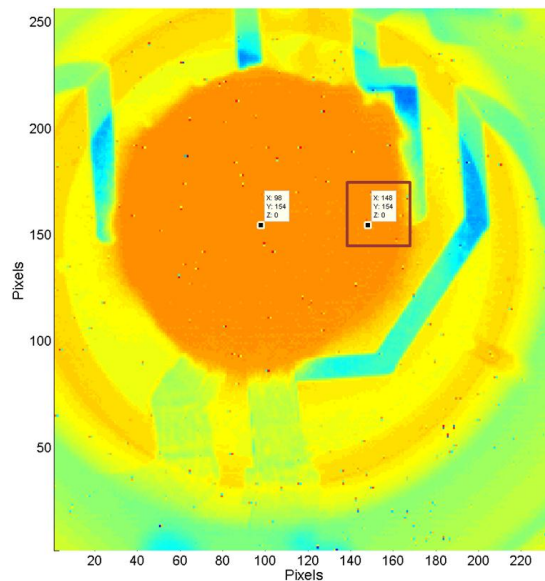


(a)

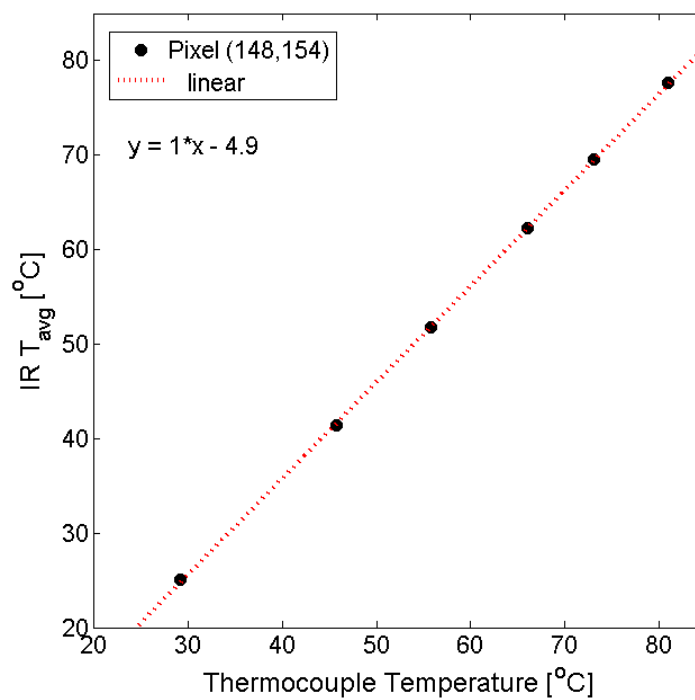


(b)

Figure E 1: Macroscale heater pixel (98,154) (a) boxed location on IR map (b) corresponding calibration curve for calibration experiment with DI water

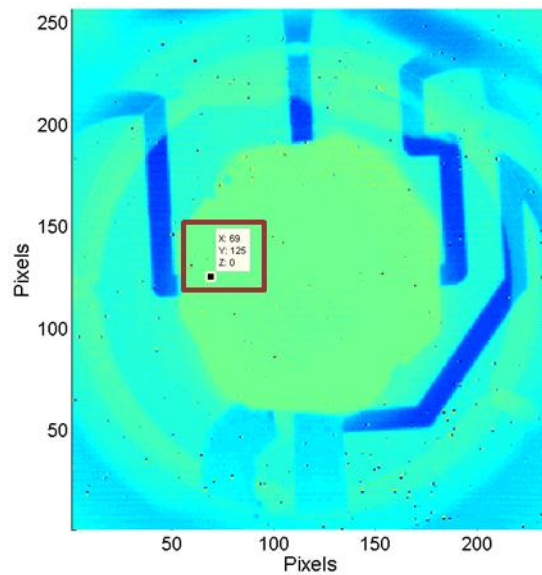


(a)

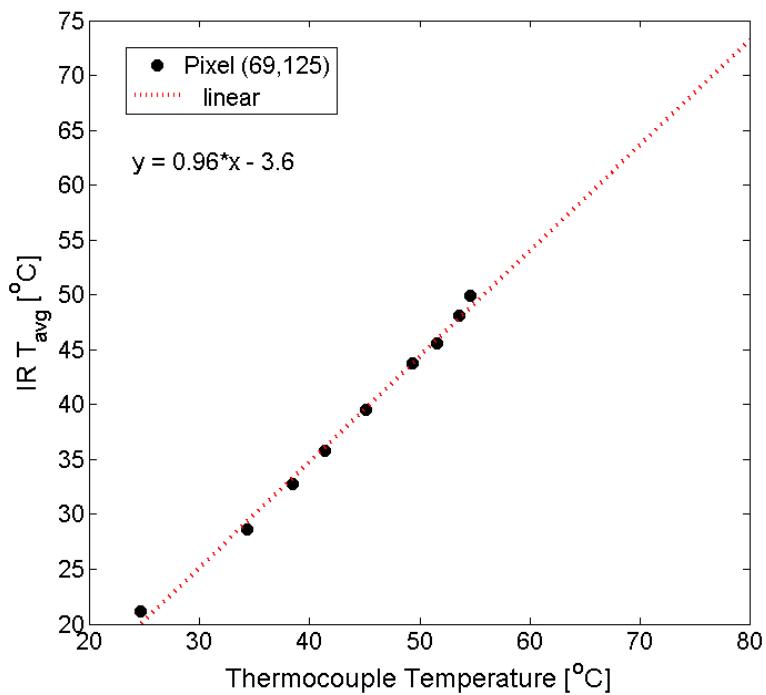


(b)

Figure E 2: Macroscale heater pixel (148,154) (a) boxed location on IR map (b) corresponding calibration curve for calibration experiment with DI water

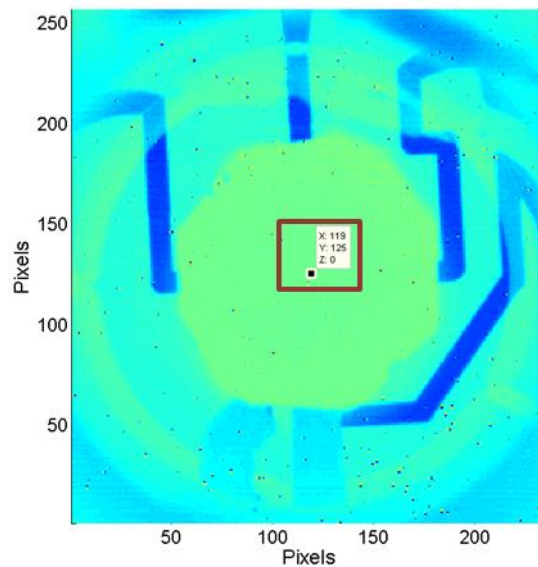


(a)

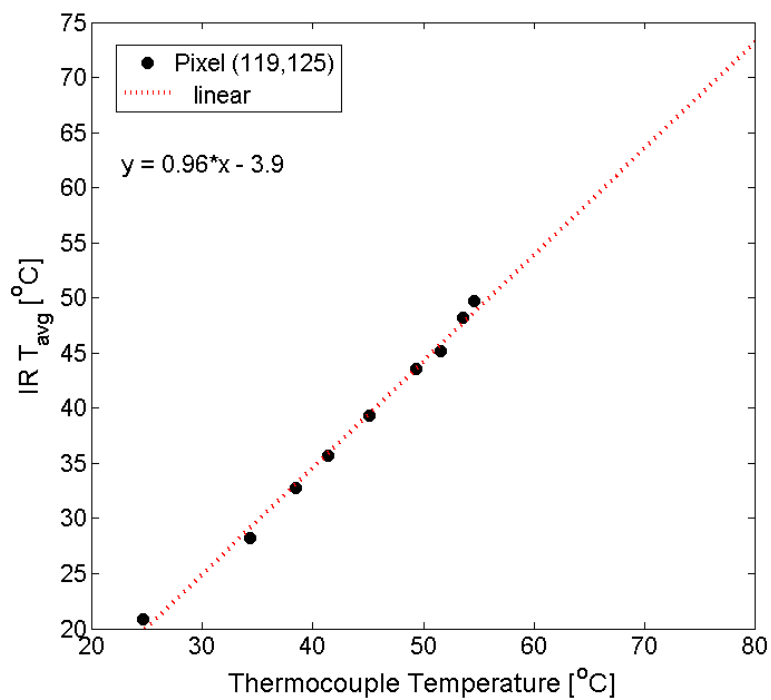


(b)

Figure E 3: Macroscale heater pixel (69,125) (a) boxed location on IR map (b) corresponding calibration curve for calibration experiment with FC-72

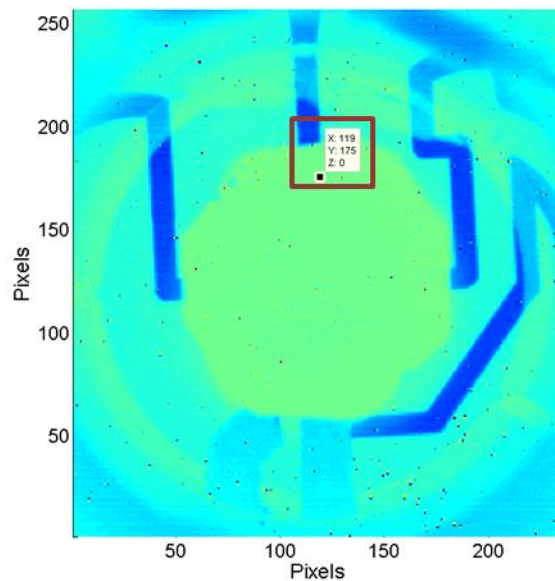


(a)

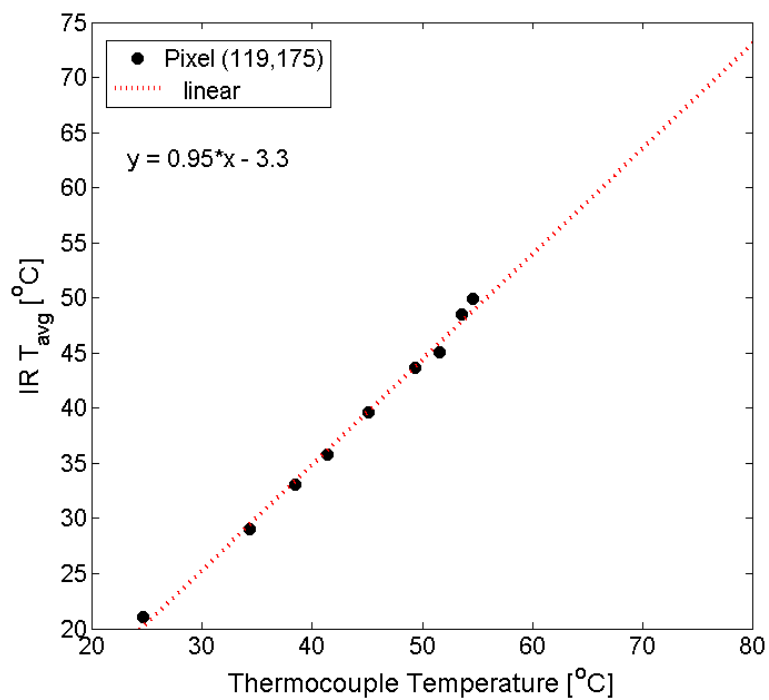


(b)

Figure E 4: Macroscale heater pixel (119,125) (a) boxed location on IR map (b) corresponding calibration curve for calibration experiment with FC-72



(a)



(b)

Figure E 5: Macroscale heater pixel (119,175) (a) boxed location on IR map (b) corresponding calibration curve for calibration experiment with FC-72

APPENDIX

F. TOP HAT FILTERING AND CONTROL VOLUME GRID INDEPENDENCE FOR IR MAPS (MACROSCALE HEATER)

Top hat filter for IR Maps of the macroscale heater

The calibrated IR maps of the macroscale heater substrate resulted in significant uncertainties in the computed conduction heat flux. Figure F 1(a and b) show the two and three-dimensional representations of the calibrated IR map of the surface during a jet impingement boiling experiment ($Re_{jet} = 5161$) with water at a heat flux of 66 W/cm^2 . The conduction heat flux computed from these maps resulted in uncertainties of 2.8 W/cm^2 and 3.06 W/cm^2 in the x and y-directions respectively.

To reduce the uncertainties in the computed conduction heat flux, the calibrated temperature maps were subjected to a top hat filter that estimates the temperature value at each pixel ($T_{filter}(i, j)$) based on a weighted average of its neighboring pixels,

$$T_{filter}(i, j) = \frac{1}{4}T(i, j) + \frac{1}{8}(T(i-1, j) + T(i, j-1) + T(i, j+1) + T(i+1, j)) + \frac{1}{16}(T(i-1, j-1) + T(i-1, j+1) + T(i+1, j-1) + T(i+1, j+1))$$

Dutton et. al. [72] employed similar filtering of thermal maps to reduce the uncertainties in recorded temperatures during liquid crystal thermometry. Figure F 1(b and c) show the two and three-dimensional representations of the calibrated IR map of the surface after one pass of the top hat filter. The filter resulted in reduced uncertainty values of 1.16 W/cm^2 and 1.05 W/cm^2 in the x and y-directions respectively.

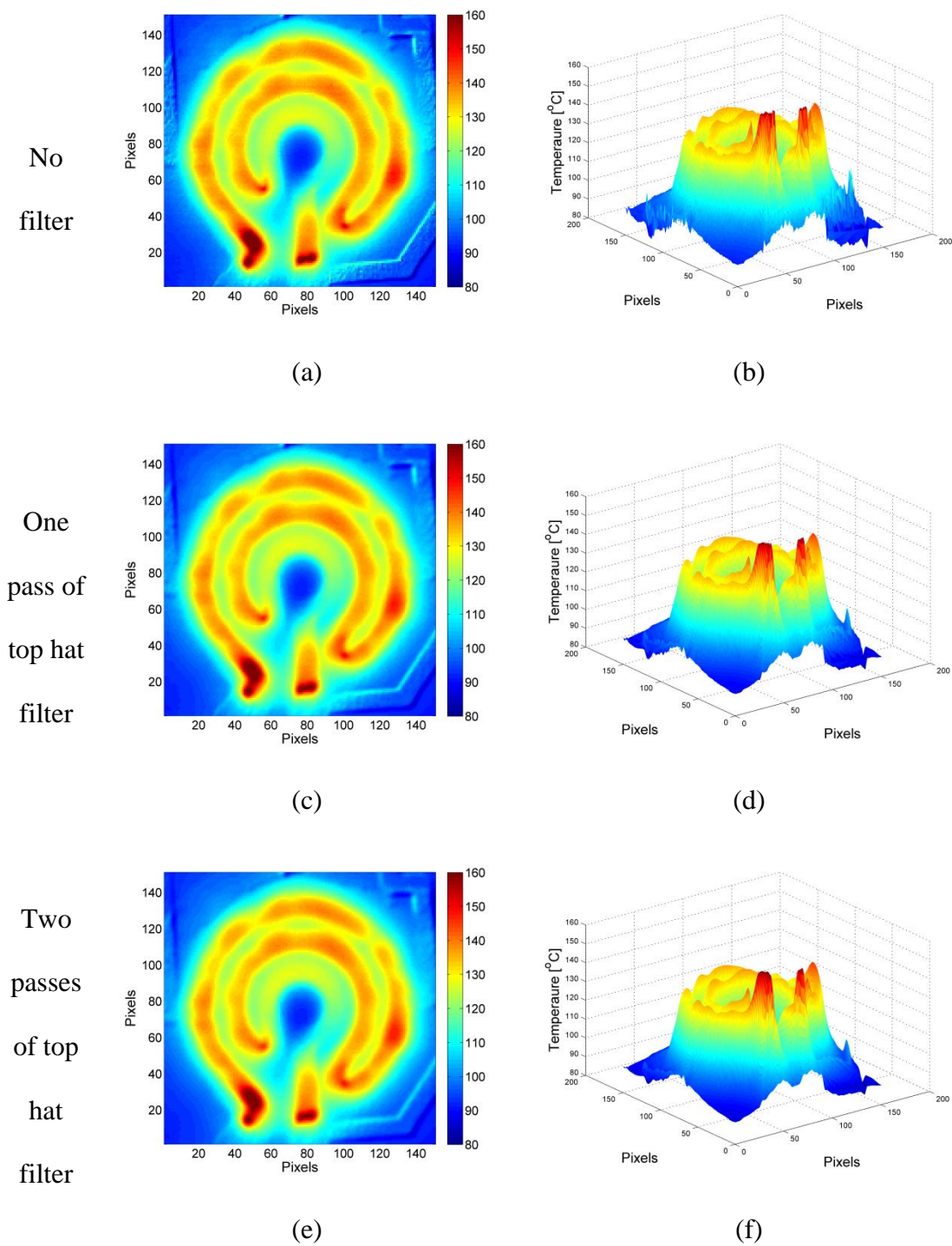


Figure F 1: Temperature maps of the macroscale heater substrate at 66 W/cm^2 in two-dimensional (left) and three-dimensional (right) representation shown for zero, one and two passes of the top hat filter

A second pass of the filter resulted in further lowering of these uncertainties to 0.9 W/cm^2 and 0.73 W/cm^2 in the x and y-directions respectively. Figure F 1(e and f) show the two and three-dimensional representations of the calibrated IR map of the surface after two passes of the top hat filter. The uncertainty values obtained after the second pass of the filter were found to be independent of any further passes of the top hat filter. As a result all calibrated IR maps were subjected to two-passes of the top-hat filter.

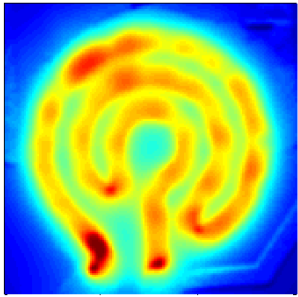
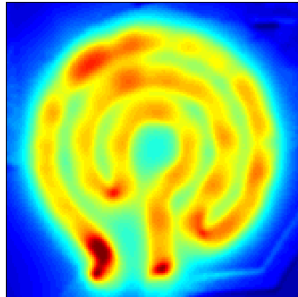
Control volume grid independence

For the analysis presented in this work each pixel was treated as a control volume with the pixel width Δ ($\Delta = \Delta x = \Delta y$) was set equal to the resolution of the IR camera for each experiment. For all the experiments conducted with the macroscale heater substrate, the pixel width $\Delta = 224 \text{ }\mu\text{m}$ on an average. Thus, Δ was approximately equal to $1.69*t$, where $t = 380 \text{ }\mu\text{m}$ (substrate thickness and the pixel height).

To ensure the independence of results on the choice of pixel dimensions it was necessary to perform a grid independence analysis. Calculations were performed for a pool boiling test case conducted on the macroscale heater substrate with DI water as the test fluid. For the set of experiments with DI water, the resolution of the IR camera was determined to be 230 microns. So the pixel/control volume dimension $\Delta = 230 \text{ }\mu\text{m}$ is approximately 1.65 times smaller than the thickness of the silicon substrate ($t=380 \text{ }\mu\text{m}$).

For the grid independence analysis a control volume of size $\Delta = \Delta x = \Delta y = 460 \mu\text{m}$, was chosen. So for this case $\Delta = 1.2 * t$ (substrate thickness). The resulting top-hat filtered temperature map, along with average temperature and heat flux values for pool boiling at the highest tested flux (66.5 W/cm^2) are shown in Table F 1. Note that for the modified temperature map plotted in Table F 1, the control volumes are 50 percent overlapped.

Table F 1: Result of increasing control volume dimensions

	Δ (DI water test)	Larger Δ
Control Volume Dimensions	$\Delta x = \Delta y = 230 \mu\text{m}$	$\Delta x = \Delta y = 2 * 230 = 460 \mu\text{m}$
Temperature Maps		
T_{avg} (full map)	$T_{\text{avg}} = 116.99 \text{ }^\circ\text{C}$	$T_{\text{avg}} = 117.29 \text{ }^\circ\text{C}$
% Difference in $T_{\text{avg}} = 0.26$ percent		
q''_{avg} (full map)	$5.23\text{e}+005 \text{ W/m}^2$	$4.97\text{e}+005 \text{ W/m}^2$
% Difference in $q''_{\text{avg}} = 5.14$ percent		

As seen in the results of these calculations, no significant differences in the resulting temperature maps were observed with change in control volume dimensions. The main reason for this result is the top-hat filtering (weighted averaging of pixels) that is performed on the temperature maps as a first step in the IR data reduction process. The temperature values averaged over the entire map before and after modifying the control volume dimensions were within 0.26% of each other. The corresponding average convective heat fluxes before and after modifying the control volume dimensions were within 5.14% of each other.

The above results indicate that the choice of control volume dimensions does not have a significant effect on the temperature maps and hence the convective heat fluxes computed, owing to the top hat filtering on the temperature maps prior to control volume analysis.

APPENDIX

G. MICROSCALE HEATER- IR IMAGE CALIBRATION

Detailed calibration analysis was conducted to obtain the best calibration fit for the IR temperature maps of the microscale heater. This was important to correct for the technical issues (see section 5.3.2) resulting from the camera positioning, oxide layer thickness and the Narcissus effect faced during calibration and actual experiments.

Calibration fits of the first, second and fourth orders were implemented to check the resulting effect on the calibration temperature points. Since calibration was performed with the test fluid FC-72 upto 54°C (below $T_{\text{sat}}=56^{\circ}\text{C}$) it was important to check the calibrated temperatures that would result from the fits for temperatures higher than the fluid saturation temperature. Figure G 1 shows the resulting fits for an on-heater pixel.

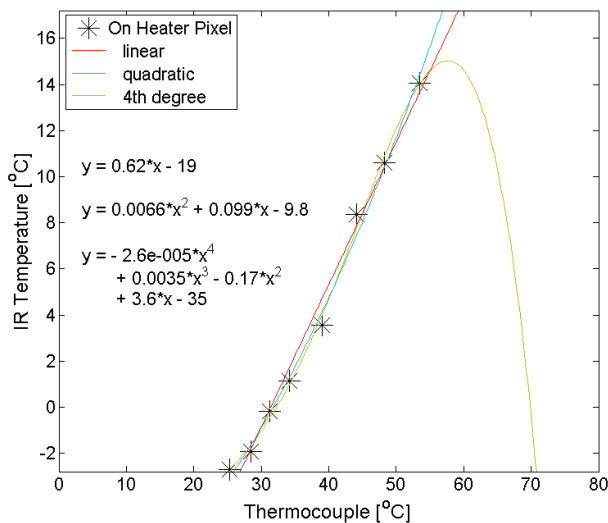


Figure G 1: First, second and fourth order calibration curves for a pixel location on the heater

Figure G 1 clearly shows that while the first and second order fits were able to extrapolate higher temperatures in the regions beyond the calibrated range, the fourth

order fit performed poorly resulting negative temperature values in these regions. Figure G 2 shows the result of applying these fits to an IR map for a 20°C subcooled pool boiling test condition. The IR maps shown here were acquired at an input power of approximately 8W.

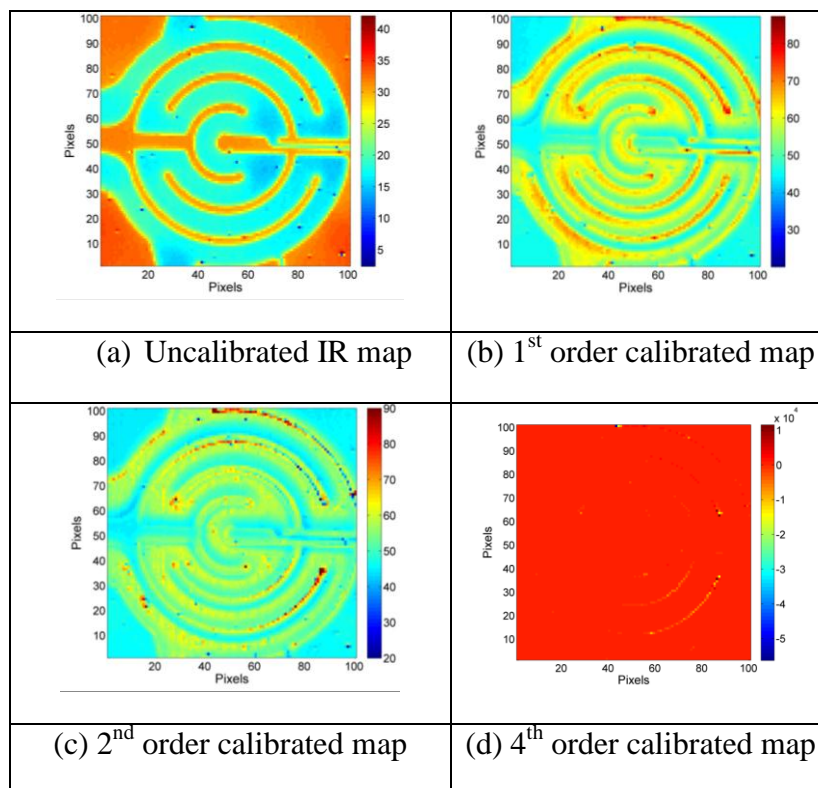


Figure G 2: Comparison of IR temperature maps obtained from first, second, and fourth order calibration fits at each pixel.

From the IR images it is evident that the fourth order fit was unable to resolve temperatures in all on-heater and off-heater locations. Similar trends were observed for a third order fit as well. Further comparisons were therefore limited to first and second order fits. Fig. G 2 also shows the importance of considering calibration results at the edge of the heater rings, as much higher temperatures resulted in these locations

post-first and second order calibration. Figures G 3- G 5 compare the performance of the first and second order fits at pixels located on the heater, off the heater and for a pixel at the edge of the heater rings, for raw as well as filtered calibration temperature values.

From Fig. G 3 it can be concluded that temperatures in the off-heater locations are predicted well by the both fits. However for the on-heater locations it is clear that the second order fit over predicts temperatures beyond the calibrated range. At the edge pixel, both fits resulted in relatively higher standard error compared to the on and off-heater locations. To improve the temperature extrapolations for the heater edge and on-heater pixels the top-hat filtering procedure described in section 5.3.1 was tested. Figure G 4 and G 5 show the calibration curves that resulted from filtering the calibration temperature maps once and twice respectively prior to applying the fits. From the images it was concluded that top-hat filtering the images twice before calibrating can serve to reduce calibration fit errors while predicting temperatures reasonably well in all imaged locations. Also first order fit consistently predicts reasonable temperatures for all locations. Based on these findings, all calibration and experimental data maps were filtered twice followed by a linear calibration fit.

Calibration curves - Pool boiling test surface calibration		Standard error
On heater pixel	<p>IR Temperature [°C] Thermocouple [°C]</p> <p>$y = 0.62x - 19$ $y = 0.0066x^2 + 0.099x - 9.8$</p> <p>Legend: * On Heater Pixel, — linear, — quadratic</p>	Linear Fit: 0.30
	<p>residuals</p> <p>Thermocouple [°C]</p>	Quadratic Fit: 0.25
Off heater pixel	<p>IR Temperature [°C] Thermocouple [°C]</p> <p>$y = 0.88x - 7.1$ $y = 0.0014x^2 + 0.77x - 5$</p> <p>Legend: * Off heater pixel, — linear, — quadratic</p>	Linear Fit: 0.14
	<p>residuals</p> <p>Thermocouple [°C]</p>	Quadratic Fit: 0.15
Heater edge pixel	<p>IR Temperature [°C] Thermocouple [°C]</p> <p>$y = 0.46x + 2$ $y = -0.0024x^2 + 0.64x - 1.4$</p> <p>Legend: * Heater edge pixel, — linear, — quadratic</p>	Linear Fit: 0.92
	<p>residuals</p> <p>Thermocouple [°C]</p>	Quadratic Fit: 1.10

Figure G 3: Comparison of first and second order calibration curves for on and off-heater locations

Calibration curves with one T_{filter} - Pool boiling calibration		Standard error
On heater pixel	<p> $y = 0.65x - 20$ $y = 0.0047x^2 + 0.28x - 14$ </p>	Linear Fit: 0.26
		Quadratic Fit: 0.25
Off heater pixel	<p> $y = 0.88x - 7.2$ $y = 0.0028x^2 + 0.66x - 3.1$ </p>	Linear Fit: 0.13
		Quadratic Fit: 0.11
Heater edge pixel	<p> $y = 0.53x - 1.8$ $y = -0.0023x^2 + 0.71x - 5.1$ </p>	Linear Fit: 0.78
		Quadratic Fit: 0.94

Figure G 4: Calibration curves with temperatures top-hat filtered once

Calibration curves with two T_{filter} - Pool boiling calibration		Standard error
On heater pixel	<p>IR Temperature [°C]</p> <p>Thermocouple [°C]</p> <p> $y = 0.66*x - 21$ $y = 0.0042*x^2 + 0.33*x - 14$ </p> <p> * On heater pixel — linear — quadratic </p>	Linear Fit: 0.25
	<p>residuals</p> <p>Thermocouple [°C]</p>	Quadratic Fit: 0.25
Off heater pixel	<p>IR Temperature [°C]</p> <p>Thermocouple [°C]</p> <p> $y = 0.88*x - 7.3$ $y = 0.003*x^2 + 0.64*x - 2.9$ </p> <p> * Off heater pixel — linear — quadratic </p>	Linear Fit: 0.13
	<p>residuals</p> <p>Thermocouple [°C]</p>	Quadratic Fit: 0.10
Heater edge pixel	<p>IR Temperature [°C]</p> <p>Thermocouple [°C]</p> <p> $y = 0.56*x - 3.6$ $y = -0.0013*x^2 + 0.66*x - 5.5$ </p> <p> * Heater edge pixel — linear — quadratic </p>	Linear Fit: 0.67
	<p>residuals</p> <p>Thermocouple [°C]</p>	Quadratic Fit: 0.80

Figure G 5: Calibration curves with temperatures top-hat filtered twice

APPENDIX

H. MATRIX OF EXPERIMENTS

Table H 1: Matrix of experiments conducted with the macroscale heater with subcooling details

Fluid	d_{jet} (mm)	H/d_{jet}	Subcooling (°C)	Re_{jet}	u_{jet} (m/sec)	Nozzle Geometry
Water	1.16	3.6	19.0	0	0	Regular
			19.0	2580	0.81	
			19.2	5161	1.6	
FC-72	1.16	3.6	0	0	0	
			0	5161	1.22	
			0	7740	1.83	
			18.9	0	0	
			18.8	5161	1.46	
			20.2	7740	2.19	
			20.1	7866	2.23	
	0.5	6	0	10778	5.92	
			0	10616	5.83	Cavitating
	1.10	6	0	18416	4.59	Cavitating
20.2			18562	5.54	Cavitating	

Table H 2: Matrix of experiments conducted with the microscale heater using a regular jet nozzle with subcooling details

Fluid	d_{jet} (mm)	H/d_{jet}	Subcooling (°C)	Re_{jet}	u_{jet} (m/sec)	Radial Location (mm)
FC-72	0.5	6	9.0	0	0	1.5
			9.1	3181	1.9	
			18.8	0	0	1.5
			19.1	3128	2.05	

APPENDIX

I. COPPER VERSUS SILICON - EFFECT OF SURFACE MATERIAL ON JET IMPINGEMENT BOILING OF FC-72

To probe the effect of surface material on the phase change heat transfer characteristics of FC-72, submerged jet impingement boiling a collaborative study was conducted on two surfaces with different surface roughness and thermal capacities. The first surface used was the macroscale serpentine heater silicon (Si) substrate described in this thesis (Fig. 13) having an average surface roughness 0.89 nm. The second was a 27.64 mm diameter oxygen free smooth copper (Cu) surface of roughness 33 nm. All tests on the copper surface were collected in the same test facility as described in this thesis and the individual results were reported by Cardenas [26]. The copper substrate was a uniform heat flux surface heated by cartridge heaters. As a result comparisons between the two surfaces were made by with the use of the area-averaged boiling curves described in the results section of this thesis. Figure I 1 compares the global boiling trends for saturated SJIB of FC-72 on the silicon (Si) test surface with the smooth copper (Cu) surface.

Figure I 1 clearly indicates that incipience overshoots for FC-72 varied randomly with the choice of surface, jet diameter and the Re_{jet} . As a result the corresponding single phase region varied significantly in its extent for each condition tested. Boiling initiated at notably lower superheats on copper than on silicon under the similar test conditions. The greater surface roughness of copper over silicon allowed for a larger number of nucleation sites permitting a transition to boiling at lower wall superheats. For polished surfaces like silicon, in contact with a highly wetting fluid the existing surface cavities flood easily, thus, requiring larger superheats for the onset of boiling. Consequently, the boiling curve for silicon was shifted to right.

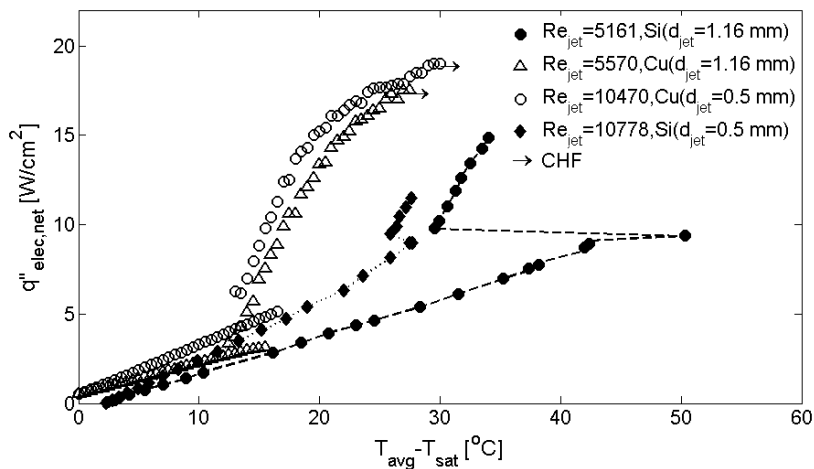


Figure I 1: SJB of FC-72 on copper and silicon surfaces

Post transition to boiling the two-phase heat transfer rates acquired with FC-72 on copper (0.58 and 0.68W/cm²°C for $Re_{jet} = 5570$ and $Re_{jet} = 10470$ respectively) were found to be higher than that obtained with silicon (~0.4W/cm²°C). Experiments with the copper surface typically attained CHF conditions around a wall superheat of 30 °C. For the silicon surface CHF was not attained due to limits of the power supply; however the superheats that were required to initiate phase change on silicon were either comparable to or in excess of the superheat temperatures at CHF for copper.

APPENDIX

J. RADIAL PROFILES OF THE HEAT TRANSFER COEFFICIENT FOR DI WATER (MACROSCALE HEATER)

The local values of the heat transfer coefficient, $h(r)$, were calculated using two different estimates of the heat flux

$$h_{elec}(r) = \frac{q''_{elec}}{(T(r) - T_{fluid})} \quad (A)$$

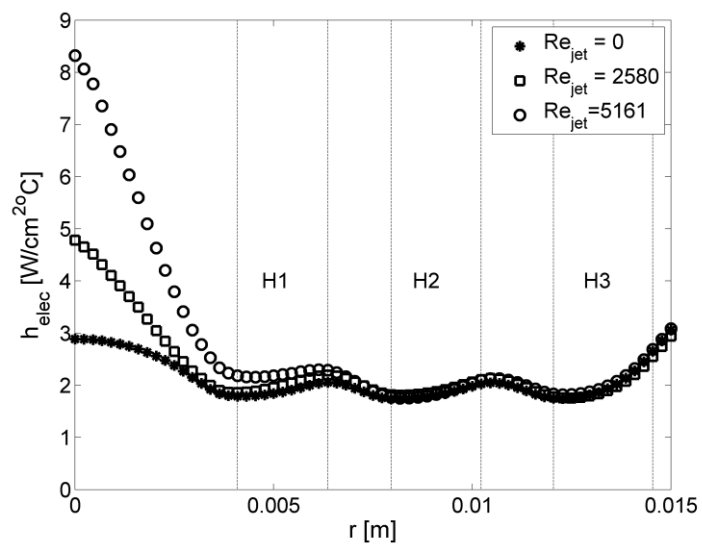
$$h_{conv}(r) = \frac{q''_{conv}(r)}{(T(r) - T_{fluid})} \quad (B)$$

where T_{fluid} was approximated as the average of the jet and pool temperatures measured by the thermocouples in each test jet impingement test case (see Eq. 10).

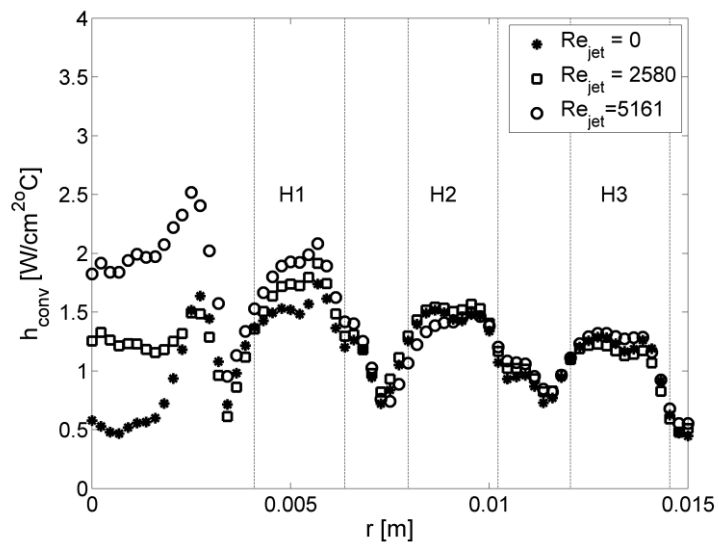
While $T_{fluid} = T_{pool}$ for a pool boiling test case.

The electrical heat flux, q''_{elec} (Eq. A) was calculated using an area equal to that occupied by the heater rings alone (A_h) (see Fig. 30), however it was assumed that the electrical heat flux input is applied uniformly over the entire 27.5 mm heated substrate (A_s). Such an estimate would represent the heat transfer coefficient distribution for a uniform heat flux boundary condition, where substrate conduction would be non-existent.

The ratio of the area occupied by the heater rings alone (A_h) to the 27.5 mm diameter heated substrate area (A_s) was 90 percent. Thus, the heat transfer coefficients calculated using the areas A_h and A_s seen to follow identical trends, with the values for the former case shifted up by about 10 percent.



(a)



(b)

Figure J 1: Circumferentially averaged profiles of the heat transfer coefficient obtained with DI water at 66 W/cm² computed using (a) q''_{elec} (b) $q''_{conv}(r)$.

Equation B, provided the heat transfer coefficient estimate based on the values of the calculated convective heat flux, $q''_{conv}(r)$. Such an estimate accounts for the radial non-uniformity in heat flux distribution, and is hence truly representative of the actual heat transfer distribution in the present experiments.

Figure J 1 compares the radial profiles for the heat transfer coefficient obtained for tests with DI water on the macroscale heater substrate at the highest tested flux of 66 W/cm² for all the three test cases. Figure J 1a depicts the circumferentially averaged $h_{elec}(r)$ profile. Figure J 1b shows the circumferentially averaged $h_{conv}(r)$ profile.

Note that in Fig. J1a, regions of higher $h_{elec}(r)$ are observed in non-heater ring regions for the case of pool boiling ($Re_{jet} = 0$). While variations in $h_{elec}(r)$ could be expected due to the random nature of pool boiling, the systematic high $h_{elec}(r)$ in the non-heater regions is attributed to the use of a constant q''_{elec} over the entire heated substrate area, whereas in reality the applied electrical heat flux in these non-heater regions is zero. A pronounced enhancement in heat transfer at and around $r = 0$, for the $Re_{jet} = 5161$ case is observed. At the stagnation point, the $h_{elec}(r)$ value is seen to increase by a factor of 1.5 with doubling of Re_{jet} . Figure J 1a clearly delineates the radial distance over which the wall jet exerts its influence. While the flow at $Re_{jet} = 2580$ enhances heat transfer close to the jet impingement point ($r = 0$) over that of the $Re_{jet} = 0$ (pool boiling) case, its radial impact diminishes at approximately 0.003 m ($2.6d_{jet}$) from the stagnation point. In comparison, the influence of the higher jet flow rate case ($Re_{jet} =$

5161) extends further out to approximately 0.007 m ($6d_{\text{jet}}$) from the stagnation point. This extent of influence is consistent with the extent of jet influence observed in the temperature profile shown in Fig.61, image 3(d). Local minima in $h_{\text{elec}}(r)$ are observed corresponding to the peaks temperatures locations observed in Fig.61, image 3(d).

Figure J 1b shows the radial profiles for the heat transfer coefficient ($h_{\text{conv}}(r)$) obtained by providing input heat flux only at the heater locations and accounting for the conduction in the substrate. Within the region of the inner ring ($r < 0.003$ m) the heat transfer coefficient is diminished with decrease in Re_{jet} which is consistent with that seen in Fig. J 1a. However the magnitude and the radial distribution of $h_{\text{conv}}(r)$ is significantly different from that of $h_{\text{elec}}(r)$ in this region. Local minima that were observed in Fig. J 1a, appear more pronounced in the $h_{\text{conv}}(r)$ due to the reduction in electrical heat flux as a result of incorporating the axial conduction. The extent of the jet influence on convective heat transport is consistent with that seen in Fig. J 1a.

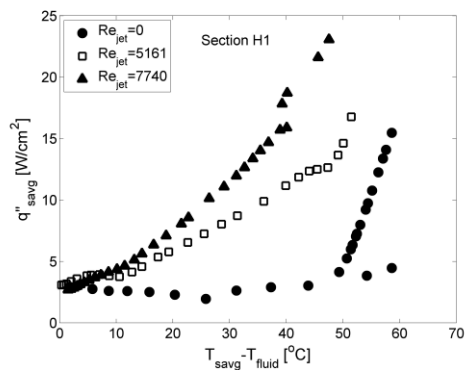
APPENDIX

K. SECTIONALLY-AVERAGED BOILING CURVES FOR SUBCOOLED FC-72 ON HEATED REGIONS H1, H2, AND H3 (MACROSCALE HEATER)

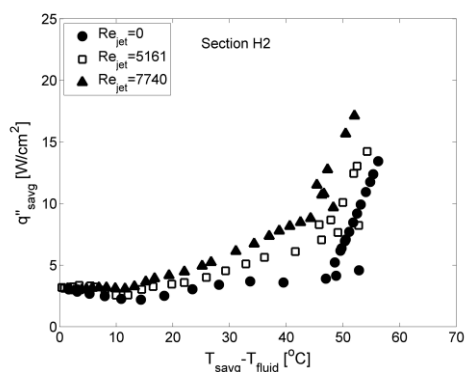
Figure K 1 depicts the sectionally-averaged boiling curves for 20°C subcooled FC-72 with increasing radial distance from the impingement point. Figure K 1a shows the boiling curves for heated section H1.

In the absence of a jet for $Re_{jet} = 0$ (pool boiling), heat transfer in H1 remained in the single phase regime ($h_{sp} = 0.07 \text{ W/cm}^2\text{°C}$) up to a temperature difference of ($T_{avg} - T_{fluid}$) of 59°C with notable changes in temperature for small increments in the convective heat flux (q''_{avg}). Initiation of boiling at this section H1 resulted in a temperature drop of about 9.3°C. With further increments in heat flux, a drastic increase in the slope of the boiling curve was observed indicative of two-phase boiling heat transfer. Jet impingement with $Re_{jet} = 5161$ enhanced the single phase heat transfer coefficient to $0.38 \text{ W/cm}^2\text{°C}$. The single phase region existed up to a temperature difference of 45.4°C. Onset of phase change resulted in a temperature drop of 3.5°C over this section. Increasing $Re_{jet} = 7740$ enhanced the single phase heat transfer coefficient to $0.43 \text{ W/cm}^2\text{°C}$. The corresponding temperature drop was only about 1.19°C.

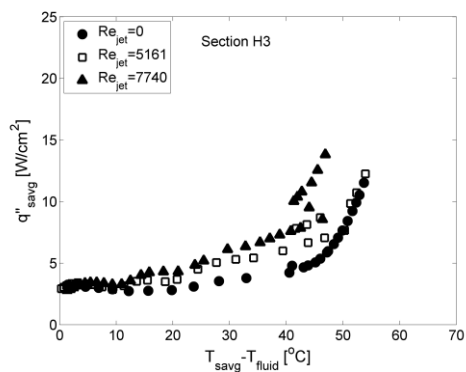
Similar to what was described for DI water (Fig. 62), the single phase heat transfer enhancement with increasing Re_{jet} was found to be most pronounced in section H1 due to its proximity to the jet impingement point. Figure K 1b and c for sections H2 and H3 clearly show that these enhancements with increasing Re_{jet} declined with increasing radial distance.



(a)



(b)



(c)

Figure K 1: Sectional boiling curves for 20°C subcooled FC-72 over the heated sections (a) H1 (b) H2 and (c) H3 of the macroscale heater substrate

The single phase heat transfer coefficients for the three test cases in section H2 were 0.17 W/cm²°C for $Re_{jet}=0$, 0.24 W/cm²°C for $Re_{jet}=5161$ and 0.26 W/cm²°C for $Re_{jet}=7740$ respectively. For the same test cases boiling at section H2 initiated at a temperature difference of 52.8°C, 52.7°C and 48.3 °C. At section H3 heat transfer coefficients of 0.23 W/cm²°C, 0.25 W/cm²°C and 0.27 W/cm²°C were achieved for $Re_{jet}=0$, $Re_{jet}=5161$ and $Re_{jet}=7740$ respectively with incipient temperature differences of 43.4 °C , 50.3 °C and 46.4 °C.

While thermal overshoots for pool boiling were found to be largest in section H1 and declined with increasing radial distance, the corresponding overshoots for the jet impingement cases were least in the section H1 and increased in sections H2 and H3 further away from the impingement point.

APPENDIX

L. CONTACT ANGLE MEASUREMENTS OF WATER ON SILICON SUBSTRATE

Equilibrium contact angle of a water droplet on a silicon substrate was estimated by conducting a sessile drop experiment. The polished silicon substrates were identical to those used for the boiling studies, with an average surface roughness of 0.89 nm and a 2 μm oxide coating.

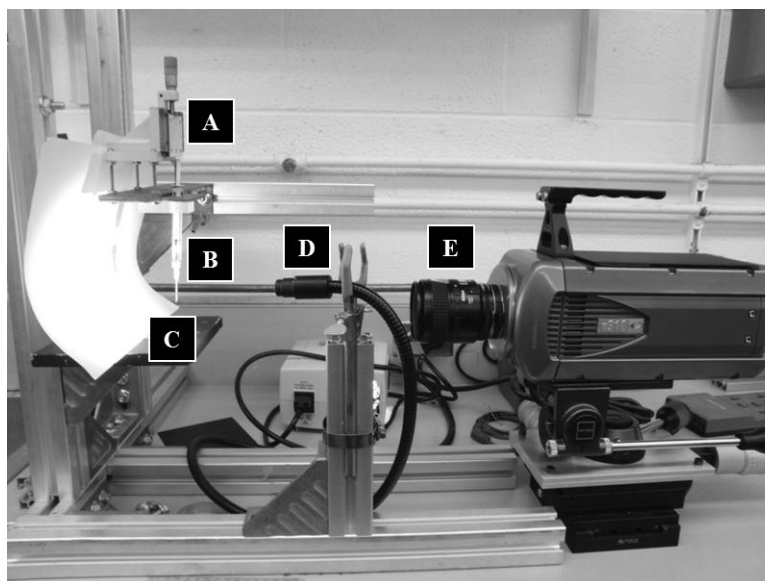


Figure L 1: Set-up for sessile drop experiment

Figure L 1 shows the experimental set-up used for the sessile drop experiments. A syringe with a one inch long, 16 gauge PrecisionGlide[®] hypodermic needle was used to dispense droplets of deionized water onto the silicon substrate positioned approximately 14 mm below the needle tip. The syringe was held at a fixed position and micrometer adjustment along the z-axis was used to generate droplets weighing approximately 20mg. The droplets released from the needle tip due the effect of gravity and impinged on the silicon substrate.

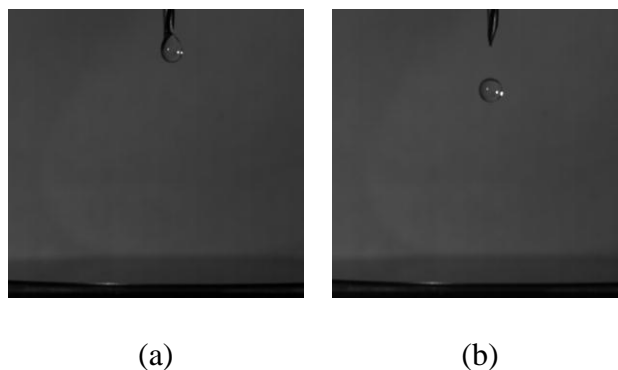


Figure L 2: Droplet shape before and after release

Figure L 2 shows the images of the droplet taken just prior to and post release. Post-impact images of the droplet on the surface were taken to determine the contact angle at equilibrium as well as the change in the contact angle over time.

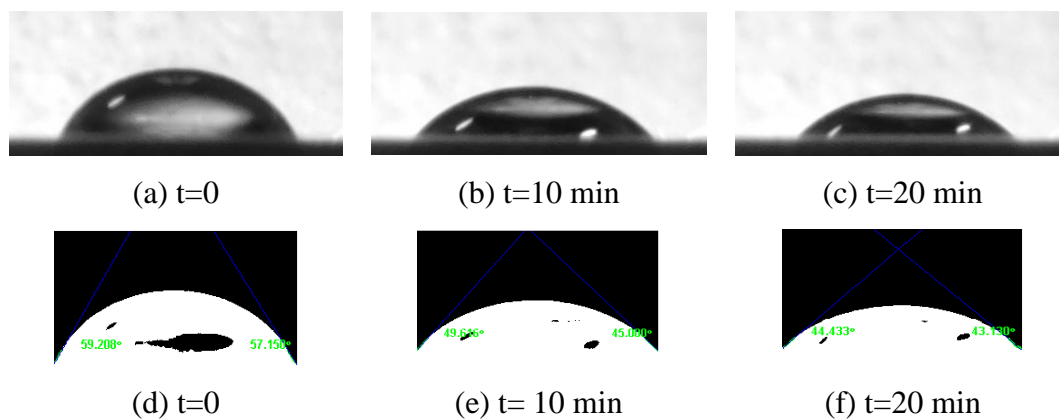


Figure L 3: Change in the profile of a water droplet on the silicon substrate as a function of time

Figure L 3 (a-c) shows the droplet profile on the silicon substrate as a function of time starting at equilibrium ($t = 0$). While no significant changes were observed in the

contact line, the apparent contact angles clearly decreased with progression of time. The acquired images were processed in MATLAB to obtain quantitative assessments of the contact angles. At first, the images of the droplet profiles were binarized following which edge detection tools in MATLAB were used to define the droplet contour. The area outlined by the contour was filled to define the region occupied by the droplet. Tangents defining the contact angles at the left and right vertices (the interface of the liquid, solid and vapor phases) of the two dimensional bubble profiles were determined by averaging ten pixels at these two interfacial points. Figure L 4 shows the variation in the average evaluated contact angle with progression of time.

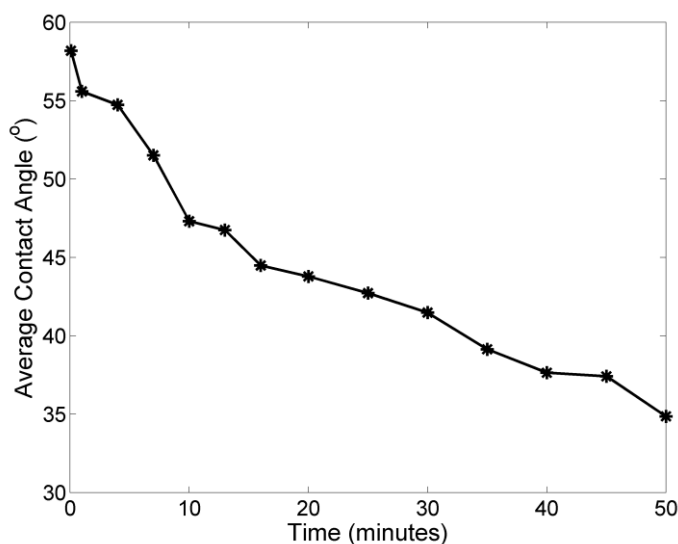


Figure L 4: Variation in the average contact angle of a water droplet on a silicon surface with time